

UNIVERSIDAD POLITÉCNICA DE MADRID

ESCUELA TÉCNICA SUPERIOR DE INGENIEROS INDUSTRIALES



*CALCULATION METHODOLOGY AND FABRICATION PROCEDURES FOR PARTICLE
ACCELERATOR STRIP-LINE KICKERS: APPLICATION TO THE CTF3 COMBINER
RING EXTRACTION KICKER AND TL2 TAIL CLIPPERS*

TESIS DOCTORAL

IKER RODRÍGUEZ GARCÍA
Ingeniero Industrial

Madrid, 2009

DEPARTAMENTO DE INGENIERÍA ELÉCTRICA

ESCUELA TÉCNICA SUPERIOR DE
INGENIEROS INDUSTRIALES



*CALCULATION METHODOLOGY AND FABRICATION PROCEDURES
FOR PARTICLE ACCELERATOR STRIP-LINE KICKERS: APPLICATION
TO THE CTF3 COMBINER RING EXTRACTION KICKER AND TL2 TAIL
CLIPPERS*

Autor: D. Iker Rodríguez García (Ingeniero Industrial)

Director: D. Marcos Lafoz Pastor (Doctor Ingeniero Industrial)

Director: D. Fernando Toral Fernández (Doctor Ingeniero Industrial)

Madrid, 2009

Tribunal nombrado por el Magfco. y Excmo. Sr. Rector de la Universidad Politécnica de Madrid, el día de de 200 .

Presidente: D. Jaime Rodríguez Arribas

Vocal: D^a. Caterina Biscari de la Hoz

Vocal: D. Francisco José Pérez Rodríguez

Vocal: D. Daniel Galaviz Redondo

Secretario: D. Luis García-Tabarés Rodríguez

Suplente: D. Francisco Blázquez García

Suplente: D^a. Cristina Vázquez Vélez

Realizado el acto de defensa y lectura de la tesis el día de de 200
en la E.T.S. Ingenieros Industriales.

CALIFICACIÓN:

EL PRESIDENTE

LOS VOCALES

EL SECRETARIO

ACKNOWLEDGMENTS

As with any experimental effort, many people have contributed to the successful completion of this project. My foremost thank goes to my thesis advisors Fernando Toral and Marcos Lafoz for their constant technical support and guidance throughout my Thesis research.

I am grateful to the people at CERN who have helped me during the development of the project: Mike Barnes and Tony Fowler for their help with the device specifications and the fruitful collaboration, and Igor Syratchev for the huge wakefields simulations.

I also thank the LNF/INFN team, especially to David Alesini, who taught me some strip-line concepts and helped me with the experimental tests.

I am especially happy to acknowledge my deeply-felt thanks to David Carrillo for our helpful discussions about RF matters and to Cristina Vázquez for her relentless encouragement.

I want to express my gratitude to Enrique Rodríguez for his help with the SolidWorks drawings, to Pablo Abramiam for manufacturing the flexible electrical connections in the kicker and to the rest of my colleagues at CIEMAT for their help throughout these four years of research.

I would also like to thank the people who have encouraged me to carry on the hard work of writing the Thesis during many endless months, especially to my girlfriend María.

Finally, I thank CIEMAT for providing the resources and general support of the project, and Vacuum Projects for the good job manufacturing and assembling the prototypes.

CONTENTS

1	Particle accelerators and particle diversion	- 19 -
1.1	<i>The particle accelerators world</i>	- 19 -
1.1.1	The purpose of particle accelerators	- 19 -
1.1.2	A brief history about accelerators	- 23 -
1.1.3	Present day machines	- 34 -
1.2	<i>Typical components in a particle accelerator</i>	- 37 -
1.2.1	Particle sources	- 37 -
1.2.2	RF cavities	- 39 -
1.2.3	Beam diversion and focusing devices	- 42 -
1.2.4	Injection and extraction devices	- 44 -
1.2.5	Diagnostics	- 46 -
1.2.6	Detectors	- 48 -
1.3	<i>Deflecting particles: Electric and Magnetic fields</i>	- 51 -
1.3.1	Slow and constant deflection	- 51 -
1.3.1.1	Dipoles	- 52 -
1.3.1.2	Septa	- 55 -
1.3.2	Fast and selective deflection	- 58 -
1.4	<i>Strip-line kickers basics</i>	- 63 -
1.4.1	Characteristic impedance	- 63 -
1.4.2	Electric and magnetic fields: RF or Pulsed Power	- 66 -
1.4.3	Fast pulse response	- 67 -
1.4.4	Dissipation load	- 71 -
1.5	<i>Conclusions</i>	- 72 -
1.6	<i>References</i>	- 73 -
2	Calculation methodology for strip-line kickers	- 75 -
2.1	<i>Basic specifications</i>	- 75 -
2.1.1	Integrated fields: the transverse voltage and deflection strength	- 75 -
2.1.2	The minimum aperture	- 78 -
2.1.3	Pulse parameters	- 79 -
2.1.4	The wakefields	- 80 -

2.2	<i>2D calculations</i>	- 89 -
2.2.1	Analytical methods computations	- 89 -
2.2.1.1	Energy and momentum	- 90 -
2.2.1.2	The transverse voltage and shunt impedance	- 91 -
2.2.1.3	Voltage, current and power. Pulser requirements estimation	- 94 -
2.2.2	Numerical methods	- 96 -
2.2.2.1	Strip-line impedance and cross section design: homogeneity	- 96 -
2.2.2.2	Wakefields axi-symmetrical calculations	- 103 -
2.3	<i>3D calculations</i>	- 106 -
2.3.1	Frequency-domain simulations	- 106 -
2.3.1.1	The scope of frequency-domain simulation	- 106 -
2.3.1.2	Numerical model set up	- 107 -
2.3.1.2.1	Model considerations	- 107 -
2.3.1.2.2	Input power	- 111 -
2.3.1.3	Transmission and reflection: S parameters and coaxial to strip-line transition	- 111 -
2.3.1.4	Integrated homogeneity	- 118 -
2.3.1.5	Lost power	- 119 -
2.3.1.6	Cross check of analytical calculations	- 120 -
2.3.1.7	High Order Modes analysis	- 121 -
2.3.1.8	Coupling and transfer impedances: The coaxial wire method.	- 126 -
2.3.1.9	Available software: HFSS	- 130 -
2.3.2	Time-domain simulations	- 135 -
2.3.2.1	The scope of time-domain simulation	- 135 -
2.3.2.2	Full wakefields calculations	- 136 -
2.3.2.2.1	Longitudinal wake potentials and loss factor	- 138 -
2.3.2.2.2	Transverse wakes and impedances	- 138 -
2.3.2.3	Available software	- 139 -
2.3.2.3.1	2D: ABCI	- 139 -
2.3.2.3.2	3D: CST Particle Studio	- 140 -
2.3.3	Application example: pillbox cavity	- 141 -
2.4	<i>Conclusions</i>	- 152 -
2.5	<i>References</i>	- 153 -

3	Fabrication procedures and tests for strip-line kickers	- 157 -
3.1	<i>Introduction</i>	- 157 -
3.2	<i>Design</i>	- 158 -
3.2.1	Material choice	- 158 -
3.2.2	Electrical connections: feedthroughs	- 160 -
3.2.3	Stand-offs	- 164 -
3.3	<i>Manufacturing</i>	- 167 -
3.3.1	Electrodes	- 167 -
3.3.2	Vacuum tank	- 168 -
3.3.3	Flanges	- 169 -
3.3.4	Beam pipe transitions	- 171 -
3.3.5	Support and alignment systems	- 172 -
3.3.6	Cleaning	- 174 -
3.4	<i>The acceptance tests</i>	- 176 -
3.4.1	Dimensional control	- 176 -
3.4.2	Vacuum tests	- 176 -
3.4.2.1	Vacuum level	- 177 -
3.4.2.2	Leak rate	- 178 -
3.4.3	RF Network analyzer tests	- 178 -
3.4.4	Unloaded voltage tests	- 180 -
3.4.5	50 Ohm loaded voltage tests	- 181 -
3.4.6	Coaxial wire method	- 183 -
3.5	<i>Conclusions</i>	- 183 -
3.6	<i>References</i>	- 184 -
4	First application to a real device: CTF3 Combiner Ring extraction kicker	- 187 -
4.1	<i>Purpose of the CTF3 Combiner Ring Extraction Kicker</i>	- 187 -
4.2	<i>Design and calculations</i>	- 192 -
4.2.1	The cross section choice	- 192 -
4.2.2	Device length and kick strength	- 194 -
4.2.3	Voltage, current and power. 2D wakefields.	- 195 -
4.2.4	Frequency domain 3D model set-up.	- 199 -
4.2.5	Coaxial to strip-line transition: S parameters	- 202 -
4.2.6	Numerical results	- 204 -
4.2.7	High Order Mode (HOM) analysis	- 207 -
4.2.8	Wakefield simulations	- 209 -

4.3	<i>CTF3 Kicker manufacturing issues</i>	- 217 -
4.3.1	Material selection	- 217 -
4.3.2	Feedthroughs	- 218 -
4.3.3	Stand-offs support	- 219 -
4.3.4	Electrodes	- 221 -
4.3.5	Flanges	- 222 -
4.3.6	Beam pipe transitions	- 223 -
4.3.7	Mechanical supports and alignment targets	- 224 -
4.4	<i>Tests results</i>	- 225 -
4.4.1	RF Network analyzer tests	- 225 -
4.4.2	Unloaded voltage tests	- 228 -
4.4.3	50 Ohm loaded voltage tests	- 229 -
4.5	<i>Conclusions</i>	- 231 -
4.6	<i>References</i>	- 232 -
5	Second application to a real device: CTF3 TL2 Tail Clippers	- 233 -
5.1	<i>Purpose of the CTF3 TL2 Tail Clippers</i>	- 233 -
5.2	<i>Calculations</i>	- 237 -
5.2.1	The cross section choice	- 237 -
5.2.2	Device length and kick strength	- 238 -
5.2.3	Voltage, current and power. 2D wakefields.	- 239 -
5.2.4	Coaxial to strip-line transition	- 241 -
5.2.5	Frequency domain 3D model set-up: S parameters	- 243 -
5.2.6	Cross talk between adjacent devices	- 245 -
5.2.7	Additional results	- 246 -
5.2.8	HOM analysis	- 247 -
5.2.9	Wakefield simulations	- 249 -
5.3	<i>TL2 Tail Clippers manufacturing issues</i>	- 253 -
5.3.1	Material selection	- 253 -
5.3.2	Feedthroughs	- 253 -
5.3.3	Stand-offs support	- 256 -
5.3.4	Electrodes	- 258 -
5.3.5	Flanges	- 259 -
5.3.6	Beam pipe transitions	- 260 -
5.3.7	Mechanical supports and alignment targets	- 261 -

5.4	<i>Tests results</i>	- 262 -
5.4.1	RF Network analyzer tests	- 263 -
5.4.2	Unloaded voltage tests	- 266 -
5.4.3	50 Ohm loaded voltage tests	- 267 -
5.5	<i>Conclusions</i>	- 270 -
5.6	<i>References</i>	- 271 -
6	Power supply considerations: Pulsed power supply	- 273 -
6.1	<i>Pulse switching technologies</i>	- 273 -
6.1.1	Introduction	- 273 -
6.1.2	Switching topologies	- 275 -
6.2	<i>Simplified Matlab-Simulink models of power supply topologies</i>	- 277 -
6.2.1	Stacked switch topology	- 278 -
6.2.2	Inductive Adder Topology	- 280 -
6.3	<i>Transmission line model of the CTF3 TL2 Tail Clipper</i>	- 283 -
6.4	<i>Putting all together</i>	- 284 -
6.5	<i>Conclusions</i>	- 288 -
6.6	<i>References</i>	- 289 -

ABSTRACT

A particle accelerator is any device that, using electromagnetic fields, is able to communicate energy to charged particles (typically electrons or ionized atoms), accelerating and/or energizing them up to the required level for its purpose. The applications of particle accelerators are countless, beginning in a common TV CRT, passing through medical X-ray devices, and ending in large ion colliders utilized to find the smallest details of the matter. Among the other engineering applications, the ion implantation devices to obtain better semiconductors and materials of amazing properties are included. Materials supporting irradiation for future nuclear fusion plants are also benefited from particle accelerators.

There are many devices in a particle accelerator required for its correct operation. The most important are the particle sources, the guiding, focalizing and correcting magnets, the radiofrequency accelerating cavities, the fast deflection devices, the beam diagnostic mechanisms and the particle detectors.

Most of the fast particle deflection devices have been built historically by using copper coils and ferrite cores which could effectuate a relatively fast magnetic deflection, but needed large voltages and currents to counteract the high coil inductance in a response in the microseconds range. Various beam stability considerations and the new range of energies and sizes of present time accelerators and their rings require new devices featuring an improved wakefield behaviour and faster response (in the nanoseconds range). This can only be achieved by an electromagnetic deflection device based on a transmission line.

The electromagnetic deflection device (strip-line kicker) produces a transverse displacement on the particle beam travelling close to the speed of light, in order to extract the particles to another experiment or to inject them into a different accelerator. The deflection is carried out by the means of two short, opposite phase pulses. The diversion of the particles is exerted by the integrated Lorentz force of the electromagnetic field travelling along the kicker.

This Thesis deals with a detailed calculation, manufacturing and test methodology for strip-line kicker devices. The methodology is then applied to two real cases which are fully designed, built, tested and finally installed in the CTF3 accelerator facility at CERN (Geneva). Analytical and numerical calculations, both in 2D and 3D, are detailed starting from the basic specifications in order to obtain a conceptual design. Time domain and frequency domain calculations are developed in the process using different FDM and FEM codes. The following concepts among others are analyzed: scattering parameters, resonating high order modes, the wakefields, etc. Several contributions are presented in the calculation process dealing specifically with strip-line kicker devices fed by electromagnetic pulses.

Materials and components typically used for the fabrication of these devices are analyzed in the manufacturing section. Mechanical supports and connexions of electrodes are also detailed, presenting some interesting contributions on these concepts. The electromagnetic and vacuum tests are then analyzed. These tests are required to ensure that the manufactured devices fulfil the specifications.

Finally, and only from the analytical point of view, the strip-line kickers are studied together with a pulsed power supply based on solid state power switches (MOSFETs). The solid state technology applied to pulsed power supplies is introduced and several circuit topologies are modelled and simulated to obtain fast and good flat-top pulses.

RESUMEN

Un acelerador de partículas es cualquier dispositivo que, mediante campos electromagnéticos, comunica energía a partículas cargadas (típicamente electrones o átomos ionizados) y las acelera y/o energiza hasta valores útiles para su propósito. Las aplicaciones de los aceleradores son innumerables, desde un simple televisor CRT, pasando por los aparatos médicos de rayos X, hasta los grandes colisionadores de iones utilizados para descubrir los más pequeños entresijos de la materia. Entre las aplicaciones más ingenieriles se incluyen dispositivos de implantación iónica para conseguir mejores semiconductores y materiales con combinaciones de propiedades sorprendentes, o incluso materiales irradiables para futuras fuentes de fusión nuclear.

Dentro de un acelerador de partículas existen decenas de dispositivos necesarios para su funcionamiento. Los más reseñables son las fuentes de partículas, los imanes de guiado y de focalización, las cavidades de aceleración mediante radiofrecuencia, los sistemas de deflexión rápida, los sistemas de diagnóstico del haz de partículas y los detectores.

La mayor parte de los dispositivos de deflexión rápida se han diseñado históricamente mediante bobinas de cobre con núcleos de ferrita que realizaban una deflexión magnética relativamente rápida, pero que necesitaban grandes tensiones y corrientes combinadas para contrarrestar la elevada inductancia de las bobinas en una respuesta del orden de microsegundos. Diversas consideraciones de estabilidad del haz de partículas y las nuevas energías y tamaños de los actuales aceleradores y sus anillos requieren de un nuevo tipo de construcción menos agresiva con el propio haz de partículas y con mayor velocidad de respuesta (nanosegundos). Esto sólo puede conseguirse mediante un dispositivo de deflexión electromagnética consistente en una línea de transmisión.

El dispositivo de deflexión de tipo línea de transmisión (stripline kicker en inglés) se encarga de desplazar transversalmente la trayectoria del haz de partículas en un acelerador a velocidades cercanas a las de la luz, para extraer las partículas una vez procesadas y llevarlas al experimento o proceso en cuestión o, simplemente, inyectarlas en otro acelerador. La deflexión se lleva a cabo mediante dos pulsos extremadamente cortos y en contrafase, apareciendo dentro del dispositivo un campo electromagnético viajero cuya fuerza de Lorentz integrada desvía las partículas en el sentido deseado.

Esta Tesis versa precisamente sobre un método detallado de cálculo, fabricación y ensayos de dispositivos de deflexión tipo línea de transmisión. El método se aplica a dos casos reales que se diseñan, construyen y ensayan y que finalmente serán instalados en el acelerador CTF3 del CERN (Ginebra). Partiendo de las especificaciones básicas, se detallan los cálculos analíticos y numéricos, tanto 2D como 3D, necesarios para obtener un diseño conceptual. Se desarrollan cálculos en el dominio del tiempo y de la frecuencia utilizando varios programas de tipo FDM y FEM. Se introducen entre otros los conceptos de los parámetros de dispersión, la problemática de los modos resonantes de orden superior, los denominados campos de estela (wakefields), etc. Dentro del proceso de cálculo se realizan varias aportaciones novedosas específicas para dispositivos alimentados por pulsos electromagnéticos.

En el apartado de fabricación se analizan los distintos materiales y componentes típicamente utilizados para la construcción de los dispositivos. También se indican distintas formas de conexión y soporte mecánico de los electrodos, mostrando algunas aportaciones novedosas en estos conceptos. Seguidamente se detallan los ensayos electromagnéticos y de vacío que es necesario realizar a los dispositivos deflectores ya fabricados para asegurar que cumplen los criterios de diseño establecidos.

Para finalizar, y de un modo únicamente analítico, se estudian los dispositivos de deflexión y su respuesta en conjunción con una fuente de alimentación pulsada con tecnología basada en interruptores electrónicos de potencia (MOSFETs). Se presenta una introducción a la tecnología de estado sólido para fuentes pulsadas y se modelan varias topologías útiles para conseguir pulsos rápidos con una zona plana estable.

CHAPTER 1

PARTICLE ACCELERATORS AND PARTICLE DIVERSION

1.1 THE PARTICLE ACCELERATORS WORLD

1.1.1 *THE PURPOSE OF PARTICLE ACCELERATORS*

Almost all the engineers around the world know the existence of particle accelerators. However, only a few of them can explain what they are used for, and even less can explain how they do work, although they are the people in charge of manufacturing those complex systems. In effect, besides particle physics, particle accelerators have much more applications in other technical areas related with engineering and medicine. However, particle physics research has always been the main driving force in the development of particle accelerators. Certainly, it was the need of atomic projectiles faster than natural radioactive sources which most improved the development of accelerators, aiming to analyse in more detail the structure of the Rutherford's atom model.

Many are the applications of the accelerators besides particle physics. These applications can be divided in three areas taking into account the type of beams used [1]:

1. Beams of particles employed as probes in the analysis of physical, chemical and biological properties of samples. Particle Induced Xray Emission (PIXE) is a notable example.
2. Beams of particles used for the modification of the physical, chemical and biological properties of matter. Sterilisation can be quoted here.
3. The most energetic beams of particles are today the main instruments for research in basic subatomic physics.

The time tree (Fig. 1.1) shows the progress of accelerators in parallel with some of their applications. It is observed that particle accelerators are very important in our society, because they provide irreplaceable contributions to human life in many knowledge areas.

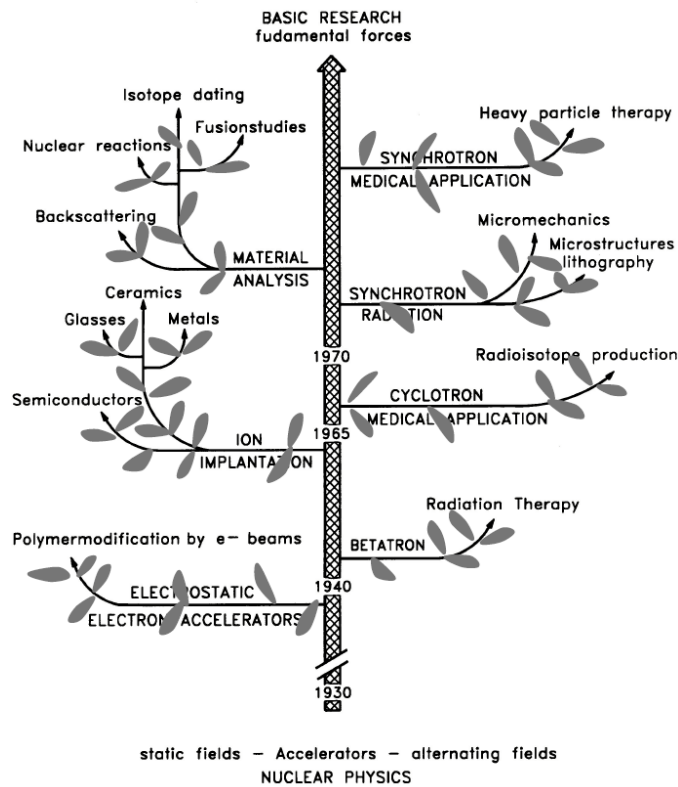


Fig. 1.1 Time tree for accelerators applications

For example, research with heavy ions has led to diverse applications and technological innovations in the past. The most spectacular example is the development of a new tumour therapy employing precision ion beams, which is presently being tested with promising results. At variance with protons, which interact with the cells essentially as X-rays, light ions better control the slowly growing radio-resistant tumours which represent about 20% of all the irradiated tumours. In 1998 the carbon ion pilot project was completed at GSI, where about 50 patients had been irradiated. In addition, radioactive atoms are being used very successfully as probes to study processes and the properties of materials. They can also be used for evaluating radiobiological risk for manned space missions, testing the materials of the spacecrafts.

In the area of femtochemistry, researchers are dealing with minuscule fractions of a second in order to trace the process of chemical reactions. Ultrafast lasers function as "cameras" taking instantaneous "snapshots" of chemical reactions with femtosecond (thousand million millionths of a second) exposure times. The principle is that an initial laser pulse triggers a photochemical reaction and a second pulse illuminates it immediately afterward. The second flash must be precisely adjustable in order to trigger the "snapshot" at a well-defined instant. A series of such instantaneous snapshots taken with varying intervals between the first and second beams produces a film of the reaction process (Fig. 1.2). The X-ray laser (obtained from synchrotron radiation) can make such films of the microcosmos with up till now unparalleled detail and time resolution. It generates an extremely intense X-ray beam and can be excellently focused. The brilliance of one single laser flash is so high that it can generate images of reacting molecules with atomic resolution. The duration of the flashes from the X-ray laser is about 100 femtoseconds. This is the time during which changes take place in reactions between molecules. The interval between two laser flashes, i.e. between the triggering pulse and the imaging pulse, can be systematically and accurately adjusted to one million millionth of a second. The X-ray laser flashes make possible to trace and comprehend the precise mechanisms of chemical reactions, reactions that might find applications in optoelectronics, photovoltaic and fuel or solar cells, for example.

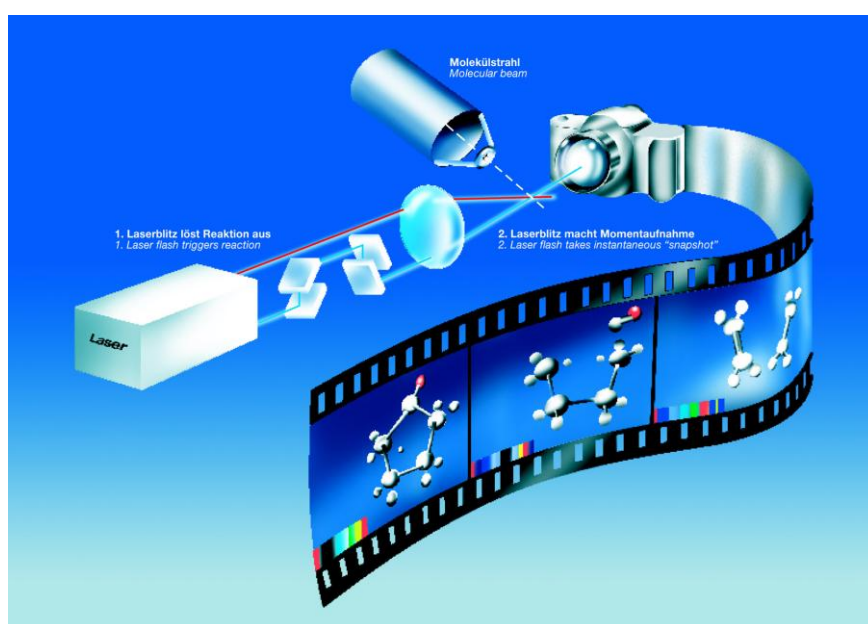


Fig. 1.2 Film of a chemical reaction using a X-ray laser

Using the intense X-rays from particle accelerators, it is now possible to analyze the structure of biomolecules in detail. The X-ray laser opens up completely new opportunities to decipher biological molecules with atomic resolution without the need for the extra step of growing crystals. The X-ray laser flashes are so intense that they can be used to create a high-resolution image of a single molecular complex. The flash duration is even shorter than 100 femtoseconds and is thus short enough to produce an image before the sample is destroyed by the intense X-rays (Fig. 1.3).

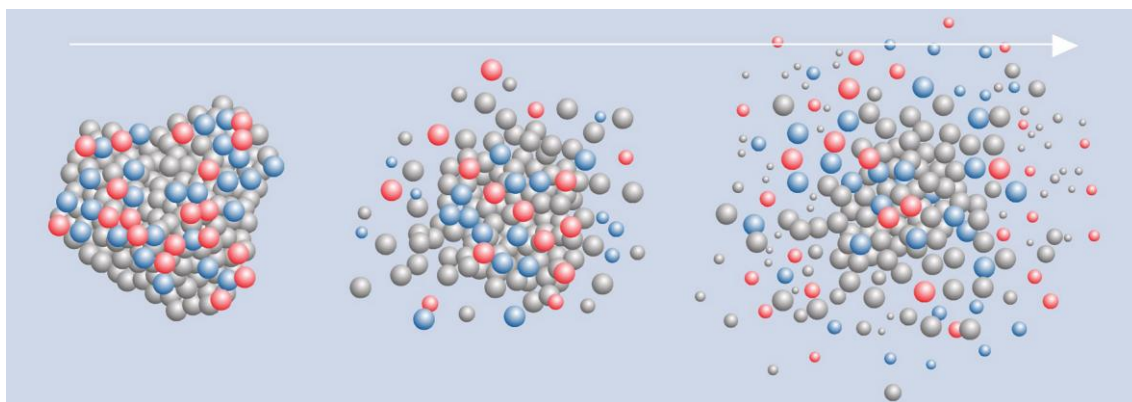


Fig. 1.3 Biomolecule exploding after receiving X-rays

Another example is friction study. Friction is highly desirable for braking, but not for the rolling of wheels and the smooth running of motors. In order to develop and improve materials, materials researchers need to understand the processes of friction and wear at the atomic level. For example, within the thin lubricant films which are used to reduce the wear of materials, so-called "stick-slip friction" occurs. The alternation of "sticking" and "slipping" is probably caused by the minutely thin film freezing and melting in turn. Such phase transitions can be examined in detail using X-ray lasers.

Finishing this brief description of accelerator applications, we cannot forget to mention fusion power. In the long term there are only three possible ways to satisfy the energy needs of mankind: solar energy, proton driven reactors and fusion. New fission reactors and future fusion power are being developed based on technologies of existing accelerators.

The number of accelerators in the world has grown rapidly in the past years. At present there are a great number of accelerators being used for many purposes (Tab. 1.1), and only a few of them are used for high energy particle physics, which means that accelerators stuff is becoming more and more common in our lives.

Tab. 1.1 Number of accelerators in the world (W. Maciszewski and W. Scharf, 2004)

CATEGORY	NUMBER IN USE
High Energy accelerators ($E > 1\text{GeV}$)	~120
Synchrotron radiation sources	>100
Medical radioisotope production	~200
Radiotherapy accelerators	>7500
Research acc. included biomedical research	~1000
Acc. for industrial processing and research	~1500
Ion implanters, surface modification	>7000
TOTAL	>17500

1.1.2 A BRIEF HISTORY ABOUT ACCELERATORS

At the beginning, particles in accelerators were really accelerated (increased their speed) since maximum energies were very low and not enough to be close to the maximum velocity (the speed of light). However, nowadays, most particle accelerators work with particles travelling close to the speed of light where the velocity is barely increased¹. Therefore, they should not be called particle accelerators but particle energizers or “massificators”, although everybody uses the historic naming.

The history of particle accelerators has been developed through the years from three separate lines [2], which are three ways of accelerating charged particles. Those accelerating mechanisms were invented in the twenties, and little has changed since then in the basics of acceleration.

¹ When a particle is travelling at a velocity very close to the speed of light, the subsequent energy contributions do not increase its velocity but only the mass of the particle, according to Einstein’s theory of relativity.

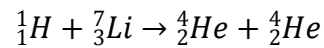
FIRST HISTORICAL LINE

Briefly, the easiest way of accelerating a charged particle is by putting it in a steady electric field, and this method corresponds to the first historical line. The particle will start moving along the electric field following the Lorentz force (Eq. 1.1). Static magnetic fields are unable to accelerate particles, as the Lorentz force is perpendicular to the particle speed.

$$\vec{F} = q (\vec{E} + \vec{v} \times \vec{B})$$

Eq. 1.1 Lorentz force on a charged particle

In 1930, John Cockcroft and Ernest Walton built the first huge electrostatic accelerator, aiming to split Lithium atoms with 500 keV protons (ionized hydrogen). In 1932 they were able to make atomic reactions splitting Lithium at only 400 keV, following the reaction in Eq. 1.2.



Eq. 1.2 First man-made subatomic reaction

Fig. 1.4 shows the Cockcroft-Walton's design, which is kept in the National Science Museum of London. It is based on several metallic tubes connected to a voltage generator, which works by half-rectifying AC current to load DC capacitors in steps, as it is shown in Fig. 1.5.



Fig. 1.4 Cockcroft and Walton accelerator in National Science Museum (London)

These accelerators are sometimes still used as the starting point of present day accelerators, as they can deliver high current beams.

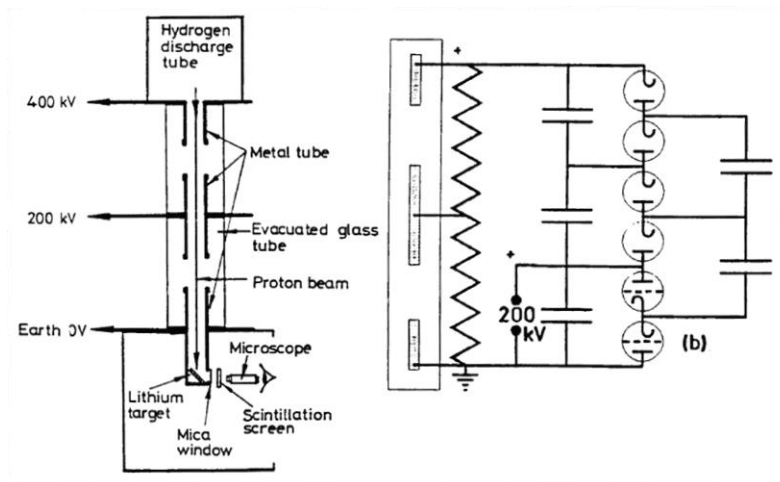


Fig. 1.5 Cockcroft and Walton accelerator schematics

The voltage of the electrostatic accelerators was shortly increased by Van de Graaff as a result of charging a metallic sphere using electrostatic principles (Fig. 1.6). He used a rolling dielectric belt charged by brushing a metallic comb connected to a small DC voltage source. The charge was displaced to a big metallic sphere by the belt and collected by another metallic comb. The maximum charge of the sphere depends on its dimension, and so depends the maximum voltage to ground. This generator could reach several MV if immersed in a dielectric pressurized gas to improve breakdown behaviour.

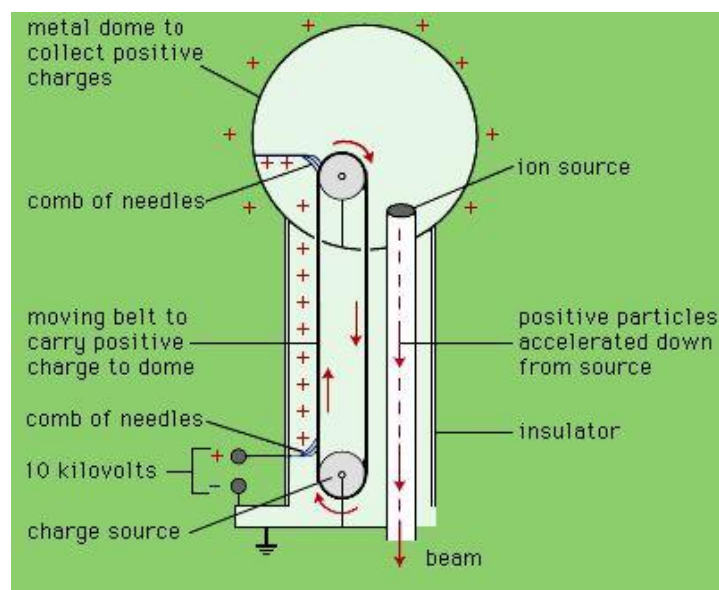


Fig. 1.6 Van de Graaff electrostatic accelerator (© Encyclopaedia Britannica)

A modification of Van de Graaff generator was called the Tandem generator, which basically double-accelerates the beam by changing the charge of the ions from negative to positive in a middle stage. As the Van de Graaff generator, it cannot provide high currents. This is the latest stage of electrostatic particle acceleration.

SECOND HISTORICAL LINE

The voltage limitation of electrostatic generators pushed the scientists to develop new methods for accelerating particles. A straightforward way of increasing the particle energy can be achieved by passing several times by the accelerating structure. But this is theoretically impossible by using DC fields (conservative), as the particles must lose the same energy when re-entering the structure as they gain when exiting it. In 1924, G. Ising has already proposed the use of alternating fields for accelerating particles, and this is the resonant acceleration still used in today's new accelerators, and hence the second historical line begins.

The second historical line uses the Faraday's Law for acceleration, which basically says that a time varying magnetic field creates an electric field rotating perpendicularly around the original magnetic field (Eq. 1.3).

$$\vec{\nabla} \times \vec{E} = -\frac{\partial \vec{B}}{\partial t}$$

Eq. 1.3 Faraday's Law

It can also be said that an azimuthally time varying magnetic field induces an electric field in the axis of rotation of the magnetic field (Fig. 1.7). Those fields encapsulated in a cylindrical cavity can resonate and this is the basis of the second historical line.

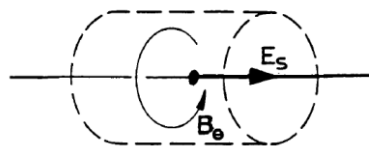


Fig. 1.7 Faraday's law for second historical line

Following Ising's idea, in 1928 Wideröe built a linear accelerator using a series of conducting drift tubes (Fig. 1.8) to accelerate sodium ions. In his design, a potential of 25,000 volts was alternated from positive to negative at radio frequencies of 100 kHz [3]. Ions were pulled into a straight cylindrical electrode by a negative potential and then pushed from the other end by a positive potential. Ions were not accelerated inside the drift tubes because they were shielded from the outer electromagnetic fields. It was possible to add more cylinders to reach higher energies, where each cylinder would be longer than the last one in order to accommodate the increasing speed of the particles.

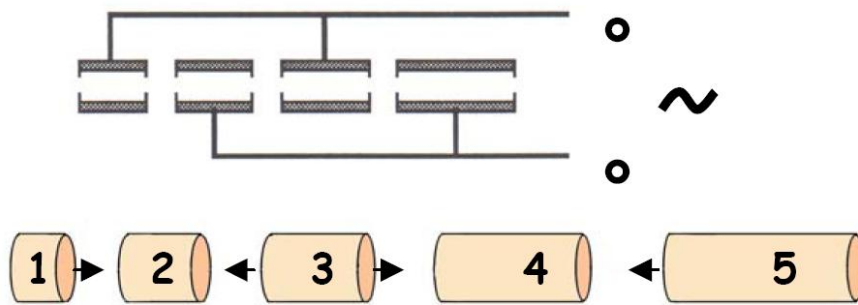


Fig. 1.8 Wideröe's linear accelerator basics

However, as the velocity increases, the drift tubes become extremely long unless the frequency is also increased, and a higher frequency means higher losses in the structure. Moreover, accelerating light ions becomes a very difficult task as they soon reach high velocities with small fields. That is why this technology was subsequently modified by enclosing the structure in a metallic cavity, where the irradiated RF power was confined. The klystron invention in 1937, using power frequencies in hundreds of Mhz range, made this technology feasible for linear accelerators. Effectively, the current large Linear Accelerators (LINACS) designs use this principle of resonant acceleration at very high frequencies (GHz).

Other application of the resonant acceleration was conceived by Ernest Lawrence in 1929, but using a totally different approach. He thought about using the RF power several times by spinning particles and passing them repeatedly through the RF structures. The cyclotron had been invented (Fig. 1.9).

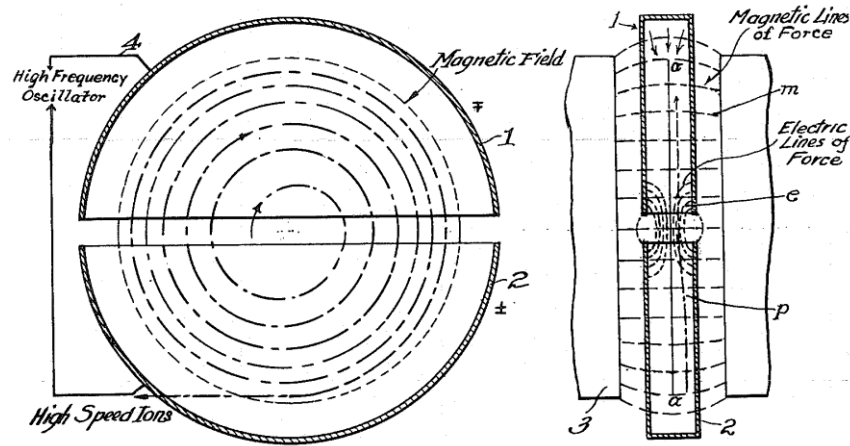


Fig. 1.9 Lawrence's cyclotron layout from his 1934 patent

The cyclotron is a metallic cylindrical pillbox split in two parts ("dees") with a gap between them. The source of particles is in the axis centre and there is a perpendicular magnetic field through the flat sides of the pillbox. When a charged particle moves in a perpendicular magnetic field, the Lorentz force (Eq. 1.1) makes it spinning around an equilibrium radius where centrifugal and Lorentz forces are equal. The particle is only accelerated in the gap where its trajectory is tangent to the electric field. Thanks to the increased velocity, the spinning radius grows after passing through the gap. Finally, the trajectory describes like a spiral and the revolution frequency is constant while the particles' mass remains almost unchanged. M. Livingston demonstrated the principle in 1931 by accelerating hydrogen ions to 80 keV.

However, the cyclotron was limited by relativistic effects because of the huge increase of mass at velocities close to that of the light. The synchrocyclotron was developed to adjust the RF frequency to keep the synchronism as the mass grows.

THIRD HISTORICAL LINE

It is also possible to take advantage of Faraday's law if the beam encircles a time varying magnetic field (Fig. 1.10). This acceleration mechanism is now known as "betatron acceleration", but Wideröe, who proposed it, called it a "ray transformer", because the beam was like the secondary of a transformer (Fig. 1.11).

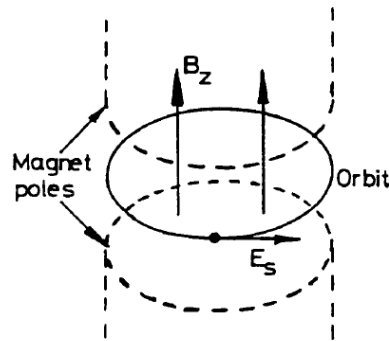


Fig. 1.10 Faraday's law for third historical line

As the magnetic field increases, the particle is accelerated by the tangential electric field created by the Faraday's law and its trajectory is curved by the own magnetic field. If the magnetic field in the orbit of the beam is equal to a half of the average magnetic field in the circle that the beam surrounds, the orbit will always be circular. Evidently, if the magnetic field decreases, the particles are decelerated. The betatron is insensitive to relativistic effects.

This device was built by D. W. Kerst many years after Wideröe's proposal, although this kind of machines were not very used for high energy physics. In 1950, Kerst built the world's largest betatron (300 MeV).

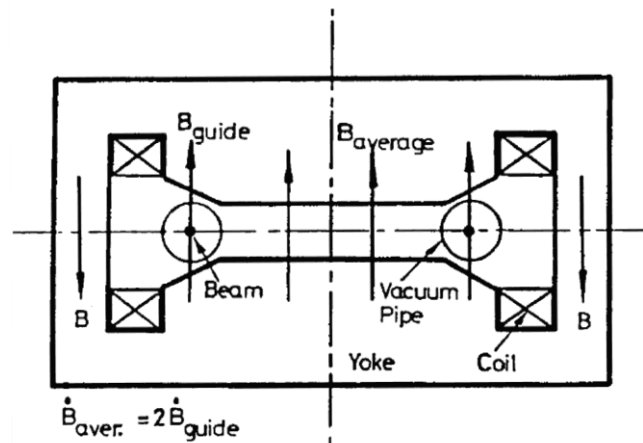


Fig. 1.11 Betatron sketch

However, the betatron was very important in the development of future accelerators. In effect, in a today's synchrotron, the oscillation of the particles about the equilibrium orbit is called the "betatron oscillation" due to historical reasons. This should be taken into account for the accurate description of particles motion.

THE SYNCHROTRON

All the acceleration mechanisms presented above lacked one of the most important topics for fruitful acceleration: the focusing for beam stability. The particle beam is unstable itself due to several reasons related to its longitudinal and transverse movement: RF acceleration, natural repulsion between particles in the beam, gravitation effects, etc. After considering the problems in the cyclotron synchronism, the stability in the longitudinal plane was studied by E. McMillan and independently by V. Veksler who discovered the principle of phase stability in 1944 and invented the synchrotron. The effect is that a bunch² of particles can be kept bunched throughout the acceleration cycle by simply injecting them at a suitable phase of the RF cycle. De facto, this makes the acceleration mechanism stable itself if a continuous beam is generated, as only the particles that are inserted in a stable phase would remain in the following turns.

The synchrotron (Fig. 1.12) accelerates particles in a constant radius orbit by increasing the guiding field as in the betatron but using RF voltage gaps for acceleration. The guiding field is given by independent magnets around the orbit (Fig. 1.13) and the RF acceleration is composed of several RF cavities in a small zone of the orbit.

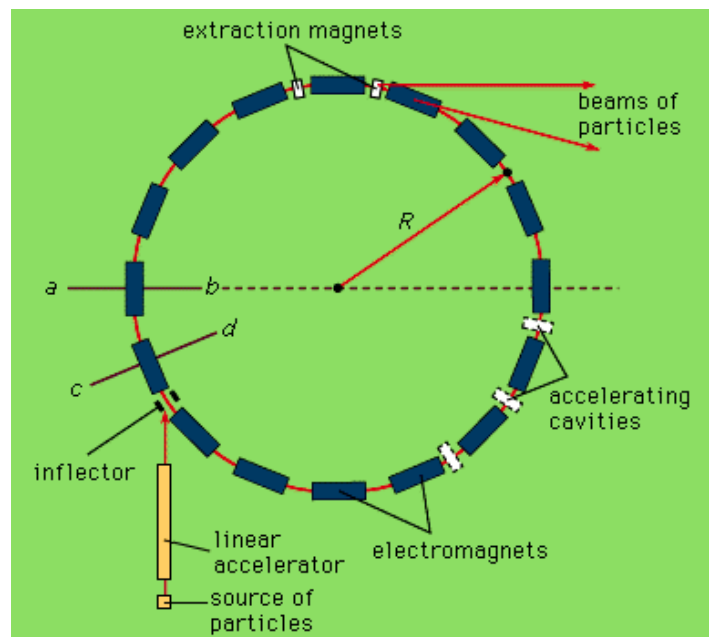


Fig. 1.12 Synchrotron schematic diagram (© Encyclopaedia Britannica)

² Particles are grouped in small discrete groups called bunches. This is needed for stable acceleration in RF structures.

In 1946 F. Goward and D. Barnes were the first to make a synchrotron work, and in 1947 M. Oliphant, J. Gooden and G. Hyde proposed the first proton synchrotron for 1 GeV in Birmingham.

However, not only longitudinal focusing is important. When the synchrotron was invented, only weak focusing mechanism was known in the transverse plane. Weak (or constant-gradient focusing) is produced in the guiding magnets. The radial plane focusing is naturally created by the centrifugal forces. For the vertical plane focusing, the guide field in the magnets decreases slightly with increasing synchrotron radius and its gradient is constant all round the circumference of the machine. This arrangement was adequate for machines in which the dimensions of the magnet gap could be appreciable in comparison with the radius of the orbit. The magnets should be large and costly and the maximum energies are low, like for the Cosmotron built in 1953 in Brookhaven National Laboratory (USA).

In 1952, E. Courant, M. Livingston and H. Snyder proposed strong focusing, also known as alternating-gradient (AG) focusing. Its principle comes from geometrical optics, where the series combined focusing and defocusing lenses have a net focusing effect (positive overall focal length), provided the distances between lenses are correct. Since then, the strong-focusing principle revolutionized accelerator design. The first synchrotron to use strong focusing was the Alternating Gradient Synchrotron (AGS), built in 1957 in Brookhaven National Laboratory. The beam was focused by the pole-tips of the bending magnets (Fig. 1.13). Tips with cross section cd focused the beam in the radial direction, while tips with cross section ab focused in the vertical direction.

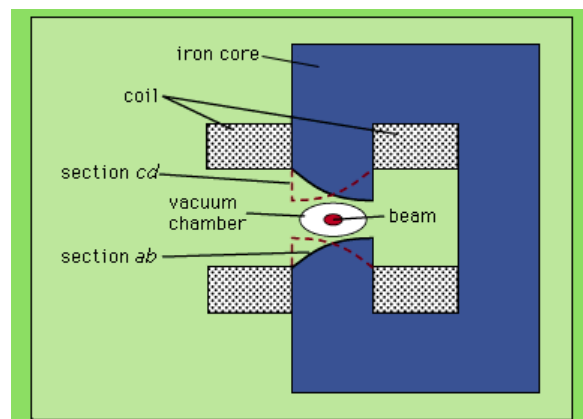


Fig. 1.13 Strong or alternating-gradient focusing (© Encyclopaedia Britannica)

Present accelerators use different magnets for bending and for focusing. The alternating gradient is created by quadrupole magnets placed alternatively to focus in vertical and horizontal planes. The quadrupoles which focus in vertical also defocus in horizontal and vice versa. This pattern is called FODO (Fig. 1.14), where F focuses vertically and defocuses horizontally, D focuses horizontally and defocuses vertically and O is a drift space or deflection magnet. The space between two vertically focusing quadrupoles is called a FODO cell, and a particle returns to the same position after a given number of cells (depending on the phase advance per cell). The oscillations of the particles around the equilibrium orbit are called betatron oscillations. That name comes from a paper published in 1941 by Kerst and Serber about oscillations in their betatron machine.

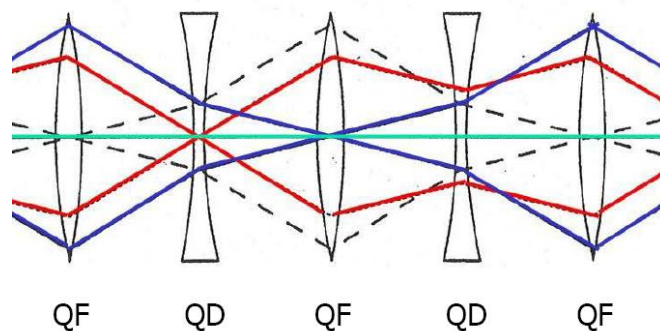


Fig. 1.14 FODO pattern to align the quadrupoles

To improve the energy of the collisions even more, the synchrotron machine was the origin of the storage ring colliders (Fig. 1.15). Instead of accelerating the particles in several turns and then colliding with a fixed target, two beams rotating clockwise and anti-clockwise were “stored” in a double synchrotron ring and then collided one against the other. A head-on collision between two particles has the combined energy of both particles, totally different as when the target is fixed, where only a fraction of the energy is liberated.

Storage ring colliders are presently the most used high energy physics accelerators. They are the preferred method of accelerating and colliding heavy particles as hadrons, because those particles are not usually accelerated close to the speed of light and the synchrotron radiation lost on each turn can be easily compensated by RF accelerating structures.

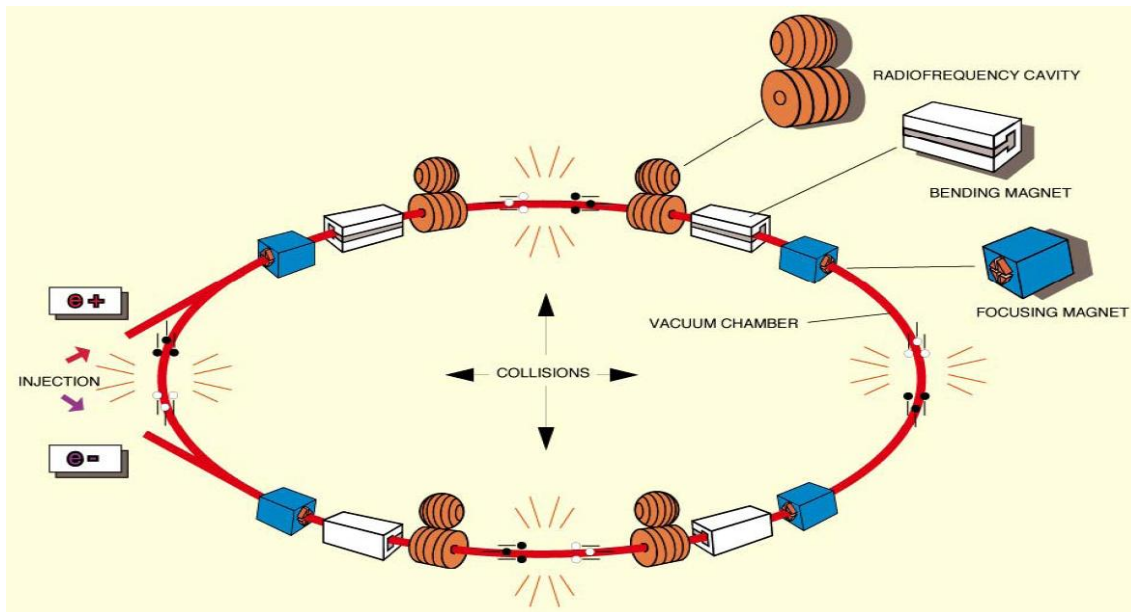


Fig. 1.15 Storage ring collider

On the other hand, the applied superconductivity has produced an enormous improvement in the accelerators to allow higher energies with not very large machine sizes. The magnets are the key devices which benefit from superconductivity, as they can be much smaller, have less power consumption and feature higher field strength than before. Superconductivity allows much higher current density in the coils of magnets, which increases the bending and focusing power of the devices without increasing the size. However, the magnets become more complicated as cryogenic facilities are required in order to maintain the low temperatures needed for the coils.

There have been other improvements and acceleration mechanisms along the history, but this has been only a brief description on the major devices. For example, the invention of the Radio Frequency Quadrupole (RFQ) in 1970 by I. Kapchinski and V. Telyakov has replaced the Cockcroft-Walton as an injector in lower energies. Besides, the Alvarez accelerator has become very popular as an injector for large proton and heavy-ion synchrotrons all over the world with energies in the range of 50–200 MeV. And stochastic and electron cooling made possible proton-antiproton colliders.

1.1.3 PRESENT DAY MACHINES

In the history of accelerators, roughly speaking, the energy has increased one and half orders of magnitude per decade. This fact can be observed in the well known Livingston chart (Fig. 1.16) where it can be observed that a new idea, which rapidly increases the available beam energy, is shortly surpassed by yet another new idea.

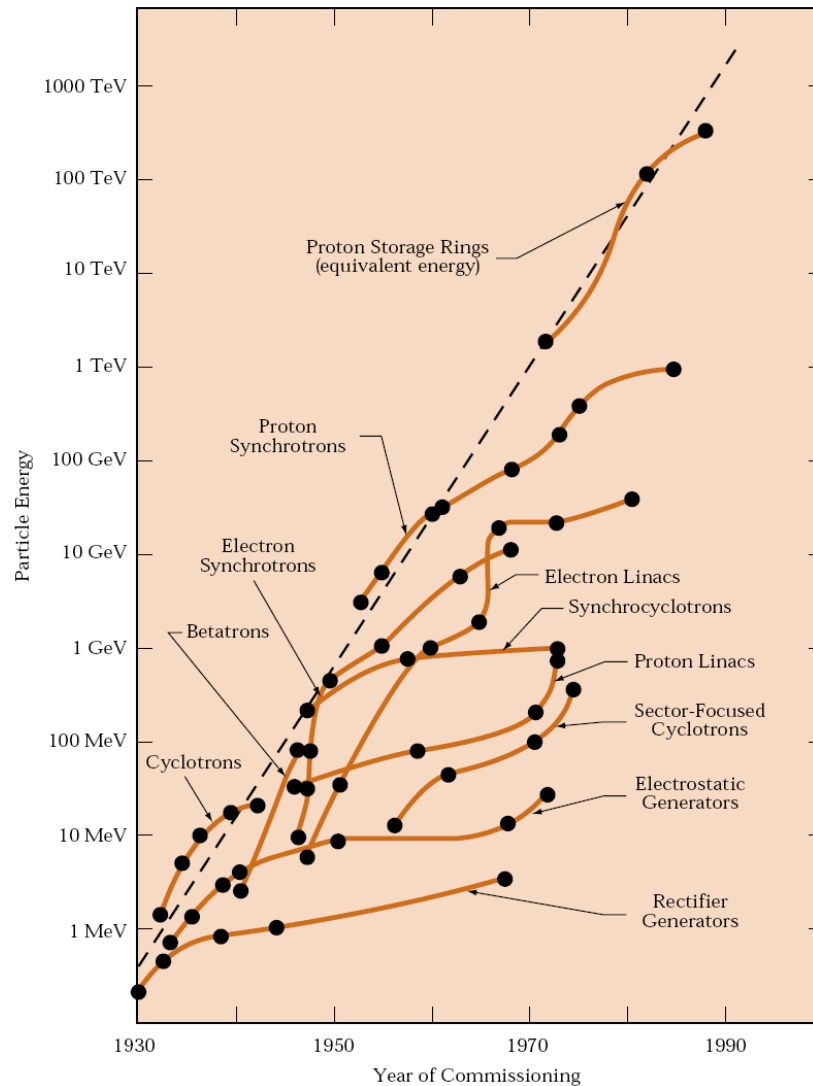


Fig. 1.16 Livingston chart

On the other hand, the electron storage rings have given birth to the synchrotron radiation sources, more usually referred to as light sources. These machines are now the fastest growing community in the accelerator world and the first commercially available compact synchrotron light source for lithography has just come onto the market.

At present, there are several big projects almost running or finishing their commissioning. Here only a brief description of some of them will be shown.

LHC at CERN: This is the largest accelerator project ever built in history. LHC means Large Hadron Collider. It is located between Switzerland and France, close to Geneva, about 100 m underground, and its main ring has a circumference of about 27 km (Fig. 1.17). It is a superconducting proton synchrotron storage ring collider [4] that aims to reach extremely high energies in order to understand the fundamental laws of Nature. Collision energies will be about 7 TeV per proton, 14 TeV per proton-proton collision and even 1150 TeV in lead-ion collisions. This machine is now being commissioned and it will be working hopefully in several months from now.

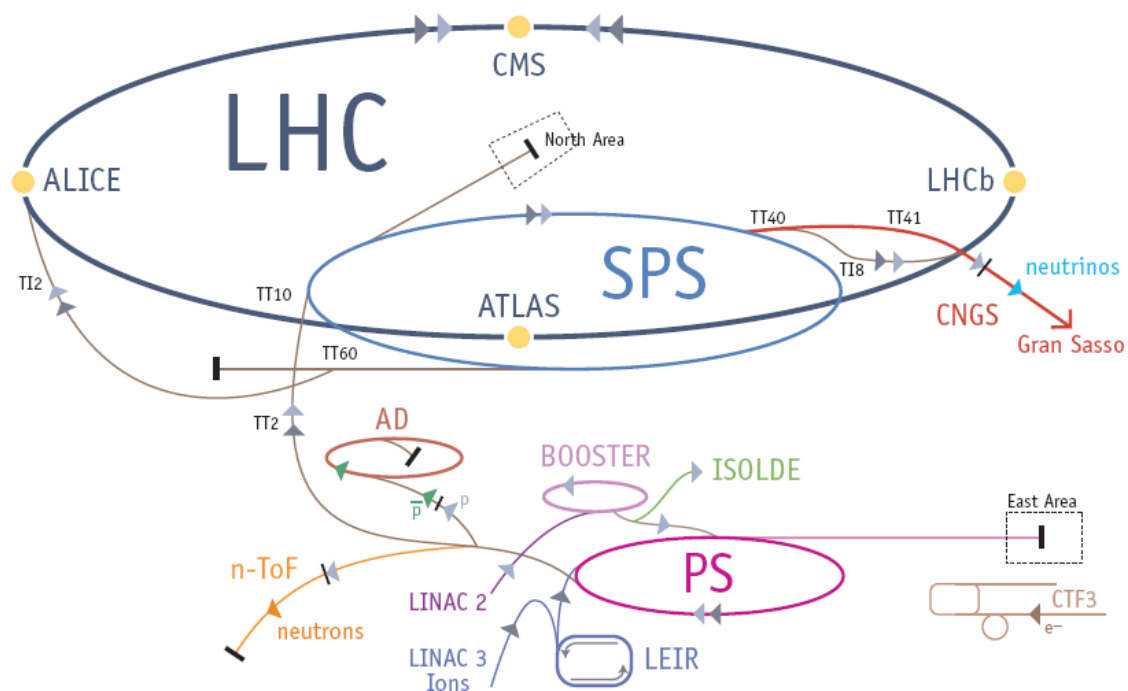


Fig. 1.17 CERN LHC sketch

XFEL at DESY: XFEL is the European X-ray Laser Project [5], located in Hamburg-Bahrenfeld. It is a 3.4 Km long X-ray Free Electron Laser fed by a superconducting linear accelerator (Fig. 1.18). This device will produce 100 femtoseconds X-ray pulses with over 10 GW of peak power, and will be able to produce intensities in the order of 10^{18} W/cm². This numbers provide an unprecedented ability to photograph molecules or film chemical reactions.

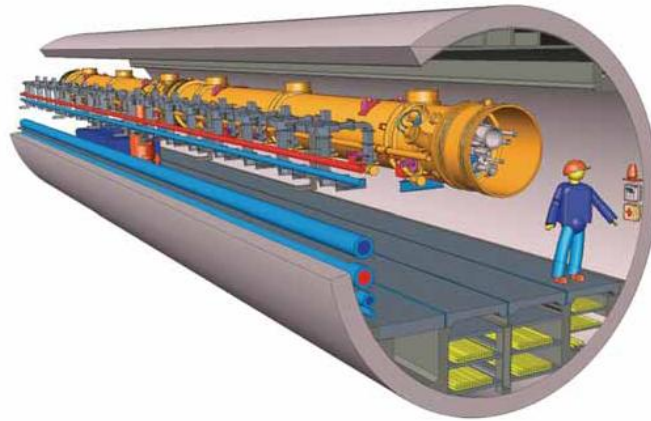


Fig. 1.18 Schematic section of the XFEL linac tunnel

FAIR at GSI: The Facility for Antiproton and Ion Research [6] is being constructed at Darmstadt (Germany). It consists of two dedicated superconducting synchrotron accelerator rings (in the same tunnel) with maximum magnetic rigidities of 100 Tm and 300 Tm respectively, complemented by a system of cooler-storage rings (Fig. 1.19). The facility is able to accelerate high mass ions, from protons and antiprotons up to Uranium and will provide high-energy ion beams of maximum energies around 35 GeV/u for fully stripped U^{92+} beams.

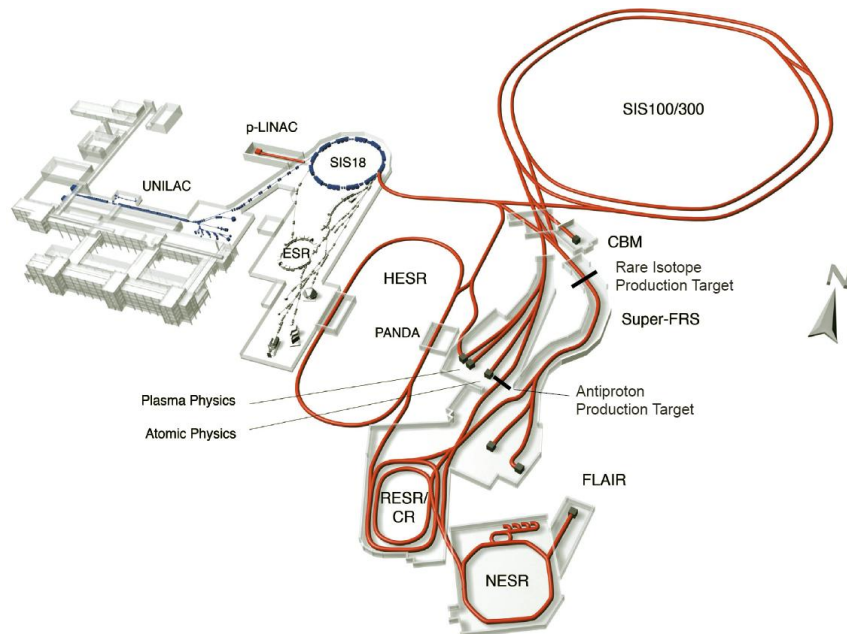


Fig. 1.19 FAIR facility

Other investigations under active development today are the Spallation sources, the Rubbia's energy amplifier and the experiments on inertial fusion, as well as the already mentioned X-ray emitting Free Electron Lasers.

1.2 TYPICAL COMPONENTS IN A PARTICLE ACCELERATOR

This section is not expected to be a detailed report on modern accelerator components, but a succinct introduction of miscellaneous devices in an accelerator. Bibliographic references should be used when more information is desired.

1.2.1 *PARTICLE SOURCES*

Every accelerator needs charged particles to accelerate, as it is not possible to accelerate neutral particles using electric fields. Those particles can be electrons, protons or ions (or even charged antiparticles). The particle sources are basically divided in electron sources and ion sources [7].

ELECTRON SOURCES

One way of generating electrons from a material is by using the thermionic emission. When a material is heated, an electron cloud appears around the material. A simple electric field is then capable of extracting the electrons.

There is another effect that can be used to generate electron bunches. The energy of an electron in a material can be increased above the vacuum energy by absorbing photons. This is called a photocathode and multiple configurations can be used for this effect. For example, a deep ultraviolet pulsed laser can excite a caesium telluride cathode (Fig. 1.20).

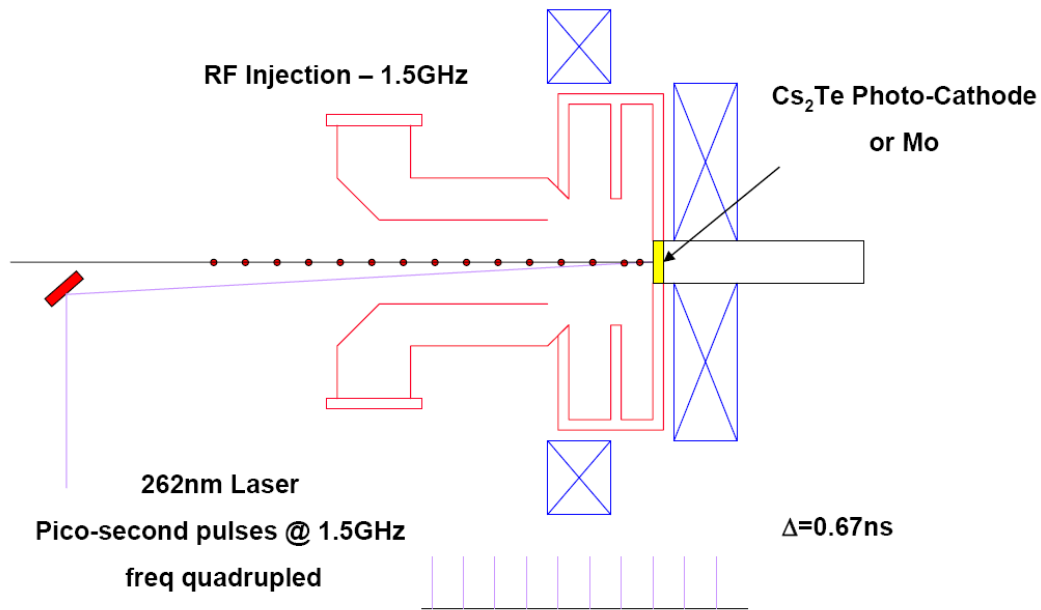


Fig. 1.20 Photo Injector Test Facility – Zeuthen

ION SOURCES

There are lots of methods for extracting ions from materials. All of them require an “ion production” region (usually a plasma) and an “ion extraction” system. The main goal of an ion source is producing the required ion type and pulse parameters also maximizing reliability, beam quality and reducing material consumption.

A Penning or Philips Ionisation Gauge (PIG) is an ion source that works using a cathode-anode discharge in a magnetic field, where electrons oscillate in a plasma, ionizing the rest gas (Fig. 1.21).

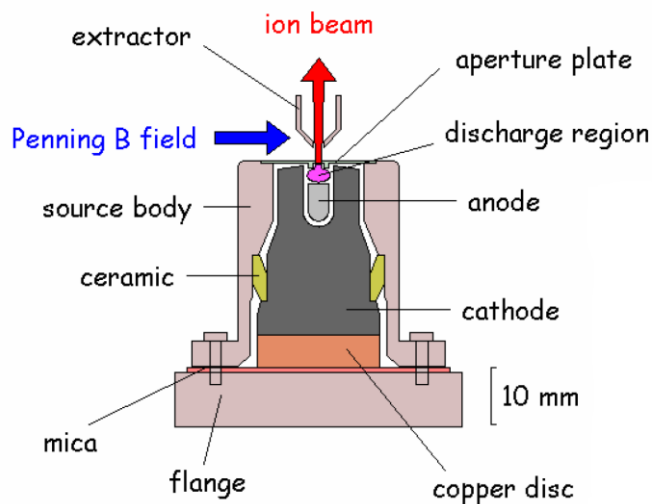


Fig. 1.21 The Rutherford ISIS Penning source

The Electron Cyclotron Resonance (ECR) heats electrons on the resonance, producing a plasma. Electrons and ions are confined in a magnetic bottle and that confinement leads to multiple collisions and highly charged-ions.

1.2.2 RF CAVITIES

There are plenty of methods to increase energy of particles in an accelerator. Several of them have already been explained in section 1.1 of this document. However, in modern accelerators, RF cavities are commonly used for that purpose. They are needed not only to increase the energy of particles but also to compensate the energy losses in storage rings due to synchrotron radiation.

RF cavities are the preferred means of accelerating particles. Typically a few tens of centimetres in length, they can use a standing wave whose frequency is set such that it gives particles an accelerating push as they pass through. For example, if a series of electron bunches are being accelerated then the sign of the wave will flip from positive to negative as the bunch passes through the cavity, returning to positive as the next bunch arrives. The size of a cavity is very important because it must be related to the frequency of the standing wave in order that there is an integer number of nodes (usually one) across it.

All the *standing wave cavities* are based on the pillbox design, which is a cylindrical volume with metallic walls where electric and magnetic field resonate at an exact frequency (Fig. 1.22). The behaviour of the cavity can be better understood if simulated as a resonating electrical circuit (series or parallel). The inductance is proportional to the magnetic stored energy and the capacitance is proportional to the electric stored energy (the resistance simulate the losses in resistive walls). In effect, when increasing the frequency in a standard DC or low frequency electrical circuit with L and C, the coil and the capacitor tend to become distorted and behave as the pillbox cavity [8].

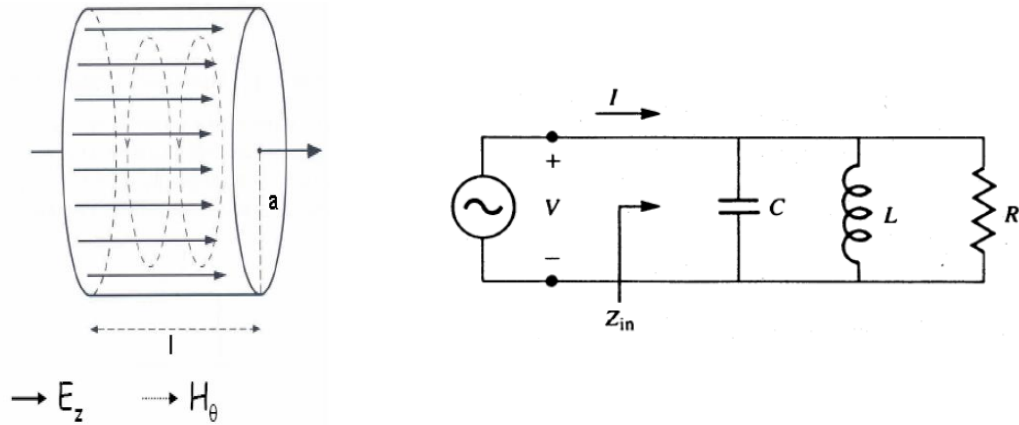


Fig. 1.22 Pillbox cavity and its corresponding RLC circuit

A real RF cavity can be obtained (Fig. 1.23) from a pillbox by several minor changes, like adding two holes for the beam to pass through, and changing the geometry to allow maximum volume with minimum surface (spherical shape) which decreases RF losses in the cavity surface.

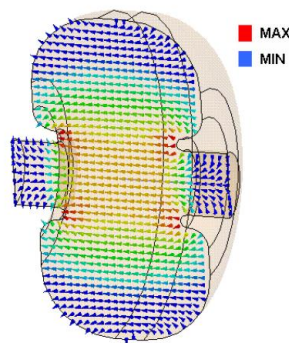


Fig. 1.23 Real RF resonant cavity with represented electric field

Standing wave cavities require from a continuous RF power source to deal with the energy losses in the resistive walls. They can also be made of superconducting materials (typically niobium) to dramatically reduce these losses (Fig. 1.24).



Fig. 1.24 Multi-cell superconducting RF cavity

However, the common design of accelerating structures consists of a circular waveguide into which metallic plates are inserted normal to the waveguide axis at periodic intervals (disc loaded waveguide). These discs are needed to reduce the phase velocity below the velocity of light, and therefore slower particles can travel along with the electromagnetic wave. Obviously, the plates have small holes in their centres to allow for the passage of the particle beam (Fig. 1.25). These cavities are called *travelling wave cavities*, and they accelerate the particles by a continuous RF wave that flows through them from an input port to a matched output port.

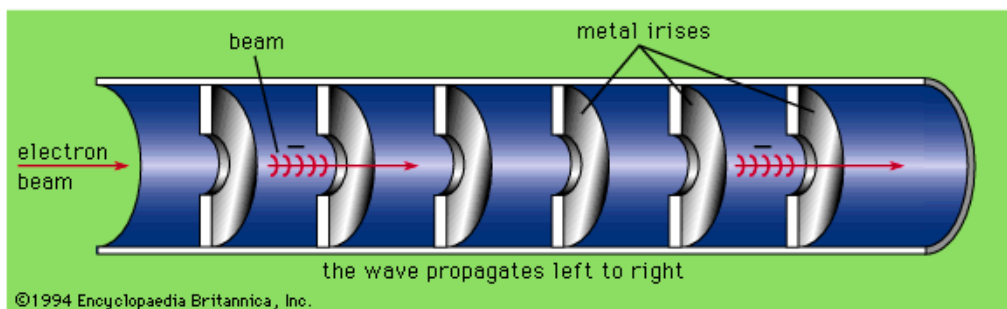


Fig. 1.25 Travelling wave cavity with irises inside

The particles travel with the electromagnetic wave in a place where electric field is adequate for acceleration, like “a surfer” over a wave (Fig. 1.26). The exhausted wave is finally absorbed by a load in the output port. Ideally no energy is wasted in the load if the beam absorbs all the power.

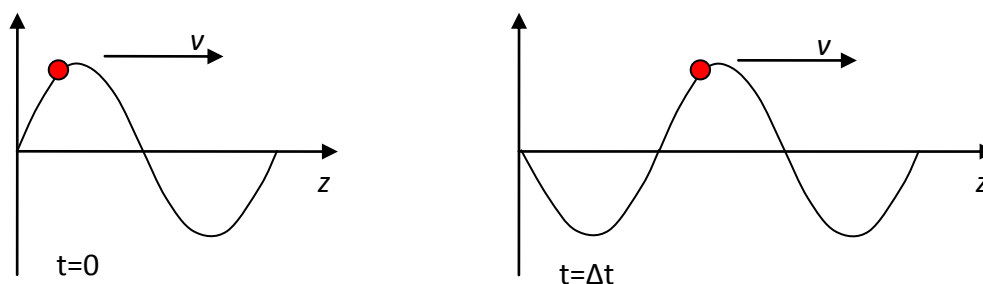


Fig. 1.26 Particle travelling on the crest of a wave

1.2.3 BEAM DIVERSION AND FOCUSING DEVICES

To reach high energies in linear accelerators, a high accelerating field or a long accelerator are necessary, because particles run through the accelerating cavities only once. On the other hand, circular accelerators repeat the acceleration process on every turn and therefore they do not need a so powerful acceleration. However, circular accelerators need the particles to rotate around a closed orbit. It has been presented in section 1.1.2 that modern synchrotrons use bending magnets as guiding field in the orbit. These magnets are called dipoles and, in modern accelerators, they are independent of other focusing devices.

Dipoles create a uniform field in a space region inside their aperture (the space where particles pass through). The uniform field perpendicular to the trajectory of the particles makes them to bend around an orbit of a radius that depends on Eq. 1.4, where ρ is the radius of curvature, p is the momentum of the particle, e is the electron charge and B_0 is the dipole field (all the magnitudes in SI units).

$$\rho = \frac{p}{eB_0}$$

Eq. 1.4 Radius of curvature of a particle in a given field

Nevertheless, magnets are not only necessary to bend the beam in a circular accelerator, but are also compulsory to keep the beam stable and focus it before the colliding point. They behave like lenses that focus and defocus the beam and correct positioning errors of particles. One must see that the diameter of a single proton is in the order of 1 fm (10^{-15} m), and electrons and positrons are much smaller. Therefore, it takes very powerful focusing to ensure that two particles travelling in an accelerator at relativistic speeds collide.

Throughout most of the acceleration process, a particle bunch is spread across the cross sectional area of the beam pipe. This helps avoid premature collisions in the case of circular accelerators which use the same beam pipe to accelerate both bunches. On attaining the energy required for the experiment, the beams are focused using quadrupole magnets. These have the property of focusing charged particles in one plane and defocusing them in the orthogonal one.

A succession of alternate quadrupole magnets at the right distance have the net effect of focusing the particle beam in both directions, just as a succession of equally strong converging and diverging lenses focuses a beam of light (FODO lattice already explained).

The classification of dipoles will be detailed in section 1.3.1.1. It can also be applied to quadrupoles and even higher order multipole magnets (Fig. 1.27).

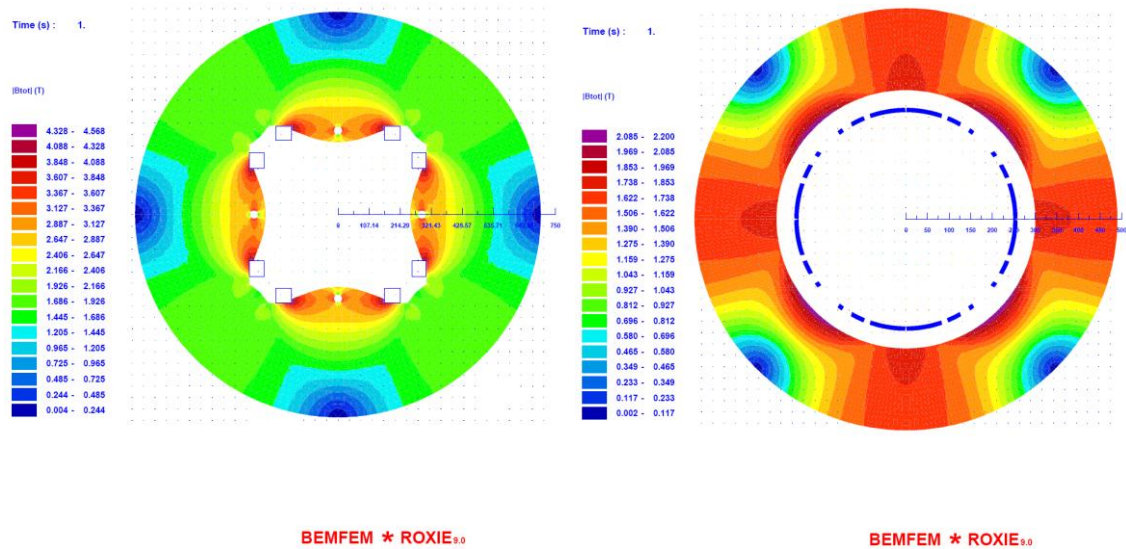


Fig. 1.27 Cross section of superferric and Cos Θ quadrupoles

Indeed, particles with different momenta are focused with different strength by the quadrupoles, leading to beam instability. These kinds of errors are described by the chromaticity, and they are corrected by higher order magnets called sextupoles (Fig. 1.28), whose focusing effect is proportional to the momentum deviation of the particle. There are also even higher order magnets (octupoles, dodecapoles, etc.) to fine tune the errors introduced by low order ones.

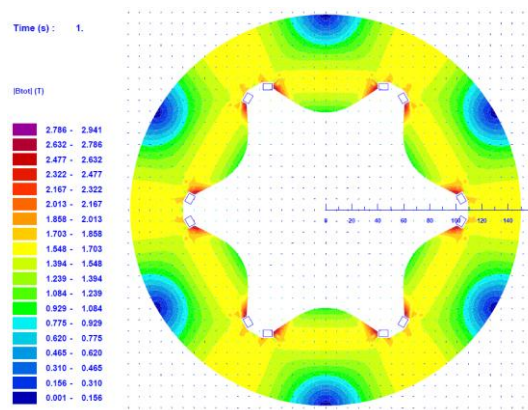


Fig. 1.28 Cross section of a superferric sextupole

1.2.4 INJECTION AND EXTRACTION DEVICES

All modern accelerators have a limited dynamic range, which means that a chain of different stages is needed to reach high energies. This fact can be seen in LHC layout (Fig. 1.17), where several rings are used to pre-accelerate the beam before arriving to the main ring. There are also experiments that need to be done out of the main rings.

Injection and extraction devices are needed to transfer the beam from its circular orbit in a synchrotron to another ring or path, and vice-versa. Those devices are totally needed in order to achieve high energy beams, combine them or to develop other experiments. They are installed in series with the beam pipe and they usually work by giving a fast transversal impulse to the beam, deflecting it from its original trajectory. However, special permanent magnets called septa (septum in singular) can also be used individually for extraction. The injection/extraction problem can be divided in three different situations [9]:

- Single turn injection/extraction: A magnetic element inflects beam into the ring and turn-off before the beam completes the first turn (it is opposite for extraction from the ring). The turn-off (turn-on for extraction) is needed to be very fast to avoid affecting the beam in the first turn, and that requirement depends on the speed of the beam and the length of the ring.
- Multi-turn injection/extraction: The system must inflect the beam into the ring with an existing beam circulating without producing excessive disturbance or loss to the circulating beam.
- Accumulation in a storage ring: A special case of multi-turn injection that continues over many turns (with the aim of minimal disturbance to the stored beam).

To inject/extract a beam in the single turn situation, the simplest solution is to use a kicker device with fast turn-off (injection) or fast turn-on (extraction). But for small rings, the revolution times can be very small ($< 1 \mu\text{s}$), which makes necessary the use of a very fast kicker device. This can only be achieved using strip-line kickers, which are fully treated in the following sections.

The multi-turn injection can be solved by phase-space manipulation, which means that the injected beam can be stored in aperture spaces (outer region of phase space) not occupied by the stored beam. This can be done by using a non-integer tune region of phase space (Fig. 1.29) which ensures many turns before the injected beam re-occupies the same region (for e- and p+) or by waiting the beam to coalesce into the central region (Fig. 1.30) due to the damping before the next injection in the unoccupied phase space (leptons only).

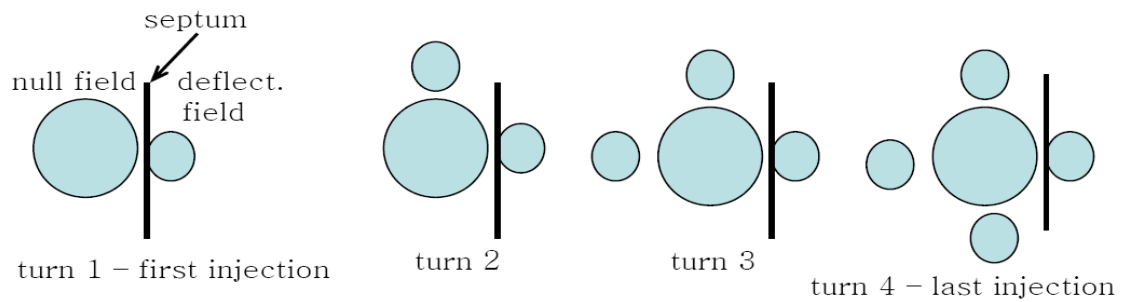


Fig. 1.29 Injection by horizontal phase space at $Q=1/4$ integer.

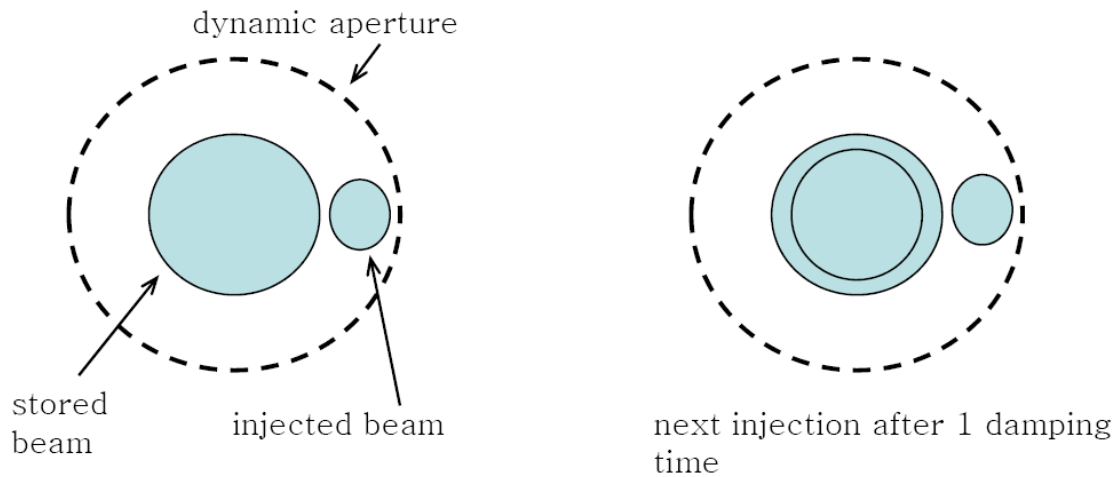


Fig. 1.30 Injection by coalescence of beam

Concerning the multi-turn extraction (Fig. 1.31), it can be achieved by removing the particles from the edge of the beam while the beam is moving in the correct direction along the aperture. This can cause some beam loss at the septum magnet.

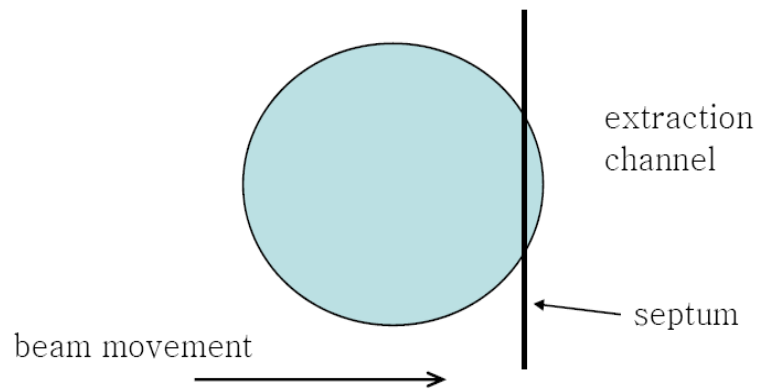


Fig. 1.31 Multi-turn extraction solution

The devices used for injection and extraction (kickers and septa) will be widely explained in section 1.3 of this document.

1.2.5 DIAGNOSTICS

An accelerator can never be better than the instruments measuring its performance [10]. Beam diagnostics are an essential constituent of any accelerator. They are particularly important when new machines are commissioned or at start-up after a long shutdown. In addition, also during routine machine operation, it is the beam measurements that tell the operator if the machine is performing correctly or not, and help to find faults in accelerator components. High knowledge of the beam dynamics and physics interaction is needed in order to understand and design beam diagnostic sensors.

Most sensors are based on one of the following physical processes:

- Interaction of the beam particles with electric or magnetic fields.
 - Coupling to the magnetic or electric field
 - Synchrotron radiation
 - Transition radiation
- Coulomb interaction between the incident beam particle and electrons in the atomic shell of intercepting matter.
- Atomic excitation with consecutive light emission.

A typical instrument for beam diagnostics consists of:

- The own sensor
- The front-end electronics
- The cabling between the tunnel and the equipment room
- Signal treatment electronics and ADC
- The front-end software to read and treat the digital signal

Tab. 1.2 shows the devices used to measure different beam properties and their effect on the beam [11]. For a detailed description of those devices, the reader can consult the bibliographical references.

Tab. 1.2 Diagnostic devices and measured beam properties

PROPERTY MEASURED →	Intensity/charge	transverse			longit.		Q-value + ΔQ	Energy + ΔE	Polarization	Effect on beam			
		Position	Size/shape	Emittance	Size/shape	Emittance				N	-	+	D
Beam transformers	●				●	●				X			
Wall-current monitors	●	●			●	●				X			
Pick-ups	●	●	●		●	●				X			
Faraday cup	●												X
Secondary emission monitors	●	●	●	●				•			X	X	
Wire scanners		●	●	●							X		
Wire chambers		●	●								X	X	
Ionization chambers	●										X	X	
Beam loss monitors		•	•	•			•			X			
Gas curtain		●	●	●							X		
Residual-gas profile monitors		●	●	●						X			
Scintillator screens		●	●								X	X	X
Optical transition radiation		●	●	●							X		
Synchrotron radiation		●	●	●	●	●				X			
LASER-Compton scattering			●	●					●	X			
Polarimetry									●	X			X
Scrapers and measurement targets		●	●	●									X
Beamscope		●	●	●									X
Q-measurement							●			X	X		
Schottky scans	●			●		•	●	●		X			
Emittance measurement				●							X	X	X
Measurement of energy								●		X	X	X	X

Effect on beam: N none
- slight, negligible
+ perturbing
D destructive

● primary purpose
• indirect use

Only the most basic measured properties are shown. There are many more, less basic, which can be derived: coupling, dispersion, chromaticity, etc. Note that to determine emittance (transverse or longitudinal), knowledge other than that obtained from the basic measurement is required. The oscillatory behaviour of the beam is observed through the time-dependance of properties (like position, size/shape, energy), often on a very fast time scale.

1.2.6 DETECTORS

After an accelerator has pumped enough energy into its particles, they collide either with a target or each other. Each of these collisions is called an event [12]. The physicists' goal is to isolate each event, collect data from it, and check whether the particle processes of that event agree with the theory they are testing.

At the energies achieved today, the collisions, or events, produce many different particles, most of which have lifetimes so short that they leave no detectable tracks before decaying. Physicists deduce these particles' existence from measuring their decay products. Large, multi-component detectors are built, each component designed to test different aspects of the event. In particular, they measure position, energy and momentum and can distinguish lot of different particle types.

Particles produced in fixed target experiments generally fly in the forward direction (Fig. 1.32). For this reason, detectors in these machines are generally positioned downstream from the target and are cone-shaped, with the pointed end of the cone being nearest the target.

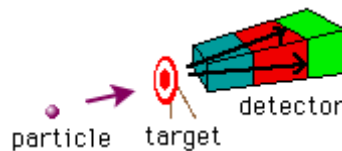


Fig. 1.32 Detector scheme in a fixed target experiment

Particles produced in colliding beam experiments travel in all directions. Hence, detectors tend to take the form of long cylinders around the part of the beam pipe in which the event occurs (Fig. 1.33).

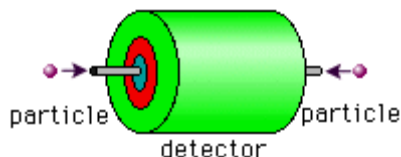


Fig. 1.33 Detector scheme in a colliding beam experiment

The components of a detector are arranged in order such that all particles can travel to their relevant part(s) of the detector as undisturbed as possible (Fig. 1.34).

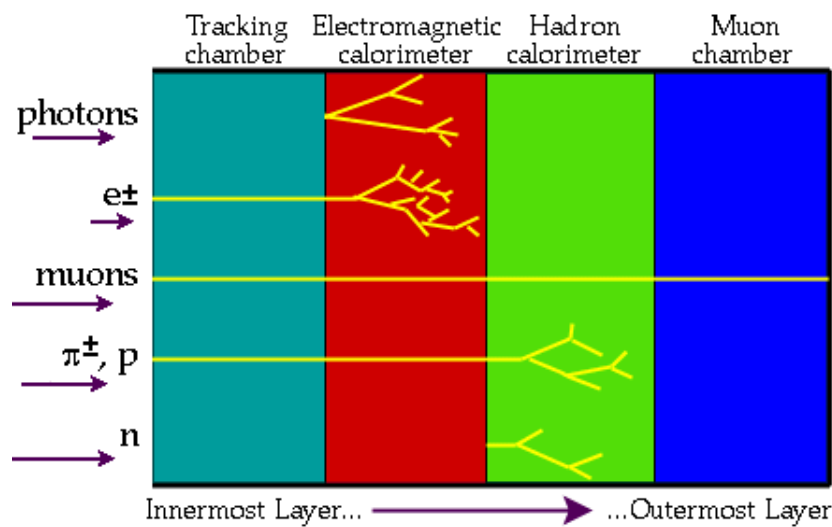


Fig. 1.34 Different parts of a typical detector

The tracking chamber is located nearest the event to measure the position of particles (Fig. 1.35). A magnetic coil outside the tracking detector is installed to bend the particle trajectories to determine momentum. The momenta of particles can be calculated since the paths of particles with greater momentum bend less than those of smaller momentum. Then the Cerenkov detectors measure the particles' velocity. Afterwards, EM and Hadron Calorimeters measure the energy of particles and finally the muon detectors are installed to detect slippery muons.

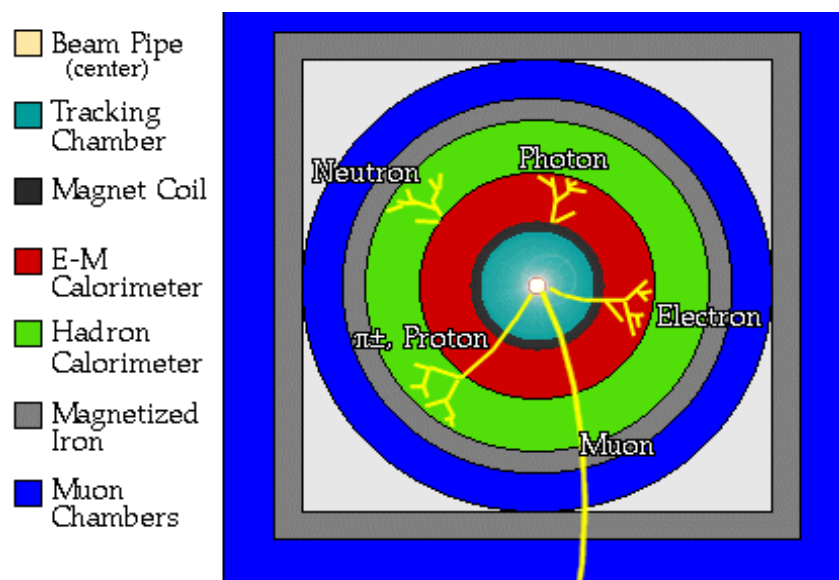


Fig. 1.35 Typical parts of a cylindrical detector

The following figures (Fig. 1.36 and Fig. 1.37) show the ATLAS detector at CERN, the largest detector of the new LHC accelerator. It is 44 m long, 25 m high and 25 m wide, and it weighs 7000 Tonnes. These numbers show the magnitude of present day particle collider projects.

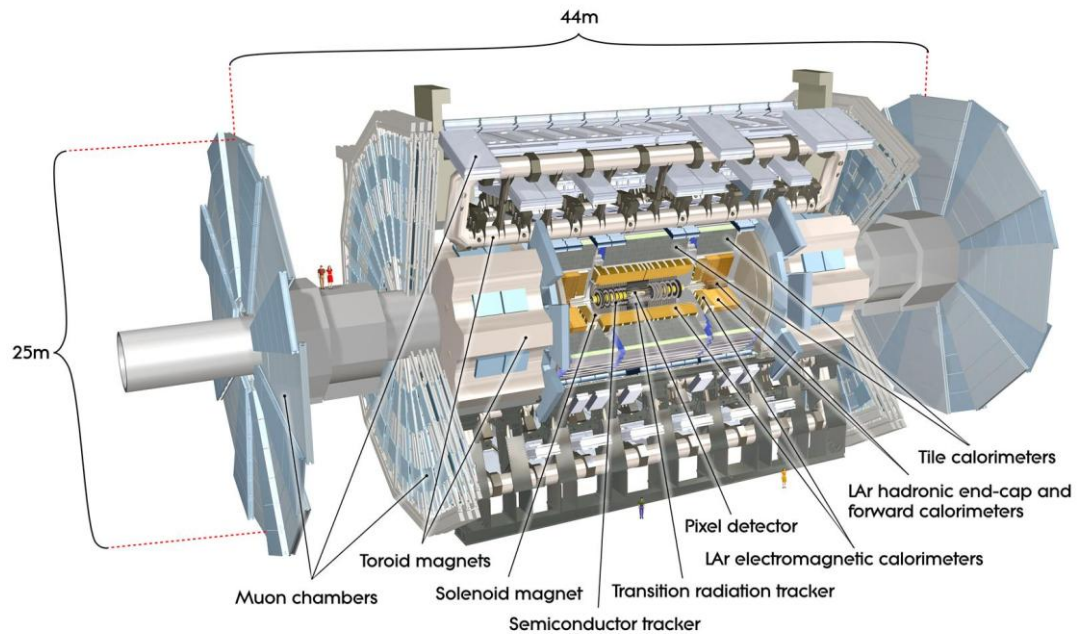


Fig. 1.36 ATLAS detector sketch

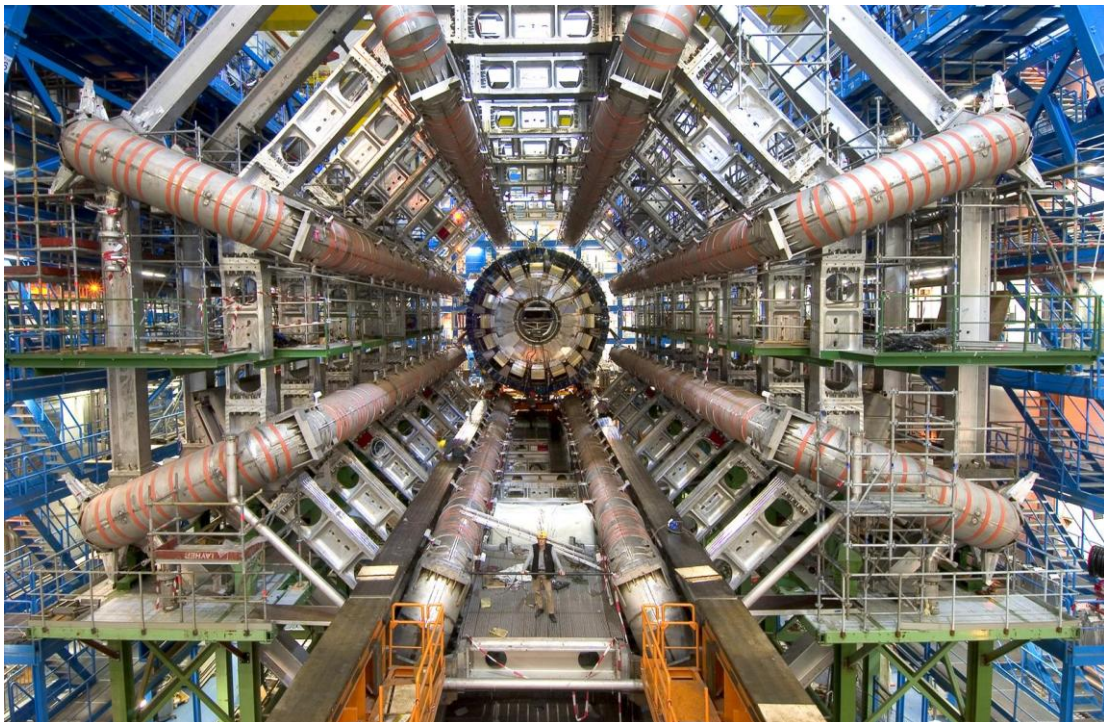


Fig. 1.37 ATLAS detector at CERN in assembly stage

1.3 DEFLECTING PARTICLES: ELECTRIC AND MAGNETIC FIELDS

Deflecting charged particles can be performed by using electric or magnetic fields, in opposition to the acceleration mechanism, which can only be carried out by electric fields as shown in section 1.1. This is explained using the Lorentz force equation (Eq. 1.1). The electric and magnetic fields exert totally different forces over charged particles. For example, a moderate magnetic field of 1 Tesla creates the same bending force on a particle travelling at the speed of light as an electric field of 300 MV/m. This represents an enormous electric field, impossible to be achieved in RF cavities at present. That is the reason why magnetic fields are more used for deflecting particles.

But the possibility of using electric fields for particle diversion opens a wide range of valid designs to build deflection devices, as it will be demonstrated in following sections.

1.3.1 SLOW AND CONSTANT DEFLECTION

Every accelerator needs slow and constant deflection devices. They are used to progressively bend the trajectory of the particles to allow them to describe circular orbits in synchrotrons. They can also be used to guide the particles along a predefined path in some linear accelerators, and even as complementary to faster devices in rapid deflection of particles.

These slow devices are the dipoles and the septa. Both use magnetic fields to divert particles. However, as they are commonly made of standard coils and soft iron, they cannot change the field very fast due to their high inductance and iron losses. In effect, dipoles are typically static or very slow ramped in most particle accelerators.

1.3.1.1 Dipoles

Dipoles are one of the first devices historically used in accelerators. They were designed to allow particles to pass through accelerating cavities more than once, as it was presented in previous sections. At present, dipoles are the limiting devices for higher energy proton synchrotrons, and the beam lifetime is limited by the field quality obtained in the magnets. They create a uniform magnetic field (usually vertical) to allow horizontal deflection of charged particles following the Lorentz law (Eq. 1.1) around a radius defined in Eq. 1.4. For a given radius, a synchrotron can only store higher energy particles if the magnetic field of the dipoles is proportionally increased. But the maximum field in a modern dipole is determined by its superconducting technology, and it can hardly be over 15 Tesla at present.

Dipoles can be built with or without using iron for the field geometry. There are several methods for designing dipoles, depending on the needed bending strength, maximum size, etc:

- Iron or coil dominated dipoles: Dipoles can be made with or without iron poles. Iron pole shape determines the field aspect inside the dipole, and contributes to the field strength by a high percentage of the total field in the aperture, but it is limited by the saturation value of the iron (about 2 T). On the other hand, dipoles without iron poles (also called *cosine theta* dipoles) have a field homogeneity determined by the positions of the conductors on the coils, and can reach higher fields. However, even dipoles without iron poles use an external iron to shield magnetic fields, which also contributes to the field in the aperture.
- Resistive or superconducting coils: Superconductivity can be applied either to iron or coil dominated dipoles. Effectively, Cos Θ dipoles use superconducting coils because the absence of iron would make them very inefficient using resistive coils. Iron dominated dipoles can be resistive (standard dipoles) or superconducting (superferric dipoles).

- Cold or room temperature iron: All the superconducting dipoles can be designed with the iron at cryogenic or room temperature. The latter can decrease cryogenic losses, but sometimes it is harder to manufacture, especially in iron dominated magnets where the coil should be isolated alone from room temperature in a cryostat.

Iron dominated dipoles are limited in field up to the saturation of soft iron and that is the reason why, nowadays, almost all high energy accelerators use cosine theta dipoles. The iron dominated dipoles can be built using several core shapes:

- ‘C’ core dipole: This is the classic design for dipoles. The iron is asymmetric around the coils, which are located at both sides of the poles. The poles need to be slightly modified using shims [13] to get good field homogeneity inside. The design can present problems with magnetic forces in the iron and coils (low stiffness) and also the high fringe field can be an issue for surrounding devices.

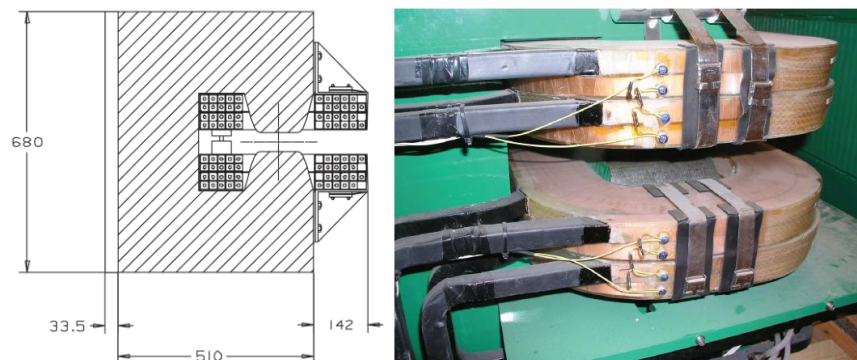


Fig. 1.38 Diamond storage ring dipole ('C' core)

- ‘H’ core dipole: The coil is embedded in an H shape iron (Fig. 1.39). The iron is symmetric and rigid, but the manufacturing is more challenging due to access problems to the coils. It still needs shims for the field quality.

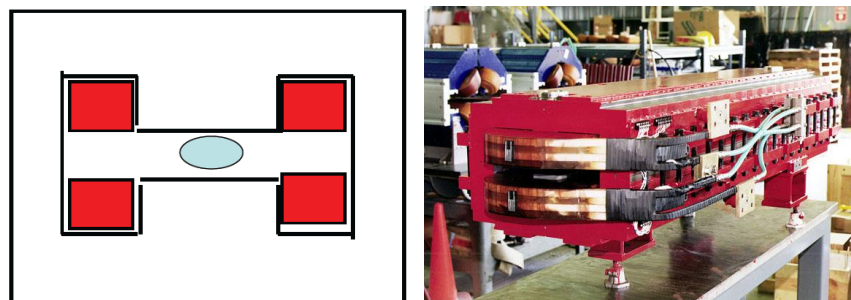


Fig. 1.39 'H' core dipole

- “Window frame” dipole: The coil fits inside a rectangular hole in the iron (Fig. 1.40). It is symmetric and very rigid, and needs no modification of the poles to get good field, but the manufacturing is much more difficult as the coils need to be out-of-plane at the ends to avoid interference with the beam pipe.

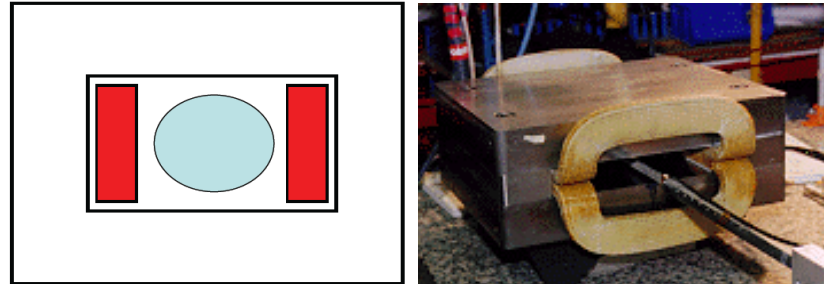


Fig. 1.40 “Window frame” dipole

Cosine theta dipoles do not need iron to generate a uniform magnetic field (Fig. 1.41). The powerful superconducting coils are more than enough to generate very high fields without the limit of iron saturation. Nevertheless, they are usually encircled by an iron cylinder which provides magnetic shielding and contributes to the field in the aperture.

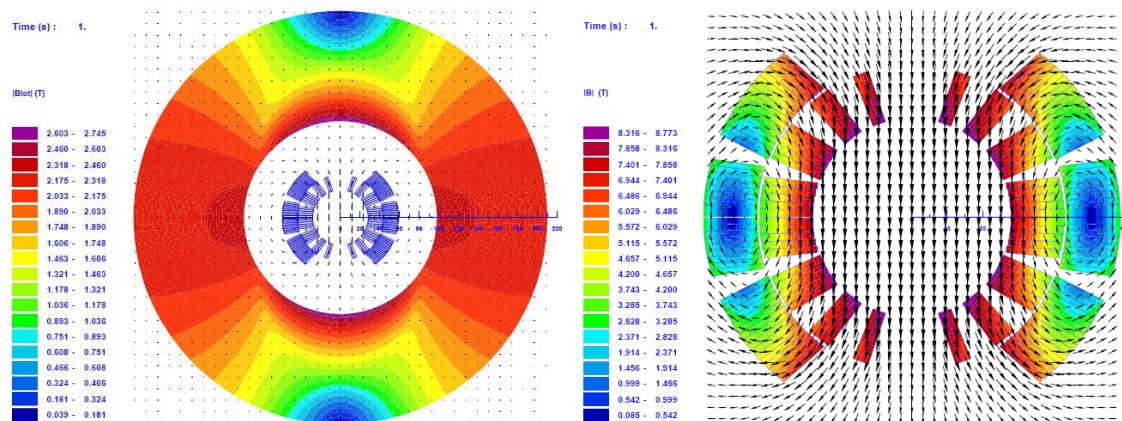


Fig. 1.41 Field map of a Cos Θ dipole, showing colour plots at iron (left) and coils (right)

The coil conductors frequently surround the beam pipe in a circular shape (saddle coils) and their position defines the geometry of the field lines. Sometimes, racetrack coils can also be used (Fig. 1.42). The maximum field inside the aperture is determined by the maximum field supported by the coils (to avoid superconductors becoming resistive³), and the coils are always the elements supporting the maximum field in the magnet (Fig. 1.41).

³ The transition between superconductor and resistive states is called “quench”.

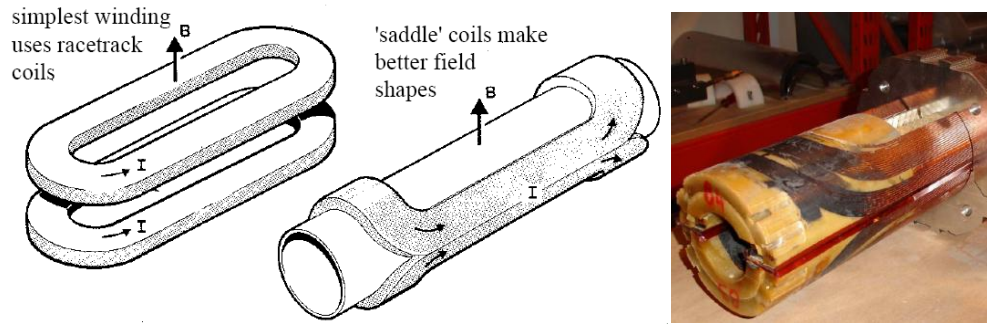


Fig. 1.42 Examples of superconducting winding

All these devices are DC or slow ramped in current. Typical values for self inductance on accelerator dipoles start from a few mili-Henries to some Henries. If a fast ramping was needed (from zero to nominal current in a couple of microseconds), the necessary voltage would be many thousands of volts according to Eq. (1.5).

$$V = -L \frac{dI}{dt} \quad (1.5)$$

The coil insulating materials could not withstand that voltage or very large insulator thickness would be needed, increasing enormously the size of the magnet.

1.3.1.2 Septa

The septum magnet (septa in plural) is a special kind of dipole. It creates homogeneous, usually vertical, B field to deflect injected or extracted beam but without deflecting the circulating beam. This is possible because the beam has already been slightly separated when arriving to the septum by phase-space manipulation or a fast kicker device (see section 1.2.4). Therefore, the septum continues deflecting the beam after an initial deflection. The trick of the system is to create a spatial separation between two regions in the beam path (Fig. 1.43); one region of high field (for deflection) and other region with very low (ideally zero) stray field for unaffected beam.

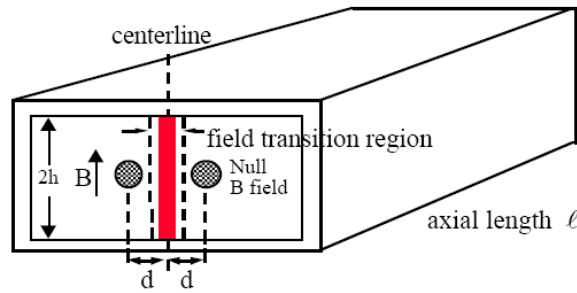


Fig. 1.43 Ideal box geometry of a septum magnet

Septa are usually combined as two magnets in series, named thin and thick septum. The thin septum magnet has the most challenging design (Fig. 1.44). It is very close to the main beam pipe of the accelerator and that is the reason why the allowed stray field is very low, usually lower than a couple of mT. It is built by a single turn coil that is only one or two mm thick in the septum plate (the metal plate closer to the beam pipe), to limit beam loss in beam pipe walls. The thin septum plate is copper made and should support the Lorentz forces, the high current density and the water pressure of the cooling circuit.

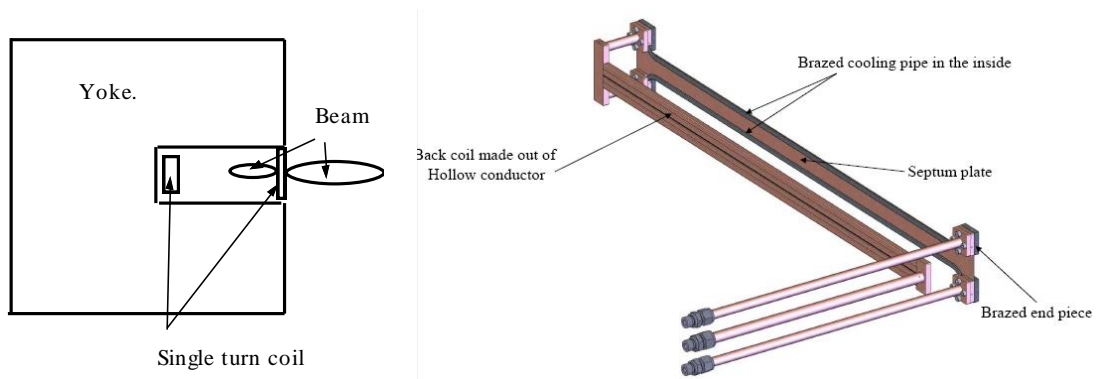


Fig. 1.44 Thin septum magnet cross section and coil installed in CTF3 CR

The thick septum magnet is more relaxed in specifications. Although it should conduct the same current as the thin septum, the thickness of the septum coil can be much larger because the beam is already deflected by the thin septum (Fig. 1.45). Effectively, the coil has constant cross section, and can have many turns, which allows for a higher field in the aperture. The coils also need water for cooling and therefore, the coil conductor is hollow.

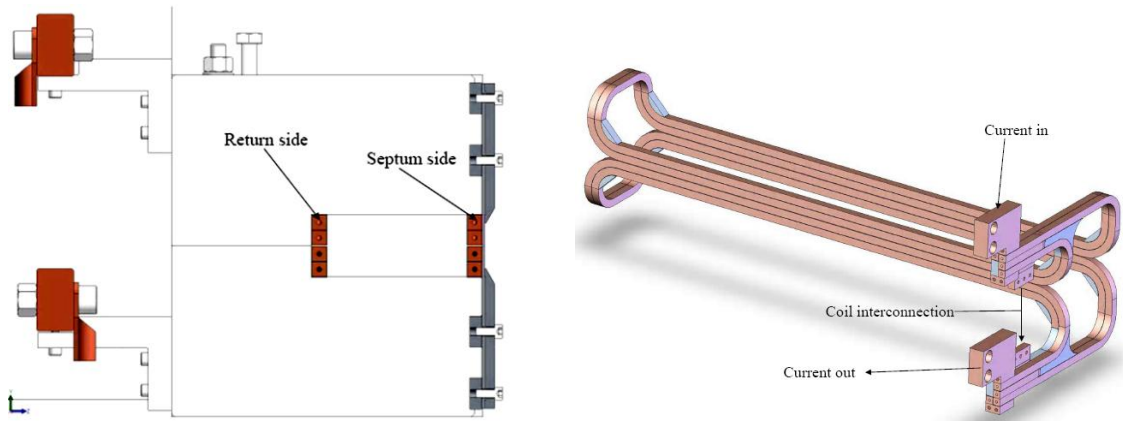


Fig. 1.45 Thick septum magnet cross section and coil model installed in CTF3 CR

Nevertheless, high current density in a thin septum results in a major thermal loading issue due to ohmic heating in the coil. The septum magnetic field can be DC or pulsed. When the effects of the eddy currents in the magnet core are ignored, there will be no differences between the DC and pulsed devices as far as the magnetic flux distribution is concerned. However, because of the high thermal loading in the septum conductor, a DC septum is possible only when the required gap field is relatively low or the septum is relatively thick. Otherwise the magnet must be pulsed, and the duty factor of the septum must be adjusted to reduce the thermal loading to an acceptable level. There are two types of pulsed septum magnets: direct drive and eddy current [14].

Direct drive septa have the same physical design as DC thin septa and also employ a thin septum coil. They use pulsed currents to generate the dipolar field in the aperture in order to reduce the thermal loading on the thin septum coil.

Eddy current septum uses a pulsed current through a cable which coils up around the iron yoke (Fig. 1.46). The eddy currents induced in the metallic septum act as a shield of the magnetic field in the outer side of the septum magnet. Cooling is easier because the eddy current shield is cooled down by conduction to the base plate. The yoke is usually made of high frequency material (ferrite⁴) to reduce losses.

⁴ Ferrite features combined high permeability and electrical resistivity at high frequencies (MHz range) to minimize eddy currents when exposed to time varying magnetic fields.

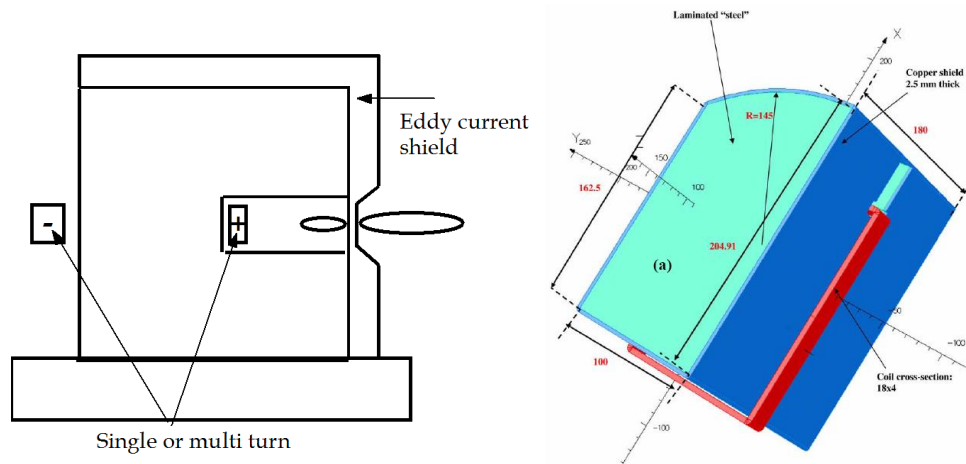


Fig. 1.46 Eddy current septum magnet

Eddy current septa work with medium frequency current pulses (tens of microseconds). A higher frequency would make the power supply much more expensive. That is the reason why the combination of fast kickers and DC septa is widely used for injection and extraction in accelerators.

1.3.2 FAST AND SELECTIVE DEFLECTION

In modern particle accelerators, injection and extraction devices are needed to make the beam follow different trajectories (see section 1.2.4). Sometimes, this task can be achieved by DC or pulsed septa. However, when a really fast response is needed, the only device capable of injecting or extracting the beam is a kicker. Injection and extraction kickers play a fundamental role in all the projects of new major accelerators currently under study. The feasibility of these accelerators depends also on the possibility to realize kickers based on unconventional design and new technologies.

A kicker is a device that creates a very fast field which deflects the particles. Kickers are usually fed by a pulsed waveform (Fig. 1.47) with very fast rise or fall times (typically $\ll 1\mu\text{s}$) and good flat-top stability.



Fig. 1.47 Schematic fast fall/rise flat-top waveforms

A good pulse flat-top is required for a uniform deflection of the whole beam (or bunches of the beam). As the beam length is finite, the field must be maintained at the same peak value for a constant and uniform deflection of all bunches. Actually, when the field is started or interrupted inside the beam, the device can be referred as a clipper. A device of this kind will also be treated in this Thesis.

The deflecting field in a kicker can be electric, magnetic or electromagnetic, as all these fields can deflect charged particles. Therefore, the kickers can be classified according to the field:

- **Magnetic kickers:** They use copper coils and high frequency magnetic material (ferrite) to generate a magnetic pulse which forms a dipolar field inside their aperture. They are built as “window frame” dipoles (Fig. 1.48), embedding a coil in the rectangular hole of a ferrite core. The beam pipe is ceramic made in order to avoid eddy currents in a possible metal pipe due to the time varying magnetic field.

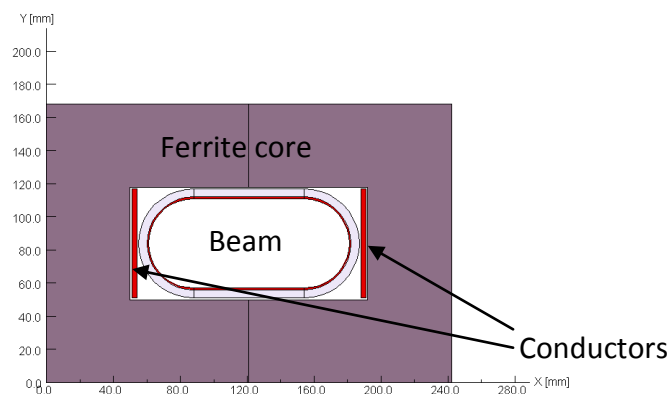


Fig. 1.48 Cross section of a magnetic kicker for BEPCII

These kickers are easy to manufacture (they do not need tight tolerances) but they have some design concerns. Firstly, it is very difficult to get good field uniformity for large apertures and flat-top stability for fast rise time pulses. Moreover, magnetic kickers usually represent the highest contribution to the beam impedance⁵ in the accelerator, owing to the ceramic beam pipe, which is “transparent” to the beam electromagnetic fields.

- Electrostatic kickers (Fig. 1.49): They consist of two parallel electrodes (flat or curved) inside a vacuum pipe (no. 1). Each electrode (no. 2) is fed by one electrical feedthrough (no. 5) to charge the capacitor formed by both electrodes and it is supported by an insulating stand-off (no. 3). The field uniformity is given by the electrodes cross section and their position (the distance between them, like in a capacitor).

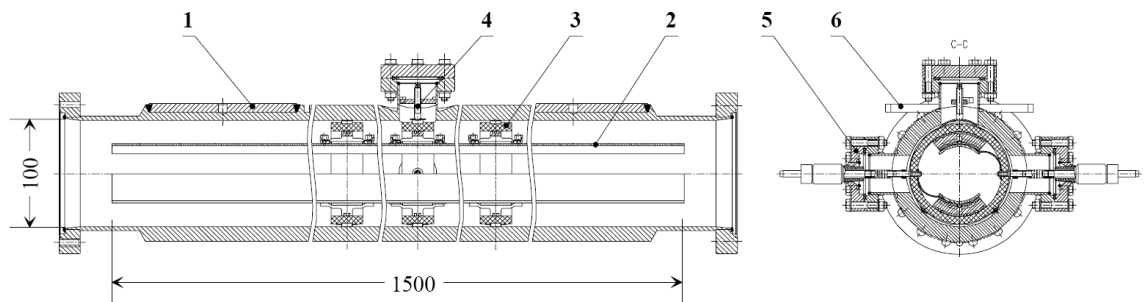


Fig. 1.49 Electrostatic kicker of the LHC transverse damping system [15]

The working method is as follows [16]: the electrodes are capacitively charged by a current source (slow), the injected beam is deflected by the electrostatic field and the plates are discharged like a transmission line (very fast).

Electrostatic kickers are even easier and simpler to manufacture than magnetic kickers, feature extremely good flat-top stability and very good beam impedance (smaller aperture). However, the technological restrictions about handling high electric fields (voltages) are the main handicap for these devices not being very powerful (maximum a few hundreds of kilovolts). Furthermore, they usually need charging times in the order of a few microseconds, not fast enough for some applications.

⁵ The beam impedance denotes the “difficulty” for the beam to pass through the devices. It is increased when the beam travels by a non uniform beam pipe and it is a major cause of beam instability.

- Strip-line kickers: These kickers are very similar in shape to the electrostatic kickers, but the working method is totally different. They also consist of two parallel metallic electrodes supported by ceramic stand-offs inside a vacuum tank. Nevertheless, the electrodes are connected at the ends by two feedthroughs each, to allow for power input and output (Fig. 1.50). The field uniformity is also given by the electrodes cross section and the distance between them.

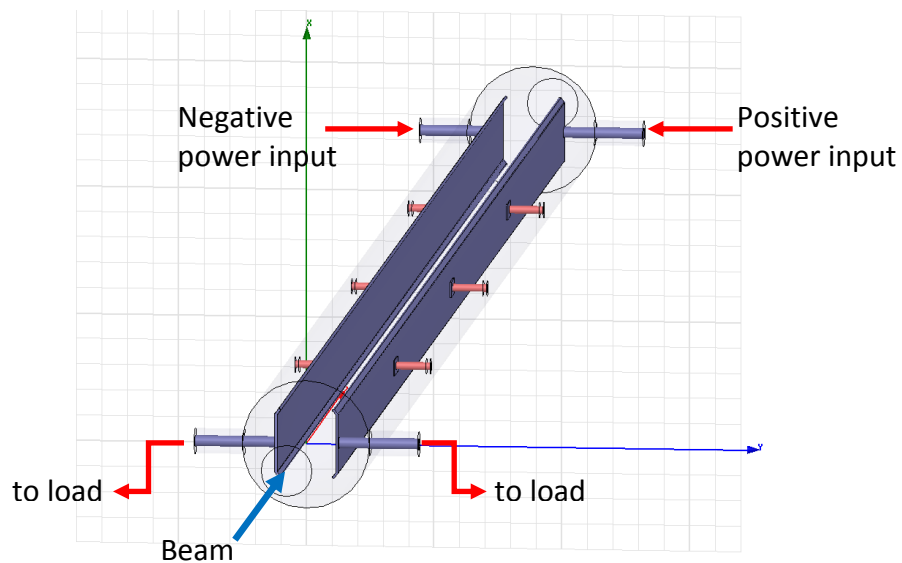


Fig. 1.50 3D model of a strip-line kicker (vacuum chamber is transparent)

The structure is similar to a pair of strip-lines where each electrode forms a transmission line with the half tank. Therefore, the working method consists of an electromagnetic (EM) wave that propagates along the strip-lines at the speed of light.

In order to generate a transverse kick, the kicker should be driven in differential mode. Consequently, the ports located downstream the beam direction should be powered by opposite polarity generators (pulse or waveform) and the upstream ports should be connected to dissipation loads. Otherwise, it can be demonstrated (Eq. 1.1) that the electric and magnetic fields of the EM wave would subtract each other or even be null in the kicker axis.

This kind of excitation gives an electric and magnetic field distribution (transverse EM wave, or TEM mode⁶) that generates a combined Lorentz force over the charged particles. If we suppose that the particles move closely at the speed of light (typically for electrons), and because of the modulus of E is related with B by the speed of light in lossless TEM propagation modes [17], the Lorentz force (Eq. 1.1) effectuated by E field is similar to the Lorentz force generated by B field over a charged particle, as shown in Eq. (1.6).

$$|\vec{E}| = |\vec{v} \times \vec{B}| \rightarrow \vec{F} = 2 q \vec{E} \quad (1.6)$$

This relation makes these devices more powerful than electrostatic kickers in terms of efficiency, as they use both electric and magnetic fields for deflecting the beam. However, the voltage used in strip-line kickers is typically lower (up to 50 kV) due to pulsed power supply problems.

Nevertheless, strip-line kickers are much faster. Both power input (like “charge”) and power output (like “discharge”) are carried out using fast transmission lines. These devices can handle rise and fall times of only a few nanoseconds, 3 orders of magnitude lower than electrostatic kickers. In contrast, they are a bit harder to manufacture, consume much more power and the flat-top stability is a challenging concern for the power supply.

⁶ TEM stands for Transverse Electro-Magnetic, a transmission mode where electric and magnetic fields are both perpendicular to the direction of propagation. This is the predominant mode in coaxial-like transmission lines.

1.4 STRIP-LINE KICKERS BASICS

1.4.1 CHARACTERISTIC IMPEDANCE

It has been noticed in section 1.3.2 that strip-line kickers operate as two joint transmission lines formed by the electrodes with the half tank. In effect, a strip-line transmission line is quite similar to a coaxial line (an inner conductor surrounded by dielectric material and metallic walls). The joint plane of the kicker strip-lines is like an electric wall generated by the opposite polarity of both EM waves (the potential of the wall could be considered zero). The symmetry plane could be substituted by a metallic plate from the point of view of the electromagnetic transmission. However, this would render the kicker unusable as the beam should travel free of obstacles in the aperture. Nevertheless, this approach is useful for modelling purposes.

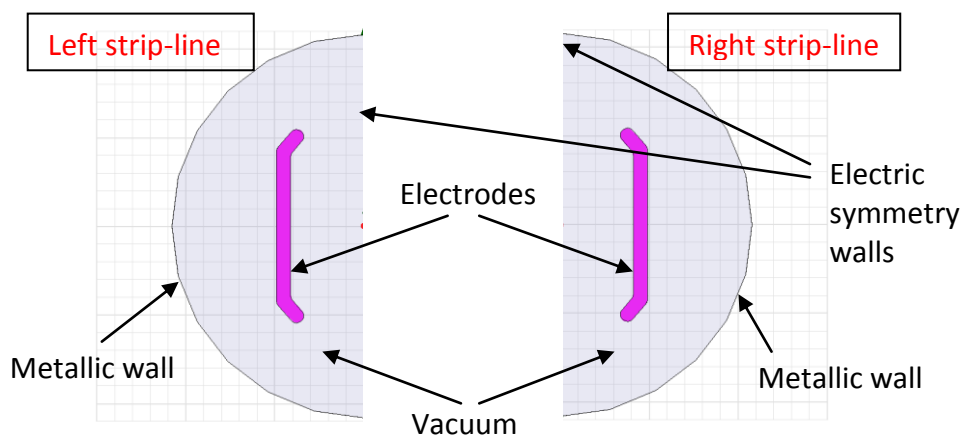


Fig. 1.51 Symmetric strip-lines to form a strip-line kicker

Every high frequency transmission line is characterized by the impedance known as characteristic impedance, usually designated as Z_0 . The characteristic impedance of a line is the input impedance of an infinite length of the line. In other words, it is the result of the infinite limit of equivalent series (usually inductors) and parallel (usually capacitors) impedances of a transmission line (Fig. 1.52 a). Therefore, if a finite length of line is terminated in its characteristic impedance, Z_0 , then its input impedance will also equal Z_0 , like if it was an infinite line (Fig. 1.52 b). This is brilliantly explained in reference [8], section 22-6.

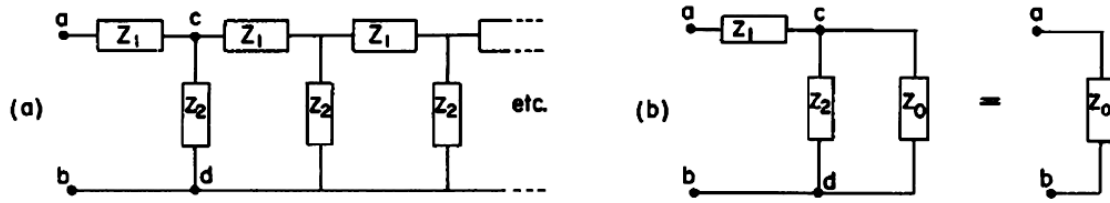


Fig. 1.52 Characteristic impedance of an infinite length transmission line

The characteristic impedance of an ideal TEM transmission line (with no dielectric leakage nor conductor resistance) can be calculated as shown in Eq. (1.7), where L_0 and C_0 are respectively the inductance and the capacitance of a unit length of the line. This impedance represents a pure resistance. Obviously, it can also be calculated by the ratio between the instantaneous voltage and current in the transmission line.

$$Z_0 = \sqrt{\frac{L_0}{C_0}} \quad (1.7)$$

When using air or vacuum insulation, the characteristic impedance is a geometrical parameter, only depending on the cross section of the transmission line. This can be analytically solved for uncomplicated geometries like coaxial [17], and generally when analytical expressions of electric and magnetic fields can be obtained in the cross section. However, in non analytical cases (Fig. 1.53), it is necessary to obtain the full solution of the electromagnetic field using a numeric method.

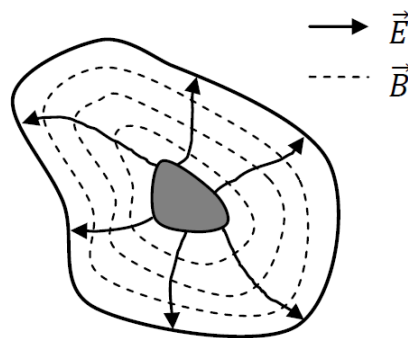


Fig. 1.53 Field lines on arbitrary TEM transmission line

Then, the inductance and the capacitance can be calculated from the stored magnetic and electric energy in that order, as shown in Eqs. (1.8) and (1.9).

$$u_e = \int \frac{1}{2} \varepsilon |\vec{E}|^2 dS = \frac{1}{2} C V^2 \quad (1.8)$$

$$u_m = \int \frac{1}{2} \frac{|\vec{B}|^2}{\mu} dS = \frac{1}{2} L I^2 \quad (1.9)$$

Voltage and current can be calculated by the line integral of E between conductors and the circulation of H around the central conductor respectively, using Eqs. (1.10) and (1.11).

$$V = \int \vec{E} \cdot d\vec{l} \quad (1.10)$$

$$I = \oint_c \vec{H} \cdot d\vec{l} \quad (1.11)$$

Anyway, it is easy to see in Eq. (1.7) that the characteristic impedance increases as the conductor spacing increases. If the conductors are moved away from each other, the distributed capacitance will decrease (greater spacing between capacitor “plates”), and the distributed inductance will increase (less cancellation of the two opposing magnetic fields).

Concerning kickers, the characteristic impedance of the power supply and strip-lines must be matched with the coaxial input and output ports to avoid reflection of the power given by the power supply (see [17], section 2.3). The dissipation loads must be matched also to the same impedance. The transition from the coaxial to the stripline should be optimized for the same reason.

The most typical figure taken for characteristic impedance in power transmission is 50 Ohm. This value represents a compromise between high power handling (30 Ohm) and low loss (77 Ohm) for air dielectric coaxial-like transmission lines⁷ and it is the impedance most extended commercially for cables and connectors.

⁷ As a matter of fact, the standardization of fifty Ohm impedance goes back to developing coax cables with air dielectric for kilowatt radio transmitters in the 1930s. If dielectric constant is higher than 1 (using semi rigid PTFE), the minimum loss point is closer to 50 Ohm.

1.4.2 ELECTRIC AND MAGNETIC FIELDS: RF OR PULSED POWER

Electric and magnetic phenomena at the macroscopic level are described by Maxwell's equations [18]. Strip-line kickers work by means of high frequency electromagnetic fields, which are governed by the non simplified form of the Maxwell's equations. Because of the high frequencies and, therefore, short wavelengths, standard circuit theory generally cannot be used directly to solve high frequency problems. This is due to the fact that, in general, the lumped circuit element approximations of circuit theory are not valid at high frequencies. A working frequency of 1GHz represents a wavelength of 0.3 m ($\lambda = c/f$), which implies that a small structure of 1 m would have different phase voltages and currents along it for a given time. In fact, standard circuit theory is an approximation of the broader theory of electromagnetism as described by Maxwell's equations.

The need for the non simplified form of the Maxwell's equations makes the kicker problem much more complicated. Given that a complex, non analytical geometry is used, all the field calculations have to be carried out through numeric method codes, which solve the full Maxwell's equations in a given region. That implies lot of calculations and large amounts of computer memory to solve the enormous electromagnetic matrices, and huge amounts of time to solve time transient effects. However, some analytical calculations can also be made as it will be shown in next chapter.

When an electromagnetic wave travels through a strip-line, the dominant transmission mode is TEM. This mode is identical to the wave transmission in free space, where \vec{E} and \vec{H} vectors are orthogonal to each other and orthogonal to the direction of propagation. TEM modes can only exist when two or more conductors are present in the transmission line [17]. However, high order modes can also exist in a strip-line (TE or TM⁸), which are intrinsically evanescent.

⁸ TE and TM stand for Transverse Electric and Magnetic field respectively, where electric (or magnetic) field is perpendicular to the direction of propagation.

Therefore, to avoid the propagation of these modes, one must be aware of the cut-off⁹ frequency of the lowest of them. In strip-line kickers, high order modes are easy to avoid when only considering the power supply input, which is determined in frequency. Nevertheless, there is another input that cannot be so controlled: the particle beam that passes through the kicker. The beam induces wakefields (dealt with the next chapter) which can be several orders of magnitude in frequency above the power supply inputs. Those wakefields are transmitted by the strip-lines and that makes the kicker analysis even more complicated.

Up to this moment, no kind of power has been specified to excite strip-line kickers. The general concept of EM wave has been used in previous sections, but with the meaning of EM power that travels through the strip-lines. Actually, the EM power can be in form of a radiofrequency (RF) wave or in form of a fast DC pulse. RF power is usually used in strip-line kickers for correcting beam instabilities [19], not for injection or extraction. RF power can be continuous or in bursts, depending on the accelerator requirements. Anyway, RF power is typically used in RF deflectors¹⁰, not strip-line kickers. In contrast, fast DC pulses are used for strip-line kickers which are designed for injection and extraction. Most of the design procedures are similar for both excitations in strip-line kickers; however, in this Thesis more emphasis will be done on pulse excitation, as it is the most challenging design since steady state calculations cannot describe the full behaviour of the device.

1.4.3 FAST PULSE RESPONSE

The integrated transverse deflecting field seen by a particle (in Volts¹¹), as a function of time, can be calculated from the kicker geometry and the input pulse shape. It is given by the convolution between the kicker response to a Dirac delta $\delta(t)$ and the input pulse, as usually done for typical responses of other linear electrical systems.

⁹ The cut-off frequency of a mode defines the frequency above which the transmission is possible. See reference [17] for more information.

¹⁰ They are essentially RF cavities (also travelling wave) working on transverse, deflecting mode.

¹¹ In the next chapter, it will be shown how the combined electric and magnetic field is transformed in an equivalent voltage, named transverse voltage.

In the ideal case, if the kicker has a constant transverse section, and matching between the pulse generator and the kicker structure is perfect, the kicker impulse response to a $\delta(t)$ is a rectangular function of length $2L/c$ where L is the kicker length, as shown in Fig. 1.54.

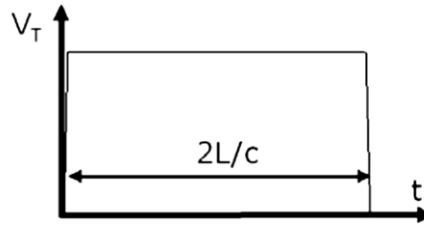


Fig. 1.54 Ideal kicker response to a $\delta(t)$

The physical meaning of Fig. 1.54 is that particles travelling at the speed of light located between a distance L to the kicker entrance ($x=-L$) and just exiting the kicker ($z=L$) will be subjected to an identical deflecting field V_T ¹². Particles that, at $t=0$ are further than $-L$ or, obviously, have passed the kicker ($z>L$), will not “see” any deflecting field. This is graphically shown in Fig. 1.55 for a particular case of a test particle.

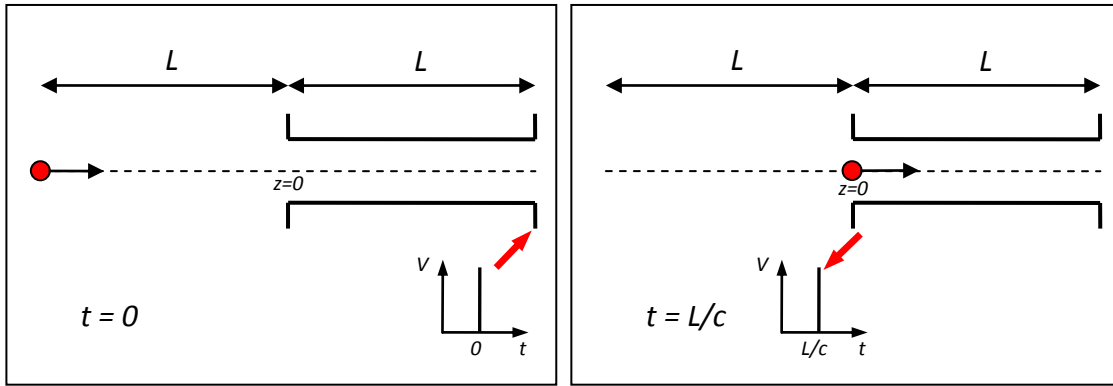


Fig. 1.55 Test particle seeing V in the limit (at L distance from the kicker)

The same can be applied to an “almost real” input, as shown in Fig. 1.56. The total deflecting field as a function of time related to pulse of Fig. 1.56 is shown in Fig. 1.57, assuming of $T_f > 2L/c > T_r$ ¹³. This assumption ensures the existence of a flat-top convoluted zone sized $(T_f - 2L/c)$ where all the particles are subjected to identical deflection field.

¹² Created by the $\delta(t)$ impulse which starts travelling along the kicker at $t=0$.

¹³ T_r stands for electrical pulse rise/decay time (identical on this assumption) and T_f is the flat-top time.

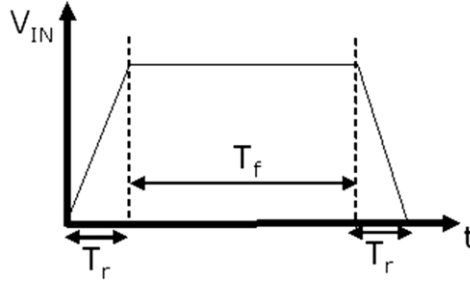


Fig. 1.56 Kicker input pulse shape (simplified)

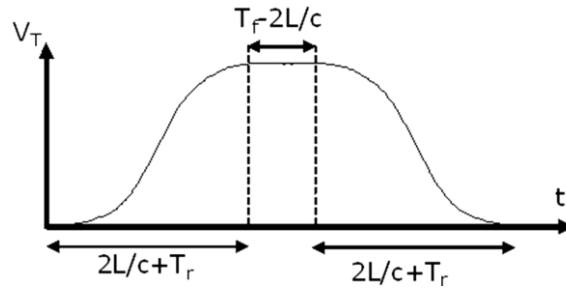


Fig. 1.57 Kicker response to a trapezoidal pulse ($T_f > 2L/c > T_r$)

Using this model it is possible to do a first evaluation of the input pulse and kicker requirements in term of rise/decay time, flat-top time, and kicker length. For example, if we need to kick a bunch of length σ_B (in millimetres), the minimum flat-top time of the input pulse is:

$$\frac{\sigma_B}{c} = T_f - \frac{2L}{c} \quad (1.12)$$

$$T_f = \frac{\sigma_B + 2L}{c} \quad (1.13)$$

However, it is quite difficult to exactly fit the bunch in a flat-top deflecting voltage of the same length. Therefore, a distance at least 4 times the length of the bunch is usually used, as shown in Eq.(1.14).

$$T_f = \frac{4\sigma_B + 2L}{c} \quad (1.14)$$

Sometimes it is required that the previous and following bunches are not subjected to any deflecting field. To fulfil this specification, the duration of the deflecting field should be two times the time space between bunches (T_B) at the most.

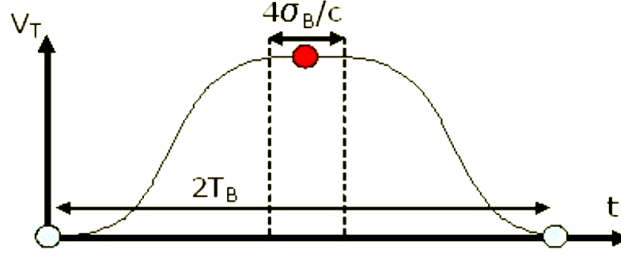


Fig. 1.58 Total deflecting field as a function of time

The required kicker length L is determined by equalling twice the time space between bunches with the full time of the convoluted response of Fig. 1.57:

$$2 T_B = T_f - \frac{2 L}{c} + 2 \left(\frac{2 L}{c} + T_r \right) \quad (1.15)$$

$$L = c \left(T_B - T_r - \frac{T_f}{2} \right) \quad (1.16)$$

The length of the kicker and the flat-top time of the pulse can be obtained by solving the system of equations formed by (1.14) and (1.16)¹⁴. The solutions depend only on beam data (time between bunches T_B and bunch length σ_B) and rise/decay time of the pulse T_r .

$$L = \frac{1}{2} (c T_B - c T_r - 2 \sigma_B) \quad (1.17)$$

$$T_f = \frac{2 \sigma_B}{c} + T_B - T_r \quad (1.18)$$

These latter relations derived by the author can also be obtained for other positions of bunches inside the convoluted voltage, just replacing $2T_B$ in Eq. (1.15) by the correct value.

All the calculations above are required when the kicker is used to inject or extract specific bunches of particles travelling at the speed of light; in other words, they are used when high precision is required in the injection or extraction, not to disturb neighbouring bunches.

¹⁴ T_r is assumed known because typically the smaller the better to avoid affecting other bunches. The limitation of rise time is only imposed by the power supply and a good impedance matching.

However, in other cases (full beam extraction, beam clipping, etc.), the designer is able to play with kicker main parameters as length, pulse duration and pulse voltage¹⁵ to get a better compromise between performance and manufacturing costs.

1.4.4 DISSIPATION LOAD

The strip-line kicker is only a transmission line; therefore, all the power transmitted by the pulse has to be dissipated at the end of the strip-lines. This is carried out by using two dissipation loads, connected to the upstream ports of the kicker. The dissipation loads must be designed to handle the voltage and current of the pulse and its averaged time power (depending on the repetition rate). The loads should be matched in impedance with the kicker and the power supply to avoid pulse reflected power. A perfectly matched load makes the kicker and the load to behave as a perfect resistor of the characteristic impedance Z_0 , from the power supply point of view (see section 1.4.1).

The load must also be designed to handle the frequency content of the pulse, keeping a good impedance match at all the frequencies. In fact, the dissipation load is physically manufactured by using very small shunt resistors of Z_0 impedance. If the resistances are small enough, the voltage and current can be considered constant on their length. Therefore, the resistances can be considered as lumped elements even when working at high frequencies.

When handling pulsed signals, the high frequency content is determined by the smallest of the rise and decay time of the pulse (T_r). It is considered that one has to bear in mind only the frequencies below $0.5/T_r$ [20] for good transmission of the pulse. If we consider the length of the rising edge $l = c T_r$, the elements smaller than $l/6$ can be considered lumped elements.

¹⁵ The pulse voltage depends on the desired deflection angle and strip-line length, as it will be shown in the next chapter.

1.5 CONCLUSIONS

A long time has passed since the first particles were artificially accelerated to discover the atom structure. Accelerators play a very important role in present science and technique and they will continue helping in future progress. The huge spread of these machines is helping to reduce their cost, which is very important to increase their use in daily medicine and industry. Moreover, the current mammoth projects with some machines around the world would help physicist to know a bit more about the origin of the universe.

Particle accelerators are composed of multiple devices to work, all of them in close relation with each other. Particle sources, RF cavities, magnets, deflecting devices, diagnostics, vacuum and detectors form a well tuned symbiosis to make the accelerator work. All the devices together integrate a very complex system where a deep knowledge of engineering and physics is fundamental for the design and operation.

The newest fast deflection kickers are one of the most important devices in present-day new accelerator projects, mainly for future linacs. The high speed response of the strip-line kickers makes possible decreasing the distance between bunches and also the time between turns, therefore decreasing the size and cost of storage, damping and combiner rings.

Strip-line kickers are transmission lines whose main parameters are the characteristic impedance, the TEM mode transmission fields (characterized by the complete Maxwell's equations) and the fast pulse response. An excellent command of these concepts is required in order to correctly understand and design these devices.

Several relations have been derived by the author of this Thesis in order to obtain the length of the kicker electrodes and the flat-top time of the pulse depending only on beam data (time between bunches T_B and bunch length σ_B) and rise/decay time of the pulse T_r . These relations are useful for precise bunch injection and/or extraction inside a beam.

1.6 REFERENCES

- [1] *The importance of particle accelerators.* **Amaldi, Ugo.** Vienna : EPAC 2008, 2000.
- [2] **Bryant, P. J.** A Brief History and Review of Accelerators. *CERN Accelerator School.* Geneva : s.n., 1994.
- [3] **Sessler, Andrew and Wilson, Edmund.** *Engines of Discovery / A century of particle accelerators.* s.l. : World Scientific Publishing Co. Pte. Ltd., 2007. ISBN-13 978-981-270-070-4.
- [4] **Group, CERN Communication.** *LHC the guide.* Geneva : CERN-Brochure-2008-001-Eng, 2008.
- [5] **DESY XFEL Project Group.** *The Technical Design Report of the European XFEL.* Hamburg : DESY, 2007. ISBN 978-3-935702-17-1.
- [6] **Gesellschaft für Schwerionenforschung mbH.** *FAIR Baseline Technical Report.* Darmstadt : s.n., 2006. ISBN 3-9811298-0-6.
- [7] *Electron and Ion Sources.* **Scrivens, R.** Zakopane : Cern Accelerator School, 2006.
- [8] **Feynman, Richard P., Leighton, Robert B. y Sands, Matthew.** *The Feynman Lectures on Physics, Vol.2, mainly electromagnetism and matter.* Pasadena : Addison-Wesley Publishing Company, INC, 1964. 978-0201021158.
- [9] *Injection and Extraction into/out of Accelerators.* **Marks, Neil.** Warrington (UK) : ASTeC, U. of Liverpool, 2008.
- [10] *Beam Diagnostics.* **Raich, Ulrich.** Zakopane : Cern Accelerator School, 2006.
- [11] *Beam Diagnostics for Accelerators.* **Kozioł, H.** Jyväskylä, Finland : CERN 94-01, 1994.
- [12] *La Rivelazione delle Particelle Elementari.* **Masterclass.** Padova : INFN, 2006.

- [13] *Conventional Magnets for Accelerators*. **Marks, Neil**. Zakopane (Poland) : CERN Accelerator School, 2006.
- [14] *Direct-drive and eddy-current septum magnets*. **Kim, S. H.** LS-292, Argonne, IL 60439 : Argonne National Laboratory, 2001.
- [15] *Transverse Feedback System (LHC Damper)*. **Hofle, Wolfgang**. Hamburg : Seminar at DESY, 2005.
- [16] **Heine, E., et al.** Pulsed Electrostatic Kickers with Low Beam Impedance for AmPS. Amsterdam : National Institute for Nuclear and High Energy Physics, EPAC 1992.
- [17] **Pozar, David M.** *Microwave Engineering*. s.l. : Wiley, 2004. 978-0471448785.
- [18] **Maxwell, J.C.** *A Treatise on Electricity and Magnetism*. Dover, N.Y. : s.n., 1954.
- [19] **Gallo, A., et al.** *The Transverse Feedback kicker*. DAFNE Technical Note, Frascati (Italy) : INFN-LNF Accelerator Division, 1995.
- [20] **Johnson, Howard and Graham, Martin.** *High-speed digital design, a handbook of black magic*. New Jersey : Prentice Hall PTR, 1993. ISBN 0-13-395724-1.

CHAPTER 2

CALCULATION METHODOLOGY FOR STRIP-LINE KICKERS

2.1 BASIC SPECIFICATIONS

2.1.1 INTEGRATED FIELDS: THE TRANSVERSE VOLTAGE AND DEFLECTION STRENGTH

The strip-line kicker works by means of a TEM wave that travels along the device aperture and exerts a transverse force over the particles. Both electric and magnetic fields contribute to the force according to the Lorentz law (see chapter 1).

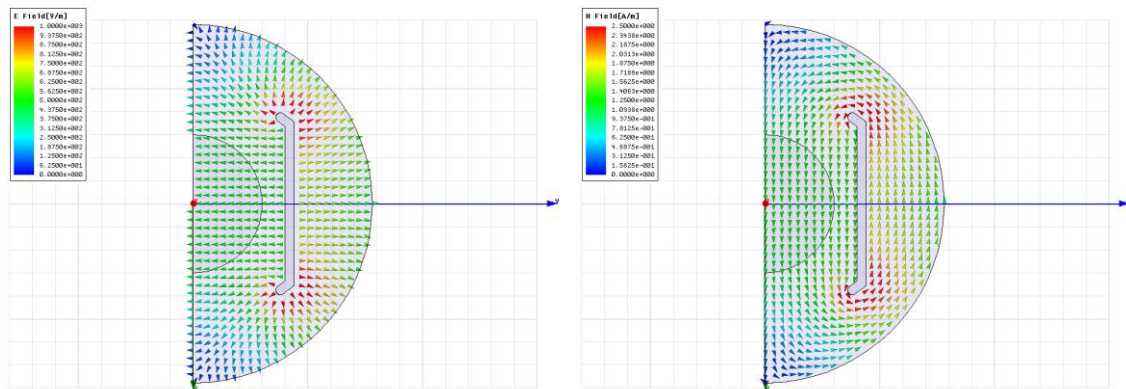


Fig. 2.1 Instantaneous E and H distributions in kicker half cross section (peak field values for 1 watt input RF power)

One of the most important specifications to start the kicker design is the required transverse voltage. The transverse voltage, usually referred to as V_{\perp} , is the integrated transverse potential (in volts) that a particle experiences when passing through the kicker due to the travelling electromagnetic fields. This magnitude is composed by the integrated equivalent potential of both, the electric and magnetic fields.

The electric component of the transverse voltage $(V_{\perp})_E$ is easy to obtain by just integrating the transverse electric field¹ \vec{E}_{\perp} along the beam trajectory, as shown in Eq. (2.1).

$$(V_{\perp})_E = \int \vec{E}_{\perp} dz \quad (2.1)$$

The magnetic component of the transverse voltage $(V_{\perp})_B$ can be calculated according to the magnetic term of the Lorentz force relation, as shown in Eq. (2.2).

$$(V_{\perp})_B = \int (\vec{v} \times \vec{B})_{\perp} dz \quad (2.2)$$

Obviously, as stated in chapter 1, the modulus of E and B fields are related by the speed of light. Therefore, the total transverse voltage can also be obtained by double the electric field contribution for relativistic particles and TEM propagation modes. The addition of both voltages results in the total transverse voltage V_{\perp} , which can be defined as the integral of the normal component of the Lorentz force along the beam axis (Eq. (2.3)).

$$V_{\perp} = \int (\vec{E} + \vec{v} \times \vec{B})_{\perp} dz \quad (2.3)$$

The transverse voltage can also be understood as the energy per unit charge given to the transverse movement of the particles in the passage through the kicker. In fact, the units of Eq. (2.3) are volts per electron charge, a unit of energy also known as electron-volts² (eV).

The transverse voltage can be affected by one of the magnitudes used for RF cavities, which is known as the transit time factor. The transit time factor defines the ratio of energy actually given to a particle passing the kicker at peak field to the energy that would be received if the field were constant with time at its peak value.

¹ In effect, there can only be a transverse component of the electric field as the propagation mode is TEM. Moreover, there should ideally only appear a horizontal component for horizontal-plane deflection kickers; however, the homogeneity of the field is not perfect, as it will be indicated in following sections.

² An electron-Volt is the energy that an elemental charge acquires when it accelerates through an electrostatic potential difference of one Volt. It equals to 1 Volt (1 Joule/1 Coulomb) multiplied by the electron charge of 1.6022×10^{-19} Coulombs: $1\text{eV} = 1.6022 \times 10^{-19}$ Joules.

If a particle is only affected by the flat-top zone of the pulse when passing through the kicker, the transit time factor would be equal to one, and the transverse voltage would not be diminished. However, some particles can be affected by the slopes of the pulse somewhere in their path, which will reduce the amount of deflection received (see section 1.4.3). For strip-line kickers it is usually important to completely deflect bunches in the flat-top zone, avoiding a transit time factor lower than one.

There is a close relation between the deflection angle given to the particles and the transverse voltage. In effect, independently of the length of the kicker and for a given particle longitudinal energy, a given transverse voltage corresponds to a specific deflection angle and vice versa. Both can be input specifications for a kicker design.

When it is said that a beam of particles has E_b (eV) energy, the mentioned energy is actually indicated for one of the particles of the beam and it corresponds to the longitudinal kinetic energy³. If the particle is entering a kicker which provides a transverse voltage V_{\perp} , the transverse acceleration energy is added in quadrature with the longitudinal energy of the particle (Fig. 2.2), resulting in a new direction and absolute value for the velocity.

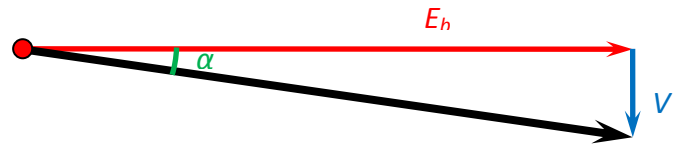


Fig. 2.2 Transverse voltage adding with the particle's longitudinal energy

The angle between the velocity vectors before and after passing through the kicker is known as the deflection angle (typically very small), and it can be calculated as shown in Eq. (2.4).

$$\alpha = \tan^{-1} \left(\frac{V_{\perp}}{E_b} \right) \cong \frac{V_{\perp}}{E_b} \quad (2.4)$$

The deflection angle is usually about a few mrad. That is the reason why a thin septum is typically needed to continue the deflection after the kicker.

³ The total energy of a particle is composed by the rest mass energy (most of the times negligible for electrons and positrons) and the kinetic energy. A bunch can contain hundreds billions of particles.

2.1.2 THE MINIMUM APERTURE

The beam inside an accelerator travels along an ultra-high vacuum metal pipe. The inner diameter of the pipe (assuming beam screens⁴ are not present) is known as the aperture. Physicists usually define a minimum value for that diameter⁵ depending on the beam characteristics [1]: energy, current, emittance, etc. The aperture must not shrink below the minimum value to avoid particle losses in the beam pipe walls. The same restrictions apply to a kicker device. One of the main specifications is the minimum aperture (or stay-clear area) to let the particles go through the device without obstacles (Fig. 2.3).

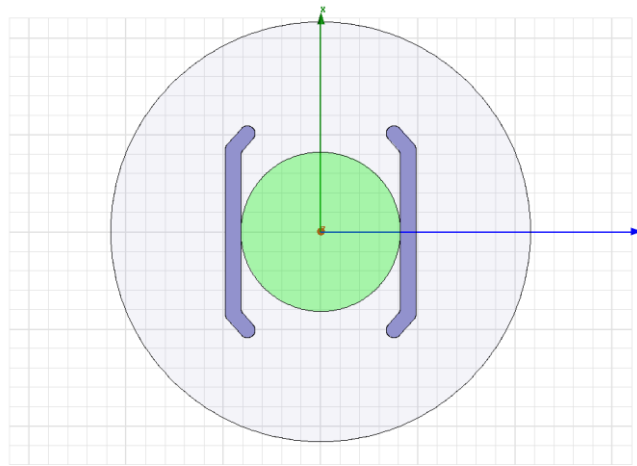


Fig. 2.3 Minimum aperture circle inside flat electrodes kicker

Keeping the aperture above a limit is more important when the kicker electrodes are curved. In that case, electrode positioning tolerances should be more restrictive because a little mistake on them implies the entire electrodes surface interfering with the stay-clear area. Nevertheless, flat electrodes as show in Fig. 2.3 would only interfere with the minimum aperture in a small zone if they were positioned closer than they should.

⁴ The beam screen is a cooled metallic liner inside the round beam pipe which reduces the heat load to the superconducting magnets refrigeration and minimises dynamic vacuum effects.

⁵ It is not necessarily a circle but also a rounded rectangle (race-track) or other configurations.

The minimum aperture is one of the parameters directly related with the uniformity (or homogeneity) of the field, as it will be presented in section 2.2.2.1. It will be shown that the good field region can be one of the most challenging specifications to fulfil in the kicker design.

2.1.3 PULSE PARAMETERS

Some indications about pulse parameters have been presented in chapter 1 (section 1.4.3), mainly regarding pulse length. Nevertheless, the necessary specifications of a kicker pulse will be indicated in this point bearing in mind that the last chapter will present the power supply configurations required to achieve these pulses.

The strip-line kicker needs a short, fast rise or decay, high voltage pulse to deflect particles as expected. The required pulse is defined by its parameters (Fig. 2.4):

- Pulse length: It is the total duration of the pulse.
- Rise time (T_r): It represents the time that the pulse takes to reach a percentage of the final amplitude, usually to go from 10 to 90% of the final pulse.
- Fall or decay time (T_d): Just contrary to the rise time.
- Flat-top time (T_f): It is the time usable for homogeneous particle deflection.
- Flat-top stability (S_f): It is the maximum variation of the pulse in the flat-top zone. It is indicated as a percentage of the total pulse amplitude and it usually represents the most challenging parameter for the pulsed power supply.

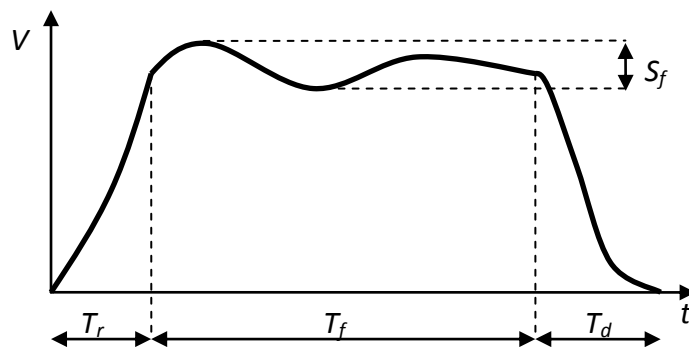


Fig. 2.4 Typical pulse parameters

The pulse parameters are based on beam characteristics and requirements. For example, short bunch-to-bunch space would require fast rise or fall time to extract bunches; high beam energy would require a higher voltage pulse; long beam (in full beam injection or extraction) would require long flat-top and also good stability.

Another important parameter of the pulse is the reproducibility. It represents the relative difference between consecutive pulses. Sometimes it is important to get a train of pulses very similar to obtain exactly the same deflection in consecutive bunches. This is not a trivial parameter as it is extremely difficult for the power supply to achieve.

The Fourier transform of the pulse returns its frequency contents, which are very useful to define the scope of the frequency domain simulations and RF parameters.

2.1.4 THE WAKEFIELDS

Although they are not usually expressed as a design specification, the wakefields are a quite important subject in strip-line kicker calculations, since they can become one of the main reasons to use strip-line kickers over other kicker technologies. The phenomenon is so complex that many books, papers and thesis describe its behaviour in all kind of accelerator structures. Therefore, this section will not provide a comprehensive analysis of wakefields but only a description and analysis of concepts related to the kicker case⁶, which will provide basic information to understand the following sections. The bibliographical references can be consulted to obtain more information; particularly [2] is a good summary with many interesting concepts.

To start the analysis, first consider the electric field \vec{E} created by a point charge q in free space, as shown in Eq. (2.5). It can be obtained solving the Maxwell's equations bearing in mind relativistic considerations.

⁶ Only wakefields for relativistic beams will be considered ($v \approx c$).

$$\vec{E} = \frac{q}{4 \pi \epsilon_0} \frac{(1 - \beta^2)}{(1 - \beta^2 \sin^2 \theta)^{3/2}} \frac{\vec{r}}{r^3} \quad (2.5)$$

In Eq. (2.5), β is the ratio between the speed of the particle and the speed of light, which will be more detailed in section 2.2.1.1. θ is the angle at which the electric field is calculated (0 degrees is collinear with the velocity of the particle). \vec{r} is the position vector of the charge.

Consider a steady charge in free space, as shown in Fig. 2.5 left⁷. The electric field that it produces is spherically symmetric as predicted by the solution of the Maxwell's equations when $\beta=0$. If the particle starts moving at high velocities (for example, a tenth of the speed of light), the electric field viewed in the laboratory frame will start to flatten in the plane perpendicular to the path (Fig. 2.5 middle). Consequently, when the particle is travelling in free space at a velocity close to the velocity of light [3], the electric field can be nearly considered lying in a plane passing through the charge and perpendicular to its trajectory (Fig. 2.5 right). This can be easily observed by calculating the limit of Eq. (2.5) when $\theta=0$ and $\theta=\pi/2$ as γ approaches infinite⁸.

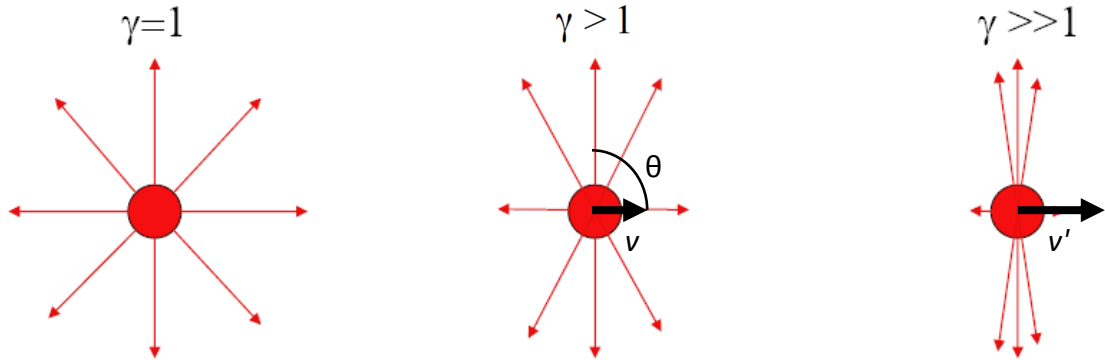


Fig. 2.5 Electric field produced by different charges. Left: steady charge, middle: travelling charge, right: charge travelling at close to the speed of light

In free space, a second charge moving behind the first one (both close to the speed of light and on the same or a parallel path) will not be subjected to any forces from the fields produced by the leading charge. Those fields are known as *direct self fields*.

⁷ Gamma is the ratio between total energy and rest energy of a particle: $\gamma = (1 - \beta^2)^{-1/2}$

⁸ Obviously γ can never be infinite as this would mean a particle travelling at the speed of light.

In contrast, when the charge travels parallel to the axis of a perfectly conducting beam pipe, it induces image charges on the surface of the wall, which travel at the same velocity as the original charge (Fig. 2.6). Those fields are known as *image self fields*. A trailing charge still will not experience the direct fields moving with the leading charge.

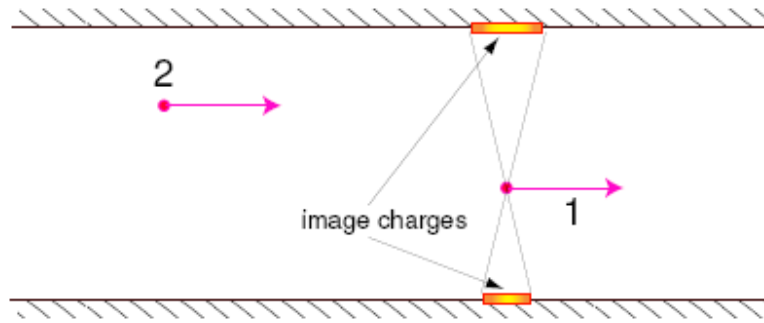


Fig. 2.6 Particles moving in a perfectly conducting pipe.

However, image self fields can scatter in metallic discontinuities and the scattered radiation can reach the trailing charge and exert forces parallel and perpendicular to its direction of motion (Fig. 2.7). The scattered fields are known as *wakefields* due to the fact that they are left mainly behind the travelling charge [2]. The integrated wakefields over a given path of the trailing charge and normalised to the own charge are the longitudinal and transverse voltages⁹ known as longitudinal and transverse wake potentials (units Volt/Coulomb).

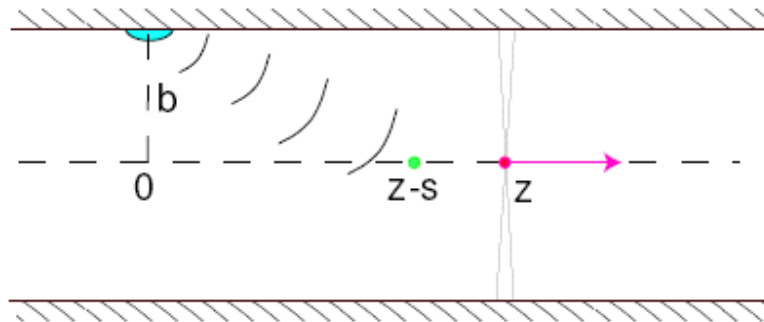


Fig. 2.7 Scattered radiation coming from a discontinuity at $z=0$ in the beam pipe. When the particle moves to location z , the scattered field arrives at point $z-s$.

⁹ Accelerating or deflecting energy given to the particle due to the fields of leading particles.

If a particle moves along a straight line very close to the speed of light, the electromagnetic field of this particle scattered off the boundary discontinuities will not overtake it and, furthermore, will not affect the charges that travel ahead of it. The field can interact only with the trailing charges in the beam that move behind it. This constitutes the principle of causality in the theory of wakefields.

It is possible to estimate the distance at which the scattered electromagnetic field produced by a leading charge affects a trailing particle travelling at a distance 's' behind it (Fig. 2.8).

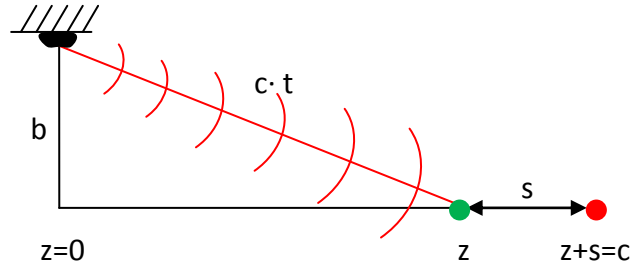


Fig. 2.8 Estimation of catch-up distance

The space that the EM wave travels from the discontinuity is equal to the space that the leading particle at the speed of light moves in a given time, as shown in Eq. (2.6).

$$(z + s)^2 = z^2 + b^2 \quad (2.6)$$

$$Z_{catch-up} = \frac{b^2 - s^2}{2s} \quad (2.7)$$

The trailing charge will not experience the scattered wakefields until it has reached a position $Z_{catch-up}$ known as the catch-up distance. Only after the leading charge has travelled $z+s$ away from the discontinuity, can a particle at a distance s behind it experience the field generated by the discontinuity. The catch-up distance is usually much larger than the distance s , and therefore it can be written as:

$$Z_{catch-up} = \frac{b^2}{2s} \quad (2.8)$$

Typically, s can be made approximately equal to the bunch length σ_z to predict the effect of the head of the bunch on the tail. Therefore, if the wake potentials are being calculated using a numerical code, the simulation length should be always greater than the catch-up distance.

The trailing charge can also experience the fields of the leading charge when the beam pipe is not perfectly conducting. In this case, there is a small Z component of the electric field behind the particle related to the dissipation in the pipe walls [3]. This perturbation is usually much less important than wakefields given by discontinuities in the beam pipe.

Let's come back to the case of a beam travelling through the axis of a circular and perfectly conducting pipe (Fig. 2.9).

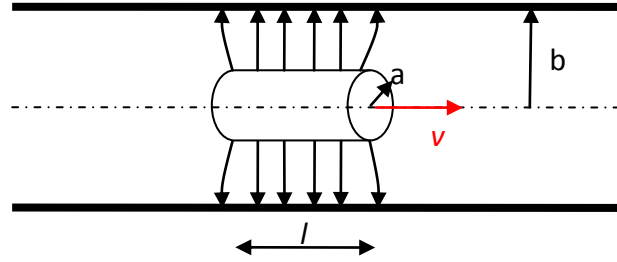


Fig. 2.9 Bunched beam at the center of the beam pipe travelling close to c

For a cylindrically bunched beam of length l , radius a , travelling at almost the speed of light $v \approx c$, the static approximation can be used [2]. The charge density ρ of this bunch (coulombs per m^3) can be expressed in terms of current I , cross section area and velocity v , as shown in Eq. (2.9).

$$\rho = \frac{I}{\pi a^2 v} \quad (2.9)$$

The electric field can be obtained by applying Gauss' law to the volume of the bunch. The integral form of Gauss' law (Eq. (2.10)) indicates that the flux of the electric field over the surface of a closed volume is equal to the volume enclosed charge over the electric permittivity.

$$\oint \vec{E} \cdot d\vec{A} = \frac{Q}{\epsilon_0} \quad (2.10)$$

There are two possible cases, for $r \leq a$ and $r > a$. Only the latter will be developed here. Applying Eq. (2.10) to the cylindrical bunch, for a point located at $r > a$:

$$E_r 2 \pi r l = \frac{I}{\pi a^2 v \epsilon_0} \pi a^2 l \quad (2.11)$$

$$E_r = \frac{I}{2\pi\epsilon_0 v} \frac{1}{r} \quad (2.12)$$

Eq. (2.12) represents the radial electric field that appears between the bunch and the beam pipe. It is possible to obtain the potential function $\varphi(r)$ by just integrating the electric field between the bunch and the beam pipe radii.

$$\varphi(r) = \int_r^b E_r(r') dr' \quad (2.13)$$

Integrating Eq. (2.12), the difference of potential between a given radius and the wall of the beam pipe is expressed in Eq. (2.14).

$$\varphi(r) = \frac{I}{2\pi\epsilon_0 v} \ln \frac{b}{r} \quad (2.14)$$

The reference potential of the beam pipe is null, $\varphi(b)=0$. The voltage drop from the beam to the beam pipe is constant along the trajectory. Therefore, there is no longitudinal or transverse electric field component which can disturb the bunch of particles when travelling by the axis of a perfectly conducting beam pipe.

However, when the same bunch passes through a changing beam pipe, the fields are different (Fig. 2.10). The field lines are redistributed to fill a larger space but the reference voltage of the beam pipe is still zero when the radius is increased.

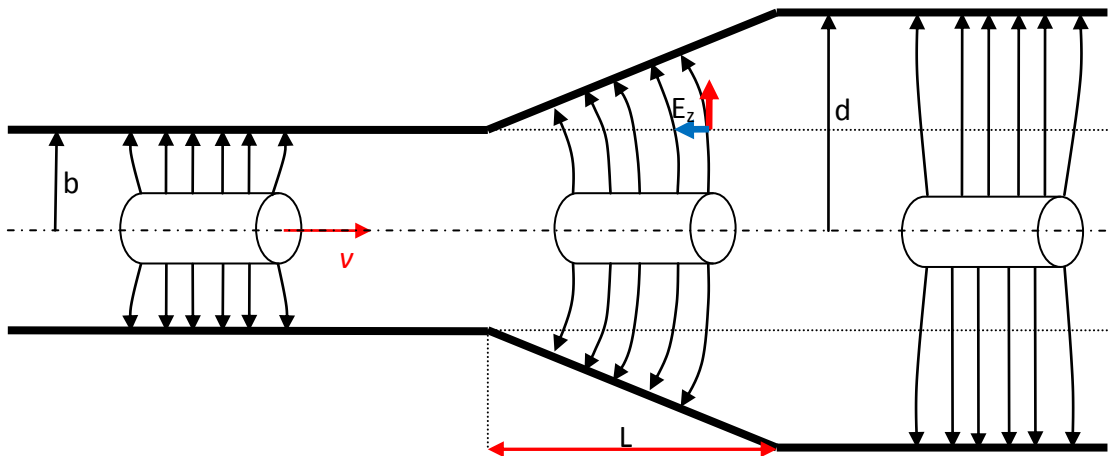


Fig. 2.10 Bunched beam passing through a pipe transition

There is a longitudinal component of the electric field $E_z(r, z)$, and a trailing charge will experience a voltage given by Eq. (2.15):

$$V = - \int_0^L E_z(r, z) dz = - (\varphi(r, L) - \varphi(r, 0)) = - \frac{I}{2 \pi \varepsilon_0 v} \ln \frac{d}{b} \quad (2.15)$$

The longitudinal voltage expressed in Eq. (2.15) is decelerating if the transition increases the diameter of the pipe ($d > b$). The power P_b lost by the beam in the transition is given by the voltage times the current and it is deposited in the energy of the fields that fills the new space available between radii b and d :

$$P_b = V I = \frac{I^2}{2 \pi \varepsilon_0 v} \ln \frac{d}{b} \quad (2.16)$$

The conical transition shown in Fig. 2.10 is very typical in strip-line kickers to reduce the energy loss and beam instabilities due to wakefields in the transition (not calculated in this ideal approximation). Eq. (2.16) gives the estimated power lost in this transition for a cylindrical bunch. In strip-line kickers, there is as well a transition to decrease the pipe diameter, which cancels the decelerating voltage of the first transition if both show exactly the same geometry. However, the losses of the metallic pipe and the reflected wakes in the transition make the process not conservative.

Going back to the wake potentials introduced before, they are defined as the change of momentum of a trailing particle caused by the wakefield generated by the leading particle at a distance z (Fig. 2.11)¹⁰.

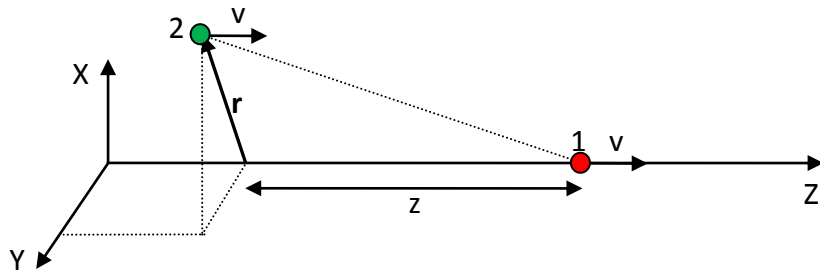


Fig. 2.11 Sketch for definition of wake potentials

They can be divided in longitudinal w_l and transverse w_t wake potentials depending on the direction of the momentum change.

¹⁰ Note here the definition for z distance, different as previously given in Fig. 2.7 and Fig. 2.8.

$$w_l(\vec{r}, z) = -\frac{c}{q} \Delta p_l \quad (2.17)$$

$$w_t(\vec{r}, z) = \frac{c}{q} \Delta p_\perp \quad (2.18)$$

The speed of light c and the charge q shown in Eqs. (2.17) and (2.18) are the normalization factors for the wake potentials.

The loss factor k can be defined from the longitudinal wake potential as the normalized energy lost by the leading charge when passing through the device. It is given by the longitudinal wake at $z=0$, except for charges travelling at the speed of light, which have a discontinuous wake potential at $z=0$. The *beam loading theorem* [4] gives the relationship between k and $w_l(z=0)$, as shown in Eq. (2.19).

$$k = \frac{w_l(z \rightarrow 0)}{2} \quad (2.19)$$

Causality requires that the longitudinal wake potential of a charge travelling at the velocity of light is discontinuous at the origin (Fig. 2.12).

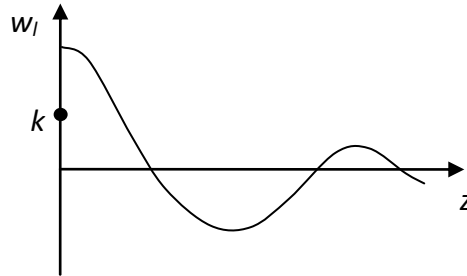


Fig. 2.12 Longitudinal wake for a charge travelling at the speed of light

However, the longitudinal wake and the transverse wake are not independent of each other. Panofsky-Wenzel theorem relates the transverse and longitudinal wake potentials as shown in Eq. (2.20).

$$\frac{\partial w_t}{\partial z} = \nabla_r w_l \quad (2.20)$$

where ∇_r is the two dimensional gradient with respect to coordinates x and y . The knowledge of the longitudinal wake function w_l allows one to find the transverse wake w_t by means of a simple integration.

The wake potentials are given as a function of the distance to the leading charge. For example, a trailing charge located at a given z distance from the leading charge (Fig. 2.11) will experience the integrated longitudinal electric field (voltage) given by the plot of Fig. 2.12 at same z coordinate.

The analysis for wake potentials has been presented for a single leading charge. The wake obtained for a single charge is a Green function¹¹ which allows obtaining the wake produced by any association of charges (bunch distribution). The wake produced by a bunch distribution is simply given by the convolution of the wake potential for a single charge over the bunch charge distribution (usually Gaussian).

The integrated voltage of the wakefields will exert a force over the trailing charges according to the Lorentz's law, which can be longitudinal, transverse or both. The longitudinal force will change the energy of the particles and it can be accelerating or decelerating. The transverse force can deflect the trajectory of the particles in both directions. Note here the similitude between the transverse wake potentials and the kicker transverse voltage shown in section 2.1.1. The energy gain (longitudinally) or the transverse kick (perpendicularly) are the integration of the longitudinal or transverse Lorentz's forces over the trajectory through the device length. This integration is performed over a given path of the trajectory. The transverse wake potential in a stripline kicker will show the "kick effect" of the device when the excitation is not external but given by the beam itself, as it will be shown in Chapter 4.

All the above definitions of wake potentials are sometimes not easy to apply in order to get the magnitude of the perturbation that a given device produces in the beam due to wakefields. Moreover, they are only useful when dealing with time domain problems as for linear accelerators or processes that do not reach the steady state (a few turns in a ring). A new magnitude is defined for periodic circular accelerators and steady state devices in frequency domain. It is known as the *coupling impedance*. The longitudinal Z_l and transverse Z_t coupling impedances are defined as the Fourier transforms of the wake potentials, as shown in Eqs. (2.21) and (2.22).

¹¹ In chapter 1, a solution for the kicker flat-top pulse response was presented by convoluting the response to a Dirac delta over the real flat-top pulse. A single charge acts as a Dirac delta excitation for the wake potentials.

$$Z_l = \frac{1}{c} \int_0^\infty w_l(z) e^{i \omega z/c} dz \quad (2.21)$$

$$Z_t = -\frac{i}{c} \int_0^\infty w_t(z) e^{i \omega z/c} dz \quad (2.22)$$

All the devices in series with the beam contribute to the global coupling impedance of the accelerator. The strip-line kickers are devices included in that case. The beam dynamics designer will provide the limits for the maximum energy loss ($\Delta E/E$) and impedance allowable for each device to be installed in series with the beam, as lower coupling impedance in a device represents a lower risk of beam instabilities.

To summarize, the beam travelling inside a changing vacuum chamber induces electromagnetic fields which may affect the dynamics of the beam itself. An accelerator can be seen therefore as a feedback device, where any longitudinal or transverse perturbation appearing in the beam distribution may be amplified (or damped) by the EM forces generated by the perturbation itself.

2.2 2D CALCULATIONS

2.2.1 ANALYTICAL METHODS COMPUTATIONS

The full design of a strip-line kicker is difficult to develop using analytical equations because there is no way to obtain analytical representation of fields inside an arbitrary geometry. However, some analytical calculations are useful to obtain rough values of the main constructive parameters, which can only be developed in 2D. Anyway, numerical calculations are finally required to fine tune the design.

2.2.1.1 Energy and momentum

Kicker analytical formulae [5] require obtaining the speed and transverse momentum of the particles. Even when these magnitudes can be simplified for our assumptions¹², the full relativistic calculation is still quite interesting to present.

The starting parameter is the beam energy specification; let's say E_b (eV). As it has already been mentioned in previous sections, this value corresponds to the kinetic energy of the particles E_k , that can also be expressed in IS of units as shown in Eq. (2.23), where q_e is the electron charge.

$$E_k = E_b q_e \quad (2.23)$$

The rest energy of the particle E_0 can be calculated as shown in Eq. (2.24). For small particles like electrons, this energy is usually negligible compared to the kinetic energy.

$$E_0 = m_0 c^2 \quad (2.24)$$

And the total energy is the sum of Eqs. (2.23) and (2.24).

$$E_T = E_0 + E_k \quad (2.25)$$

The relation between the total energy, rest energy and linear momentum can be written as:

$$E_T^2 = E_0^2 + p^2 c^2 \quad (2.26)$$

The linear momentum of the particle can be obtained from relation (2.26). The relativistic gamma γ is defined as the ratio between total energy and rest energy of a particle, as shown in Eq. (2.27).

$$\gamma = \frac{E_T}{E_0} \quad (2.27)$$

And therefore, the speed of the particle can be calculated using the relativistic linear momentum (Eq. (2.28)).

¹² The kickers analysed in this document will deflect electrons or positrons travelling close to the speed of light as shown in chapter 1. Strip-line kickers are not usually applied for slow travelling particle deflection.

$$p = \gamma m_0 v \quad (2.28)$$

The relativistic beta β is defined as the ratio between the speed of the particle v and the speed of light c . For our assumption, β can be approximated to 1 as $v \approx c$.

$$\beta = \frac{v}{c} \quad (2.29)$$

If the particles arrive at the kicker only with longitudinal speed (Fig. 2.2), the increment of speed and momentum needed to deflect the particles¹³ can be expressed as shown in Eqs. (2.30) and (2.31), using the deflection angle calculated in Eq. (2.4).

$$\Delta v_{\perp} = v \tan \alpha \quad (2.30)$$

$$\Delta p_{\perp} = (m_k + m_0) \Delta v_{\perp} \quad (2.31)$$

where m_k and m_0 are the kinetic mass and rest mass respectively.

2.2.1.2 The transverse voltage and shunt impedance

Relation (2.3) requires the existence of a full field solution inside the kicker to calculate the transverse voltage, which means that finite element software is needed when the geometry is not analytically resolvable. However, the transverse voltage is also defined in [5], so it is possible to calculate it using the results of the section 2.2.1.1.

$$V_{\perp} = \frac{\beta c \Delta p_{\perp}}{q_e} \quad (2.32)$$

It is straightforward to obtain a relation to directly calculate the transverse voltage using previous relativistic relations:

$$V_{\perp} = \frac{\beta^2 c^2 (m_k + m_0) \tan \alpha}{q_e} \quad (2.33)$$

Assuming $v \approx c$ and a negligible rest mass¹⁴, Eq. (2.33) can be written as:

¹³ Supposing a constant force along the kicker, which is true for particles deflected in the pulse flat top.

¹⁴ This is only valid for particles travelling at energies much higher than their rest energy. Rest energy of proton: 938 MeV; rest energy of electron: 0.51 MeV. Note the relation $m_k = E_k/c^2$.

$$V_{\perp} = \frac{E_k \tan \alpha}{q_e} \quad (2.34)$$

Relation (2.34) is similar to Eq. (2.4), just changing the energy units from IS to electron-volts. This development has demonstrated the scope of Eq. (2.32) defined in [5] and validates the relation shown in Fig. 2.2.

The efficiency of the kicker can be measured by the transverse shunt impedance (R'_s), which relates the transverse voltage (strength) with the power inserted into the kicker (P). The equation that gives the relationship for sinusoidal excitation comes from the practice used for RF cavities¹⁵, and it is given by:

$$R'_s = \frac{V_{\perp}^2}{2 P} \quad (2.35)$$

where P is the time-averaged power travelling by both strip-lines. The transverse shunt impedance (measured in Ohms) increases with the efficiency of the kicker. Introducing fixed power in Eq. (2.35), the greater the transverse shunt impedance, the higher the transverse voltage over the particles, so it is important to obtain R'_s as big as possible.

It is possible to find in [5] a way to obtain the transverse shunt impedance for sinusoidal excitation (Eq. (2.36)), depending only on frequency and geometrical parameters of strip-line kickers:

$$R'_s = 2 Z_0 \left(\frac{\tanh\left(\frac{\pi \omega}{2 h}\right)}{k h} \right)^2 \sin^2(k l) \quad (2.36)$$

where $k = \omega/c$ (the wave number), h is half the minimum aperture, l is the electrode length and Z_0 is the characteristic impedance¹⁶. The transverse shunt impedance can be expressed as shown in Eq. (2.37) when the frequency approaches to zero.

$$R'_{s DC} = \lim_{\omega \rightarrow 0} R'_s = 2 Z_0 \left(\frac{l}{h} \right)^2 \quad (2.37)$$

¹⁵ Cavity peak voltage is related with the averaged power by the shunt impedance (longitudinal).

¹⁶ Before calculating R'_s one must design the cross section of the strip-line kicker as it is shown in section 2.2.2.1 in order to obtain h and Z_0 .

It is possible to obtain the electrode length as shown in section 1.4.3 (for precise injection/extraction). In other cases, a good approximation can also be obtained bearing in mind the maximum allowable voltage for the pulse according to power supply or dielectric rigidity specifications. The peak voltage of the flat-top pulse is related with integrated electric field, deflection strength and electrode length. The electric field between the strip-lines is easily estimated by twice the maximum electrode voltage to ground V_k over the electrode separation (Eq. (2.38)).

$$E = \frac{V_k}{h} \quad (2.38)$$

Supposing a constant electric field along the strip-lines, the length can be calculated using the transverse voltage as shown in Eq. (2.39). This relation comes from the affirmation expressed in the paragraph below Eq. (2.2).

$$l = \frac{V_{\perp}}{2 E} \quad (2.39)$$

Fig. 2.13 shows a typical plot of the transverse shunt impedance versus frequency (Eq. (2.36)) for a kicker driven in RF. It takes into account the transit time factor for the transverse voltage which most influences the deflection efficiency at higher frequencies¹⁷. That is the reason why R'_s is almost constant at DC and low frequencies, and starts to decrease (the efficiency decreases) when the particles are more influenced by the transit time factor at higher frequencies. There is a first point where R'_s becomes null, which implies no deflection for that frequency as the transit time factor is also zero. Then the transit time factor increases again. At zero crossing points, which depend on strip-line length, the RF peaks and valleys cancel when integrating fields along the strip-lines and no net deflecting force is achieved.

¹⁷ The wavelength is small compared to the length of the device and the particles experience different phase of TEM wave depending of their input position.

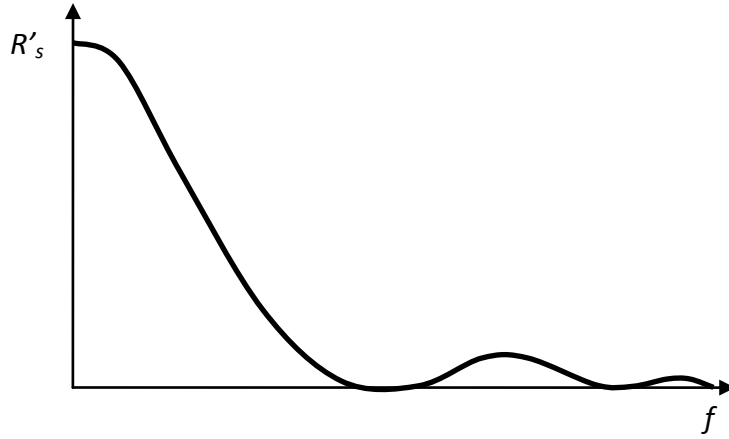


Fig. 2.13 Typical transverse shunt impedance variation with frequency

All the relations coming from [5] are specified for RF sinusoidal excitation. However, the author has extended their use to a pulsed kicker to calculate voltage, current and power in the next paragraph. Therefore, a kicker driven by a pulse with flat-top zone can be estimated using the DC evaluation of the transverse shunt impedance (Eq. (2.37)) in order to analytically calculate electrical magnitudes. The Eq. (2.35) should be therefore modified for DC power, where P_{DC} represents the combined power of both strip-lines for a DC excitation:

$$P_{DC} = \frac{V_{\perp}^2}{R_{sDC}} \quad (2.40)$$

2.2.1.3 Voltage, current and power. Pulser requirements estimation

Relations (2.37) together with (2.40) are useful to obtain the voltage, current and power of a kicker driven by a pulse.

The combined power of both strip-lines (P_{DC}) can be calculated by means of Eq. (2.40). The obtained power is twice the power input in one kicker coaxial port when excitation is DC (infinite flat-top pulse). Obviously this power is not the real power of the pulse, only its peak maximum power. It should be averaged by the duty cycle of the pulse to obtain the approximate requirements of the pulsed power supply in both mirror pulses.

$$P_{avg} = Duty \cdot P_{DC} \quad (2.41)$$

The duty cycle of the pulse can be approximated by the pulse duration times the repetition rate. For example, if a 200 ns pulse has a repetition rate of 50 Hz, the duty cycle would be $200 \times 10^{-9} \times 50 = 1 \times 10^{-5}$.

The peak voltage to ground that appears in the electrodes and coaxial cables (V_k) should be calculated by using the power in one of the electrodes, that is $P_{1DC} = P_{DC} / 2$. Relation (2.42) shows the required formula. The voltage is opposite in one electrode respect to the other.

$$V_k = \sqrt{P_{1DC} Z_0} \quad (2.42)$$

The peak current on one electrode is direct straightforward to calculate:

$$I_k = \frac{V_k}{Z_0} \quad (2.43)$$

V_k and I_k represent the voltage and current that would appear in DC mode. The values are identical to the peak voltage and current which would appear in the strip-lines when a flat-top pulse is applied. Eqs. (2.42) and (2.43) make use of the well known Ohm's law to calculate the voltage and current in a resistive circuit of impedance Z_0 . As it was presented in chapter 1, a well matched high frequency circuit is presented to the power supply as a Z_0 ohms resistance. The kicker is acting only as an ideal transmission line. The power supply estimated requirements are summarized in Tab. 2.1.

Tab. 2.1 Basic kicker power supply requirements

Magnitude	Value	Units
Pulse maximum instantaneous power	$P_{DC} = \frac{V_{\perp}^2}{R_{sDC}}$	W
Pulse maximum instantaneous power per electrode	$P_{1DC} = \frac{P_{DC}}{2}$	W
Averaged power per electrode	$P_{1avg} = Duty \cdot P_{1DC}$	W
Flat-top pulse voltage (electrode to ground)	$V_k = \sqrt{P_{1DC} Z_0}$	V
Flat-top pulse current per electrode	$I_k = \frac{V_k}{Z_0}$	A

2.2.2 NUMERICAL METHODS

2D finite element software is required to numerically calculate important kicker parameters such as characteristic impedance and field homogeneity and to obtain a rough approximation of the wakefield behaviour.

2.2.2.1 Strip-line impedance and cross section design: homogeneity

A strip-line kicker is usually a long device with constant cross section¹⁸. Most important kicker dimensions are related with the 2D straight cut of the structure, which indicates the great importance that the cross section has over the whole design. It defines the characteristic impedance of the strip-lines and the homogeneity of the field inside the aperture.

The cross section definition is one of the first stages in the design of a strip-line kicker. Whatever the cross section outline, the characteristic impedance must be determined and matched before other considerations. It was presented in chapter 1 that the optimal and most extended impedance for high frequency power transmission is 50 Ω . It is important to opt for commercial extended impedance because cables, connectors, feedthroughs, etc. are difficult to manufacture and cheaper if commercially obtained. Therefore, once decided this figure, it is possible to continue the choice of the cross section shape.

There are several issues to bear in mind when designing the shape of the cross section:

- Electrodes: The electrodes cross-section of a strip-line kicker can be shaped in multiple forms. All of them can be suitable for a determined design bearing in mind following considerations.

¹⁸ The cross section can also present small variations along the kicker length to improve impedance matching, as it will be shown in following sections.

Curved electrodes (Fig. 2.14) are good for getting higher fields in the aperture axis¹⁹ and therefore smaller external tube for same deflection strength. However, they feature bad uniformity of the dipolar field in the aperture, which can make them unusable when uniformity specifications are tight.

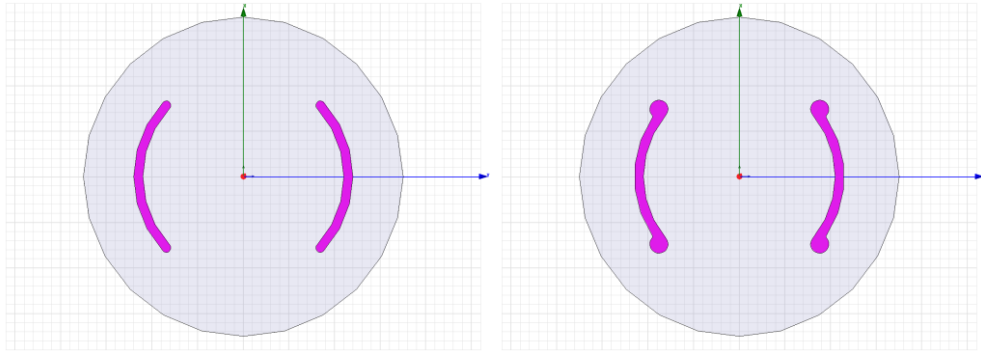


Fig. 2.14 Curved electrodes cross sections

They can be simple circular electrodes (Fig. 2.14 left) or with thick ends (Fig. 2.14 right). The latter can be useful to provide mechanical stiffness with the aim of avoiding electrode bending if long electrodes are required. It can also help reducing the electric field concentration in the ends to decrease the risk of electrical discharge in very high voltage applications.

Flat electrodes (Fig. 2.15) provide better homogeneity in the aperture but they have less field strength in the axis for the same aperture and voltage. They require a larger diameter external tube to maintain the characteristic impedance, which deteriorates the beam coupling impedance.

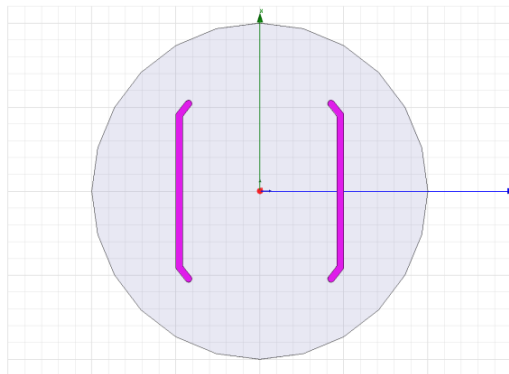


Fig. 2.15 Flat electrodes cross section

¹⁹ It is easy to see in the electrostatic case that the contribution to the field in the axis is higher as more metal at a given potential is located closer to the axis.

The flat electrodes are usually designed with bent ends to improve mechanical stiffness and diminish the end effects in the uniformity of the field.

There are other possible cross sections with characteristics between circular and planar shapes, as the elliptical electrodes. They feature intermediate field strength and uniformity, but can be very useful for some shapes of external tube.

- Vacuum chamber: The external tube that encloses the electrodes can also be shaped in multiple forms (Fig. 2.16). It can be circular, elliptical, race track, or combinations of these. Circular shape is the easiest to manufacture from commercial tubes, but typically needs to be larger to maintain characteristic impedance for a given electrode dimension. Elliptical or race track cross sections can fit easier the electrodes but are much more complex to manufacture, as usually require CNC machining in two halves and then welding.



Fig. 2.16 Racetrack and elliptical cross sections

Once the straight section shape is selected, it is time to decide its initial dimensions. The starting parameter is always the minimum aperture inside the electrodes. No part of the electrode can interfere with the minimum aperture zone (Fig. 2.3). However, the electrodes should be located as close as possible to it in order to increase the efficiency of the kicker²⁰.

After that, the thickness of the electrodes can be estimated. They should be thick enough to avoid deformation due to their own weight (case of long electrodes). If the material²¹ is hard enough, like stainless steel, electrodes can be thinner, but typically a thickness of two to five millimetres is enough for any metal at usual lengths.

²⁰ The transverse shunt impedance is higher which involves a higher transverse voltage for a given pulse voltage.

²¹ Material selection is not important at this moment because characteristic impedance is a geometrical parameter. The materials of all the components will be detailed in following chapter.

Then, the dimensions of the external main tube can be initially estimated. If the tube is circular, the best practice is to choose a commercially available inner dimension where the electrodes fit loosely. If the shape is different, the initial estimation depends on the designer experience. It is important to propose the minimum possible inner diameter for the external tube, because the wakefield loss factor depends on the ratio between this diameter and the aperture, as shown in Eq. (2.16).

At this moment it is time to start the optimization of the first estimated cross section. The parameters that will define the quality of the cross section are the characteristic impedance and the homogeneity of the field. Both can be calculated by using the FEM²² in the 2D electrostatic case of an electrode at an arbitrary potential inside a half tube.

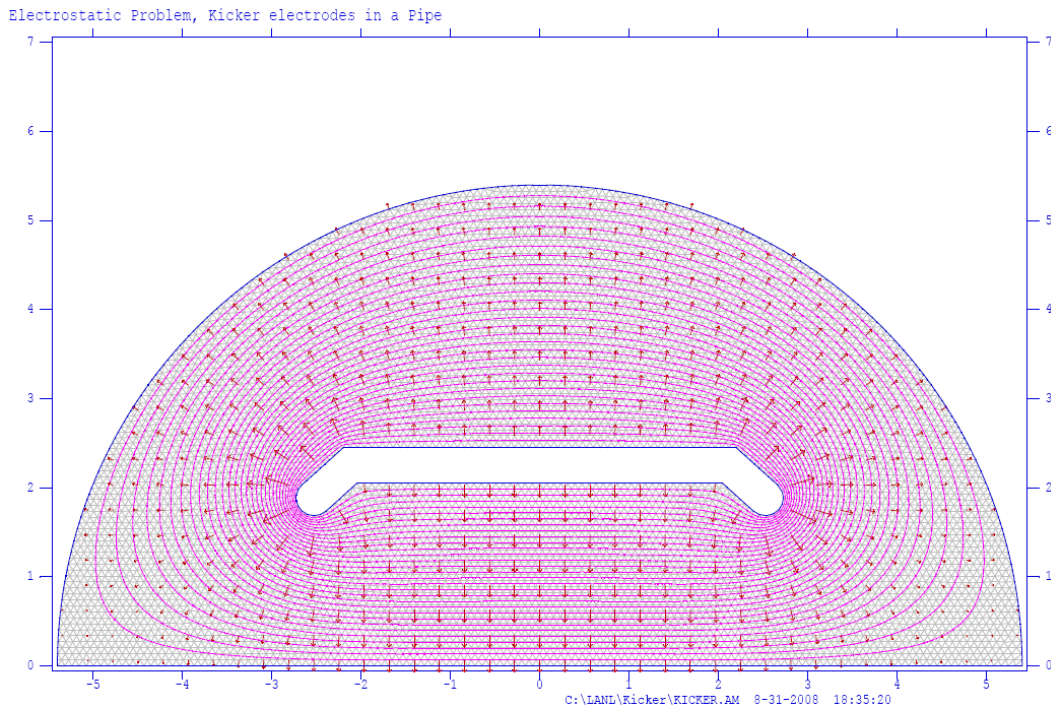


Fig. 2.17 2D FEM code solution for a kicker

The characteristic impedance in a lossless TEM mode can be calculated as explained in chapter 1:

$$Z_0 = \sqrt{\frac{L}{C}} \quad (2.44)$$

²² FEM stands for Finite Element Method

In a lossless transmission line, the velocity of propagation is the speed of light c , and it is related [6] with the line parameters as shown in Eq. (2.45).

$$c = \frac{1}{\sqrt{L C}} \quad (2.45)$$

Therefore, only the capacitance per unit length C is required to calculate the characteristic impedance of a cross-section, as presented in relation (2.46).

$$Z_0 = \frac{1}{c C} \quad (2.46)$$

The capacitance per unit length is easy to find by calculating the stored electric energy of the cross section in FEM code, as shown in chapter 1. Then the characteristic impedance can be obtained using Eq. (2.46).

Regarding the homogeneity, it corresponds to the uniformity of the dipolar fields in the kicker aperture. It mainly depends on the geometry of the electrodes. For example, two parallel plates of a capacitor generate a perfect unidirectional E field between them except from the end effects (Fig. 2.18). Those end effects distort the pure unidirectional field in the space between the plates, and obviously this is more noticeable close to the ends. The same happens for the magnetic field in TEM propagation mode. The homogeneity is measured as a variation percentage of the unidirectional field component in an area. It is typically specified in a circle of radius equal two thirds of the minimum aperture, but this specification mainly depends on beam optics requirements.

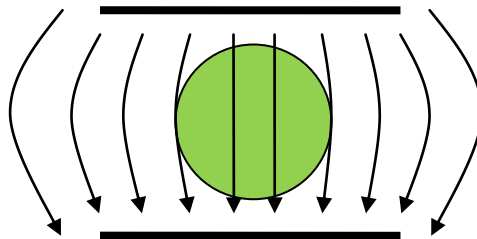


Fig. 2.18 Electric field in parallel plates capacitor with end effects (not at scale).

There are multiple ways to calculate the homogeneity of the kicker dipolar field:

- One alternative is to use the same algorithm used for measuring magnetic field quality in accelerator magnets [7]. The magnetic field magnitude is calculated at the circumference of homogeneity (reference radius) and the series of values are processed by the Fourier transform to obtain the harmonic content of the field sinusoidal variation. For a symmetric dipolar field, the harmonics that appear in such distribution are the main dipole harmonic and the undesired harmonics numbers 3, 5, 7... This algorithm is well known and provides excellent results for detecting even the smallest anomalies in the homogeneity. However, the homogeneity required in a strip-line kicker is several orders of magnitude worse than for dipole magnets. Therefore, this algorithm is oversized and not the most appropriate for strip-line kickers. Moreover, it is not suitable when the area of homogeneity is not circular.
- It is also possible to measure the homogeneity by finding the maximum and minimum values of the deflecting field component in the area of homogeneity. This is easy to do by most FEM codes once they have the full field solution inside the area. The variation percentage between maximum and minimum values over the field in the centre is the homogeneity (usually given in $\pm \%$).
- If FEM code cannot automatically calculate the extreme values of the deflecting field component in an area, it is still possible to calculate the homogeneity by observing the variation of the main field component in several cross section lines (Fig. 2.19).

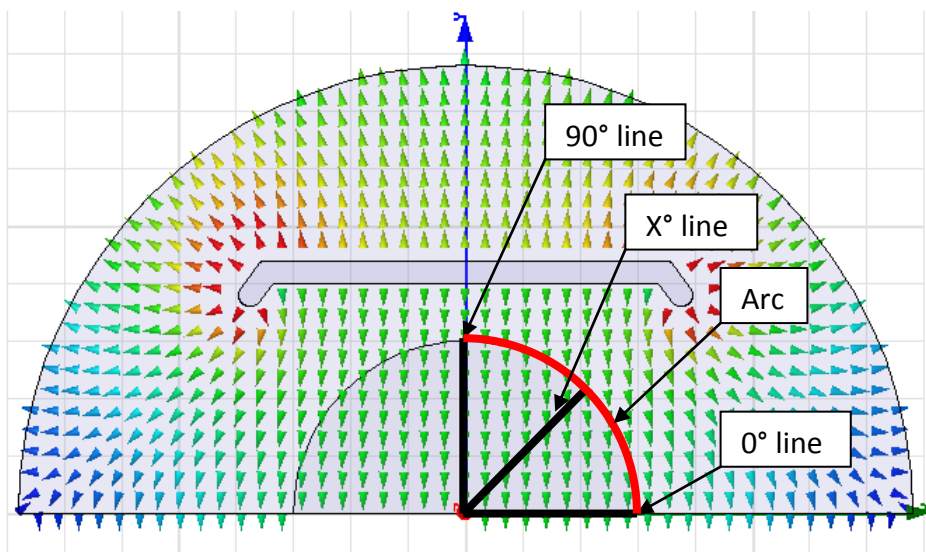


Fig. 2.19 Homogeneity calculation lines in strip-line kicker

For example, in Fig. 2.19, the maximum Y field value along the arc would represent the point of the whole area with maximum field. The minimum field can then be found by representing the Y field values along the three lines, and then the homogeneity can be calculated as before using maximum and minimum values.

All the optimization process can be carried out manually or by an automatic optimization in FEM code. The variables of the optimization process are the geometric dimensions of the cross section (diameter of the main tube, electrode parameters as radius, width, thickness, ends length, coverage angle²³, etc.). The objective function can be constituted only by the characteristic impedance or even include the uniformity, depending on the FEM code capabilities. A matching precision of ± 1 ohm is enough for characteristic impedance in most devices, although it is better to be below ± 0.5 ohm in calculations as margin of safety.

3D FEM software can also be utilized to optimize the 2D cross section. This process is sometimes even more successful than using 2D codes because 3D codes are typically more powerful and easier to pre and post process. The optimizations can be frequently done automatically by the 3D code. The cross section must be modelled as a thin slice of the strip-line kicker cross section (Fig. 2.20) and powered by RF or electrostatic voltage with adequate boundary conditions. The number of volume FEM elements is therefore reduced and the calculation time is typically very short. Nevertheless, an actual 2D calculation is always faster.

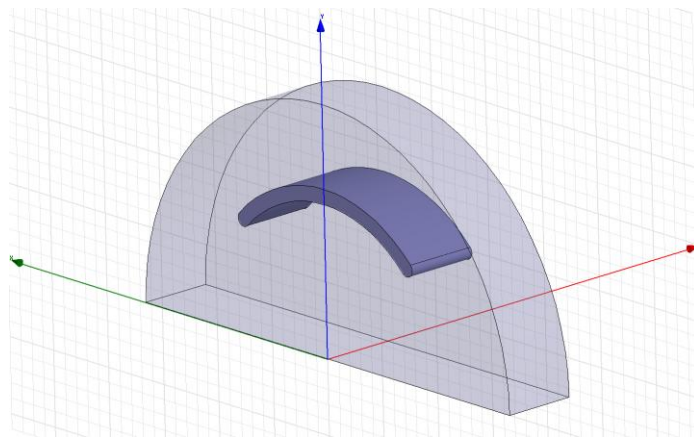


Fig. 2.20 Example of a cross section design in 3D code

²³ The coverage angle is mainly defined for circular and elliptical electrodes. It is the angle formed by the two lines which connect the ends of the electrode with the centre of the cross section.

The optimization process usually obtains several possible cross section designs that match the required characteristic impedance and homogeneity. However, only one of them presents the smaller internal dimension of the main tube which optimizes the beam coupling impedance of the device. Obviously, the overall dimensions should not be too small as this would make manufacturing much harder. Moreover, a very small cross section is not valid for high voltage pulses as an electric breakdown could occur between the electrodes and the main tube.

2.2.2.2 Wakefields axi-symmetrical calculations

The study of the wakefields requires solving the Maxwell equations in a given structure taking the beam current as source of fields. This is a quite complicated task for which it has been necessary to develop dedicated computer codes, which solve the EM problem in the time domain [8; 9]. They make use of the Finite Difference Method [10] to solve the differential form of the Maxwell's equations in time domain.

2D wakefield calculations represent the device as an axi-symmetric structure along its length. Therefore, it is not possible to exactly model devices with no symmetry around the longitudinal axis, as strip-line kickers. However, it is very useful to obtain a first approximation of wake potentials, loss factors and coupling impedances from the 2D simulation because the CPU requirements are small and the device is easy modelled. For example, a typical strip-line kicker with circular electrodes can be simulated in 2D axi-symmetric code (Fig. 2.21) as it would have a complete cylindrical electrode (Fig. 2.22). The revolution of the geometry shown in Fig. 2.21 around the axis would result in a 3D model as shown in Fig. 2.22. The simulation of the axi-symmetric structure is on the safe side because the energy lost by the beam when passing through the real structure is expected to be a bit lower. This is due to the sharp transition that the beam passes between the vacuum chamber and the electrodes, which is larger in the axi-symmetric structure.

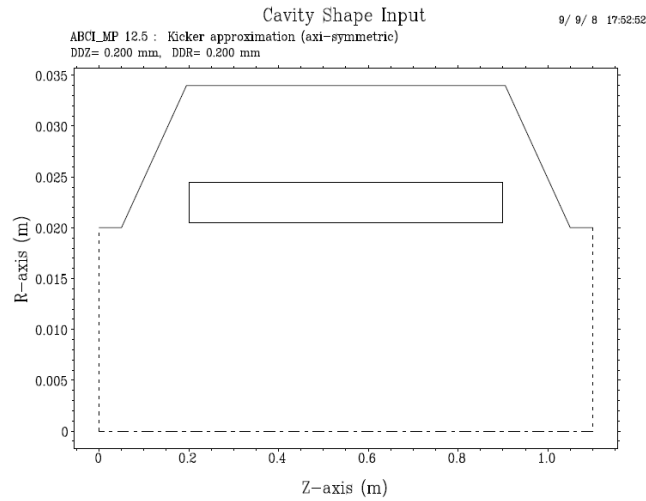


Fig. 2.21 2D axis-symmetric geometry for a strip-line kicker in ABCI [11]

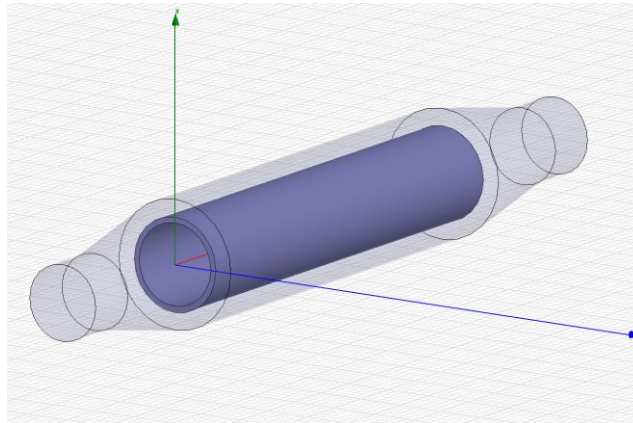


Fig. 2.22 Equivalent 3D geometry for 2D axis-symmetric simulation of a strip-line kicker

To estimate the longitudinal bunch energy loss and the energy spread in the passage through the device, the longitudinal loss factor (k_l) and the minimum and maximum longitudinal wake potentials (W) should be calculated. The 2D axis-symmetric code needs the geometry input of the device (Fig. 2.21), the size of the bunch in millimetres²⁴ and the length of the simulation in metres²⁵. Other data as mesh refinement factors, time steps, etc. are specific to each code and should be carefully selected for good precision to computing speed ratio.

²⁴ The charge distribution of the bunch is also required. In most codes, it is a Gaussian distribution by default.

²⁵ The simulation length represents the maximum distance from the leading charge at which the wakefields are calculated. Wakes peak close to the leading charge, and therefore the simulation distance should be more than ten times the bunch length for a good result. Distance between bunches can also be taken into account.

Then the calculations are simple. The longitudinal wake loss factor will give the average energy lost per particle in one passage through the device, as shown in Eq. (2.47).

$$\Delta E = -k_l Q \quad (2.47)$$

Q stands for the charge of the bunch in pico coulombs.

The maximum longitudinal energy spread that particles in a bunch can experience in one passage through the device is given by the difference between maximum and minimum peaks of longitudinal wake potentials around the bunch charge distribution, as shown in Eq. (2.48).

$$E_s = |W_{max} - W_{min}| Q \quad (2.48)$$

The previous paragraphs are best suited for a kicker running far from the steady state from the point of view of the beam, as it happens in linear accelerators or rings with reduced number of turns. However, if the kicker is working in storage rings or other synchrotrons where the number of beam passages through the device is very large, the fields reach the steady state and the power dissipated by the beam is then given in terms of the beam coupling impedances and the beam transfer impedance²⁶. The required simulation is not a time domain simulation but a frequency domain simulation and the coaxial wire method [12] should be applied for the calculation, as it will be shown in following sections.

²⁶ The beam transfer impedance is defined as the ratio of the voltage at the coaxial output ports to the beam current.

2.3 3D CALCULATIONS

2.3.1 FREQUENCY-DOMAIN SIMULATIONS

2.3.1.1 The scope of frequency-domain simulation

Once the 2D cross section is perfectly defined, a 3D code in the frequency domain is required to calculate and optimize the kicker, even if the kicker is not actually fed by an RF wave. The 3D code has several objectives:

- Optimize the transition between the coaxial feedthroughs and the strip-lines to avoid power reflection.
- Check the good transmission of the power through the structure (scattering parameters, stand-off effects, etc.).
- Estimate the power losses in the structure due to the travelling RF wave.
- Cross check the analytical calculated values for voltages, currents and power.
- Calculate the integrated 3D homogeneity of the deflecting field.
- The beam coupling and transfer impedances can also be calculated to obtain the loss factor and power released by the beam to the structure for steady state beams (best suited for synchrotrons and storage rings).

The frequency domain code calculates the steady state fields in the structure with input and output ports for a given frequency or for a frequency range. It is possible to obtain all the voltages and currents given by an RF excitation and convert them to equivalent pulse magnitudes. It is also possible to calculate the reflected and transmitted power at every simulated frequency.

2.3.1.2 Numerical model set up

2.3.1.2.1 Model considerations

Regardless of the 3D code used, the kicker has to be modelled according to some general considerations valid for every frequency domain FEM code.

- Symmetries: A 3D model needs usually large amounts of memory and processing capabilities to be simulated. Symmetries can effectively diminish the size of the problem, reducing the memory requirements to $\frac{1}{4}$ for every half symmetry. The kicker can be simulated by using up to two symmetries on its length (Fig. 2.23) and one more by cutting it in a straight section (Fig. 2.24).

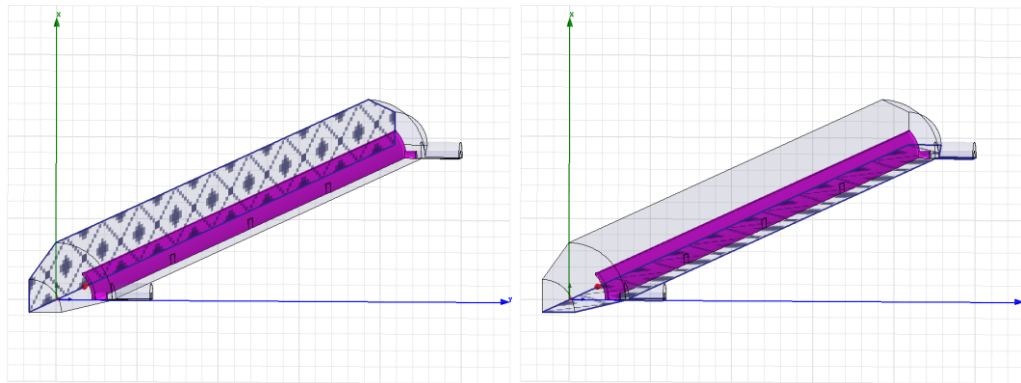


Fig. 2.23 Longitudinal symmetries for a kicker $E_t=0$ (left) and $H_t=0$ (right).

Symmetries must be well conditioned by assigning an adequate boundary condition on them. For a strip-line kicker which deflects particles in the horizontal plane (Fig. 2.23), the electric field is perpendicular to the mid vertical plane ($E_t = 0$) and the magnetic field is perpendicular to the mid horizontal plane ($H_t = 0$). Therefore, if the model is cut by those planes, the surface fields must be defined as indicated.

It is also possible to cut the kicker anywhere along its length (Fig. 2.24). This is not exactly a symmetry because it makes the kicker to appear as an infinitely long transmission line. The cross section cut has to be defined using a wave port, which will absorb all the waves in the selected transmission modes.

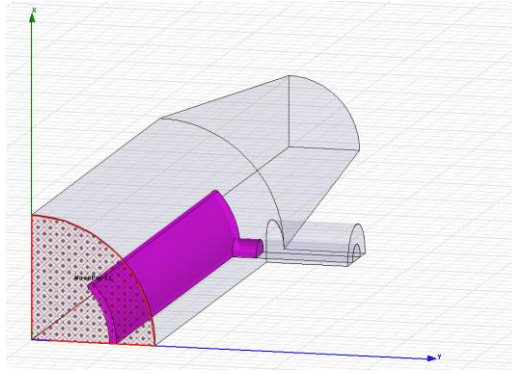


Fig. 2.24 Wave port in a kicker cut along its length

The wave port removes the reflections of the waves and therefore the simulation is not exactly the same as for the full length structure. However it is useful for optimizing the transition between the coaxial and the strip-lines.

Symmetries have to be taken into account when entering power into the structure and calculating characteristic impedances. Indeed, the power input in a kicker with horizontal symmetry (Fig. 2.23) should be half the power needed when no horizontal symmetry is used. This adjustment of power is recommendable to obtain the same fields (voltages and currents) as with no symmetry. Vertical symmetry of Fig. 2.23 would not need any power consideration in the coaxial input as it does not change the current of one strip-line in the model.

- **Stand-offs:** Ceramic stand-off insulators are needed to maintain the mechanical stiffness of the electrodes along their length. Each electrode is maintained straight by several supports (ceramic stand-offs) which electrically insulate the electrode from the tube. The electromagnetic influence of the stand-offs on the model solution has to be considered by simulating the transmission and reflection coefficients over the full structure. The stand-offs are usually made of *steatite*, a ceramic material which features good high frequency dielectric and mechanical properties while keeping high vacuum compatibility.
- **Parameterization:** It is very important to develop a parameterized model in the initial steps of the design. This allows changing and optimizing different parameters without remodelling the entire 3D structure. 3D codes usually have

the possibility to put variables for every geometric dimension. It is useful to employ variables to define the length of the electrodes, the position of the feedthroughs, the taper length, etc.

- Mesh refinement: The field values obtained in 3D simulations are very affected by the quality of the mesh. This is particularly important when post-processing absolute field values, as for 3D homogeneity calculations. Therefore it is recommended to define small regions along the aperture of the device where the mesh is more refined (Fig. 2.25) to allow a better precision without increasing the number of elements too much.

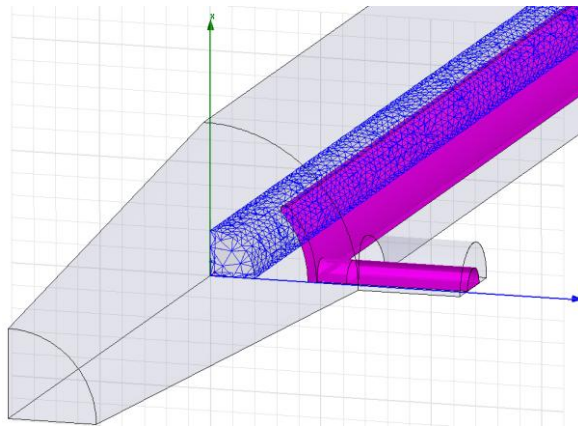


Fig. 2.25 Special mesh refinement in the aperture of a kicker.

- Excitations: The excitations in frequency domain codes are sinusoidal permanent waves. However, in the actual kicker things are a bit different because the excitation is a flat top pulse. For most deflection methods, the particles pass through the kicker when the pulse is in the plateau and therefore they experience the fields nearly constant along the path. However, in frequency domain codes at a given simulation frequency, the absolute field values along the structure change depending on the simulated frequency, the length of the device and the phase of the wave. If the wavelength at a given frequency is much larger than the structure, a wave that peaks at the input port (phase = 0 degrees) has nearly identical magnitude at this time at the output port. To integrate fields along the kicker, a flat top pulse excitation should be taken into account, and using a wave that peaks at input port could be a noticeable mistake when wavelength is not much larger than device length.

Therefore, if flat top pulse magnitudes (voltages and currents) are to be accurately calculated in frequency domain codes, the fields should be obtained at a peak value everywhere in the model taking real plus imaginary components independently of the phase. The simulation frequency should be about $(2T_f)^{-1}$, being T_f the flat top pulse duration.

The input of excitations²⁷ is achieved via the wave ports drawn in the coaxial terminations (Fig. 2.26). Those ports fill the entire surface of the coaxial and represent an infinite waveguide connected to them in the same transmission mode (TEM in this case). It is useful to define an integration path for the electric field in the port which ensures the desired TEM transmission mode in the simulation. Power considerations will be shown in the following section.

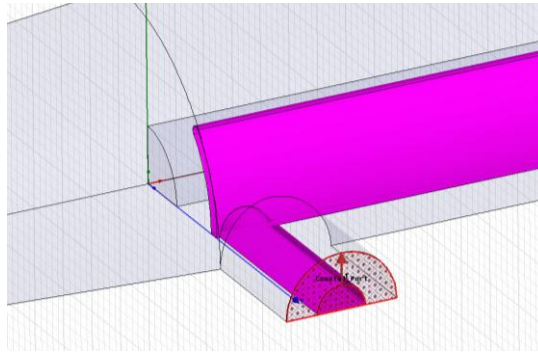


Fig. 2.26 Coaxial port excitation

- **Materials:** Frequency domain codes allow selecting materials for different parts of the model. The materials are simulated in high frequency codes as a resistivity over the surfaces bearing in mind the skin depth of the material. The effect of the materials resistivity is a second order factor in transmission line devices (not resonant) like the strip-line kickers and therefore, real materials are not needed to be simulated in most cases. This improves simulation speed because the terms of the calculation matrices are not complex and therefore the size of the problem is a half. However, for the simulation of the stand-off effects, it is necessary to use the real characteristics of the ceramic insulators to obtain a good approximation to the real behaviour.

²⁷ The physical connection from the coaxials to the electrodes can be initially estimated as a simple perpendicular contact. In following sections this will be optimized if necessary.

2.3.1.2.2 Input power

Every magnitude in frequency domain codes is a peak phasor, and therefore peak phasor considerations should be used to handle fields, potentials and currents. Power at the input ports in frequency domain codes is usually a time averaged quantity (peak power over 2), so this should be taken into account when exciting ports. For example, assume that one watt of power flowing through a coaxial line model generates a peak voltage of 10 V and a peak current of 0.2 A. Obviously, RMS values for sinusoidal magnitudes are given by the peak magnitude over the square root of 2. Therefore, the averaged power of this example can be obtained as $P = V_{RMS} I_{RMS}$ which corresponds to 1 watt averaged power or 2 watts peak power.

The averaged power input at the 3D model wave ports²⁸ comes from the analytical calculations developed in section 2.2.1.3. Only the downstream ports should be powered in the 3D simulation. The upstream ports are automatically matched to the characteristic impedance of the coaxial line²⁹. The averaged RF power for one electrode is $P_{1DC}/2$. However, if the magnetic symmetry cuts the coaxial port as in Fig. 2.23, the boundary condition forces the power to be the half needed to get the same fields inside. So the power needed at the input port in a symmetry condition would be $P_{1DC}/4$.

2.3.1.3 Transmission and reflection: S parameters and coaxial to strip-line transition

Once the 3D model is drawn and set up with adequate boundary conditions and power, it is time to solve the transmission coefficients (scattering parameters³⁰) to obtain the transmitted and reflected power in a range of frequencies. This simulation measures the ability of the kicker to transmit all the power from the source without reflecting it back due to any impedance mismatching.

²⁸ Four ports are necessary if no symmetries are used and only two ports (full or half) if longitudinal symmetries are used.

²⁹ Therefore it is very important to design a coaxial line with a characteristic impedance identical to the strip-line.

³⁰ Better known as S-parameters.

The scattering parameters in RF define the transmission and reflection of voltage waves through a multi-port electrical network or device [6; 13]. For a two-port device like the one shown in Fig. 2.27, S-parameters are defined based on the voltage waves a_1 , a_2 , b_1 and b_2 normalized to a desired characteristic impedance Z_0 .

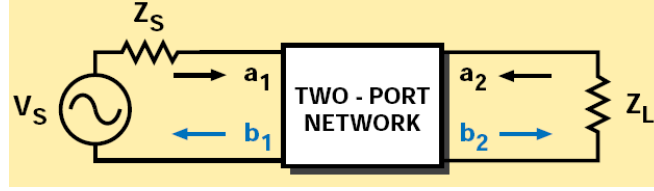


Fig. 2.27 Two-port network showing incident and reflected waves

The independent variables a_1 and a_2 are defined as shown in Eqs. (2.49) and (2.50), where V_{in} is the incident voltage wave on port n .

$$a_1 = \frac{V_{i1}}{\sqrt{Z_0}} \quad (2.49)$$

$$a_2 = \frac{V_{i2}}{\sqrt{Z_0}} \quad (2.50)$$

Dependent variables b_1 and b_2 are defined as shown in Eqs. (2.51) and (2.52), where V_{rn} is the reflected voltage wave from port n .

$$b_1 = \frac{V_{r1}}{\sqrt{Z_0}} \quad (2.51)$$

$$b_2 = \frac{V_{r2}}{\sqrt{Z_0}} \quad (2.52)$$

Then, the two-port network can be described using the linear equation system shown in Eqs. (2.53) and (2.54).

$$b_1 = s_{11}a_1 + s_{12}a_2 \quad (2.53)$$

$$b_2 = s_{21}a_1 + s_{22}a_2 \quad (2.54)$$

S_{11} is the input reflection coefficient with the output port terminated by a matched load ($Z_L=Z_0$). S_{22} is the output reflection coefficient with the input terminated by a matched load. S_{21} is the forward transmission gain with the output port terminated in a matched load. And S_{12} is the reverse transmission gain with the input port terminated in a matched load (Eq. (2.55)).

$$s_{11} = \left. \frac{b_1}{a_1} \right|_{a_2=0} \quad s_{22} = \left. \frac{b_2}{a_2} \right|_{a_1=0} \quad s_{21} = \left. \frac{b_2}{a_1} \right|_{a_2=0} \quad s_{12} = \left. \frac{b_1}{a_2} \right|_{a_1=0} \quad (2.55)$$

However, the most important relation that comes from previous voltage waves is that the coefficients (s-parameters) are simply related to power gain and mismatch loss. For example, $|a_1|^2$ is the power incident on the input of the network, that is, the power available when the source impedance is Z_0 . And $|b_1|^2$ is the power reflected from the input port of the network. Therefore, bearing in mind Eq. (2.55), $|S_{11}|^2$ is the RF power per unit that going into port one is reflected back to the source. If the network has no loss and no gain, the output power must equal the input power and therefore this case $|S_{11}|^2 + |S_{21}|^2 = 1$.

3D frequency domain codes calculate the full scattering matrix of S-parameters according to the number of ports simulated in the system. For example, a system with 4 ports would have a square scattering matrix of 16 elements. However, the kicker simulated with symmetries only has 2 ports and therefore the scattering matrix has only 4 elements. Fig. 2.27 then represents the equivalent circuit for a kicker fed by a power source and discharged in a load. The power source has internal impedance Z_s and the load is Z_L . The two-port network is the strip-line transmission line designed with Z_0 characteristic impedance. Therefore, the maximum power dissipated in the load happens when $Z_s = Z_L = Z_0$, which means that there is no reflected wave going back to the power source.

A typical plot of S_{11} parameter for a strip-line kicker is shown in Fig. 2.28. The reflection increases with frequency depending on the coaxial to strip-line transition quality. Furthermore, there is a maximum-minimum pattern which depends on the distance between feedthroughs (approx. electrode length plus both transitions). The identical mismatching in both transitions of the strip-line allows the existence of standing waves in the transmission line. There are reflection nodes at kicker lengths equal to multiple quarter wavelengths ($\lambda/4$, $3\lambda/4$, $5\lambda/4$, etc.) which represent a perfectly matched transmission for the correspondent frequencies [14]. At those approximate frequencies, the reflected waves between both transitions separated by the transmission line present a null interference at odd multiples of $\lambda/4$ due to the composite S_{11} parameter of both transitions.

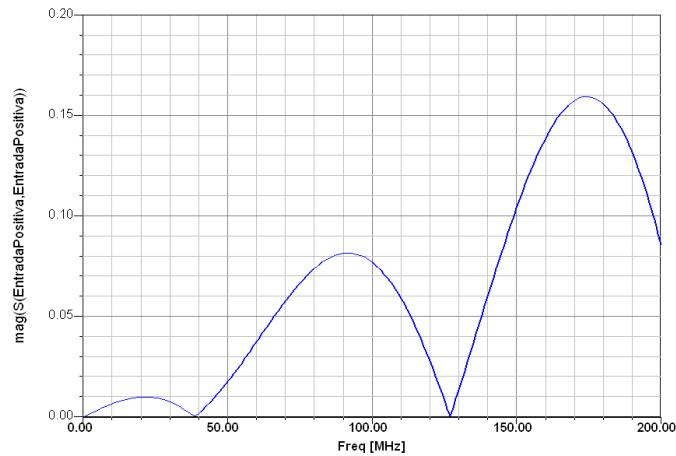


Fig. 2.28 Typical S_{11} plot for a strip-line kicker

The frequency range where the transmission is expected to be good depends on the pulse frequency contents (Fig. 2.29). The power supply pulse contents frequencies depending mainly on the rise and fall times as expressed in section 1.4.4. As it was already indicated, only frequencies below $0.5/T_r$ have to be considered to guarantee a good transmission of the pulse through the kicker.

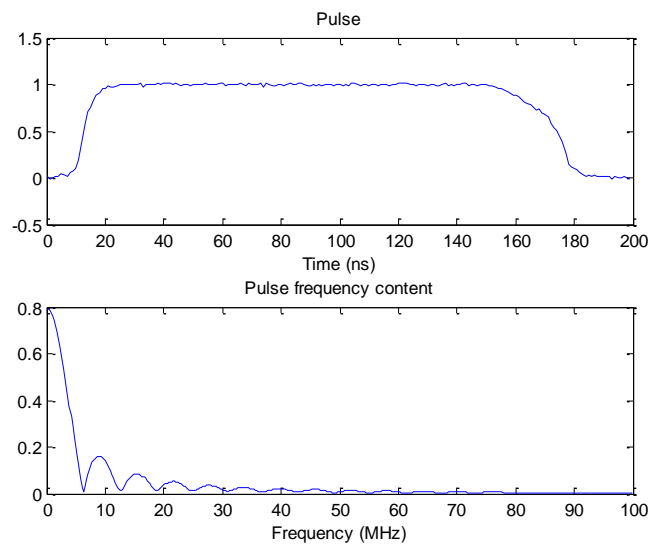


Fig. 2.29 Pulse and Fourier transform

Therefore, if S_{11} parameter stays small below the calculated frequency, the coaxial to strip-line transition can be considered valid. Considering that squared S_{11} parameter is the reflected power per unit, a small value can be estimated as 1% of power, always bearing in mind power supply designer specifications. $|S_{11}| < 0.1$ is usually a good design consideration from the power supply point of view³¹.

However, the initially designed coaxial to strip-line transition can be not good enough for an adequate power transmission. In this case, it is necessary to redesign the connection between the coaxial input and the strip-line. The most important idea to make a good design is trying to smooth the transition between the coaxial and the strip-line to avoid abrupt variations of the characteristic impedance. Indeed, the coaxial and the strip-line are both 50 Ohms impedance, and therefore the transition should ideally maintain this figure along its distance. There are several possibilities to design well matched transitions, one of them proposed by the author.

- Tapered electrodes: The transition can be smoother if the electrodes decrease their cross section as they approach to the coaxial connectors (Fig. 2.30).

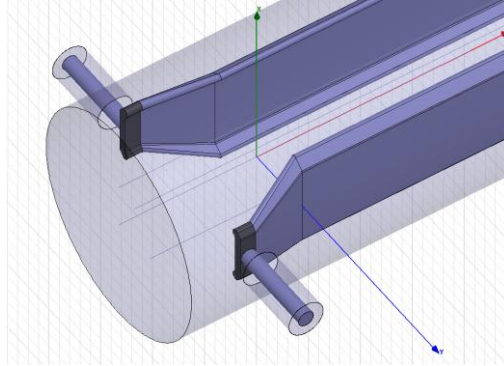


Fig. 2.30 Transition by tapering the electrodes

Obviously, the cross section of the smallest part of the electrode should maintain the characteristic impedance, which requires a 2D design and optimization of the new straight section. This optimization will put the electrode closer to the tube wall in order to maintain the characteristic impedance (see chapter 1).

³¹ It is recommended to design the S_{11} reflection to be well below 0.1 if high order modes or wakefield problems are expected in the kicker. A smaller reflection indicates better transmission and therefore, fields excited by the beam (usually of high frequency) and coupled to the coaxials are easily taken out from the structure through the coaxial ports.

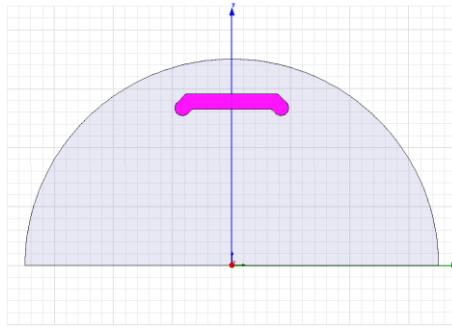


Fig. 2.31 2D optimization of the tapered electrode

The length of the tapering depends on the required frequency response and the electrode length. Long tapering improves high frequency transmission, but the efficiency of the kicker (transverse shunt impedance and transverse voltage) is reduced because the small part of the electrode cannot contribute to the field in the axis as much as the regular part. Indeed, the end effects are more important and the homogeneity can be seriously distorted in 3D. Therefore it is required to design an optimized length transition.

The transition of the electrode between the small and large cross section is usually linear to make the modelling and manufacturing process easier. However, if this transition is long, it is recommended to split it in several cuts, each of them featuring the optimized characteristic impedance.

It is important to be careful when approaching the electrode to the kicker tube. If the distance is too small and the electrode voltage is large, there could be sparking even in high vacuum. Although there are several criteria to predict this issue (Paschen's law, Kilpatrick's criteria for RF), if problems are expected, it is recommended to make empirical measurements.

- Tapered electrodes inside the tube tapers: The author proposed the tapering of both the electrodes and the tube at once (Fig. 2.32). This makes the transition even smoother without increasing total kicker length³² although manufacturing costs are a bit higher and assembly is more complicated.

³² The tapers of the tube (which are always necessary) increase the kicker length without increasing the effective length because they cannot contribute to the field. Using this method, the electrodes can start contributing to the field from the beginning.

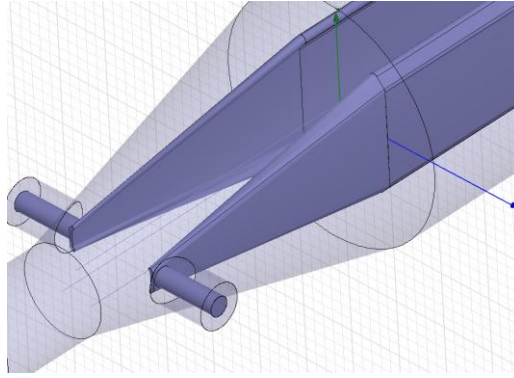


Fig. 2.32 Transition by tapering both the tube and the electrodes

It is still necessary to check the electrical breakdown due to the proximity of the electrodes to the external tube tapers. The characteristic impedance concerns are the same as for the previous method.

All these transitions can also be applied to any other electrode cross section (circular, elliptical, etc.) and even when the tube is not cylindrical but racetrack or elliptical. The design depends on the abilities of the designer to obtain a smooth and easy to manufacture transition.

The optimization of these transitions should be carried out by means of the 3D code. This involves a lot of calculations and time. However, as it was pointed out in section 2.3.1.2.1, it is possible to cut the kicker just after the transition and put an absorbing TEM wave port there (Fig. 2.24). Therefore, the size of the problem is enormously reduced and the optimization of the transition length and the power reflection is easier to do. However, the S_{11} parameter plot is not exactly the same as for the full structure because the wave port avoids the reflections at the distances related with the electrodes length. The plot is a linear increase of the S_{11} parameter (Fig. 2.33), then it must be optimized trying to minimize the slope of S_{11} .

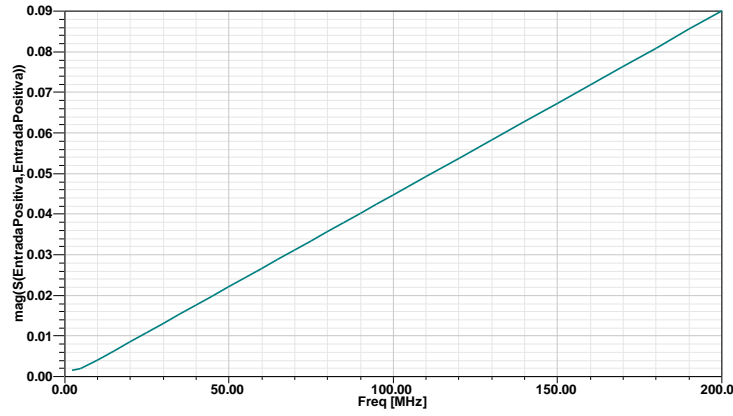


Fig. 2.33 S_{11} parameter for the transition alone in a cut model

2.3.1.4 Integrated homogeneity

The particles experience the transverse voltage kick when they travel through the kicker aperture. However, the magnitudes analytically calculated in previous sections are always for a particle travelling along the kicker axis when electrodes are longitudinally homogeneous. The real particles usually travel out of the axis and experience the end effects of the electrodes along their trajectory when entering and exiting the kicker. The former is the reason why the 2D homogeneity has to be calculated; the latter is the reason to calculate the 3D homogeneity.

The 3D homogeneity is the maximum variation of transverse voltage that different particles in a beam can experience when passing through the dipolar field of the kicker. Ideally, all the integration paths along the kicker length should return an identical transverse voltage. The 3D homogeneity can be obtained in the 3D code by means of only the electric field³³ in the area of interest as shown in Eq. (2.56).

$$H_{3D} = \frac{(\int E_{\perp} d\vec{l})_{max} - (\int E_{\perp} d\vec{l})_{min}}{(\int E_{\perp} d\vec{l})_{axis}} \quad (2.56)$$

³³ This is possible due to the identical transverse voltage given by both E and B fields.

3D codes usually allow defining integration lines to calculate any field component along them. To simplify, the maximum and minimum electric field paths along the kicker can be taken from the 2D homogeneity calculations. The integration paths are assumed to be straight and parallel to the longitudinal axis, although the actual particles will be deflected in their trajectory. This assumption is acceptable as the deflection angle is usually very small, the betatron oscillation is neglected and the field variation due to deflection is almost negligible. The integration lines should start well before the electrodes and end well after the electrodes to ensure that the entire fringe field is included in the calculation.

The 3D homogeneity is very sensitive to mesh refinement and it is recommended to take it as an approximate value in very long devices where a fine calculation (including stand-off effects) would require enormous amounts of computing power.

2.3.1.5 Lost power

The passage of the pulse through the kicker induces some heat in the electrodes and tube due to the resistive surfaces. This energy has to be estimated because the refrigeration of the electrodes is very difficult in high vacuum and a small energy deposition can create high temperature increments.

There are several ways to obtain the energy loss when a pulse passes through the kicker by using a 3D frequency domain code. The first one takes advantage of S-parameters to calculate the power retained inside the device. The RF power can be calculated as shown in Eq. (2.57).

$$P_{lost} = P_{input} (1 - S_{11}^2 - S_{21}^2) \quad (2.57)$$

Alternatively, the 3D frequency domain code can calculate the power input and output through the coaxial ports by integrating the normal Poynting vector over their surface [6]. This is only possible if the simulation is effectuated using lossy materials, which requires twice the computer memory as for lossless materials. Then the power lost inside the device is calculated by the difference between the power input and output.

The power calculated by one of the presented methods has to be averaged in time by the pulse duration and repetition rate as it was expressed in Eq. (2.41). Therefore, P_{input} should be the equivalent peak power of the RF wave.

2.3.1.6 Cross check of analytical calculations

The analytically calculated values of transverse voltage, electrodes voltage and current can be also calculated in the 3D frequency domain code bearing in mind the model considerations exposed in section 2.3.1.2.1. The calculated values in 3D are expected to be more exact than analytical results because they include the 3D effects (transitions, stand-offs, etc) and the actual cross section geometry of the electrodes and tube.

- Transverse voltage: The 3D code obtains the full field solution in the calculation domain using the input power as shown in 2.3.1.2.2. It is therefore easy to numerically calculate the integral of Eq. (2.3) by just defining a straight line in the axis and calculating both E and B components at peak values. The speed of the particles can be safely rounded to c for electrons or positrons.

It is also possible to calculate the transverse shunt impedance variation with frequency for a kicker fed in RF by considering the transit time factor in the calculation. If the kicker was not fed by a pulse but by a RF wave, the particles would see the change of the field as they go along the kicker. It is therefore necessary to de-phase the wave to the actual value in space as the relativistic particle goes forward while integrating the transverse voltage.

- Electrodes voltage: The voltage of the electrodes is easily calculated by the line integral of the E field between the electrode surface and the tube (voltage to ground) or between the electrodes (voltage between electrodes).

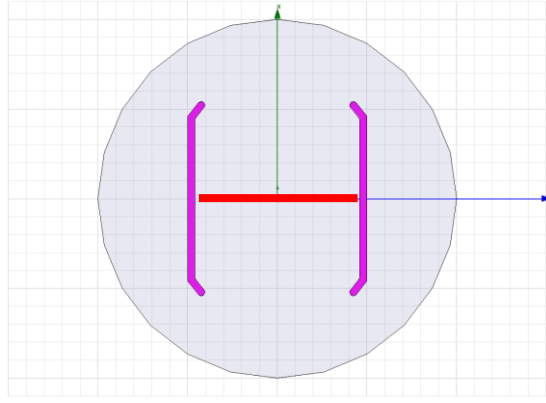


Fig. 2.34 Electric field integration path

- Electrodes current: The current can be calculated by the circulation of H field around any path enclosing the electrode. If symmetry is used, the resultant current will be half the real one.

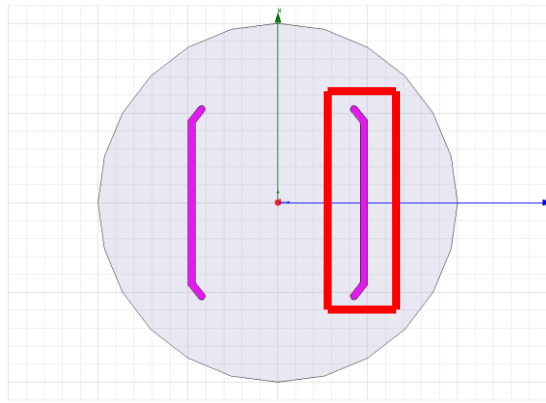


Fig. 2.35 Magnetic field integration path

2.3.1.7 High Order Modes analysis

When the beam passes through the kicker, it can excite all the frequencies of its entire frequency spectrum inside the device. Depending on the geometry of the kicker (length, cross section dimensions, shape, etc.), it can present some resonant frequencies where a small excitation can present a huge amplification of the electromagnetic fields.

Those resonating frequencies, depending only on geometrical parameters, are known as High Order Modes (HOMs), which are potentially a source of coupled bunch instability if trapped inside the device. This behaviour is related with the wakefields presented in previous sections in the sense that wakefields are usually the exciters of HOMs. However, if the beam has no frequencies that match any of the geometrical possible HOMs, there will be no resonances due to the beam excitation.

The first step of the analysis is to define the approximate frequency range to search for HOMs. As the beam pipe and the kicker tube are somehow circular waveguides, only TM and TE modes can propagate over certain cut-off frequencies [6]. As a resonant mode propagates forward and backward inside the kicker (this means resonance), only the frequencies that can propagate in the pipe could be HOMs. Because of that, the approximate lower range of frequency for HOMs inside the kicker is the kicker's tube cut-off frequency, and the higher range of frequency is the beam pipe's cut-off frequency³⁴. Nevertheless, those frequencies depend on the considered mode. There are multiple modes that can propagate in circular waveguides of diameters between the diameter of the beam pipe and the diameter of the kicker tube (all TM or TE). All those modes can be studied in the analysis but, sometimes, a specific mode seems the most dangerous for the beam and could require a deeper study.

For example, if the modes with longitudinal E field are the most dangerous for a given accelerator, only TM modes have to be studied. In this case³⁵, although the dominant mode on a circular waveguide is TE_{11} , the first TM mode is TM_{01} . The cut-off frequency of TM_{01} mode for a circular pipe of radius r is analytical and can be calculated as shown in Eq. (2.58):

$$f_c = \frac{2.405}{2 \pi r \sqrt{\mu \epsilon}} \quad (2.58)$$

Using Eq. (2.58) it is possible to calculate a range of frequencies between the radius of the main tube and the radius of the beam pipe where HOMs based on TM_{01} can exist. This can be repeated for other possible dangerous modes close to the frequency

³⁴ Waves at higher frequency than beam pipe's cut-off are not reflected back and go outside the kicker flowing through the beam pipe.

³⁵ Considering a circular kicker tube and a circular beam pipe.

spectrum of the beam. The different cut-off frequencies for circular and rectangular waveguides can be found in [6]. It is also possible to obtain the exact cut-off frequency for a given cross section by using a 3D frequency domain numeric code.

In principle, the HOMs in a pulsed kicker can be excited not only by the beam but also by the pulsed power supply. However this is rather difficult as the pulse usually does not contain frequencies over 1 GHz and they all are well coupled with the coaxial ports (they cannot stay inside the kicker).

Anyway, only TE or TM modes have been presented above. However, other combined modes can also resonate inside a tubular device when the beam passes through it at fixed periods of time (circular accelerators or storage rings). The beam represents somehow a central conductor with RF power, which forms with the pipes a coaxial like transmission line. This transmission line can excite different configurations of electric and magnetic fields in the device.

An important parameter for HOM simulations is the damping that the kicker structure is creating for each frequency. For a HOM to be dangerous, the quality factor Q ³⁶ should be high, and the transmission to the outside by the coaxial ports should be small (close to full reflection or $S_{11} \approx 1$). This means that all the power released by the beam at this frequency remains inside the kicker, and if that frequency matches a kicker resonant frequency, it could be amplified and produce beam instability.

Concerning the 3D frequency domain code, HOMs can be calculated by using the eigenmodes solver. It has been indicated that the HOMs depend only on the geometry of the resonant device. Therefore it is possible to obtain the frequencies at which a structure can resonate by calculating the eigenmodes of the electromagnetic fields [15]. This is a typical running mode in 3D frequency domain codes. The size of the problem can be huge when high frequency HOMs are studied in a long structure due to the small mesh required³⁷.

³⁶ The quality factor of a resonant mode is defined as the stored electromagnetic energy at the resonant frequency over the dissipated power.

³⁷ The maximum element size should not be larger than a tenth wavelength of the higher frequency HOM to obtain acceptable precision in the HOM calculations.

In addition, if the Q factor has to be calculated by the 3D code, it is necessary to model the kicker using lossy materials, which doubles the size of the problem. However, it is also possible to calculate the Q factor in lossless models [16] using Eq. (2.59).

$$Q = \frac{2 \int H^2 dV}{\delta \int H_t^2 dS} \quad (2.59)$$

where H_t is the tangent magnetic field in the lossy surfaces and δ is the skin depth of the material at the resonant frequency (σ is the electrical conductivity in Ω^{-1} and μ is the magnetic permeability in H/m):

$$\delta = \sqrt{\frac{2}{2 \pi f \sigma \mu}} \quad (2.60)$$

The solution of the whole structure without symmetries usually requires large amounts of computer memory and processing time. In addition, many modes can be found in a structure when no symmetries are used, and this makes difficult to individually analyse them. Therefore, it is recommended to cut the structure in one quadrant (as it was done for normal simulations) and define different symmetry boundary conditions in the cut planes to reduce the number of HOMs that can appear in each simulation, also reducing the memory and computer requirements. The possible boundary conditions are E field perpendicular to the cut plane and H field perpendicular to the cut plane, which results in 4 possible combinations for one quadrant structure.

Only the unloaded HOMs³⁸ can be obtained using the eigenmodes solver because the structure must be closed with no wave ports for the solver to run. However, absorbing boundaries can also be defined at the ports to obtain approximate results for loaded HOMs. The boundaries can be manually or automatically defined. Some 3D codes allow automatically defining absorbing boundaries in surfaces although it is always possible to put a thick material with high losses (high loss tangent and low electrical conductivity) to absorb the incoming waves.

³⁸ If a HOM is resonating freely without exit ports, it is then unloaded. It is also possible to simulate loaded HOMs in eigenmode simulations using absorbing boundary materials in the ports.

The eigenmodes of the model can also be obtained with a perfectly conducting thin wire in the axis (Fig. 2.36) to simulate the beam. This method is quite similar to the coaxial wire method that will be studied in following sections. The symmetry conditions should be changed to match the beam fields' geometry³⁹.

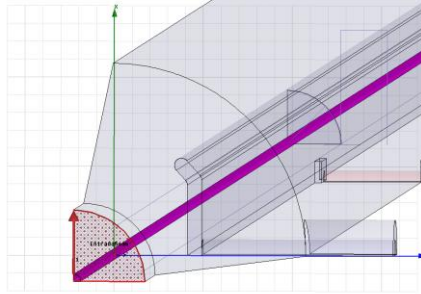


Fig. 2.36 Central wire and beam wave port for HOM simulations.

The thin wire in the axis and the symmetry boundary conditions force the resonating HOM fields to be the ones that could be directly excited by the authentic beam. An example of a typical resonating mode obtained using this method can be observed in Fig. 2.37.

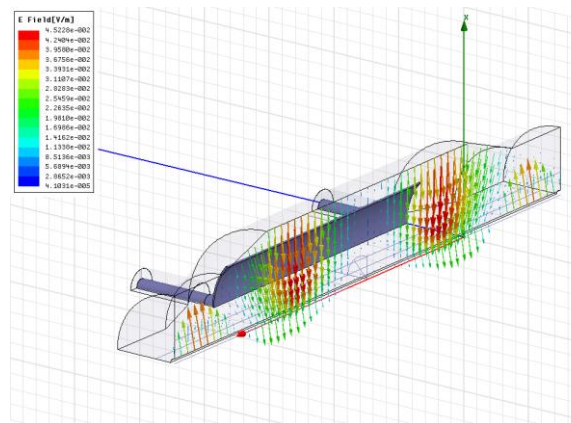


Fig. 2.37 Resonating mode using a wire in the axis.

All the identified modes should be studied and checked. Sometimes most of them are not real or possible to be excited and should be rejected⁴⁰. This is not an easy task and requires deep knowledge and experience on EM fields analysis.

³⁹ Magnetic field perpendicular to both longitudinal symmetry planes.

⁴⁰ Modes with very low quality factor, false modes due to artefacts of the wire method, etc.

If an identified mode seems dangerous for the beam, it is necessary to damp it. The damping can be achieved by installing a coupling device correctly located inside the kicker, typically a loop to couple the magnetic field of the mode. The loop should be connected to an external load to absorb the power of the mode⁴¹. It is also possible to damp a resonating mode by using an absorbing material located in the right place inside the kicker volume. This absorbing material can be a ferrite or other ceramic like SiC with high loss tangent and low electrical conductivity. It is important to avoid locating the absorbing material in a place where it can disturb the main TEM wave travelling by the kicker and the beam itself.

2.3.1.8 Coupling and transfer impedances: The coaxial wire method.

The coupling and transfer impedances are very useful tools for characterizing devices installed in periodical accelerators such as synchrotrons and storage rings. They define the behaviour of the device when the beam passes through it and the excitation fields achieve the steady state. However, the coupling impedances can also be useful for other accelerators (for example linacs) if the wake potentials are calculated from the inverse Fourier transform of the coupling impedances.

Longitudinal impedance

One of the best suited methods to empirically calculate the longitudinal beam impedances of a device is the coaxial wire method [12; 17]. It permits to obtain the coupling and transfer impedances without really passing a beam through the device. Only a thin copper wire, some impedance matching and a vector network analyzer are required for this purpose (Fig. 2.38).

⁴¹ The loop can be connected to a coaxial line with characteristic impedance matched to the load (usually 50 Ohm).

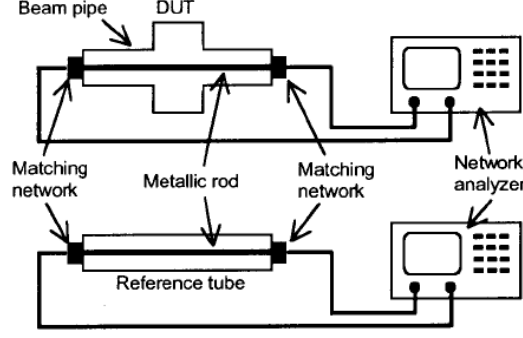


Fig. 2.38 Experimental set-up for the longitudinal impedance measurement

The method works by converting the beam in a metallic wire and the device under test (DUT) in a coaxial like transmission line. The excitation of the new coaxial line in a frequency range simulates the fields that a beam will produce when passing multiple times through the device. The wide frequency response (s-parameters) of the device is measured through the created coaxial line by a network analyzer.

Empirically, the procedure is a bit more complex as the device should be physically connected to the network analyzer using some “handmade” matching networks (see references) which are quite difficult to make for high frequencies. However, the same coaxial wire method can be simulated in a 3D frequency domain code to obtain the beam coupling and transfer impedances, without the intrinsic empirical problems. Once the device has been simulated and the scattering parameters are obtained, the longitudinal coupling impedance can be calculated as shown in Eq. (2.61).

$$Z_l = 2 Z_0' \left(\frac{S_{21ref}}{S_{21DUT}} - 1 \right) \quad (2.61)$$

where Z_0' is the characteristic impedance of the coaxial line formed by the beam pipe and the inner wire, S_{21DUT} is the s-parameter of the simulation between input and output of the coaxial line and S_{21ref} is the s-parameter of a same length tube with constant cross section.

Ports 1 and 2 are the beam coaxial input and output ports. The reference tube is the comparison structure for the empirical measurement. It features the same cross section as the beam pipe which is identical to the device's initial cross section. S_{21ref} should be approximately equal to 1 (full transmission), but the phase of the scattering

parameters depends on the length of the tube. Therefore, for 3D code simulation, S_{21ref} magnitude can be approximated to 1 (phase cancels with S_{21DUT}).

The relevant upper frequency limit for impedance calculation in the code is approximately obtained from the minimum longitudinal bunch length σ_z that will pass through the device as shown in Eq. (2.62). The coaxial wire method simulation results are reliable below frequency where no significant HOMs are found. It also introduces a small shift in frequency in the impedances due to the strong distortion of the wire in the fields.

$$f_{max} = \frac{c}{2 \sigma_z} \quad (2.62)$$

When the device has input/output ports (like the coaxial ports in the strip-line kickers), it is also possible to calculate the beam transfer impedance (Z_{trf}) for every port. For the port number i , it can be obtained from the s-parameters as shown in Eq. (2.63).

$$Z_{trf} = \frac{|S_{i1DUT}/S_{i1ref}|}{|S_{21DUT}/S_{21ref}|} \sqrt{Z_0 Z_0'} \quad (2.63)$$

where Z_0 is the characteristic impedance of the i port. The scattering parameter between the real device i port and the reference tube beam coaxial port (S_{i1ref}) is not measurable because the reference tube does not have ports. However, this quantity can be estimated in the empirical measurements as $\sqrt{S_{21ref}}$, or better in the 3D code $|S_{i1ref}| = |S_{21ref}| = 1$.

Transverse impedance

The transverse impedance can be obtained with a little modification of the coaxial wire method. A pair of wires is inserted into the structure and aligned on the horizontal plane if horizontal impedance has to be measured or aligned on the vertical plane to measure vertical impedance (Fig. 2.39).

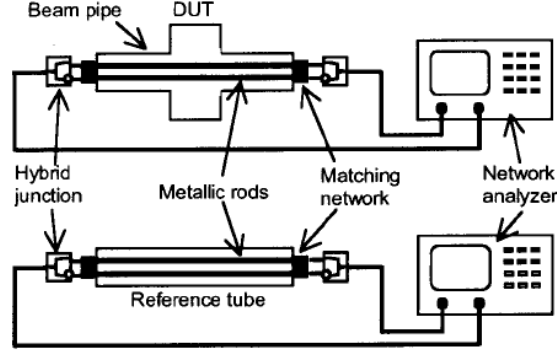


Fig. 2.39 Experimental set-up for the transverse impedance measurement

The wires are driven by two identical currents in opposite direction (like the kicker strip-lines), to generate a TEM wave as shown in Fig. 2.40.

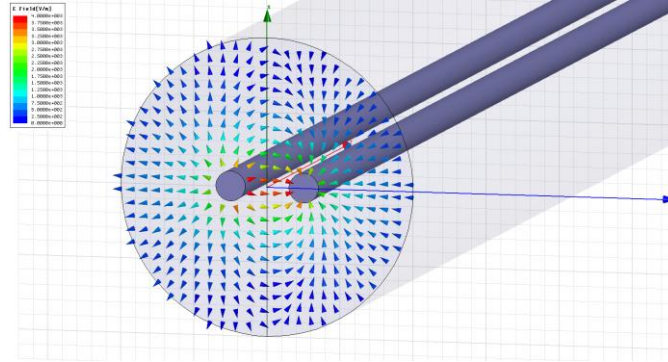


Fig. 2.40 TEM field generated by two parallel conductors driven in differential mode

The transverse coupling impedance is given by Eq. (2.64).

$$Z_t = Z_0' \left(\frac{S_{21ref}}{S_{21DUT}} - 1 \right) \quad (2.64)$$

where Z_0' is the characteristic impedance of the transmission line formed by a single wire and the pipe halved by an electric symmetry plane. The simulation and calculation in 3D frequency domain code is similar as for the longitudinal impedance.

Using previous relations and a defined current spectrum for the beam it is possible to calculate the total power released by the beam to the structure and the power flowing through the coaxial lines in steady state. For these and other relations, see [2].

2.3.1.9 Available software: HFSS

All the calculations and considerations shown in the previous sections can be easily implemented in almost any 3D frequency domain code. In this Thesis, the 3D frequency domain software used to calculate all the prototypes is HFSS⁴² [15]. However, other codes such as CST Microwave Studio can also provide identical features with very little changes in the user interface although they have not been extensively tested by the author.

HFSS is one of the best frequency domain 3D codes for high frequency EM simulation. It presents a user friendly environment to easy define the geometry and boundary conditions of the models (Fig. 2.41).

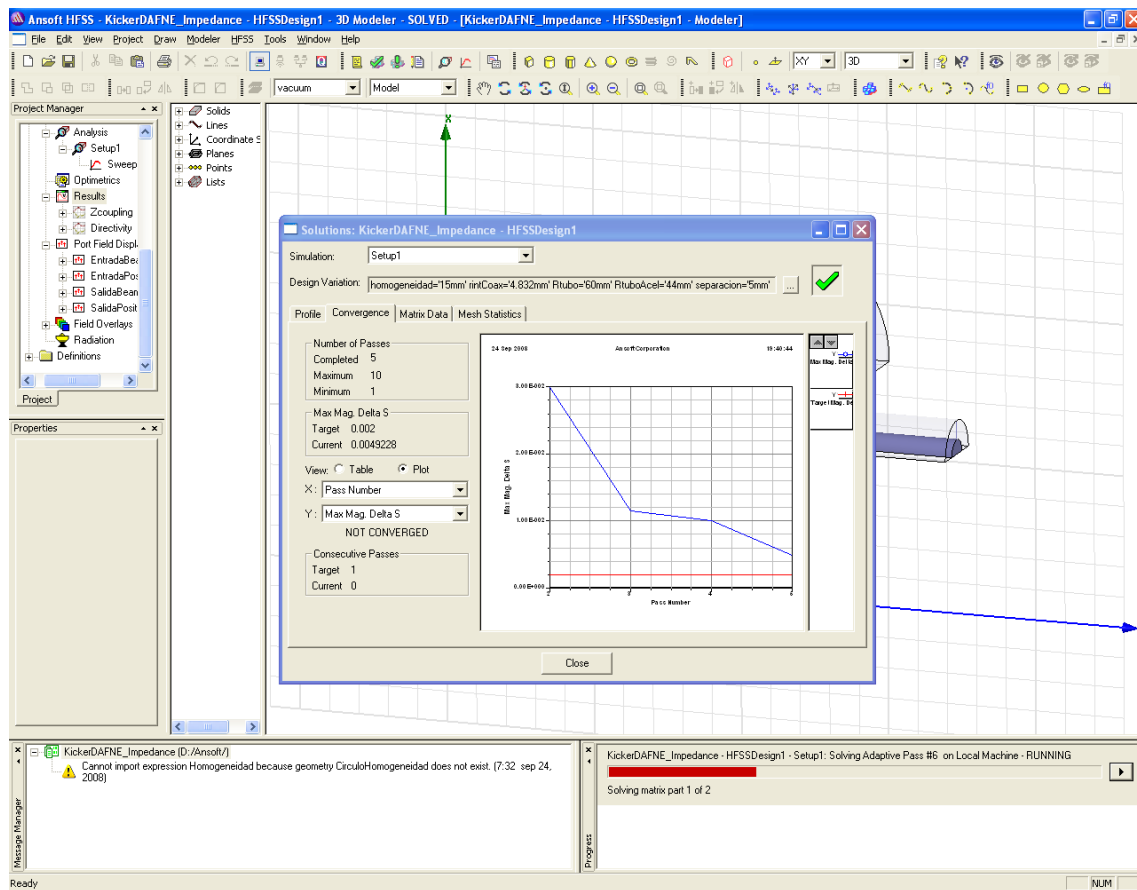


Fig. 2.41 HFSS interface

⁴² HFSS stands for High Frequency Structure Simulator, from Ansoft Corporation.

HFSS works in the frequency domain using phasors for representing electromagnetic magnitudes. The scattering parameters and the characteristic impedances are automatically solved, and also the eigenmodes solver returns the frequency and quality factor of the modes (Fig. 2.42).

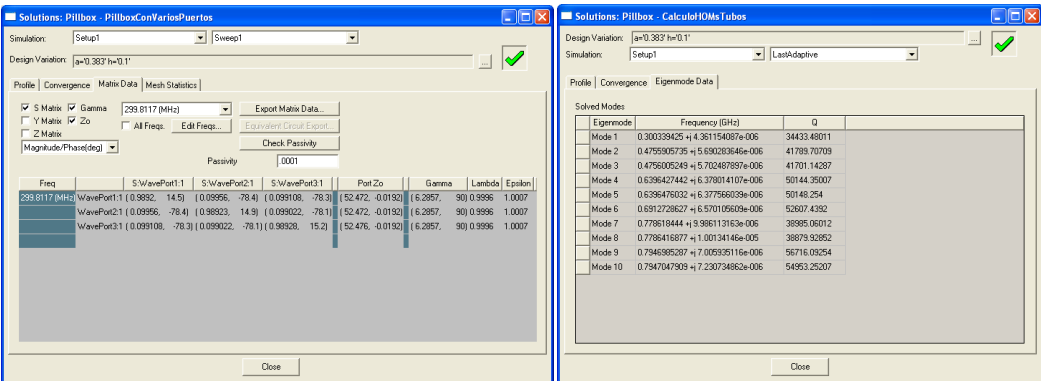


Fig. 2.42 Scattering matrix (left) and eigenmodes calculation (right) in HFSS

It is also possible to make the desired fields calculations by using the HFSS integrated calculator (Fig. 2.43), which allows making almost any mathematical operation including fields and geometries [18].

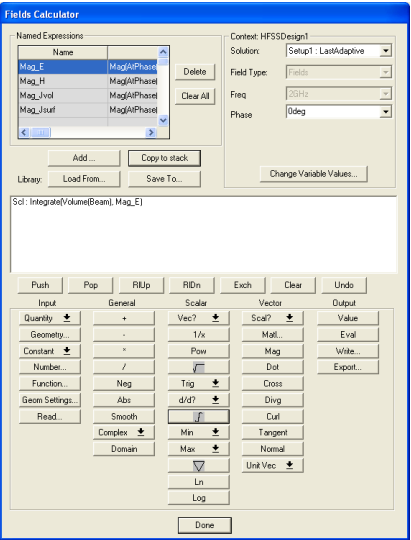


Fig. 2.43 HFSS calculator for field magnitudes

Regarding the fields calculator, most of the operations presented in previous sections have been developed by the author using HFSS v.10 calculator scripts to automate the calculations of typical strip-line kicker magnitudes. These scripts can be defined step by step in the calculator or imported from a .clc text file:

- Transverse voltage: The transverse voltage integral for a flat-top pulse can be calculated in HFSS calculator via the following commands:

```
$begin 'Named_Expression'
    Name('Vtransversal_v2')
    Expression('Integrate(Line(LinealIntegracionLongitudKicker, 1000), ScalarY(+ (Cross(<0, 0, 299792000>, *(CmplxMag(<Hx,Hy,Hz>, 1.25664E-006)), CmplxMag(<Ex,Ey,Ez>))))')
    Vector_Constant(0, 0, 2.99792e+008)
    NameOfExpression('<Hx,Hy,Hz>')
    Operation('CmplxMag')
    Scalar_Constant(1.25664e-006)
    Operation('*')
    Operation('Cross')
    Fundamental_Quantity('E')
    Operation('CmplxMag')
    Operation('+')
    Operation('ScalarY')
    EnterLine('LinealIntegracionLongitudKicker')
    Operation('LineValue')
    Operation('Integrate')
$end 'Named_Expression'
```

To use this script, it is necessary to previously define in the 3D model an integration line along the axis of the kicker named “LinealIntegracionLongitud Kicker”.

This definition does not include the transit time factor. If the kicker is fed by a RF wave, it should be included and the calculator commands are:

```
$begin 'Named_Expression'
    Name('Vtrans')
    Expression('Abs(Integrate(Line(LinealIntegracionLongitudKicker, 1000), ScalarY(+ (Cross(<0, 0, 299792458>, *(AtPhase(<Hx,Hy,Hz>, /(omega*(Z), 299792458)), 1.25663706143592E-006)), AtPhase(<Ex,Ey,Ez>, /(omega*(Z), 299792458))))))')
    Vector_Constant(0, 0, 2.99792e+008)
    NameOfExpression('<Hx,Hy,Hz>')
    Scalar_Function(FuncValue='Z')
    MaterialOp('Omega (w)', 1)
    Scalar_Constant(2.99792e+008)
    Operation('/')
    Operation('AtPhase')
    Scalar_Constant(1.25664e-006)
```



```

Operation('*')
Operation('Cross')
Fundamental_Quantity('E')
Scalar_Function(FuncValue='Z')
MaterialOp('Omega (w)', 1)
Scalar_Constant(2.99792e+008)
Operation('/')
Operation('AtPhase')
Operation('+')
Operation('ScalarY')
EnterLine('LinealIntegracionLongitudKicker')
Operation('LineValue')
Operation('Integrate')
Operation('Abs')
$end 'Named_Expression'

```

- Electrodes voltage: The line integral of the electric field can be calculated via the following commands:

```

$begin 'Named_Expression'
    Name('Mag_V')
    Expression('CmplxMag(+{CmplxR(Integrate(Line(LinealIntegracionPlacas, 1000),
Dot(Real(<Ex,Ey,Ez>), LineTangent))), Cmplxl(Integrate(Line(LinealIntegracionPlacas, 1000),
Dot(Imag(<Ex,Ey,Ez>), LineTangent)))))')
    Fundamental_Quantity('E')
    Operation('Real')
    Operation('Tangent')
    Operation('Dot')
    EnterLine('LinealIntegracionPlacas')
    Operation('LineValue')
    Operation('Integrate')
    Operation('CmplxR')
    Fundamental_Quantity('E')
    Operation('Imag')
    Operation('Tangent')
    Operation('Dot')
    EnterLine('LinealIntegracionPlacas')
    Operation('LineValue')
    Operation('Integrate')
    Operation('Cmplxl')
    Operation('+')
    Operation('CmplxMag')
$end 'Named_Expression'

```

A line named “LineaIntegracionPlacas” between the electrode and the tube (Fig. 2.34) must be previously defined in the 3D model for this script to work.

- Electrodes current: The integral of the magnetic field can be calculated via the following commands:

```
$begin 'Named_Expression'
    Name('Mag_I')
    Expression('CmplxMag(*(+(CmplxR(Integrate(Line(BucleCalculoIntensidad,
    1000),
    Dot(Real(<Hx,Hy,Hz>), LineTangent))), CmplxI(Integrate(Line(BucleCalculoIntensidad,
    1000),
    Dot(Imag(<Hx,Hy,Hz>), LineTangent))), (2, 0)))')
    NameOfExpression('<Hx,Hy,Hz>')
    Operation('Real')
    Operation('Tangent')
    Operation('Dot')
    EnterLine('BucleCalculoIntensidad')
    Operation('LineValue')
    Operation('Integrate')
    Operation('CmplxR')
    NameOfExpression('<Hx,Hy,Hz>')
    Operation('Imag')
    Operation('Tangent')
    Operation('Dot')
    EnterLine('BucleCalculoIntensidad')
    Operation('LineValue')
    Operation('Integrate')
    Operation('CmplxI')
    Operation('+')
    Complex_Constant(2, 0)
    Operation('*')
    Operation('CmplxMag')
$end 'Named_Expression'
```

A line named “BucleCalculoIntensidad” between the electrode and the tube (Fig. 2.35) must be previously defined in the 3D model for this script to work. The value is multiplied by 2 at the end of the calculations to cope with the symmetry.

- Power losses: The integral of the pointing vector in the coaxial ports can be calculated via the following commands:

```

$begin 'Named_Expression'
    Name('PotenciaPerdidaKicker')
    Expression('*(Integrate(Surface(PuertoCoaxialSalida), Dot(Real(Poynting), SurfaceNormal)),
Integrate(Surface(PuertoCoaxialEntrada), Dot(Real(Poynting), SurfaceNormal))), -2)')
    NameOfExpression('Poynting')
    Operation('Real')
    Operation('Normal')
    Operation('Dot')
    EnterSurface('PuertoCoaxialSalida')
    Operation('SurfaceValue')
    Operation('Integrate')
    NameOfExpression('Poynting')
    Operation('Real')
    Operation('Normal')
    Operation('Dot')
    EnterSurface('PuertoCoaxialEntrada')
    Operation('SurfaceValue')
    Operation('Integrate')
    Operation('+')
    Scalar_Constant(-2)
    Operation('*')
$end 'Named_Expression'

```

The value is multiplied by 2 at the end of the calculations to cope with the symmetry used at the input and output ports. This should be changed according to the symmetries used. Two surfaces over the coaxial ports named “PuertoCoaxialSalida” and “PuertoCoaxialEntrada” have to be defined for this script.

2.3.2 TIME-DOMAIN SIMULATIONS

2.3.2.1 The scope of time-domain simulation

Time domain simulations in 3D represent the most intuitive analysis of a device. They can simulate a pulse feeding the strip-line kicker or a beam passing through the axis, solving the full fields in the whole structure for every time step.

For that reason, voltage in ports, currents, power, losses, etc. can be directly obtained in time domain for the real input signal without developing conversions between frequency and time domain simulations. Wakefields are directly integrated without the need of a simulated “beam wire” which leads to some distortions. However there are some disadvantages: time domain simulations are much longer and required computing resources are usually enormous. In addition, they are not very appropriate when the system rapidly reaches the steady state (in terms of beam and/or excitations) and an easier frequency domain simulation is feasible.

Therefore, time domain simulations will only be used for wakefield calculations in strip-line kickers installed in linacs or rings featuring small number of turns. Nevertheless, developing a time domain simulation of the real pulse feeding the kicker can also be very intuitive for a better understanding of the kicker behaviour.

2.3.2.2 Full wakefields calculations

The 3D simulation of a beam passing through the strip-line kicker results in the full wakefields calculations for the real structure. This process is very time-consuming and requires lot of computing power, and therefore it is usually done just before the final design is available.

The 3D geometry for the 3D time domain code can be exactly the same as for the 3D frequency domain code and most of the model considerations already given for the frequency domain code can also be applied to the time domain code. However, time domain code requires different element discretization [9; 10] and input parameters.

The meshing in finite differences method is applied over the whole problem region, not only in the vacuum inside the device (Fig. 2.44). Mesh elements are parallelepipeds called “cells” and their minimum size mainly depend on the bunch size (frequency content).

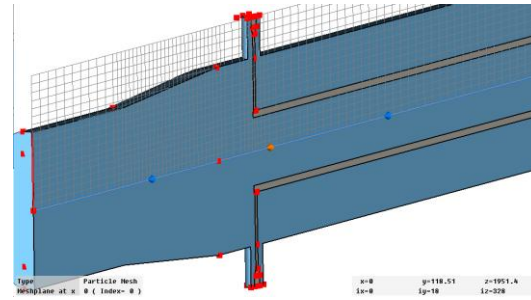


Fig. 2.44 3D time domain mesh for wakefields calculation

A minimum of 20 elements per wavelength at the maximum frequency spectrum of the beam are required to get a good simulation. This represents a big concern when the bunch size is much smaller than the device length. The whole model has to be meshed using a very fine mesh and the computer memory requirements increase a lot. However, some time domain codes use a fine moving mesh which follows the bunch [11] to reduce the number of required mesh points in the whole structure.

Waveguide ports can also be defined to directly obtain the peak voltages in the coaxials of the strip-line kicker due to the passage of the bunch. Besides, wave ports absorb coupled power from the beam and thus the structure can be simulated as a loaded cavity (like in the real world). The full field solution of the 3D time domain code permits to calculate any desired magnitude after the simulation, even plotting the electric or magnetic fields in time domain as the bunch passes through the structure (Fig. 2.45).

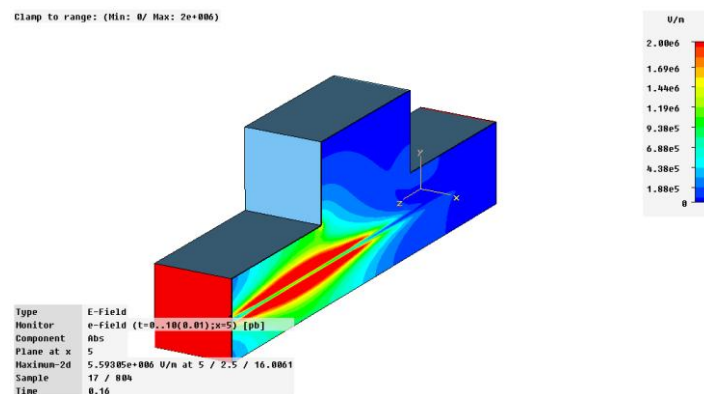


Fig. 2.45 Bunch passing through a small discontinuity

2.3.2.2.1 Longitudinal wake potentials and loss factor

The longitudinal wake potential and the loss factor are directly calculated by the 3D time domain code. Even when the model and calculations are very complex and time consuming, these results are close to the 2D time domain ones because many strip-line kickers are geometrically not very different from axi-symmetric devices.

The wake potential and loss factor are usually given in V/pC. Using these results, the beam power transferred to the structure and the energy spread can be calculated through Eqs. (2.47) and (2.48).

2.3.2.2.2 Transverse wakes and impedances

Once the longitudinal wake is obtained, the transverse wake can be directly calculated by the 3D time domain code or manually by using the Panofsky-Wenzel theorem as shown in Eq. (2.20).

The 3D time domain code can also automatically calculate the longitudinal and transverse coupling impedances. The coupling impedances are the Fourier transforms of the wake potentials. Therefore, a long time domain simulation is required to get a good frequency spectrum detail when transforming the signal. This depends on the bunch frequency contents⁴³ and device length, but a minimum distance of several meters of wake potential has usually to be simulated to get good accuracy. That is the reason why it is sometimes better to calculate impedances using a frequency domain code than using a time domain code.

⁴³ A small Gaussian bunch contains high frequencies which can excite HOMs at high frequencies. A long time domain signal is therefore required to discern those high frequencies in the Fourier transform.

2.3.2.3 Available software

2.3.2.3.1 2D: ABCI

ABCI stands for Azimuthal Beam Cavity Interaction [11]. It is one of the best 2D axis-symmetric codes for wakefields calculation. It can compute wake fields generated by a bunched beam passing through an axis-symmetric structure on or off axis. The input file defines the geometry, the beam parameters and the desired simulation results (see references). Then the code calculates the wake potentials, wake loss factor, coupling impedances, frequency spectrums, etc (Fig. 2.46 and Fig. 2.47).

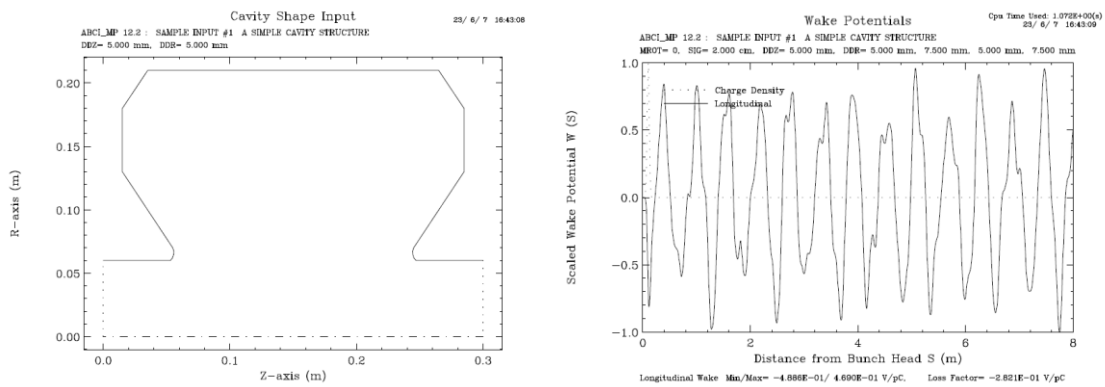


Fig. 2.46 Cavity designed in ABCI (left) and wake potential up to 8 meters (right)

Although ABCI does not have a user friendly frontend, it is very powerful and easy to use. The input parameters and the geometry are defined in a text file and the output results are given in a text file and plots in TopDrawer format (easy to convert to PostScript and PDF).

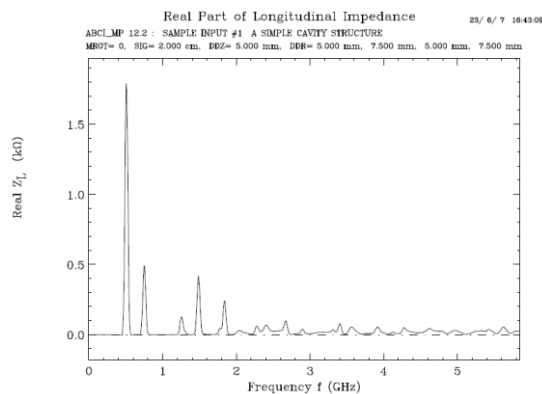


Fig. 2.47 Longitudinal impedance of cavity design

One of the main advantages of ABCI is the speed of simulation. Most of the structures can be simulated with moderate precision in a couple of minutes using modern computers. However, it is not possible to define wave ports in the software, and therefore, the code cannot calculate the loaded wakefields or voltages in coaxial ports.

2.3.2.3.2 3D: CST Particle Studio

Wakefields can be calculated using 3D time domain codes, which is mandatory if the device is not axi-symmetric. CST Particle Studio is a good and user friendly 3D time domain code for this purpose (Fig. 2.48).

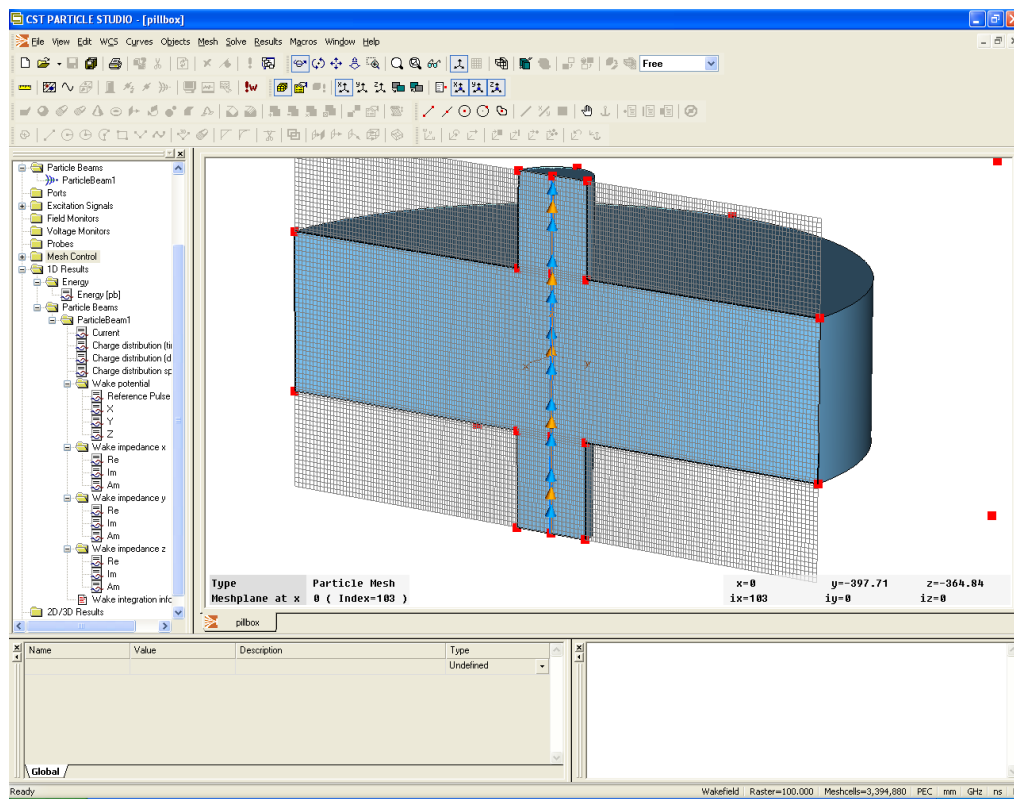


Fig. 2.48 CST Particle Studio interface

It uses the Finite Difference method to numerically solve the Maxwell's equations in time domain. Then it automatically calculates the most important parameters for a structure (wake potentials, longitudinal and transverse impedances, loss factor, etc). The solver allows using wave ports in the simulation to absorb the energy lost by the beam and therefore it is easy to obtain the signals and power in coaxial connections of the structure (Fig. 2.49).

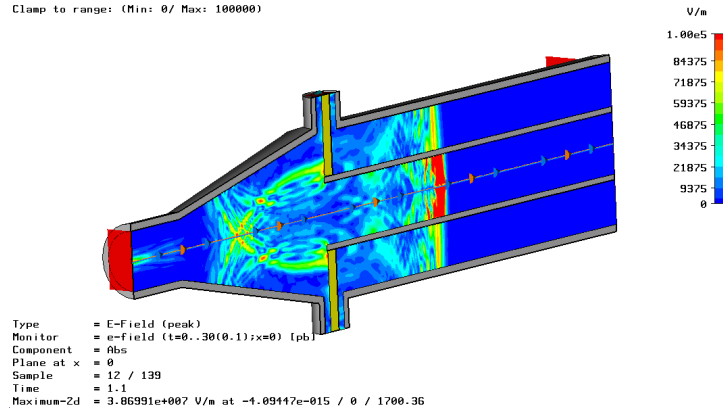


Fig. 2.49 Electric field plot of the wakefield of a bunch in a strip-line kicker

The beam is defined as a Gaussian bunch of charge q and length σ_z , travelling at a velocity v . The integration of the fields for the wakefields calculation can be executed in the axis or in a trajectory shifted from it. Other codes also exist for this task, like GDFidl [19].

2.3.3 APPLICATION EXAMPLE: PILLBOX CAVITY

The exposed procedure to develop 2D and 3D calculations in frequency and time domain is not easy to understand at a first glance. Although two prototypes will be developed in the following chapters, they are complex devices and an easier application is recommended for a better understanding of the procedure. Following example will show how to apply all the previous concepts to a simple device: an accelerating cavity with ideal pillbox shape. A pillbox is a cylindrical cavity attached to the beam pipe in the axis (Fig. 2.50). In a pillbox, the electric and magnetic fields resonate at a fixed frequency in a way that there is an alternating AC field in the aperture to accelerate the particles which pass through. A brilliant analytical study of the pillbox cavity basics can be found in [20].

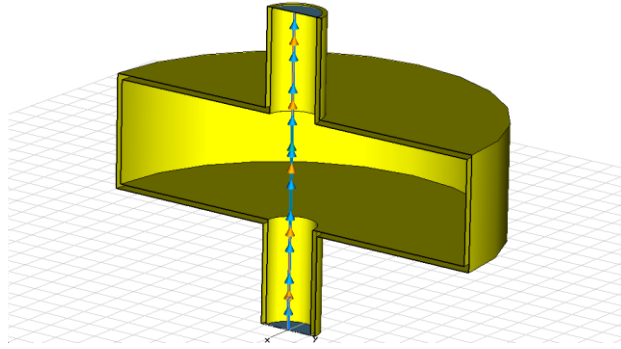


Fig. 2.50 Pillbox cavity

The pillbox is not a transmission line, so the main working mode is not a TEM mode but a resonating mode (TM_{01}). Here only the common aspects with the strip-line kicker will be studied and, therefore, no detailed calculations for the working system of a cavity will be shown. However, HOMs can also exist and disturb the beam like in the strip-line kicker. Wakefield analysis is also very similar and it will be included in the analysis.

The studied pillbox is a 0.383 m inner radius, 0.2 m high copper hollow cylinder. The main resonating frequency valid for acceleration (TM_{01} mode) can be analytically or numerically calculated, and it is about 299.5 MHz [21]. Q factor of this mode is about 34300 and skin depth is about 3.82×10^{-6} m. Using these data, the R , L and C of an equivalent resonant circuit can be calculated for this resonating mode and the behaviour of the cavity at the resonating frequency is therefore totally defined. In HFSS, the resonating mode can be found by means of eigenmode solver or by feeding the resistive cavity by a magnetic loop and analyzing S -parameters (Fig. 2.51).

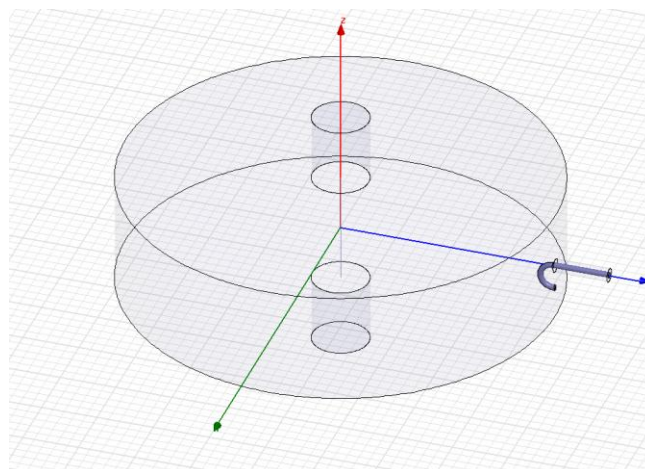


Fig. 2.51 Pillbox fed by a magnetic loop in HFSS

Massive power dissipation in the resistive walls of the pillbox appears when the reflection parameter S_{11} decreases abruptly (Fig. 2.52). This indicates the existence of a resonating mode at this frequency⁴⁴.

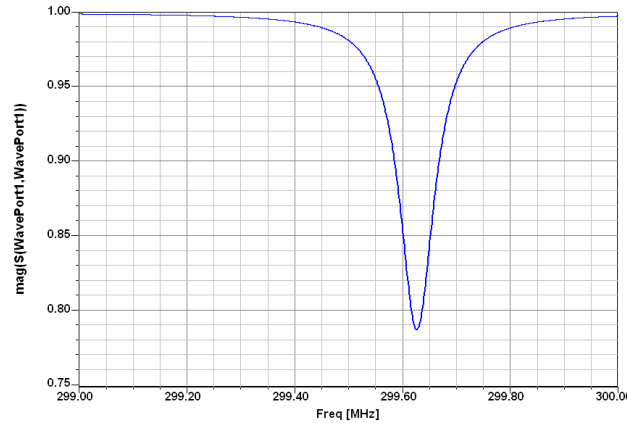


Fig. 2.52 S_{11} parameter near the resonating frequency of a resistive pillbox

It is also possible to detect the resonance using lossless materials by adding other loop and looking at S_{12} . The transmission increases abruptly in the resonance due to the better coupling of high fields between magnetic loops.

The beam pipe attached to the pillbox negligibly affects the resonating mode as the cut-off frequency is much higher than resonating frequency of TM_{01} and no power propagates through the beam pipe.

To calculate possible HOMs other than the working frequency, the simulation of first 30 resonating modes has been effectuated using the eigenmodes solver in HFSS on the copper pillbox model (Fig. 2.53). The main TM_{01} mode appears at first (slightly shifted due to numerical error) and then several modes appear, which are quite similar in frequency and Q between them. These almost identical modes represent the same resonance but in the different possible geometrical orientations inside the pillbox⁴⁵. Therefore, they physically represent the same resonating mode.

⁴⁴ The increase of stored energy implies increased power losses in the walls.

⁴⁵ Due to the cylindrical symmetry, the resonance can rotate 90, 45 ... degrees also fulfilling the Maxwell's equations.

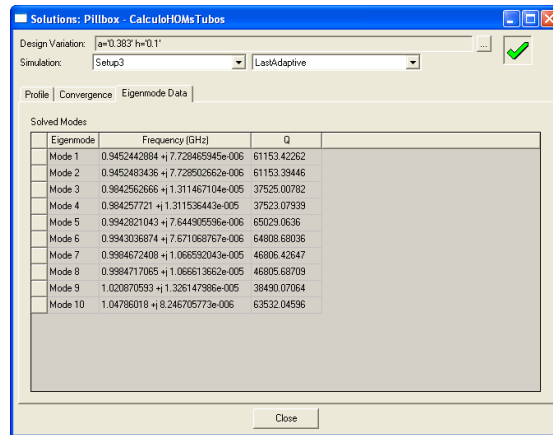
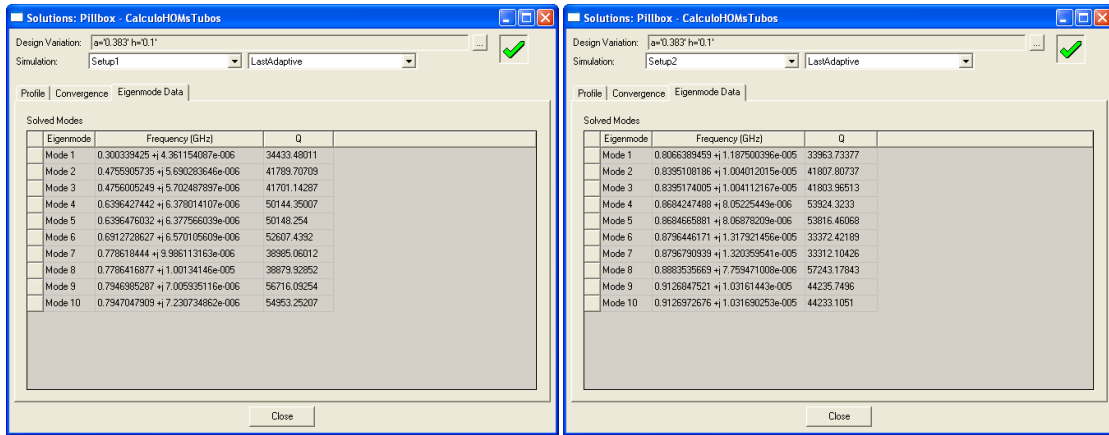


Fig. 2.53 Eigenmodes simulation for a copper pillbox in HFSS

Not all the modes in Fig. 2.53 can be excited by the beam, and therefore are not dangerous. To discern these modes, a coaxial wire simulation or a time domain simulation is required. The time domain simulation will be presented before.

The pillbox dimensions have been used as input geometry for ABCI code. The pillbox is axi-symmetric, and therefore the simulation in ABCI is exact. The command file for ABCI is:

```
&FILE LSAV=.F., ITEST=0, LREC=.F. &END
PILLBOX 299.6 MHZ
&BOUN IZL=3, IZR=3 &END
&MESH DDR=0.005, DDZ=0.005 &END
#CAVITYSHAPE
0.0
0.000 0.000
0.050 0.000
```

```

0.050 0.120
0.383 0.120
0.383 0.320
0.050 0.320
0.050 0.440
0.000 0.440
0.000 0.000
9999. 9999.

&BEAM SIG=0.050, MROT=0, NBUNCH=1, BSEP=0 &END
&TIME MT=10, NSHOT=5 &END
&WAKE &END
&PLOT LCAVIN=.T., LCAVUS=.T., LPATH=.T., LPLW=.T. &END
&PRIN LSVW=.T., LSVF=.T. &END
CONTINUE
&BEAM MROT=1 &END
&PLOT LCAVIN=.F., LCAVUS=.F., LPLW=.T. &END
CONTINUE
&BEAM MROT=0 &END
&WAKE UBT=8.00 &END
&PLOT LCAVIN=.F., LCAVUS=.F., LPLW=.T., LFFT=.T., LSPEC=.T., LINTZ=.T. &END
CONTINUE
&BEAM NBUNCH=8, BSEP=0.4 &END
&WAKE UBT=16.00 &END
&PLOT LCAVIN=.F., LCAVUS=.F., LPLW=.T., LFFT=.F., LSPEC=.F., LINTZ=.F. &END
STOP

```

The geometry generated by these commands can be seen in Fig. 2.54.

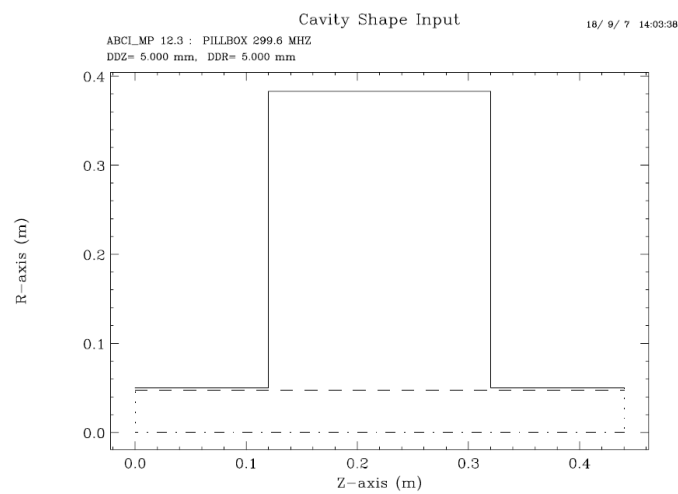


Fig. 2.54 ABCL geometry for the pillbox

The longitudinal dimension of the bunch used for the simulation is Gaussian $\sigma_z=50$ mm, the charge is normalised to 1 pC and the bunch travels at the speed of light. The first simulation shows the short range longitudinal wake potentials and the charge density of the bunch in the same plot (Fig. 2.55).

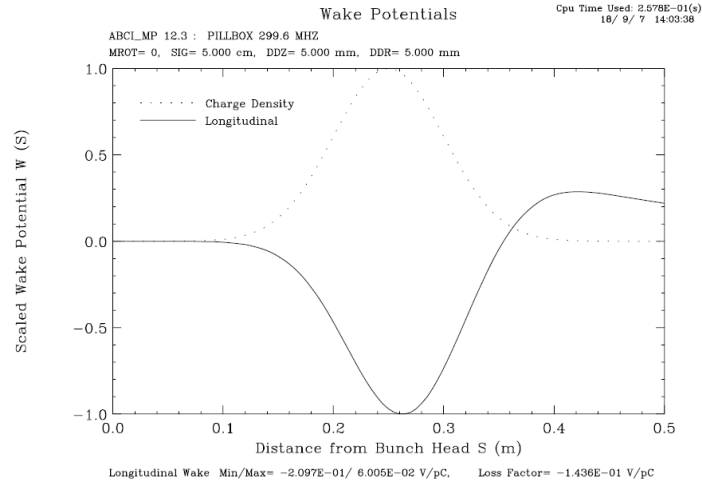


Fig. 2.55 Wake potential and loss factor in pillbox short simulation in ABCI

The results of Fig. 2.55 are given in Volts per picoCoulomb and the plot is scaled to the maximum and minimum values indicated below the plot. The loss factor is -1.436×10^{-1} V/pC, which means that every particle (on average) in the bunch is losing 0.1436 V per picoCoulomb when passing through the pillbox due to wakefields. For example, a bunch of $\sigma=50$ mm and $q=240$ nC will lose $0.1436 \times 240000 = 34464$ eV of average energy per particle when passing through the pillbox.

The concept of wake potential is easily observed in Fig. 2.55. Given a charge which moves at 0.263 m of distance from the bunch head, the integrated voltage that it will experience passing through the pillbox is -0.2097 Volts due to the wakefields created by the whole bunch.

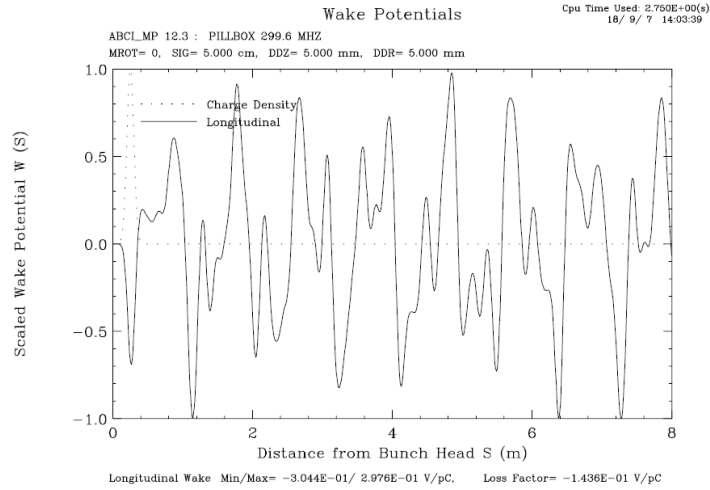


Fig. 2.56 Longitudinal wake potential for the pillbox long simulation in ABCI

The calculation of the wake potentials has been extended up to 8 meters in ABCI (Fig. 2.56) to accurately calculate the Fourier transform and therefore, the longitudinal impedance (Fig. 2.57).

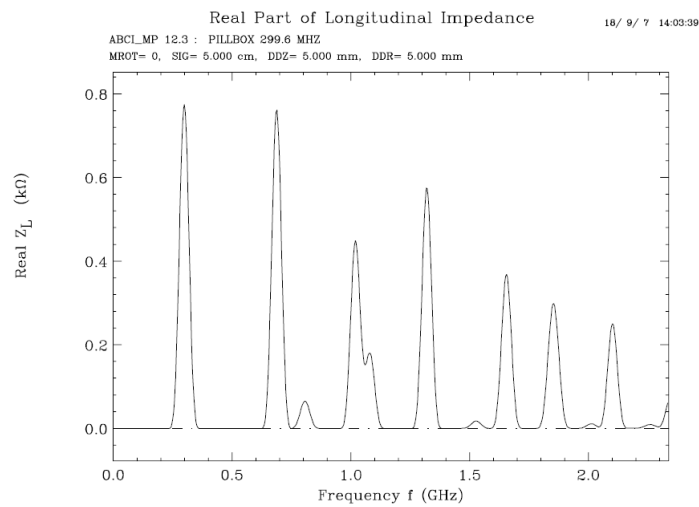


Fig. 2.57 Longitudinal wake impedance of a pillbox in ABCI

The HOMs that can be excited by the beam are presented in Fig. 2.57. There are several frequencies that have HOMs coupled to the beam. The main resonating mode (about 300 MHz) also appears because its geometry presents a strong coupling with the beam. The modes indicated in Tab. 2.2⁴⁶ can be easily identified with some of the HFSS calculated modes.

⁴⁶ The plot data of the wakes and impedances is stored by ABCI in a .pot file.

Tab. 2.2 ABCI calculated resonances from longitudinal impedance data

Frequency (MHz)	Impedance (Ω)
299.67	774.4
689.24	761.3
809.11	64.9
1018.9	449.2
1078.8	180.5
1318.5	574.7

If the pillbox is installed in a steady state ring, almost all the modes represented in Tab. 2.2 (apart from the first) could be dangerous for the beam because they represent high impedance and Q factor. Once identified, the field geometry has to be checked in HFSS to see if any of them has the maximum electric or magnetic field in the axis of the pillbox near to the beam location. If that happens, damping will be required for that mode. The damping device can also be located and optimized through HFSS simulations, trying to reduce the Q factor of the mode.

The pillbox is an axi-symmetrical device and therefore ABCI is the best suited code for its simulation. However, in order to show and compare, CST Particle studio will also be used to simulate the pillbox. Same beam parameters have been used.

The model is very intuitive to draw and simulate in CST Particle Studio. A long time (space) has been calculated to get good Fourier transforms of the wake potentials.

Short wake potential plot (Fig. 2.58) is almost identical to ABCI's plot (in a different scale)⁴⁷ and the wake loss factor is -0.1433 V/pC, also identical to ABCI's calculated value.

⁴⁷ CST begins the simulation with the centre of the bunch in $t=0$. That is why the plots begin a bit earlier than in ABCI (at $s \approx -5 \cdot \sigma$).

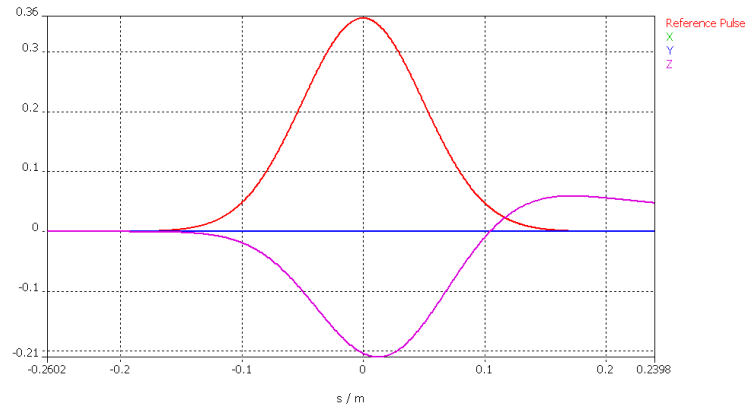


Fig. 2.58 Show longitudinal wake potential for the pillbox in CST Particle Studio

The long range wake potential (Fig. 2.59) is exactly the same as in ABCI.

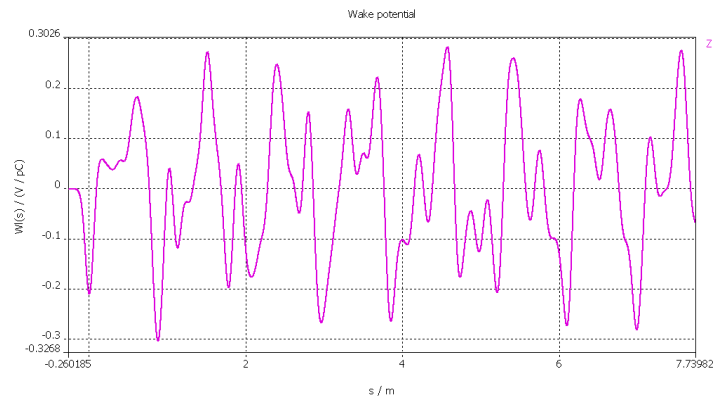


Fig. 2.59 Long range longitudinal wake potential for the pillbox in CST Particle Studio

The longitudinal impedance also presents the same peaks as ABCI (Fig. 2.60).

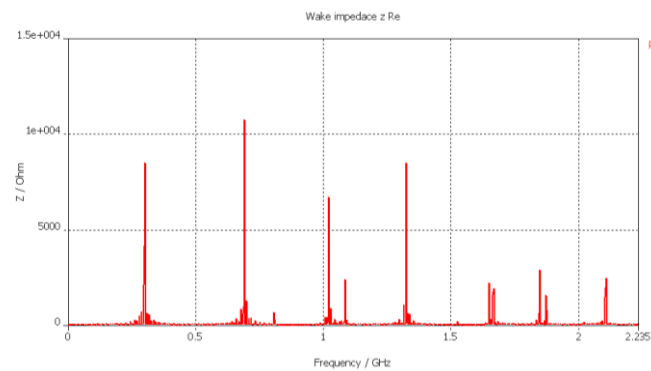


Fig. 2.60 Longitudinal impedance of a pillbox in CST Particle Studio

Calculation time of 3D model is much slower as for the 2D model, and the results are exactly the same for axi-symmetrical devices. However, the time to set up the simulation is much lower for the 3D code because of its user friendly interface, and post-processing plots and animations can be rapidly represented (Fig. 2.61).

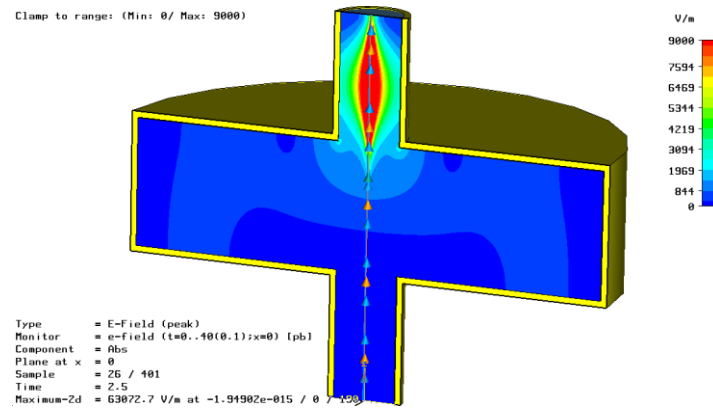


Fig. 2.61 Electric field of a bunch exiting the pillbox (CST Particle Studio)

The coaxial wire method can also be applied to find the possible resonances induced by the beam. The pillbox model has been modified to include a thin wire in the axis and quarter symmetry has been used (Fig. 2.62). The defined boundary conditions in the cut planes are a magnetic field perpendicular to them. Two ports have been added in the coaxial line formed by the beam pipe with the wire (named 4 and 5).

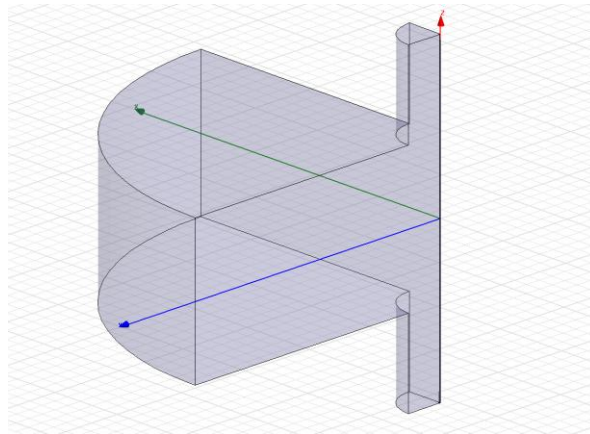


Fig. 2.62 Quarter pillbox for coaxial wire simulation

There is no need to make the calculation of Eq. (2.61) if the only purpose is to find the resonant frequencies. Obviously, the peaks of S_{45} magnitude in a frequency sweep are identical to the result of Eq. (2.61). The result of a frequency sweep of S_{45} between 300 MHz and 1.5 GHz is shown in Fig. 2.63.

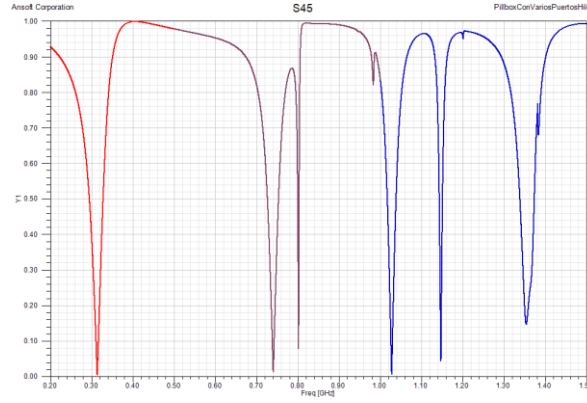


Fig. 2.63 Frequency sweep of S_{45} in the coaxial wire method for pillbox

Fig. 2.64 shows the longitudinal impedance calculated by means of Eq. (2.61).

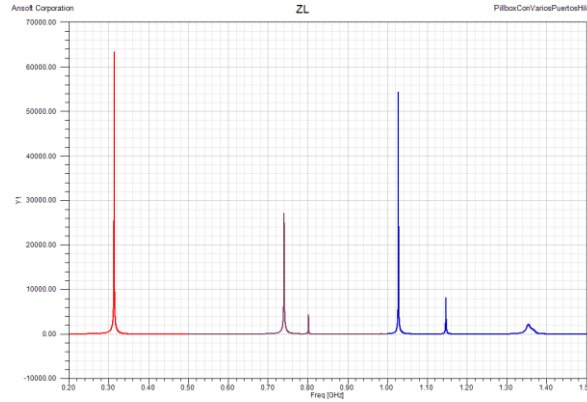


Fig. 2.64 Longitudinal impedance in a pillbox calculated via the coaxial wire method

The frequency of the peaks is quite similar to the values presented in Tab. 2.2. Some of the peaks are a little shifted due to the strong distortion that the wire introduces in the resonance. The amplitude given by Eq. (2.61) is only valid when the impedance of the device can be considered as a "lumped" impedance⁴⁸ (see section 7.5.1 in [22]). However, it has been demonstrated in the previous analysis that any of the indicated methods are valid for HOMs and wakefields calculations.

⁴⁸ This happens when the physical length of the device is equal or smaller than the beam pipe diameter.

2.4 CONCLUSIONS

The full electromagnetic design of a strip-line kicker is not an easy task. Many aspects have to be considered and a deep knowledge of the theory is required to make a good design.

The basic specifications to start the design of a strip-line kicker are the transverse voltage or deflection angle, the minimum stay clear aperture, the pulse shape (rise and fall times, flat top duration) and possibly the maximum allowable length of the device or other specific conditions. All those initial specifications have to be integrated in the analytical calculations to obtain the early estimations for the voltage, current, power and the approximate relation between electrodes length and transverse voltage. The author has extended those calculations on existing [5] RF equations for pulse excitation calculations.

The definition of the cross section shape (electrodes and main tube) has to be chosen regarding homogeneity, wakefield behaviour and efficiency considerations. The optimization of the initially estimated shape is carried using a 2D FEM code, taking the characteristic impedance and the homogeneity as the optimization parameters. The first estimation of the wakefield behaviour is then obtained by using a 2D axis-symmetric code.

Once the main parameters have been defined and the estimations of the main kicker parameters are obtained, a full 3D analysis of the device is required, which can be clearly separated in terms of frequency and time domain simulations.

The frequency domain simulations are useful to fine tune most of the strip-line kicker dimensions. Several considerations are necessary to define the 3D model in frequency domain and to obtain results compatible with a pulse excitation. The radiofrequency transmission S-parameters can be used to improve the coaxial to strip-line transition and to calculate power losses. The author has contributed in this point with a highly optimized transition by tapering both the electrodes and the vacuum chamber at a time, which greatly improves the RF matching while reduces wakefield problems.

The full field solution of the 3D code is necessary to obtain the 3D homogeneity and cross checking the analytical figures. Regarding this issue, the author has contributed with some scripts in HFSS including the transverse shunt impedance calculation together with the transit time factor.

Finally, the frequency domain code is also useful to calculate the possibly trapped HOMs and impedances through the coaxial wire method. Those parameters are helpful for devices installed in multi-turn rings or even for calculating wake potentials through the inverse Fourier transform. However, the coaxial wire method cannot precisely obtain the exact frequencies of the modes.

Time domain simulations in the 3D structure are mainly used for wakefields calculations. This analysis is carried out only in the final design process due to the extreme computer requirements of the simulation. The 3D time domain codes can provide a precise behaviour of a full device when the beam passes through it and cross-check the previously axi-symmetric calculated values. The beam coupling impedances can be directly obtained without frequency shifts.

The last section of this chapter presents the HOMs and wakefields calculations in a simple device: a pillbox. This easy application of the presented method allows for a better understanding of the most complex design step for any device in series with the beam.

2.5 REFERENCES

- [1] *Introduction to transverse beam optics*. **Holzer, Bernhard**. Zakopane : Cern Accelerator School, 2006.
- [2] **Palumbo, L., Vaccaro, V. G. and Zobov, M.** *Wake Fields and Impedance*. Frascati (Italy) : SIS - Pubblicazioni, INFN, 1994.

- [3] **Wilson, P. B.** *Introduction to wakefields and wake potentials*. Stanford (California) : SLAC, 1989.
- [4] **Boussard, D.** *Beam Loading*. s.l. : Proceedings of CERN Accel. School, CERN 87-03.
- [5] **Goldberg, D.A. and Lambertson, G.R.** *Dynamic Devices, a Primer on Pickups and Kickers*. Lawrence Berkeley Laboratory California : American Institute of Physics, 1992.
- [6] **Pozar, David M.** *Microwave Engineering*. s.l. : Wiley, 2004. 978-0471448785.
- [7] *Conventional Magnets for Accelerators*. **Marks, Neil**. Zakopane (Poland) : CERN Accelerator School, 2006.
- [8] **Weiland, T.** A discretization method for the solution of Maxwell's equations for six-component fields. s.l. : Electronics and Communication, 1977. Vol. 31, pp. 116-120.
- [9] —. TBCI and URMEL - New computer codes for wake field and cavity mode calculations. s.l. : IEEE Transactions on Nuclear Science, 1983. Vols. NS-30, 4.
- [10] —. Time domain electromagnetic field computation with finite difference methods. s.l. : International Journal of Numerical Modelling, 1996. Vol. 9, pp. 295-319.
- [11] **Chin, Yong Ho.** *User's Guide for ABCI*. s.l. : KEK Report 2005-06.
- [12] **Sands, M. and Rees, J.** *A bench measurement of the energy loss of a stored beam to a cavity*. California : Stanford Linear Accelerator Center, 1974.
- [13] **Hewlett-Packard Company.** S-parameter techniques. *Test and Measurement Application Note 95-1*. California : Hewlett-Packard Company, 1997.
- [14] **Kuphaldt, Tony R.** Lessons In Electric Circuits. [Online] 2003. http://www.faqs.org/docs/electric/AC/AC_14.html.

- [15] **Ansoft Corporation.** HFSS release 11 online help. *Technical notes*. 2007.
- [16] **Whittum, David H.** Introduction to Electrodynamics for Microwave Linear Accelerators. California : Stanford Linear Accelerator Center, 1998.
- [17] **Marcellini, F., et al.** Beam coupling impedance measurements of the DAΦNE vacuum chamber components. Frascati (Italy) : LNF-INFN.
- [18] **Ansoft Corporation.** ANSOFT HFSS Fields Calculator Cookbook. 2000.
- [19] **Bruns, W.** The GdfidL Electromagnetic Field simulator. <http://www.gdfidl.de>.
- [20] **Feynman, Richard P., Leighton, Robert B. y Sands, Matthew.** *The Feynman Lectures on Physics, Vol.2, mainly electromagnetism and matter*. Pasadena : Addison-Wesley Publishing Company, INC, 1964. 978-0201021158.
- [21] **Caspers, F. and Kroyer, T.** JUAS RF Course. Archamps (France) : s.n., 2006.
- [22] **Wu Chao, Alexander and Tigner, Maury.** *Accelerator Physics and Engineering*. Singapore : World Scientific, 1998. ISBN 9810235003.

CHAPTER 3

FABRICATION PROCEDURES AND TESTS FOR STRIP-LINE KICKERS

3.1 INTRODUCTION

The main geometry of the strip-line kicker is now well defined after passing through the calculation methodology presented in chapter 2. Feedthroughs main characteristics, electrodes shape, beam pipe diameter, etc. have already been obtained from analytical and numerical calculations. The next step to achieve is the successful manufacturing and testing of a first prototype. Even when most important components (Fig. 3.1) are already dimensioned in the calculations, the design process is not trivial and it is very necessary to develop a detailed fabrication procedure for the strip-line kicker. The details to fix the electrodes, weld the feedthroughs and attach the supports are very specific for a given model and have to be well defined in order to successfully assemble the device. Some guidelines are presented in this chapter.

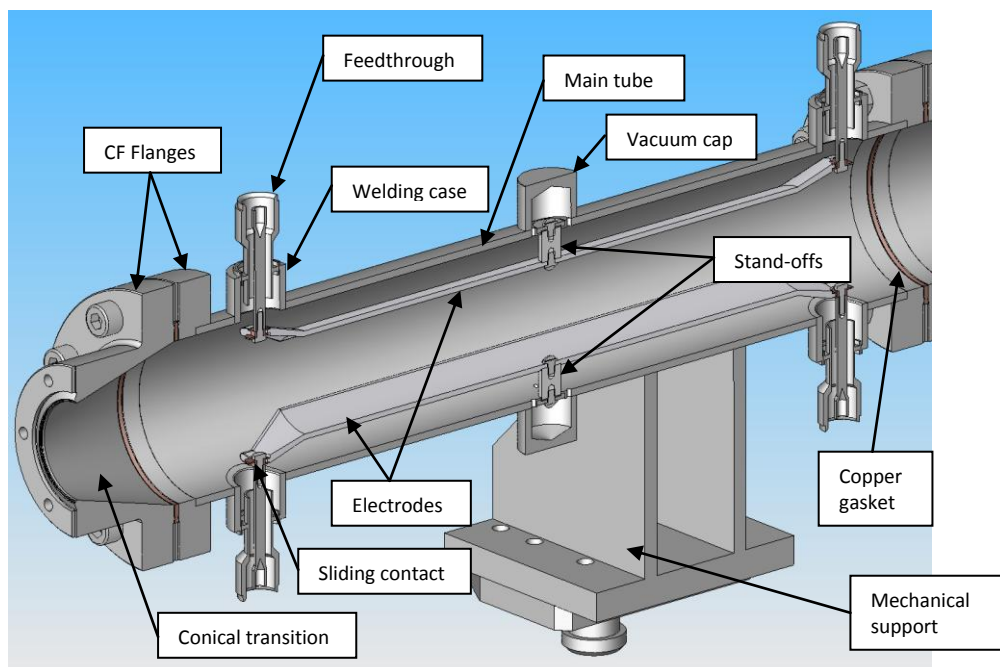


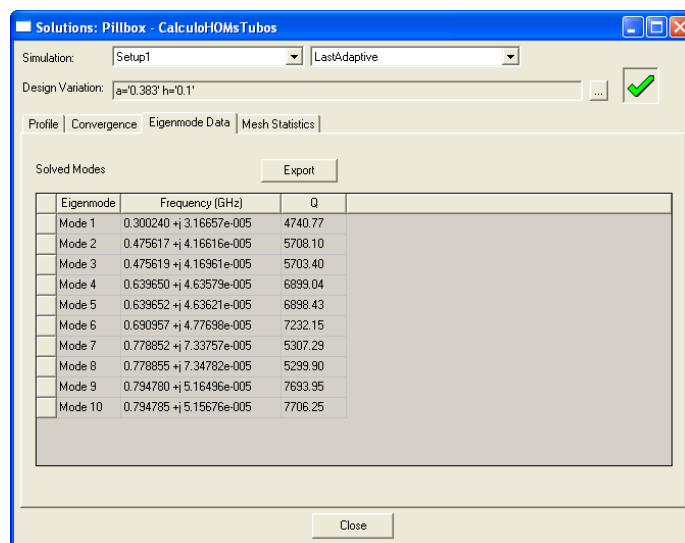
Fig. 3.1 Cut view of a strip-line kicker model showing the main components

3.2 DESIGN

3.2.1 MATERIAL CHOICE

Most of the electromagnetic calculations described in chapter 2 do not require resistive materials in the simulations unless high precision solution is necessary. Strip-line kickers operate as transmission lines; therefore, the resistive materials in the electromagnetic behaviour of the TEM transmission mode are a second order effect that can be neglected most of the times. However, the material selection is very important for the manufacturing of the strip-line kicker because all the manufacturing procedures depend on it. In addition, sometimes there are some restrictions regarding materials depending on the accelerator where the kicker is installed. The material selection can be done following the subsequent aspects:

- Electromagnetic considerations: The resonance of HOMs in the kicker has to be avoided in general terms. Materials with lower conductivity do not allow for a high Q factor when a frequency matches the geometrical resonating HOM. Therefore, stainless steel can sometimes be better suited than copper or aluminium, for example. Fig. 3.2 shows the first HOMs calculated for a pillbox identical to the one in chapter 2 (Fig. 2.53), but made of stainless-steel. The resonant frequencies are exactly the same but the quality factor is much lower.



Eigenmode	Frequency (GHz)	Q
Mode 1	0.300240 +j 3.16657e-005	4740.77
Mode 2	0.475617 +j 4.16616e-005	5708.10
Mode 3	0.475619 +j 4.16961e-005	5703.40
Mode 4	0.639650 +j 4.63579e-005	6899.04
Mode 5	0.639652 +j 4.63621e-005	6898.43
Mode 6	0.690957 +j 4.77698e-005	7232.15
Mode 7	0.778852 +j 7.33757e-005	5307.29
Mode 8	0.778855 +j 7.34782e-005	5293.90
Mode 9	0.794780 +j 5.16496e-005	7693.95
Mode 10	0.794785 +j 5.15676e-005	7706.25

Fig. 3.2 First HOMs calculated for the stainless-steel pillbox

- Beam related considerations: The strip-line kicker is a device installed in series with the beam pipe. In some accelerators, materials like stainless steel are not valid for elements in the proximities of the beam because they can remain activated a long time if the beam strikes against their surface [1]. This restriction has to be indicated by the safety radiation team in charge of the accelerator.
- Mechanical considerations: Strip-line kickers are slender devices, particularly the electrodes. Consequently, the stiffness of the materials is particularly important to avoid large widths and weights. A long electrode made of aluminium should be thicker than the same electrode made of stainless-steel to avoid deformations due to its own weight.
- Manufacturing considerations: Sometimes it is necessary to use complex manufacturing methods for some parts of the kicker (Computer Numeric Control, CNC). Small roughness CNC requires plenty of time to machine the components. Soft materials as aluminium (but not copper) are easier to machine than harder materials. In addition, the fixation of the feedthroughs to the kicker tube forces the same material for both parts because homogeneous welding is always possible and easier than dissimilar materials one.
- Vacuum considerations: Strip line kickers are integrated in the accelerator beam pipe and therefore they require the same vacuum specifications. Not all the materials are valid for ultra high vacuum conditions ($< 10^{-8}$ mbar). Therefore it is important to check the specifications with the vacuum designer before selecting some materials. Aluminium, copper, stainless-steel and some ceramics are valid materials, although they usually have to feature very high quality grades¹.

¹ Stainless-steel of grade LN (316LN) is usually required for ultra high vacuum applications. 316LN has nitrogen added as a strengthening agent, increasing overall hardness and strength. It retains the hardness at elevated temperatures, especially after repeated bake-outs (see section 3.3.6), or high temperature system degassing procedures (firing).

3.2.2 ELECTRICAL CONNECTIONS: FEEDTHROUGHS

The feedthroughs are devices which transfer power from the ambient conditions to a container in a controlled atmosphere (different pressure or temperature). The strip-kicker requires ultra high vacuum inside and therefore the high voltage power should go in and out by means of coaxial feedthroughs.

High vacuum feedthroughs are devices very difficult to manufacture because they require good electrical insulation together with vacuum tightness. This is achieved by brazing² the metallic inner pin to the ceramic insulator, and this process is very delicate and requires a special brazing furnace. Therefore, it is always preferred to select a commercial feedthrough if possible (Fig. 3.3). Some companies manufacturing these devices are Ceramaseal [2], Fischer [3], Trinos [4], etc.

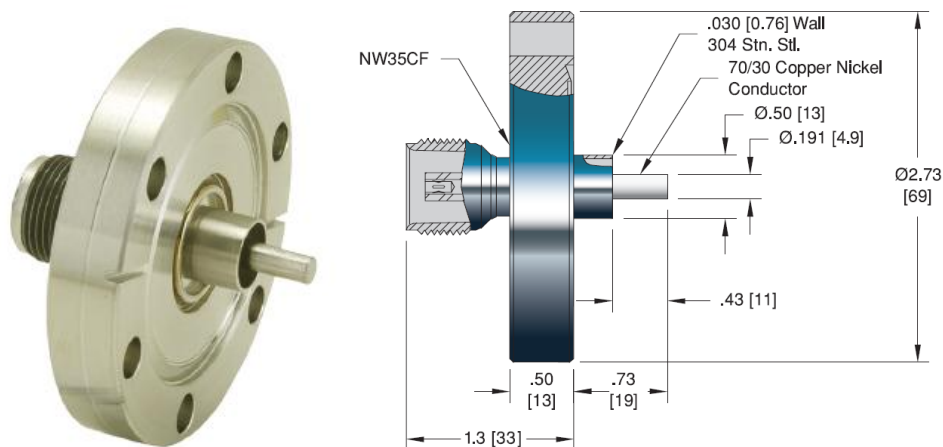


Fig. 3.3 HN-type commercial [2] feedthrough of 50 Ohm characteristic impedance (flange assembly)

The coaxial feedthroughs for a strip-line kicker must be designed for RF transmission. This means that they should feature constant characteristic impedance, and it should be obviously in accordance with the characteristic impedance designed for the kicker (usually 50 Ohm). This feature is not easy to find in high voltage, high power commercial feedthroughs. Going over 7 kV at 50 Ohm usually requires custom made feedthroughs.

² Brazing is a joining process whereby a filler metal or alloy is heated to melting temperature above 450 °C and distributed between two or more close-fitting parts by capillary action. At its liquid temperature, the molten filler metal and flux interacts with a thin layer of the base metal, cooling to form a strong, sealed joint.

However, the impedance mismatch of a variable impedance feedthrough does not usually represent a big concern for normal pulsed kickers³. The feedthrough only constitutes a small portion of the matched transmission line and the reflection scattering parameters do not deteriorate so much when a variable impedance feedthrough is installed.

Coaxial feedthroughs feature various types of “air side” connectors. High voltage, high power 50 Ohm feedthroughs usually use HN connectors while variable impedance feedthroughs typically use SHV (Fig. 3.4).

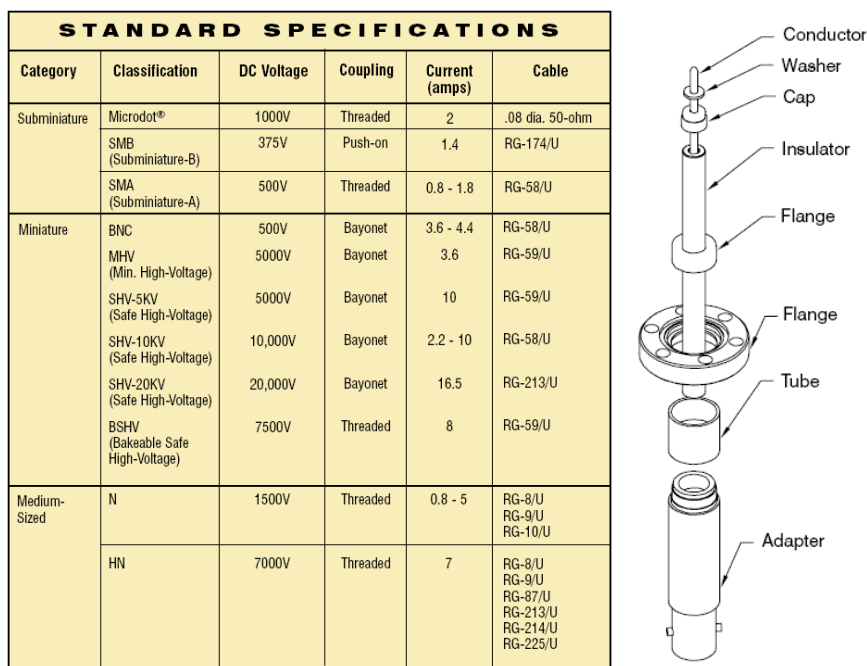


Fig. 3.4 Different connectors from Ceramaseal [2] (left) and typical feedthrough schematic (right)

Table of Fig. 3.4 shows the maximum current for each feedthrough. This figure is usually quite low. However it is referred to peak current in a constant radio frequency wave. Nevertheless, the pulsed strip-line kickers do not operate with a RF wave but with a pulse at a given repetition rate. Therefore, if the repetition rate of the fast pulse is not very high, the indicated feedthroughs can be used without problems in higher instantaneous power applications.

³ The kickers that are not extremely fast (rise time and/or fall times longer than 10 ns).

The approximate calculation is quite simple. For example, let us take an HN feedthrough which can stand continuously with 7 kV DC and 7 Amperes. For 50 Ohm load and a pulse of 7 kV flat-top, $7000/50 = 140$ A peak will pass through the feedthrough and the electrodes. The current is much higher than 7 A, however it should be averaged with the pulse length and repetition rate. If the pulse is 100 ns flat-top and it repeats every 20ms (50 Hz repetition rate), the averaged current is $140 \times 100 \times 10^{-9} / 20 \times 10^{-3} = 7 \times 10^{-4}$ A, much lower than 7 A. However this calculation is only an approximation as a very high short duration current can instantaneously melt the feedthrough pin due to the instantaneous flowing energy (like the i^2t energy criterion for the domestic fuses). Therefore, it is always recommended to check with the manufacturer for the validity of a feedthrough at a specific pulse voltage, current and repetition rate.

Regarding the feedthrough external structure, it is also necessary to select a fixation method to the kicker main tube. The feedthrough shown in Fig. 3.3 has an integrated small flange, which allows installing it by using simple CONFLAT flanges welded to the kicker tube. This is very useful if the device needs to be dismountable. However, sometimes a feedthrough directly welded to the kicker tube is desirable (Fig. 3.5), for example, when the space is a concern. In that case, the feedthrough is much smaller than when using flanges and this allows longitudinal space saving in the device.

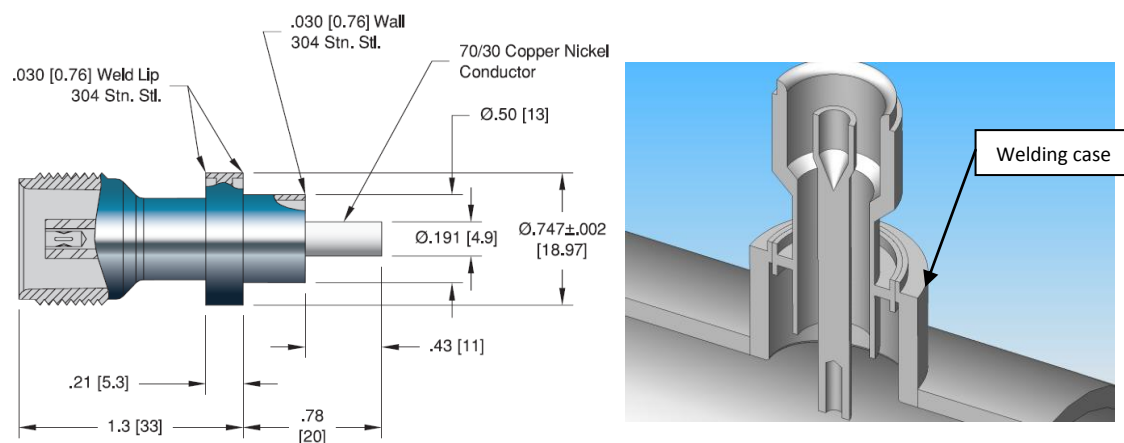


Fig. 3.5 HN Ceramaseal [2] feedthrough for welding installation (left) and cut 3D model of a feedthrough assembled in a tube using a welding case (right)

If a welded feedthrough is required (or preferred), it can be welded to a hole drilled on the kicker tube. The feedthrough weld lip (Fig. 3.5 left) is usually much thinner than the kicker tube. The difference of thicknesses makes the welding quite difficult as the heat required for melting the thick zone is too high for the thin zone. It is possible to avoid this concern by manufacturing a welding case (Fig. 3.5 right) for adapting both thicknesses. The revolution case should have a thin lip for welding to the feedthrough and a thick lip for welding to the kicker tube. Its length should be as long as required by the device to connect the feedthrough to the electrode⁴.

As it was presented before, the materials of the kicker tube, feedthrough and case should be compatible for welding (the commercial feedthroughs are almost always made of stainless-steel). In other cases, brazing would be necessary and the joint becomes much more complex.

To finish this section, one of the most complex manufacturing issues is the design of the electrical contact between the feedthrough and the electrode. The current flowing through the electrodes heats them depending on the averaged power of the pulse and the electrode resistivity. Therefore, a small linear expansion of the electrodes is always expected. This makes necessary the use of flexible contacts between the feedthrough and the electrode to avoid breaking the brazed ceramic inside the feedthrough due to excessive radial stress. There are several designs that can cope with this issue:

- Sliding contact: The pin of the feedthrough can be fixed to a sliding assembly which contacts the electrode. The sliding piece can be a small bent metal sheet acting as a spring to ensure contact or a high precision double washer. The electrode must be machined with a small slot to allow for a constant electrical contact when the feedthrough pin slides along it, as shown in Fig. 3.6.

⁴ More details about this method will be given in the following chapters

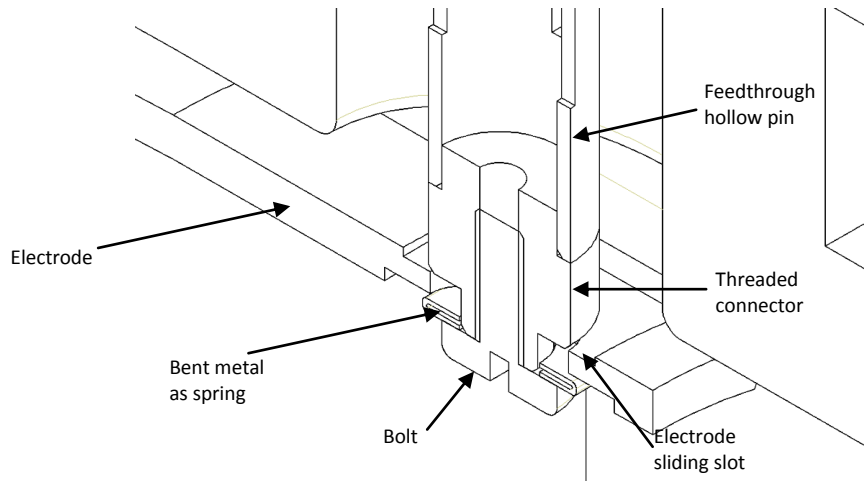


Fig. 3.6 Sliding contact for DAΦNE strip-line kicker [5]

- **Flexible contact:** The feedthrough pin can be connected via a flexible cable to the end of the electrode, which ensures the electrical contact. The cable must be highly flexible to avoid possible breaking when many thermal cycles are applied to the electrode. It must also be as short as possible to maintain the characteristic impedance of the transition.

3.2.3 STAND-OFFS

The mechanical support of the electrodes to the external tube was advanced in chapter 2 for the EM study. The electrodes must be fixed to the kicker tube and electrically insulated from ground potential. This is accomplished by using a rigid, low permittivity electrical insulator valid for high vacuum, like ceramic. Ceramic insulators are commercially available from many manufacturers, usually also specialized in vacuum components as the feedthroughs.

The stand-offs are usually made of a kind of ceramic named Steatite which features interesting thermal and electrical properties. It can be manufactured in almost any shape with accurate dimensions because it is formed by sintering⁵ the ceramic powder in a mould in a furnace. This process permits a screwed hole in the ceramic to allow fixing it by using bolts (Fig. 3.7).

⁵ Sintering is a method for making objects from powder, by heating the material (below its melting point - solid state sintering) until its particles adhere to each other. Sintering is traditionally used for manufacturing ceramic objects, and has also found uses in such fields as powder metallurgy.

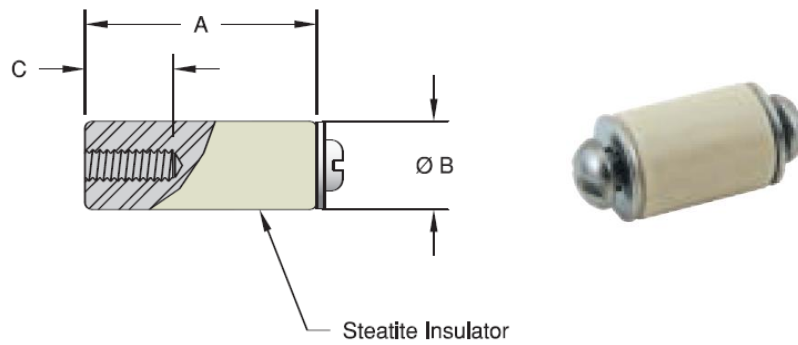


Fig. 3.7 Steatite Stand-off [2]

However, the screwed hole cannot be very precise because it cannot be machined, and the threads are quite fragile. The stand-offs may fix loose to the electrode and the screw fixation torque is very limited. That's the reason why sometimes other methods can be used to fix the stand-offs to the kicker tube and the electrode. It must be taken into account that gluing is not permitted in high vacuum applications. One possible solution developed by the author is to use a metallic interference fit case hooped around the ceramic stand-off (Fig. 3.8). However the process is not easy as the ceramic cannot experience large temperature increments in a short time without being broken. Therefore it is not possible to heat the case several hundred Celsius degrees to fit in the ceramic because it will break the steatite due to the extremely different temperature contact.

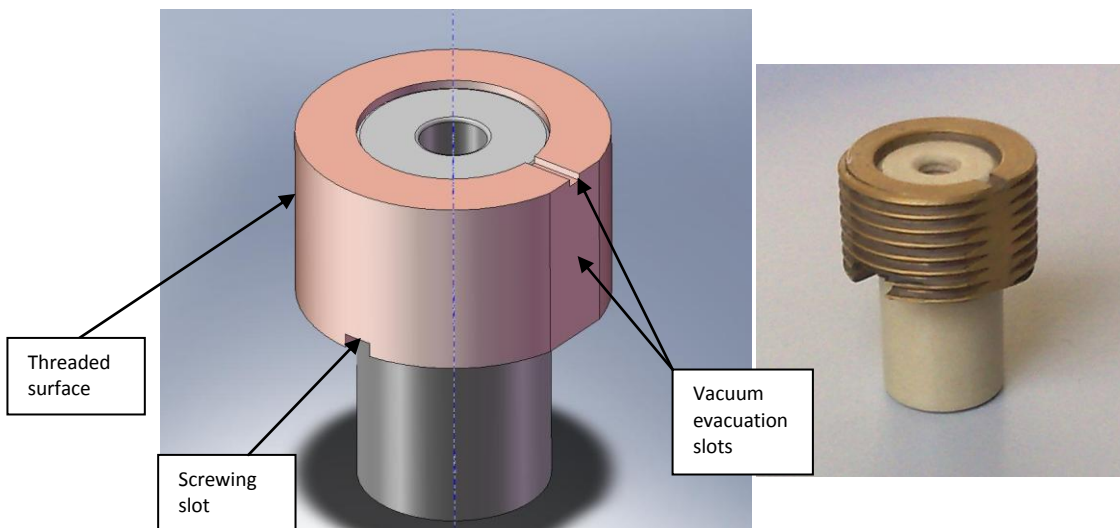


Fig. 3.8 Metallic case fixed to the stand-off (left) and dummy assembly for testing (right)

However, the steatite features a thermal expansion coefficient much lower than metals, especially soft metals as copper or aluminium. Therefore, both elements (the stand-off and the metallic case) can be heated together in an oven to the same temperature and, due to the different thermal expansion coefficients, the metallic case will expand a bit more than the ceramic and will fit correctly. The interference between them has to be carefully calculated to avoid fluency of the metal due to tensile stress or high compressive stress in the steatite⁶. In effect, a stainless-steel case can cause an enormous stress in the ceramic when shrinking only a few microns due to its large elasticity modulus. Consequently, the use of a soft metal like copper is recommended for the case. After the case is fixed to the ceramic, it can be easily screwed to a case or directly welded to the kicker tube (if both materials are weldable).

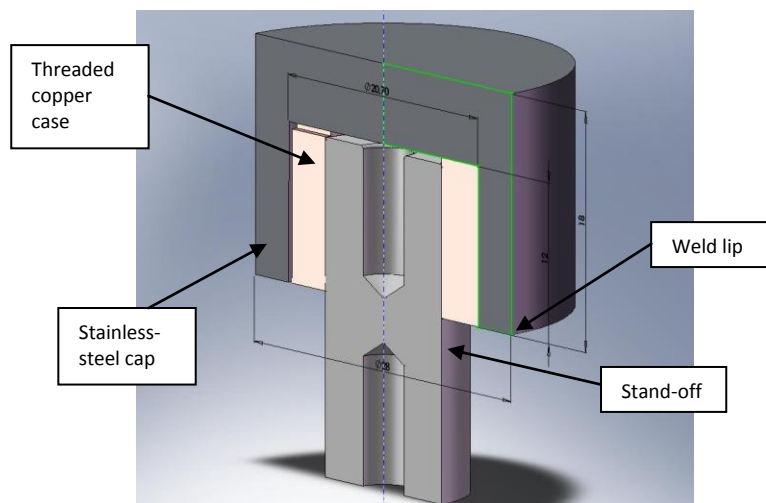


Fig. 3.9 Full assembly for stand-off fixation

When more than one stand-off is required, the fixation must be sliding in the additional stand-offs to allow for thermal enlargement of the electrode (as indicated for the feedthroughs electrical connection). The sliding mechanism can use a spring or a mechanical loose-fitting tolerance (Fig. 3.10) because contact pressure is not required.

⁶ The threaded hole in the steatite represents a concern when an external pressure is applied. Stresses can be dangerous in the inner zone of the hole. A mechanical FEM code is required to calculate the detailed stresses in these zones.

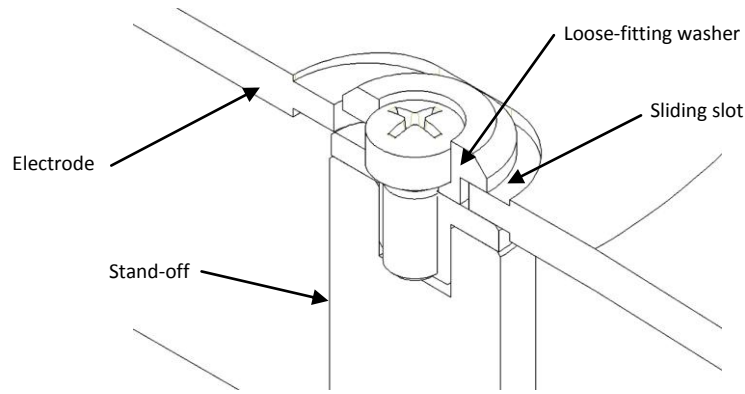


Fig. 3.10 Sliding fixation of a ceramic stand-off in DAΦNE strip-line kicker [5]

3.3 MANUFACTURING

3.3.1 ELECTRODES

The electrodes are the main component of a strip-line kicker. They transport the current of the pulse and their geometry contributes to the deflection strength and characteristic impedance. They are usually very long and slim; therefore mechanical considerations have to be taken into account in the design.

The straight section of the electrodes is determined in the EM design process, as explained in chapter 2. Besides, the transition between the coaxial feedthrough and the strip-line is also designed regarding EM and space considerations. Therefore, the matter in this section is the manufacturing method of the already designed electrode. There are several possibilities when no special transitions are required:

- Flat electrodes: The flat electrodes can be manufactured starting from a metal sheet of the required thickness and larger width. The edges can be bent before cutting to the final dimension, to permit an easy bending in a bending machine. The rounded edges can be easily rounded because no high precision is necessary for this operation. The rounding is only needed to avoid electric field concentration in sharp edges.

- Curved electrodes: A bending tool can be applied over a metal sheet of the required thickness to form the electrode shape (circular, elliptical, etc.). Then it can be cut to the final dimension and the edges can also be rounded.

If tapered transitions are required, the typical best procedure is CNC machining of the whole electrode shape starting from a thick metal bar. CNC requires the machining of the full piece, removing high amounts of material. That is why the choice of a soft material for the electrodes is much better suited for complex geometries that require CNC machining. However, a soft material can bend over its weight, and higher thickness or more supporting stand-offs could be required for long electrodes. In addition, deep machining can cause residual stresses in long metal pieces.

3.3.2 *VACUUM TANK*

The vacuum tank geometry is also determined in the EM design process. It can be manufactured, depending on its shape, as follows:

- Cylindrical tank: The easiest way to manufacture a cylindrical tank is by using a commercial tube of the required inner diameter and several millimetres thickness. However, the dimensions of commercial tubes are very limited and given in discrete steps not usually coincident to the required inner diameter. Therefore it is recommended to choose the inner diameter in the EM design process according to a commercially available dimension, if possible.

If a commercial tube is not available, it can also be manufactured by machining the inner side of a thicker tube. This is only possible if the tube is not very long, because the machining tool can break or have strong vibrations when turning inside a long cylinder.

- Elliptical or racetrack tanks: Tanks featuring shapes other than cylindrical are better manufactured by machining two halves and welding them together. This method allows a much easier assembly of the electrodes, stand-offs and feedthroughs but it requires two long vacuum welds along the tank, which could deform the desired final geometry if they are not carefully done.

All the welds in the vacuum tank must be vacuum tight. The vacuum in an accelerator is very high, usually better than 10^{-8} mbar. Therefore the welds should be carefully made to avoid any leak. It is also required to neutralize the atmosphere when welding to avoid burning the metal with the oxygen in the air (carbonization). The typically used gas for this purpose is Argon.

3.3.3 FLANGES

Ultra high vacuum flanges are required to connect the strip-line kicker to the beam pipe. One of the possible flanges is named CF or Conflat flange (Fig. 3.11) and it features standard dimensions.

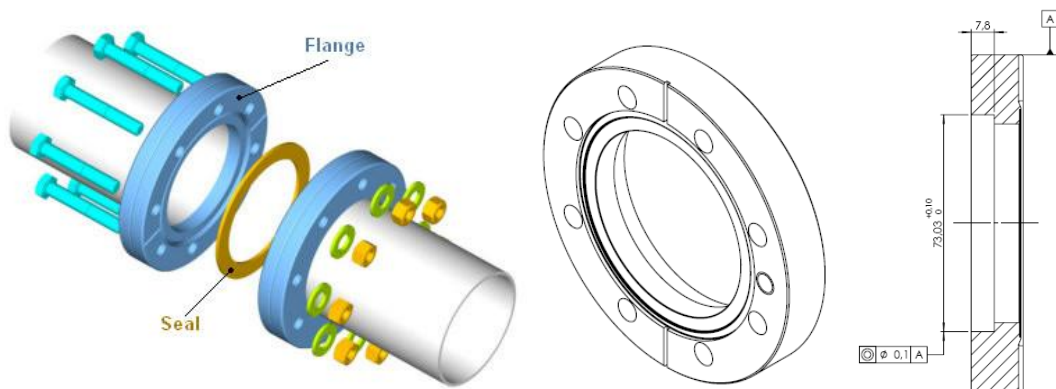


Fig. 3.11 Typical CF flanges with a copper gasket

CF flanges permit mounting and dismounting of a high vacuum device by using a copper gasket⁷ between them. The copper gasket is deformed by the knife-edge of both flanges when first mounted and therefore sealing is guaranteed. A new gasket is required if the flanges are detached anytime.

⁷ The copper gasket can also be silver coated to improve the vacuum tightness.

CF flanges must be welded to a pipe and therefore, they should be made of a material compatible with the pipe. They are usually made of good quality stainless-steel, sometimes aluminium or even hybrid steel-aluminium to connect different material pipes. Aluminium flanges support a lower number of mounting cycles.

The strip-line kicker requires at least two flanges to be connected to the beam pipe. This number can be higher if the transitions are independently manufactured. In that case, four more CF flanges would be needed to connect the transitions to the tail clipper and to the beam pipe.

The angular position of the flanges should be according to the beam pipe flanges, in order to adequately position the kicker in the correct orientation (vertical or horizontal plane deflection). Rotatable flanges are sometimes required when the relative positions are not known in the design state (Fig. 3.12) or to ease installation.

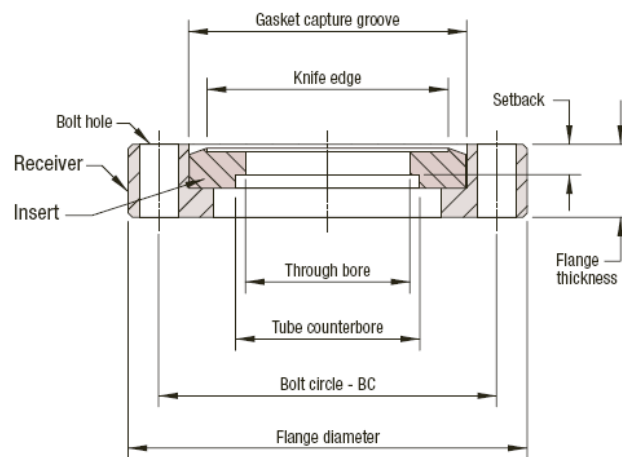


Fig. 3.12 Rotatable CF flange parts

When the kicker vacuum tank is not cylindrical, custom flanges must be used. Racetrack flanges are very typical in accelerator applications because the beam pipe cross-section is usually racetrack. Racetrack beam pipes can also be connected using circular CF flanges (Fig. 3.13).

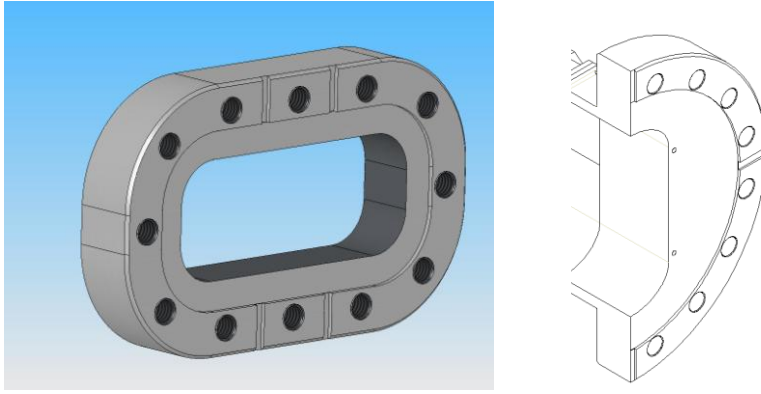


Fig. 3.13 Racetrack flange (left) and circular-racetrack flange (right)

3.3.4 BEAM PIPE TRANSITIONS

The wakefield behaviour of accelerator devices in series with the beam was presented in chapter 2. One of the main conclusions is the great importance of a smooth beam pipe to avoid beam instabilities. Therefore, strip-line kickers require beam pipe transitions to make smoother the passage from the beam pipe to the kicker cavity and vice-versa. The transitions should be as smooth as possible to optimize the wakefield behaviour.

A transition is manufactured by connecting two CF flanges of different diameters using a conical shape. There are some commercial transitions available, but usually the dimensions are not suitable for the requirements. Therefore they must be specifically manufactured. Short conical transitions can be manufactured from a solid bar by turning, machining afterwards the shape of the flanges in the ends of the bar. However, when the conical transition is long (Fig. 3.14), it is better to bend a metal sheet and weld along its length or even weld two different commercial cones in series.

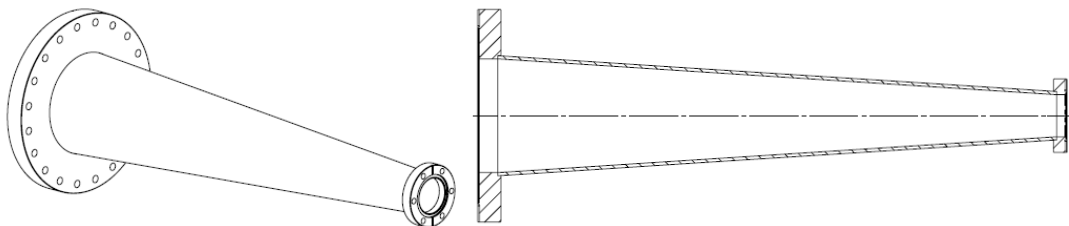


Fig. 3.14 Conical transition with two CF flanges

When different CF flanges are connected (circular and racetrack, for example), the inside part is not a revolution cone (Fig. 3.15) and it should be preferably manufactured using CNC machining.

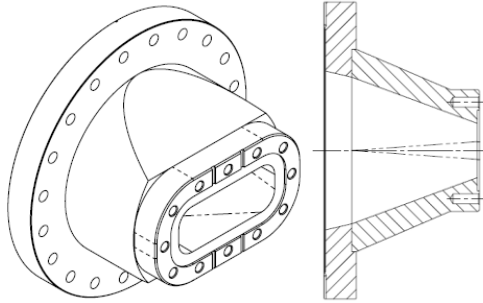


Fig. 3.15 Racetrack beam pipe to cylindrical kicker transition

The beam pipe transitions are usually separate pieces in the strip-line kicker, connected by CF flanges to the device. This is common when the vacuum tank is cylindrical and manufactured from a commercial tube. However, beam pipe transitions can also be manufactured in one piece with the vacuum tank. This is preferable when the tank is made in two halves and then welded (case of non cylindrical tanks).

3.3.5 SUPPORT AND ALIGNMENT SYSTEMS

The strip-line kicker must be supported on a girder at the same level of the beam pipe. The vertical displacement is achieved by regulating the vertical position of the girder. Mechanical support and alignment systems are used to get a precise position for the horizontal alignment of the kicker axis. Therefore, support systems must be precisely adjustable in horizontal position. As an example, CERN uses the supports shown in Fig. 3.16, which use a male part bolted to the device and a female part clamped to the girder. The two threaded holes in the female part are used to insert two bolts that push the male part to the required position. Three of these devices are typically required to precisely position a strip-line kicker, to provide the necessary degrees of freedom. Obviously, other systems are also possible.

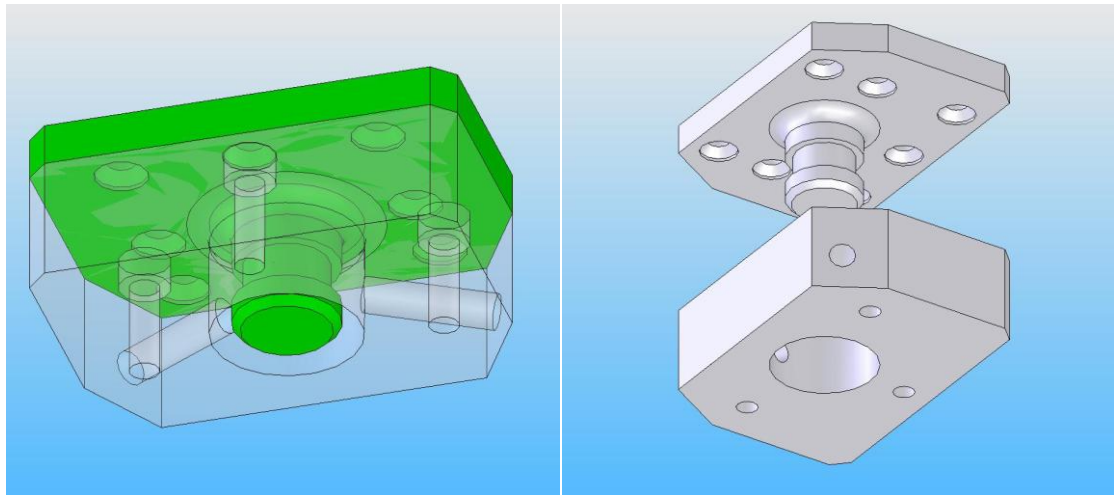


Fig. 3.16 Typical supports used at CERN

Besides, it is necessary to perfectly know the kicker position according to the beam axis. Laser targets (Fig. 3.17) are used to align different devices along the beam trajectory. They are fixed above the device in an elevated and very precise position. Therefore, the support for these targets has to be machined with tight tolerances in reference to the device axis. Indeed, the targets feature a pin hole in the lower surface to accurately position them on the strip-line kicker.

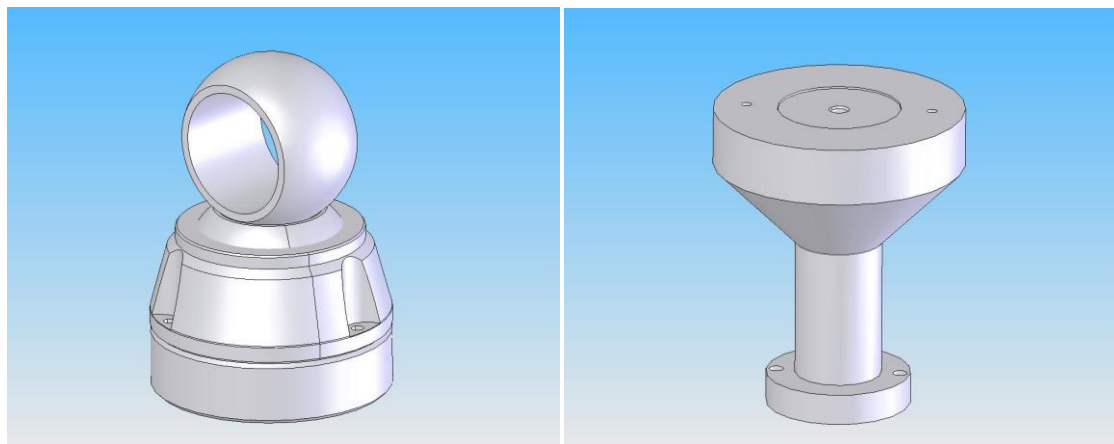


Fig. 3.17 Laser target used for alignment (left) and possible target support (right)

Target supports have to be rigid enough to avoid vibrations and deformations when machining their surface. Fig. 3.17 (right) shows a typical support for a laser target. The top surface must fit in a tight flatness and positioning tolerance. However, target supports are only required when the device has not any planar surface at the required elevation to position the targets.

3.3.6 *CLEANING*

Ultra high vacuum devices require a high degree of cleanliness to achieve the required vacuum level. All the pieces immersed in high vacuum need to be perfectly cleaned and degreased⁸. Indeed, machining of vacuum components must be carried out using vacuum compatible lubricants as halogen free cutting fluids or alcohol. Lubricants based on chlorine or sulphur should be avoided, especially for copper. Oily based lubricants are totally forbidden. An ultrasonic bath is the best option to clean the corners and difficult areas in the pieces, not easy to clean by other methods. The summarized procedure of vacuum cleaning according to CERN specifications is the following [6; 7]:

- All the stainless-steel pieces are degreased with perchloroethylene and then cleaned by an ultrasonic bath using ALMECO 18 (P3 VR580 17*) Henkel or equivalent during 30 minutes at 60 °C and full power. The aluminium parts are cleaned by an ultrasonic bath using NGL 17.40 sp ALU III NGL Cleaning Technology SA [8] or equivalent during 30 minutes at 50 °C and half power. Then, all the pieces are immediately rinsed twice using demineralised water and dried with hot air.
- Vacuum valid gloves are used for the whole process of manual handling and assembly.
- All the vacuum welds are carried out by using enough Argon gas to avoid corrosion and carbonization remains. If necessary, the pieces are treated by chemical etching.

Sometimes the required vacuum level is not achievable by simply cleaning the surfaces. The small molecules in air (especially H₂, CH₄, CO₂, H₂O) can fit in the molecular structure of the metals and produce the outgassing phenomenon. The metal immersed in vacuum slowly losses the gases inside, which makes reaching high vacuum almost impossible in a reasonable time. This process can be sped up by heating the pieces, which is called bake-out.

⁸ Degreasing is especially important to improve vacuum level.

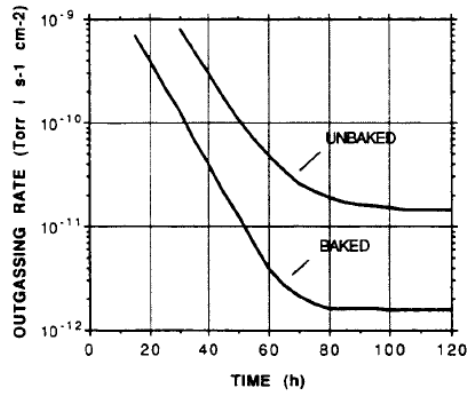


Fig. 3.18 Baked vs. unbaked pieces outgassing [6]

The bake-out is a controlled heating of the device while pumping at once to remove the desorbed gasses. It can take days to achieve the extremely low levels of vacuum required in some accelerators. For unbaked surfaces, the outgassing rates are roughly 10 times higher, contain other gases apart from H₂ and take longer to pump down to the equilibrium pressure.

A special and strong type of bake-out used to reduce the hydrogen outgassing of stainless-steel components is called firing. It is made by heating the material at high temperatures (950 °C) while pumping up to a pressure of 10⁻⁵ mbar (Fig. 3.19). It is a very aggressive process and can only be applied to high grade stainless steels (like 316 LN).

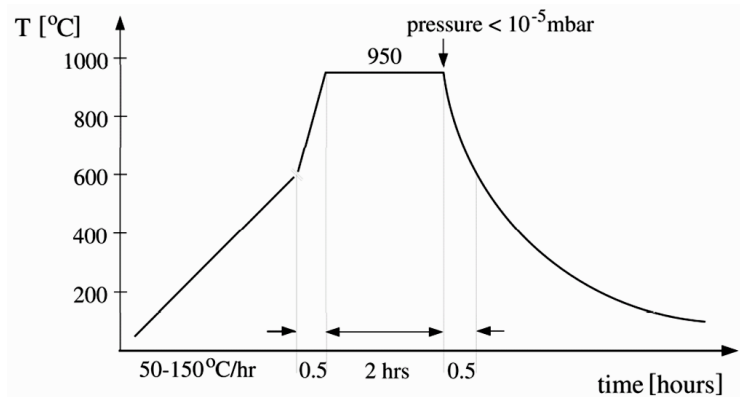


Fig. 3.19 Standard heating cycle for vacuum firing of stainless-steel components according to CERN procedure

3.4 THE ACCEPTANCE TESTS

The manufactured device has to be tested for conformance with specifications. These tests include the dimensional control, vacuum level and electromagnetic tests, as it will be detailed in the following sections.

3.4.1 *DIMENSIONAL CONTROL*

Most of the electromagnetic characteristics of the strip-line kickers will be checked after manufacturing by the means of electromagnetic tests (RF and pulsed power supply tests). However, the field homogeneity (both 2D and 3D integrated) and the integrated transverse voltage can only be indirectly measured by a detailed dimensional control. The locations of the electrodes inside the vacuum chamber and their dimensions and tolerances (parallelism, planarity, and distance between them) have to be carefully measured after the manufacturing and assembly process. If any out-of-tolerance measurement is obtained, the strip-line kicker will have to be re-simulated in a 3D code to check the new dimensions. Anyway, a sensitivity analysis of the main dimensions is always required in the calculation process in order to set-up these maximum tolerances for the manufacturing process.

3.4.2 *VACUUM TESTS*

The vacuum tests check the validity of the manufacturing and assembly process in terms of the achievable vacuum level and leak rate. Those values are extremely important in accelerators because an ultra high vacuum level ($<10^{-8}$ mbar) is usually required in all the devices in series with the beam pipe. Moreover, the leak rate should be kept below some given limits (usually below 10^{-10} mbar.l/s) to avoid high pumping rate requirements.

3.4.2.1 Vacuum level

The vacuum level achieved in any device is mainly related to the outgassing level of its internal surfaces and the presence of "virtual leaks"⁹ in the design and assembly process. The pumping flow rate is a specification given by the vacuum team in charge of the accelerator. If the device is long enough, additional pumping ports could be required in the device to keep the desired pumping rate.

When the strip-line device is tested for vacuum level, the pumping must be done from one of the beam pipe flanges while the vacuum is measured in the opposite one, assuming no additional pumping ports are installed (Fig. 3.20). The pumping test is usually effectuated in strip-line devices using a combination of a rotary pump and a turbo-molecular pump [6]. The vacuum level achieved after several hours pumping will show if the device requires additional bake-out or it has an important design or assembly defect which should be repaired. It must be noted that the pumping flow rate when the device is installed in the accelerator will usually be higher than in the tests and therefore, the vacuum level achieved in the working conditions is expected to be better.

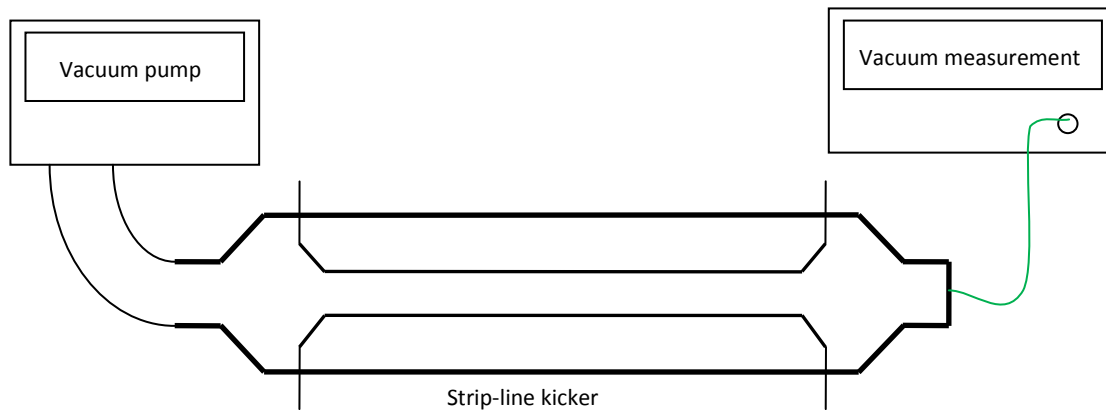


Fig. 3.20 Vacuum test in a kicker

⁹ The virtual leak is usually described as a gas load that comes out of a trapped volume during the pumping down phase. The size of the path connecting the internal volume of the virtual leak to the vacuum system will determine the gas flow rate. If the path were large enough, then there would not be any virtual leak any more as the internal volume will be pumped down as the same rate (speed) as the volume of the vacuum system. If the path is very narrow then the internal volume will take a much longer time to get pumped down affecting the pump down time of the vacuum system.

3.4.2.2 Leak rate

The leak rate is mainly related to the external leaks present in the device. The external leaks are the results of poor welds or improper usage of seals that create a path between the vacuum side and the outside of the system. Such leaks reduce the performance of the pumping system as they add some gas load forcing the designer to increase the size of the pumping system to compensate for it. These leaks are usually easily to detect using a helium leak detector¹⁰. Since there is a path between the inside and outside of the device, a tracer gas such as helium is sprayed outside the system that is detected by the leak detector connected to the vacuum side. This process also allows locating and measuring leaks to repair them.

3.4.3 *RF NETWORK ANALYZER TESTS*

The RF tests show the conformity of the manufactured device with the frequency domain calculations developed in chapter 2. However, the empirical tests are much difficult to set up than simulations due to the intrinsic empirical limitations. A device named Vector Network Analyzer [9] is connected to all the strip-line kicker ports to obtain the scattering parameters. The network analyzer inputs an RF signal of a given frequency (usually a short bunch of sine-waves) through one of the coaxial ports of the kicker and reads the signal coming from the other coaxial port connected to the same strip-line. This is done consecutively using waves of the desired range of frequencies (the frequency sweep to be tested). Consequently, it analyzes the transmission and reflection coefficients from and to the ports in the specified frequency range. Nevertheless, the strip-line kicker has 4 ports and needs to be fed in differential mode, which implies that two opposite signals (de-phased 180 degrees) have to be used as the input (Fig. 3.21) to fully characterize its behaviour.

¹⁰ The helium leak detector is used to detect small leaks in a vacuum device. It features an helium mass spectrometer which can detect extremely small quantities of helium in a vacuum volume.

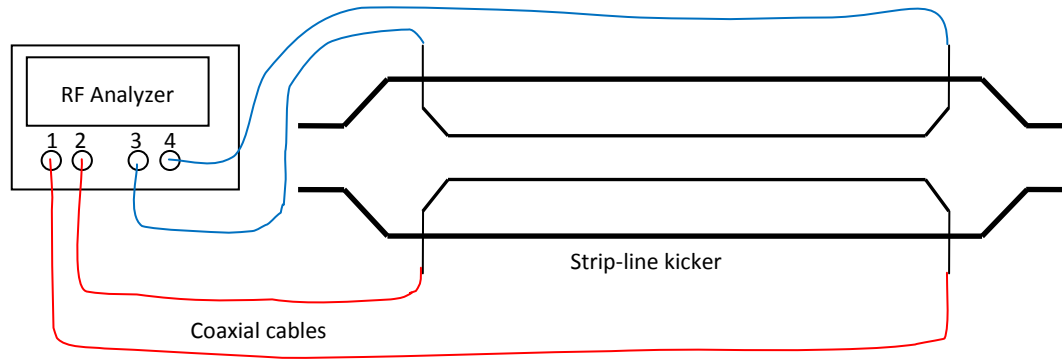


Fig. 3.21 4-port network analyzer feeding a kicker

That is the reason why the strip-line kicker ideally requires a 4-port network analyzer to obtain the complete transmission behaviour. However, if a 4-port network analyzer is not available in the laboratory, a 2-port network analyzer is also valid when hybrids are used (Fig. 3.22), although the behaviour of the independent strip-lines cannot be obtained. Hybrids are RF passive devices that split and de-phase a RF signal. They can de-phase the signal 90 and 180 degrees, depending on the hybrid type. However they can usually work only in a small frequency range. Therefore the RF tests must be subdivided according to the hybrids frequency range. The testing frequencies are obviously the same as for the simulations.

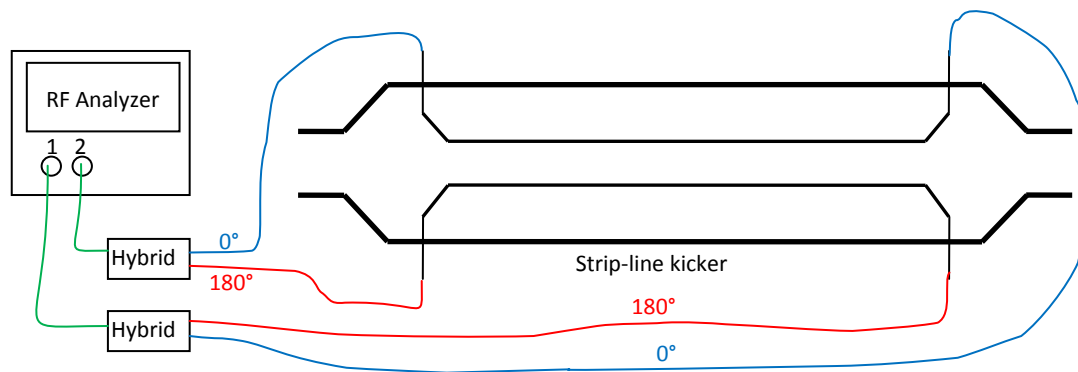


Fig. 3.22 2-port network analyzer with hybrids feeding a kicker

The network analyzer automatically plots the scattering parameters for each input and output port combination. In the 2-port case (Fig. 3.22), S_{11} is the reflection coefficient for both strip-lines. In addition, the lengths of the coaxial cables which connect the hybrids to the strip-lines have to be exactly the same for every hybrid, to avoid signal de-phasing at the strip-line input (feedthroughs).

The RF test does not require the device to be in vacuum. The RF wave signal is not affected by the relative permeability and permittivity of the air (both equal to 1).

3.4.4 UNLOADED VOLTAGE TESTS

The strip-lines have to be tested under high voltage to check the electric rigidity of the insulations (and distances to the tank in high vacuum, see Fig. 3.23). The testing voltage is usually a bit higher than the maximum pulse voltage, depending on the feedthrough maximum nominal voltage. The device should ideally be tested at working conditions although a lower vacuum level is sometimes also valid. A high voltage DC power supply is required for this test. The strip-lines are unloaded (not connected to the 50 Ohm loads) and therefore no power is required from the power supply. Only a sporadic electric breakdown consumes power from the capacitive electrostatic power supply (it instantaneously discharges the power supply).

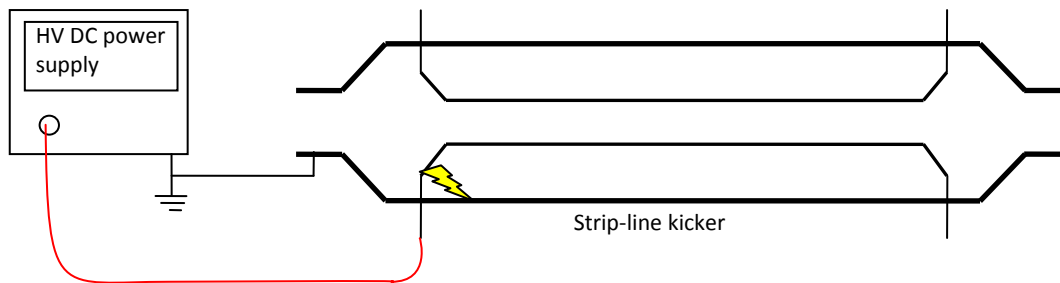


Fig. 3.23 Unloaded high voltage test

The test is usually not registered but manually confirmed. Any electrical spark inside the device is not only noisy but also the vacuum level is abruptly diminished due to the vaporised material in the vacuum tank. Some sparks can appear initially because of small dust particles on the surfaces. However, they are automatically eliminated after some sparking. If the device is constantly sparking, maybe there is a fault inside it. Electric field is concentrated in metal tips and it is important to round them in the design.

Only one strip-line is usually tested at a time. The testing voltage is then electrode-to-ground voltage. However, the kicker is fed by two pulses in opposition, which produces a voltage difference between the electrodes of twice the pulse flat-top voltage. A DC power supply with two opposite voltages would be required to test both electrodes at once. However, the electric insulation between the electrodes is very high because the distance between them is usually very large. Therefore, it is sometimes not needed to test the electrodes at the differential voltage.

3.4.5 50 OHM LOADED VOLTAGE TESTS

These tests are the most similar to the real strip-line kicker operation. The kicker is simultaneously fed by two opposite high energy pulses which test the transmission of the strip-lines and the ability of the kicker to handle high instantaneous current (Fig. 3.24). This test can be developed using the real pulsed power supply which will feed the kicker in the accelerator (the preferred option) or a different power supply. In case that any different power supply is used, it should feature peak voltage and rise and fall times in the same order of magnitude as the real pulsed power supply. The pulse duration is not so important for this test.

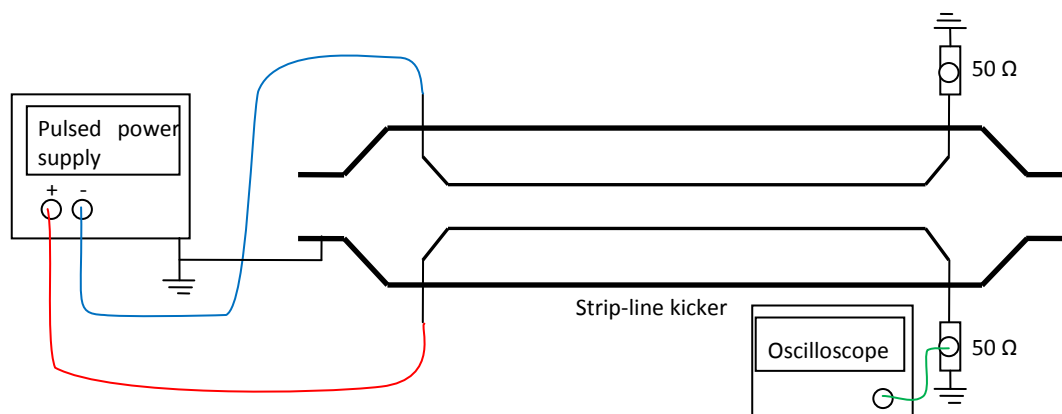


Fig. 3.24 Pulsed voltage test

To monitor the test results, the 50 Ohm loads should have a measuring port (Fig. 3.24) to connect an oscilloscope. The pulse shape after travelling by the strip-lines can be monitored and compared to the pulse shape of the power supply directly connected to the 50 Ohm load. The difference between these two pulses shows the frequency of signals absorbed by the strip-lines. If the transmission of the pulse is very good, both pulse shapes will be identical. If not, higher frequency peaks of the original pulse will be smoothed when passing through the strips.

However, it is sometimes impossible to obtain a pulsed power supply with two symmetrical pulse outputs. When this happens (and the real pulser is also not available), the test can also be carried out in two steps by feeding only one strip-line at each time (Fig. 3.25).

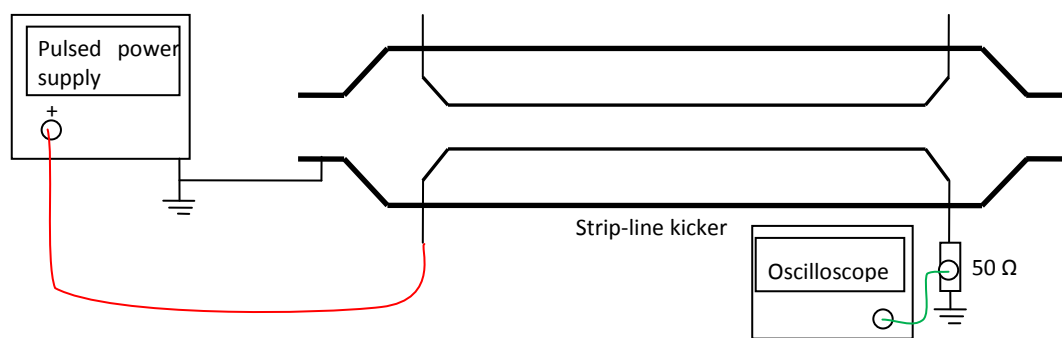


Fig. 3.25 Pulsed voltage test on only one strip-line

Given the explanations indicated in section 2.2.2.1, it is easy to understand that this operation method is not exactly the same for high frequency transmission. The electric wall symmetry between the two strip-lines is lost when one of them is not powered, and therefore the characteristic impedance of the individual strip-line is never more 50 Ohms. The pulse travels through a strip-line of different characteristic impedance and the mismatching increases the reflected power. However, the characteristic impedance is not very different and the error is acceptable. Therefore it is also possible to safely develop this test using only one pulse per strip-line at once, bearing in mind the indicated limitations.

3.4.6 COAXIAL WIRE METHOD

This method was detailed in chapter 2. Frequency domain simulations using the coaxial wire method can obtain important information for strip-line kickers installed in many-turn accelerators, bearing in mind some important limitations. However, empirical tests are much difficult to develop than simulations, and they are perfectly described in [10]. A reference tank must be build and matching networks are required to connect the network analyzer to the kicker tank. In addition, the kicker must be tested in vertical position (to avoid catenary effect on cable) which represents an additional difficulty for long devices. All these facts make the test very difficult and expensive, and not recommended unless totally necessary.

The prototypes developed in following chapters will not strictly require impedance measurements and therefore this section will not be detailed. The theoretical approach shown in 2.3.1.8 and the indicated bibliography is good enough to empirically test any device (if required) using the coaxial wire method.

3.5 CONCLUSIONS

The most important components in a strip-line kicker are the feedthroughs. They represent the technological limit of voltage and power in the kicker, and they are extremely difficult to manufacture if not commercially found. Constant impedance feedthroughs are even harder to find and sometimes have to be made-to-measure. The flexible connection to the strip-line is another difficult issue to solve in the kicker design.

Ceramic stand-offs are well known devices to insulate and support the electrodes. Their weak point is usually the fixation threaded hole. The author proposes an alternative fixation method for those devices based on a thermal interference fitting. This method will be applied to one prototype in the following chapters.

Many parts have to be manufactured for the full assembly of a kicker. CNC machining is usually required for most of them because of the complex shapes obtained in the EM design. All the pieces have to be carefully cleaned for ultra high vacuum and sometimes they have to be baked-out to reduce further outgassing. The assembly procedure strongly depends on specific considerations for a given design and no general recommendations can be indicated.

There are many possible ways to fix and position the device in the accelerator. The specifications for the fixation method and alignment systems must be given by the team in charge of the accelerator layout. However, CERN support and alignment systems have been described in this chapter.

After the manufacturing is finished, the strip-line kicker has to be tested for compliance with electromagnetic specifications. RF, high voltage and pulsed power tests are the minimum required to ensure correct operation. Coaxial wire method is the most difficult test and not always worth the effort. Failure in any of these tests would require a modification in the failing part or even a full redesign of the strip-line kicker.

3.6 REFERENCES

- [1] **Hanson, A.L., Snead, C.L. and Greene, G.A.** Activation of materials proposed for use in superconducting Linac applications. s.l. : Brookhaven National Laboratory, 1998. 65396.
- [2] **CeramTec North America.** <http://www2.ceramtec.com>.
- [3] **Fischer Connectors Inc.** <http://www.fischerconnectors.com>.
- [4] **Trinos Vacuum Systems Inc.** <http://www.trinos.eu>.
- [5] **Alesini, David.** Private communication.

- [6] **Mathewson, A. G.** Vacuum System Design. *Internal note*. s.l. : CERN ISR Vacuum Group.
- [7] **Ferreira, Leonel.** Atelier de Nettoyage. *Traitements de Surface*. Geneve : s.n., 2003. Vol. EDMS Document No. 798034, 867.xx.
- [8] **NGL Cleaning Technology SA.** <http://www.ngl-cleaning-technology.com>.
- [9] **Byrd, J.M. and Caspers, F.** *Spectrum and Network Analyzers*. Geneva : Lawrence Berkeley National Laboratory, 1998.
- [10] **Marcellini, F., et al.** Beam coupling impedance measurements of the DAΦNE vacuum chamber components. Frascati (Italy) : LNF-INFN.

CHAPTER 4

FIRST APPLICATION TO A REAL DEVICE: CTF3 COMBINER RING EXTRACTION KICKER

4.1 PURPOSE OF THE CTF3 COMBINER RING EXTRACTION KICKER

CTF3 (CLIC Test Facility III) is the third facility of the CLIC (Compact Linear Collider) project being developed at CERN. The CLIC study focuses on high-gradient, high frequency (30 GHz¹) acceleration for multi-TeV linear colliders [1]. 30 GHz is considered close to the limit beyond which standard technology for the fabrication of normal conducting travelling wave accelerators cannot longer be used.

Since conventional RF power sources based on modulators and klystrons are not available at this specially high frequency, CLIC was based on the novel and promising concept of Two-Beam Acceleration (TBA). The basic idea of the TBA is to properly recombine the electron bunch train (Drive Beam) generated by a conventional linear accelerator in order to create a high peak current beam with a time spacing between bunches considerably short (Fig. 4.1). This bunch structure is realized by a novel technique of bunch combination which converts a long bunch train with a large bunch spacing of 64 cm into a sequence of short trains with a bunch spacing of only 2 cm, which is used for 30 GHz power production. The bunch manipulation is done in three rings, using RF deflectors, giving a multiplication of the bunch repetition frequency by a factor of two in the first one and four in each of the two others. The electron beam is then decelerated and the extracted RF power is used to accelerate the beam in the main linac at 30 GHz.

¹ Based on performance and cost optimisation, the CLIC parameters are presently being updated for a RF frequency of 12 GHz and a gradient of 100 MV/m.

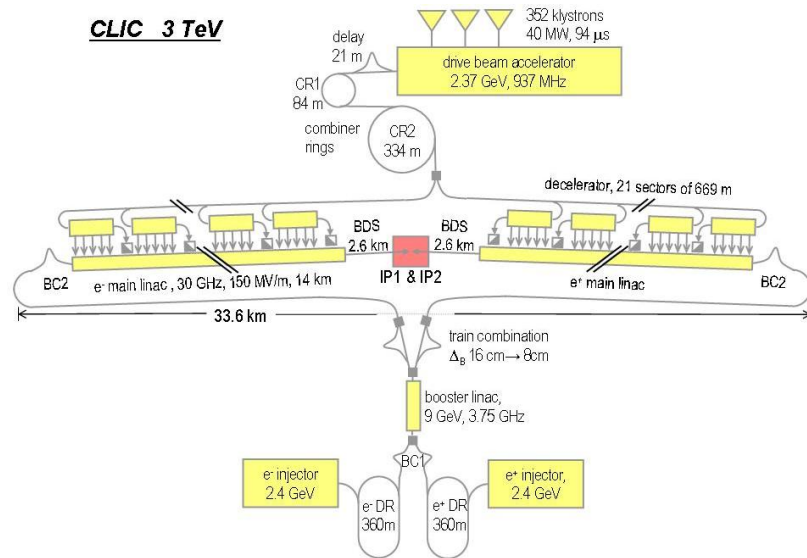


Fig. 4.1 CLIC general layout

CTF3 [2] is an important proof-of concept facility for many vital components of CLIC. Its main aim is to prove the principle of the RF power source design and to produce 30 GHz power at the nominal CLIC parameters. Fig. 4.2 shows the layout of the CTF3 experiment together with the extraction kicker location.

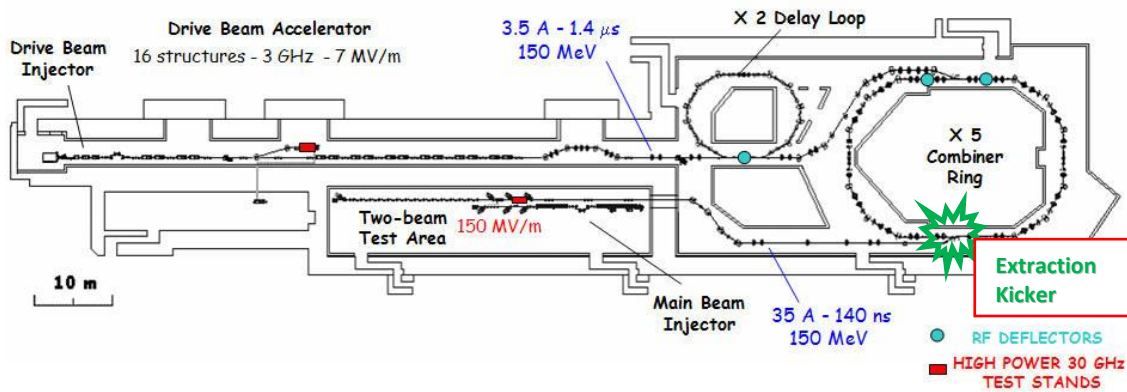


Fig. 4.2 CTF3 general layout and extraction kicker location

One of the most important issues to be tested in CTF3 is the frequency multiplication by the bunch interleaving novel technique. In CTF3, a long train of short bunches with a distance of 20 cm between bunches is converted into a series of short bunch trains, with the individual bunches spaced by 2 cm. This is done in two stages, first by a factor of two in the delay loop, then by a factor of 5 in a Combiner ring². A first stage of electron pulse compression and bunch frequency multiplication is obtained using a 1.5 GHz transverse RF deflector and a 42 m delay loop, as shown in Fig. 4.3.

² The new specifications only require 4 turns in the combiner ring. This change does not affect the kicker design.

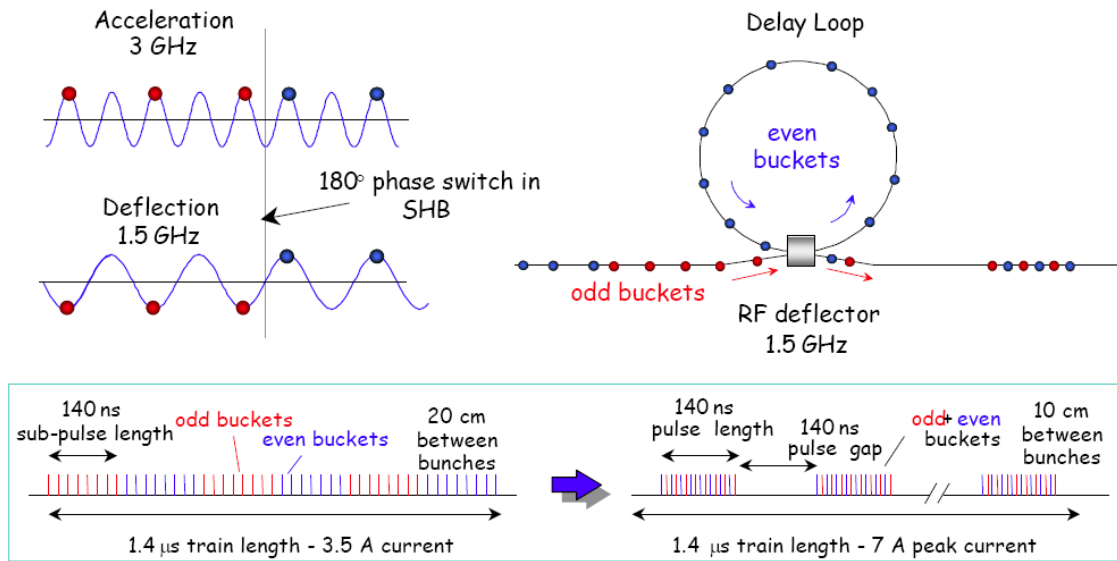


Fig. 4.3 Delay loop x2 multiplication scheme

This is followed by an 84 m combiner ring, in which a further factor of five in pulse compression and frequency multiplication is obtained (Fig. 4.4). At this point the drive beam pulse is 140 ns long with a current of 35 A, 150 MeV, and the 2.3 nC bunches are spaced by 2 cm.

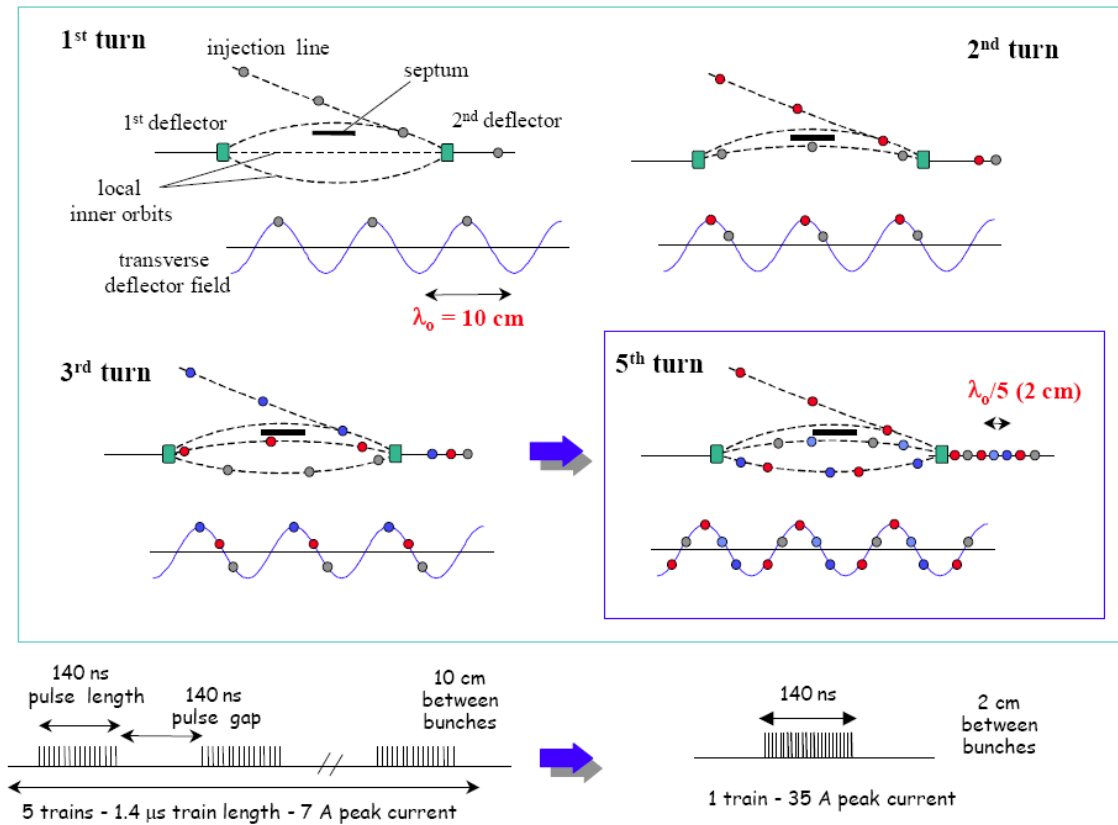


Fig. 4.4 Combiner Ring x5 multiplication scheme

The individual bunches are then compressed in length to about 0.5 mm RMS in a magnetic bunch compressor and transported to an experimental area to produce 30 GHz RF power in a high-power test-stand. In the same area, another linac will provide a main beam for a CLIC two-beam module and a test decelerator will be used for drive beam stability studies. A full schematic layout of CTF3 is presented in Fig. 4.5.

The extraction kicker is installed at the exit of the combiner ring. After the combination of bunches has been completed, the extraction kicker horizontally extracts the beam of 35 A, 140 ns and 150 MeV. The kicker pulse is then required to feature a flat-top zone long enough to extract 140 ns of bunches. In addition, the rise time should be fast enough to reach the flat-top field in the kicker when the pulser powers it in the last turn after the beam exits the kicker and before the beam arrives again to the kicker to be extracted. An electron beam at 150 MeV travels almost at the speed of light (see chapter 2). Consequently, a particle makes a complete turn at the combiner ring (84 m) in only 280 ns (double of beam's final length). The kicker can only be powered when the last bunch has exited it to avoid undesired deflection, which involves that the bunch train head is located at a maximum of 140 ns of "distance" from the kicker when it is powered³.

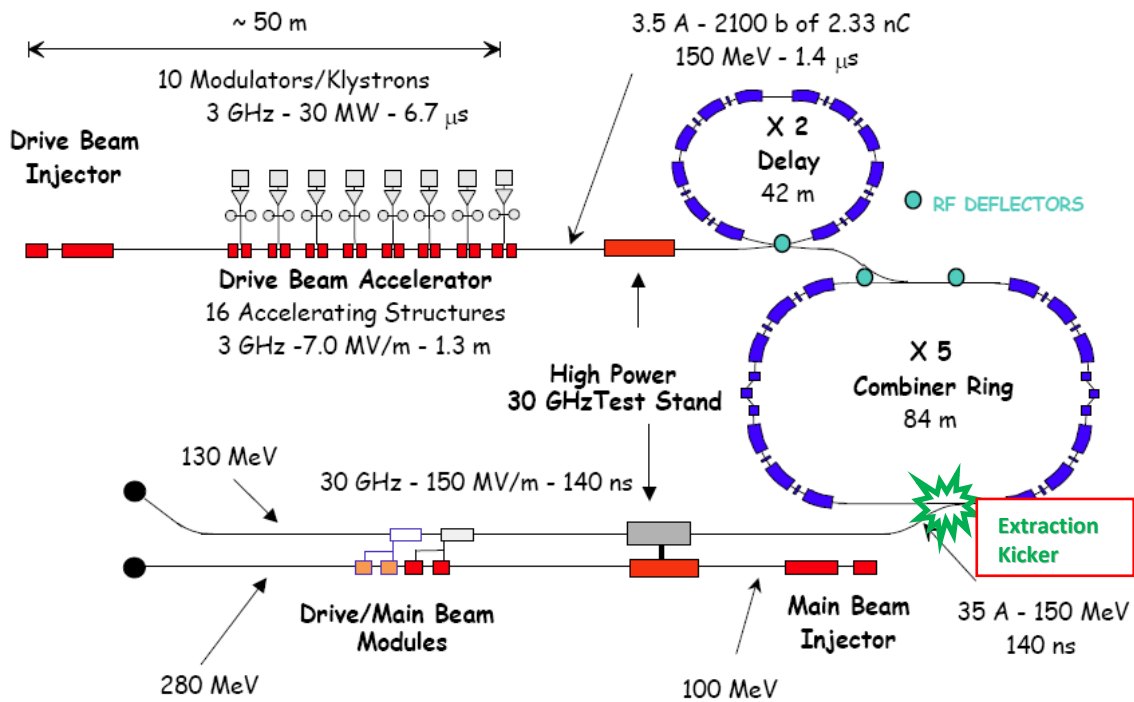


Fig. 4.5 CTF3 schematic layout

³ This time is indeed lower because the kicker length has to be subtracted.

So that, the kicker has to be fully powered at flat-top field when the beam arrives at its entrance and this should happen in less than 140 ns. Actually, this time has to include the rise time of the pulse (about 70 ns are specified for this device) and the time to fill the kicker length with the flat-top pulse power (about 6 ns). The required rise time does not justify the selection of strip-line technology for this kicker, as kicker magnets are also well fitted. However, the CTF3 requirements to lower the beam impedance make the strip-line technology the ideal solution for extracting CTF3 high current beams.

The kicker is followed in the CTF3 layout by thin and thick septa to continue the deflection until the beam is driven to the next section (named TL2).

The specifications to be fulfilled by the kicker are given by the CTF3 beam optics team, and summarized in Tab. 4.1.

Tab. 4.1 Extraction kicker original specifications

Magnitude	Value	Units
Beam Energy	300	MeV
Deflection Angle	5	mrad
Integrated Field	5	mT.m
Rise/Fall-times (0-100%)	≤70	ns
Pulse length (max.)	200	ns
Flat-top reproducibility	±0.1	%
Flat-top stability (including droop)	±0.25	%
Repetition rate (Initial-Nominal)	5-50	Hz
Available length (flange to flange)	2000	mm
Vertical aperture	≥40	mm
Horizontal aperture	≥40	mm
Field homogeneity (±1%)	30	mm

Some of the specifications in Tab. 4.1 do not agree with CTF3 parameters given above. Regarding the beam energy, this happens because the kicker has to be designed to deflect higher energy beams for tests, although the nominal energy is lower. Required rise time is lower than expected from previous comments, maybe because of diagnostics or other operations delaying the kicker powering up.

The specification about integrated magnetic field is not adequate to this design because, in strip-line kicker devices, electric field is as powerful as magnetic field and not only the magnetic field integration should be considered (see chapter 2). Nevertheless, this specification comes inherited from the old magnetic kicker previously installed in the Combiner Ring. Anyway, taking this value by itself, the value of 5 mT.m corresponds to an equivalent transverse voltage (Eq. 2.4) of $300 \cdot 10^6 \times 0.005 = 1.5$ MV, which gives approximately a 5 mrad deflection angle. Therefore, the exact specification for a strip-line kicker should be: Transverse voltage = 1.5 MV.

Deflection angle was increased to 8 mrad ($V_{\perp}=2.4$ MV) during the design process due to a CTF3 team request. Therefore, all the calculations will be done with the new deflection value. The field homogeneity is the most challenging parameter in this design. Other parameters in Tab. 4.1 are strictly related to the power supply and not to the kicker itself.

4.2 DESIGN AND CALCULATIONS

4.2.1 THE CROSS SECTION CHOICE

The cross section of the CTF3 kicker should be matched to 50 Ω characteristic impedance. As it was presented in chapter 1, this figure represents the optimal trade-off between power transmission and losses, and its use is widely extended.

Four possible cross sections have been considered to start the design of the kicker (Fig. 4.6), all of them using a cylindrical external pipe⁴. Using a thin slice in HFSS 3D code, the characteristic impedance of each one has been calculated and optimized to 50 Ω .

⁴ A cylindrical pipe is the easiest shape for manufacturing the kicker starting from a commercial pipe. It is always recommended to select this shape as the first consideration.

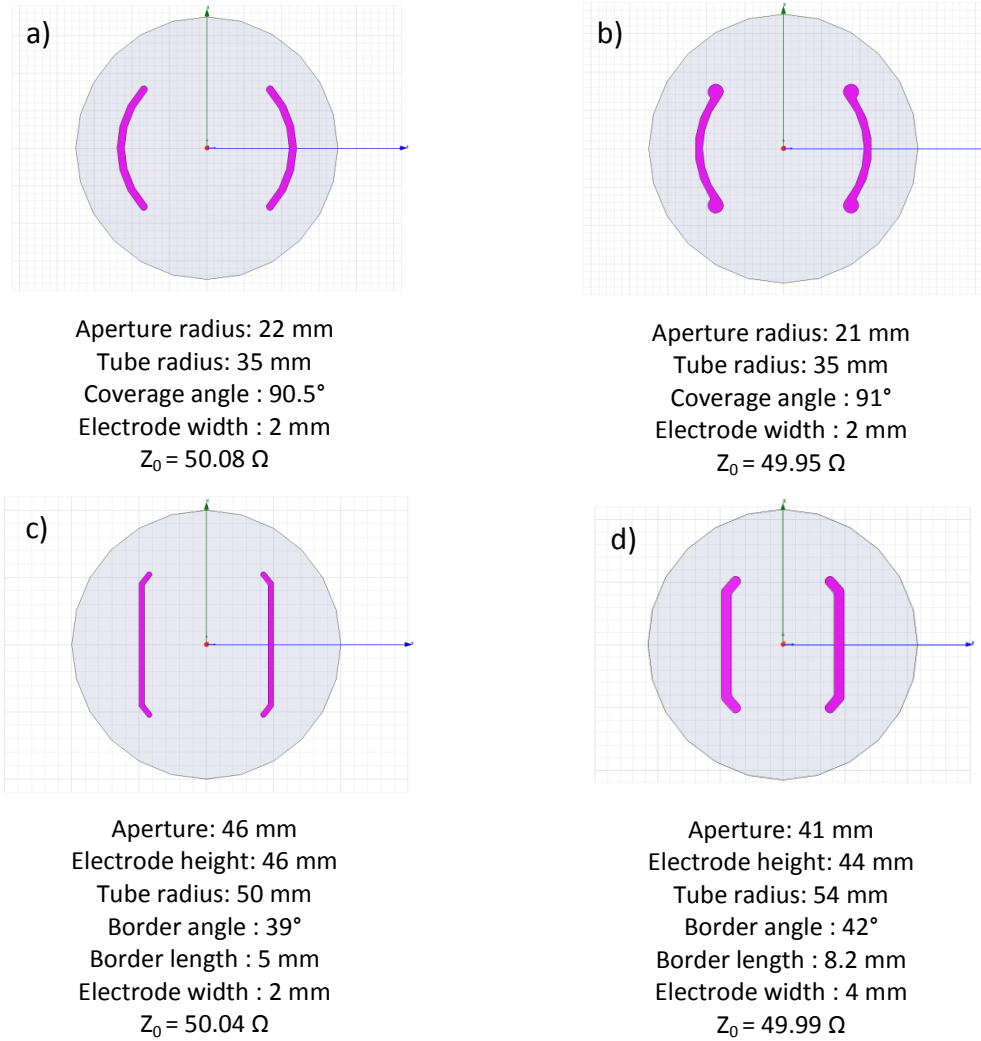


Fig. 4.6 Four possible cross sections for kicker: a) circular electrodes; b) circular round-edged electrodes; c) planar electrodes square aperture; d) planar electrodes rectangle aperture

The homogeneity of the kicker is expected to be better in cross sections *c* and *d*. However they require a much larger diameter tube. Straight sections *a* and *b* only differ in the edges of the electrodes. The objective of those edges is both reducing the electric field concentration and generating mechanical stiffness to avoid electrode bending; nevertheless they do not have any effect on the homogeneity and they complicate the electrode manufacturing process. The minimum aperture should be as small as possible to increase the deflecting field for a given voltage. Consequently, cross sections *a* and *d* are the preferred for this design. However, homogeneity should be better in cross section *d*, and this is a major specification to comply. Thus, the homogeneity has only been calculated in cross sections *a* and *d* using HFSS (Fig. 4.7).

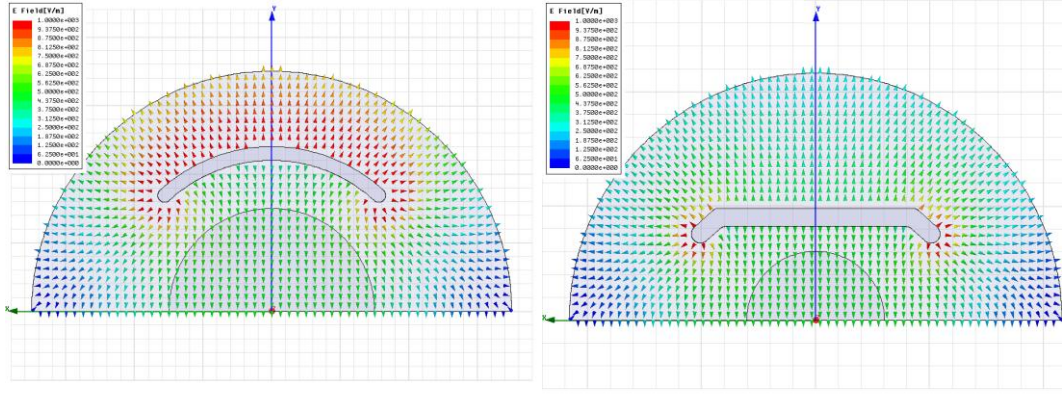


Fig. 4.7 Electric field map in *a* and *d* cross sections respectively (figures not at same scale, magnitude is not relevant). Note the central 15 mm homogeneity circle.

The resultant homogeneity is about $\pm 15.6\%$ in circular electrodes cross section and about $\pm 0.79\%$ in planar electrodes cross section. It is therefore required to select the *d* cross section for the kicker design to comply homogeneity specifications. In addition, *d* cross section has been matched to a 108 mm inner diameter tube, which is close to a standard dimension of commercial stainless-steel tubes (108.5 mm). This will ease the fabrication process.

However, *d* cross section requires a large diameter tube and the field strength in the axis is smaller than in *a* cross section for a given voltage. Slightly larger beam impedance is also expected for the planar electrodes cross section⁵.

4.2.2 DEVICE LENGTH AND KICK STRENGTH

It has been previously presented that an 8 mrad deflection angle corresponds to 2.4MV transverse voltage as indicated by Eq. 2.4. Simplifications assumed by that relation are possible because the particles passing through the CTF3 extraction kicker are electrons (or positrons), and their velocity at 300 MeV energy is extremely close to the speed of light (Eqs. 2.23 to 2.29). The required transverse voltage can be obtained with different electrode lengths by increasing or decreasing the electrode voltage.

⁵ The pipe diameter is larger and the electrodes are less axi-symmetric in the planar electrodes case.

In order to calculate the voltage and the transverse shunt impedance at DC for pulse excitation (Eq. 2.37), the electrode length has to be previously established. The length of the CTF3 extraction kicker cannot be defined by a precise extraction of bunches as indicated in chapter 1. However, the maximum flange to flange length specification in Tab. 4.1 is the limiting value to define the electrode length, which in principle should be as long as possible to reduce the voltage required. This specification is 2 metres⁶, and electrodes should be fit inside this length⁷. However, space for flanges and feedthrough assembly will be needed for manufacturing. Therefore, the initial estimation for electrode length is about 1.7 metres.

Using this estimated length, the required electrode-to-ground peak voltage of the pulse can be obtained from Eqs. 2.38 and 2.39, and it is about 14.47 kV. This voltage seems adequate for today's power supply and feedthrough technologies.

The transverse shunt impedance can now be calculated using Eq. 2.37. The obtained value is 687.69 k Ω , which will be used in the calculations of the following section.

4.2.3 VOLTAGE, CURRENT AND POWER. 2D WAKEFIELDS.

Once the electrode length and transverse shunt impedance are calculated, the current and power in the electrodes can also be obtained as shown in Tab. 2.1. The calculated values can be observed in Tab. 4.2. The averaged power per electrode has been calculated using a duty cycle of 10^{-5} , coming from the 200 ns pulse length and the 50Hz repetition rate given by the specifications in Tab. 4.1.

⁶ Flange to flange specification is not very tight in this design as expressed by CTF3 team. Indeed, the final design will be a bit more than 2.1 meters long.

⁷ The longer the electrodes, the lower the required voltage. It is recommended to lower the voltage as much as possible to avoid insulation problems and make easier the feedthrough selection. The power supply is also cheaper for a low voltage design.

Tab. 4.2 CTF3 CR Kicker electrical requirements

Magnitude	Value	Units
Pulse maximum instantaneous power (P_{DC})	8.38	MW
Pulse maximum instantaneous power per electrode (P_{1DC})	4.19	MW
Averaged power per electrode (P_{1avg})	41.88	W
Flat-top pulse voltage (electrode to ground, V_k)	14.47	kV
Flat-top pulse current per electrode (I_k)	289.41	A

All the analytical magnitudes have already been calculated. However, before starting the 3D numerical calculations required to fine tune the kicker design, it is recommended to estimate the wakefield behaviour using an axi-symmetric code.

ABCI code has been used to simulate an axi-symmetric model of the kicker. The 1.7 meter long electrode and 2 meter long tube have been drawn in an ABCI input file. The transitions from 40 mm beam pipe to 108 mm kicker tube are conical in this simulation. The bunch size is $\sigma = 2$ mm. The ABCI input file is as follows:

```
&FILE LSAV=.F., ITEST=0, LREC=.F., TMAX=360000, TSOS=3600, LCPUTM=.T. &END
CTF3 Kicker approximation (axi-symmetric)
&BOUN IZL=3, IZR=3 &END
&MESH DDR=0.0002, DDZ=0.0002 &END
#CAVITYSHAPE
0.0
0.000 0.000
0.020 0.000
0.020 0.050
0.054 0.195
0.054 1.905
0.020 2.050
0.020 2.100
```



```

0.000 2.100
0.000 0.000
0.0205 0.2
0.0205 1.9
0.0245 1.9
0.0245 0.2
0.0205 0.2
9999. 9999.

&BEAM SIG=0.002, MROT=0, NBUNCH=1, BSEP=0 &END
&TIME MT=4, NSHOT=5 &END
&WAKE UBT=0.2 &END
&PLOT LCAVIN=.T., LCAVUS=.T., LPLW=.T. &END
&PRIN LSVW=.T., LSVF=.T. &END
CONTINUE
&BEAM MROT=1 &END
&PLOT LCAVIN=.F., LCAVUS=.F., LPLW=.T. &END
CONTINUE
&BEAM MROT=0 &END
&WAKE UBT=30.0 &END
&PLOT LCAVIN=.F., LCAVUS=.F., LPLW=.T., LFFT=.T., LSPEC=.T. &END
CONTINUE
&BEAM NBUNCH=420, BSEP=0.1 &END
&WAKE UBT=30.0 &END
&PLOT LCAVIN=.F., LCAVUS=.F., LPLW=.T., LFFT=.F., LSPEC=.F. &END
STOP

```

Fig. 4.8 shows the simulated model used as input for the CTF3 extraction kicker calculation. The wake loss factor for this structure is 2.391 V/pC (Fig. 4.9).

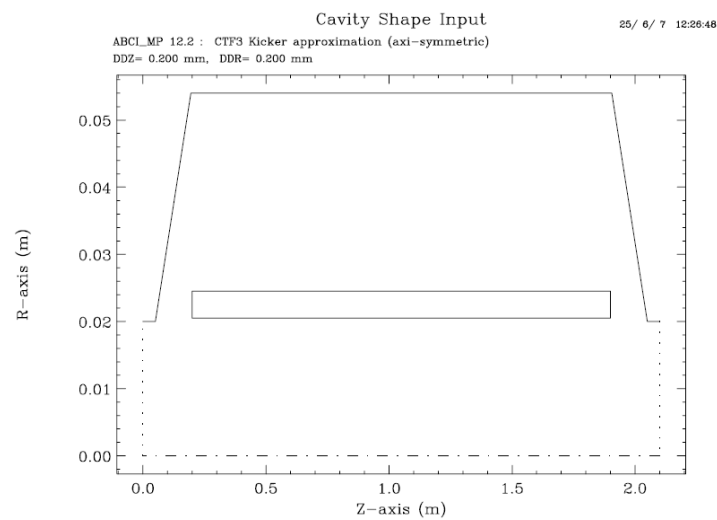


Fig. 4.8 CTF3 Kicker model in ABCI

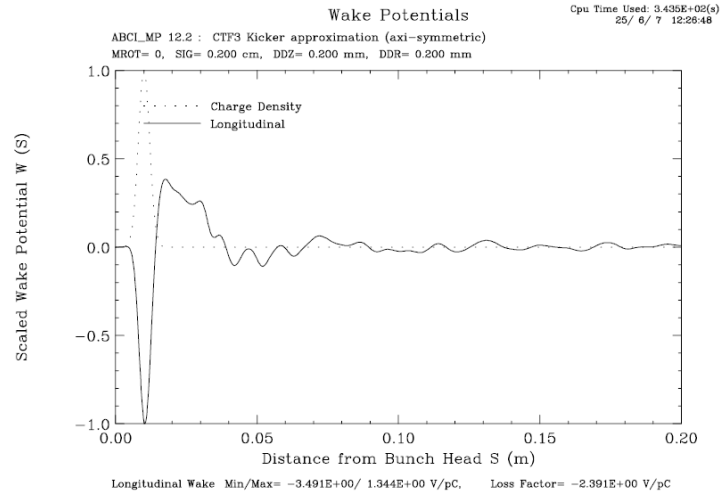


Fig. 4.9 Wake potential for 2 mm bunch passing through the kicker

It has to be noticed in Fig. 4.9 that the wake potential is opposite to the bunch charge density just at the beginning. This confirms the simulation because it complies with the causality principle explained in chapter 2.

Using the previous data, it can be calculated (Eq. 2.47) that a 2.33 nC, 2 mm bunch loses about $2.391 \times 2330 = 5571\text{V}$ of energy per turn, which results 22.3 keV in 4 turns in the Combiner Ring. The maximum energy spread accumulated by the bunch is given at Eq. 2.48, resulting in 45.1 keV gained in 4 turns. These results are much smaller than that of the RF deflectors in CTF3 CR, and a bit overestimated as the simulation is axi-symmetrical.

The long range wake potentials have also been simulated (Fig. 4.10). The wake potential is being repeated (with diminishing amplitude) every 4.2 metres, which agrees with the double kicker length. This is easily explained by the forward/backward reflection of the wake initially generated by the bunch along the kicker length. A trailing particle located at about 4.2 metres behind the leading particle will experience the reflected wake returning back when it enters the kicker. The reflection is produced between the conical transitions due to the smaller cut-off frequency of the beam pipe compared to the kicker tube.

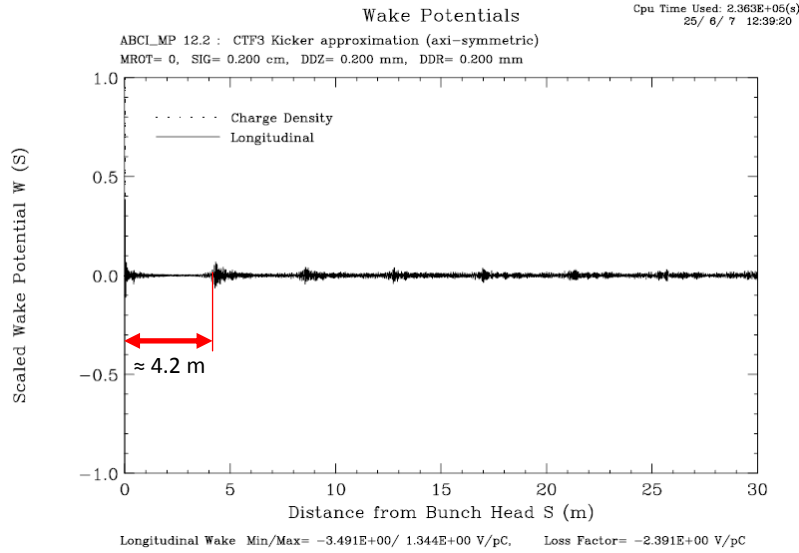


Fig. 4.10 Long range wake potential simulation (normalized to max-min wake values)

4.2.4 FREQUENCY DOMAIN 3D MODEL SET-UP.

The kicker main dimensions and shapes are already calculated. Now it is possible to define a 3D model for frequency domain simulations considering the indications given in section 2.3.1.2.

Five stand-offs have been projected to support each of the 1.7 m electrodes⁸. Two sliding stand-offs are required close to the electrode ends to avoid vibrations due to the cantilever ends (when shipping the kicker). One central stand-off is also required to fix the electrode. Two more sliding stand-offs will also be installed between the others. Developed static FEM calculations do not appear to require these two additional stand-offs (Fig. 4.11 and Fig. 4.12), but they are not difficult to install and they give additional security when moving the device. A modal analysis has not been considered because no strong vibrations are expected during shipping or handling.

⁸ The stand-offs barely affect the EM behaviour of the kicker because they represent an extremely small fraction of the transmission line length. Therefore they will not be modelled in all the simulations.

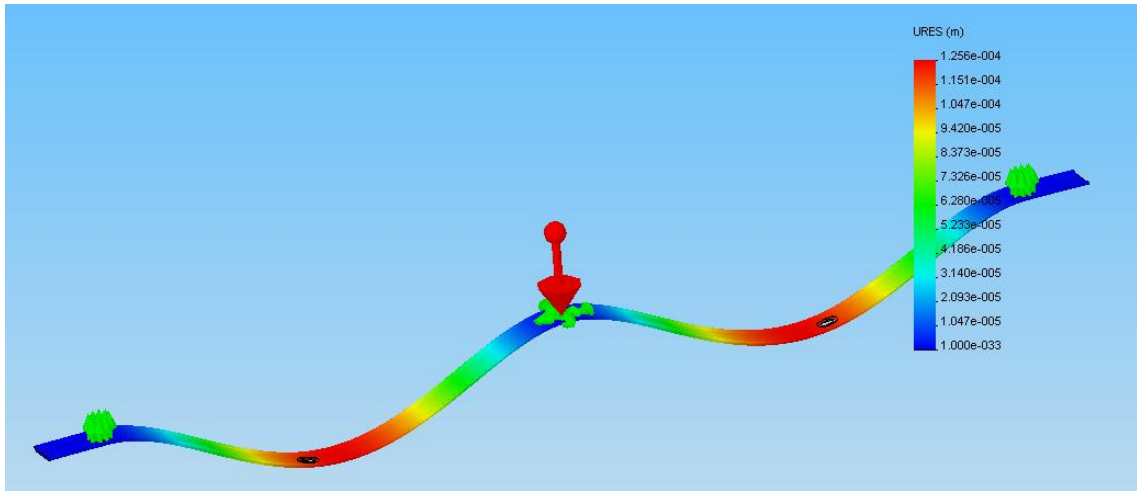


Fig. 4.11 Electrode supported by three stand-offs bent over its weight (1000:1 deformation)

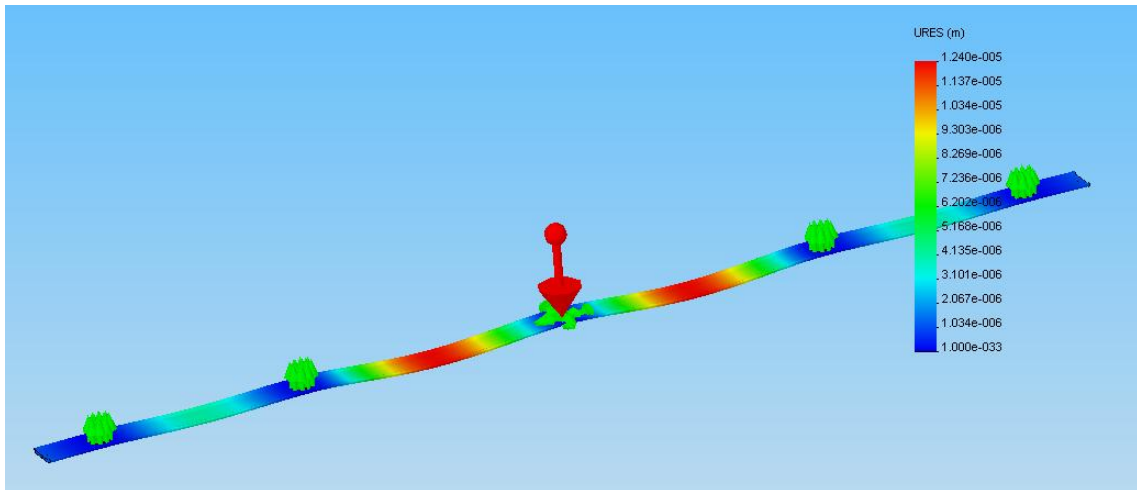


Fig. 4.12 Electrode supported by five stand-offs bent over its weight (1000:1 deformation)

Conical transitions will be initially used to connect the 40 mm beam pipe to the 108 mm kicker tube. However, these transitions do not change the typical frequency domain results (S parameters, homogeneity, voltages and currents) as they are only important for beam impedance calculations.

The 3D model is developed starting from the 2D cross section shown in Fig. 4.6 *d*. All the dimensions are parameterized for an easy optimization of the model. Several auxiliary lines are drawn to calculate integrated fields (transverse voltage, coaxial voltage and current). Symmetry is $\frac{1}{4}$, one magnetic wall and one electric wall. Only two stand-offs are used for the electromagnetic model (Fig. 4.13) because they hardly affect the S parameters. The chosen coaxial to strip-line transition is detailed in the following section.

Frequency for the simulation is as similar as possible to a sinusoidal wave whose positive zone is like the feeding pulse. For a 200 ns pulse, the frequency of the equivalent RF wave equals to $(2 \times 200 \times 10^{-9})^{-1} = 2.5$ MHz. This is not a critical number for the initial RF simulation in pulsed kickers, but it is convenient to take it as similar as possible to the real pulse.

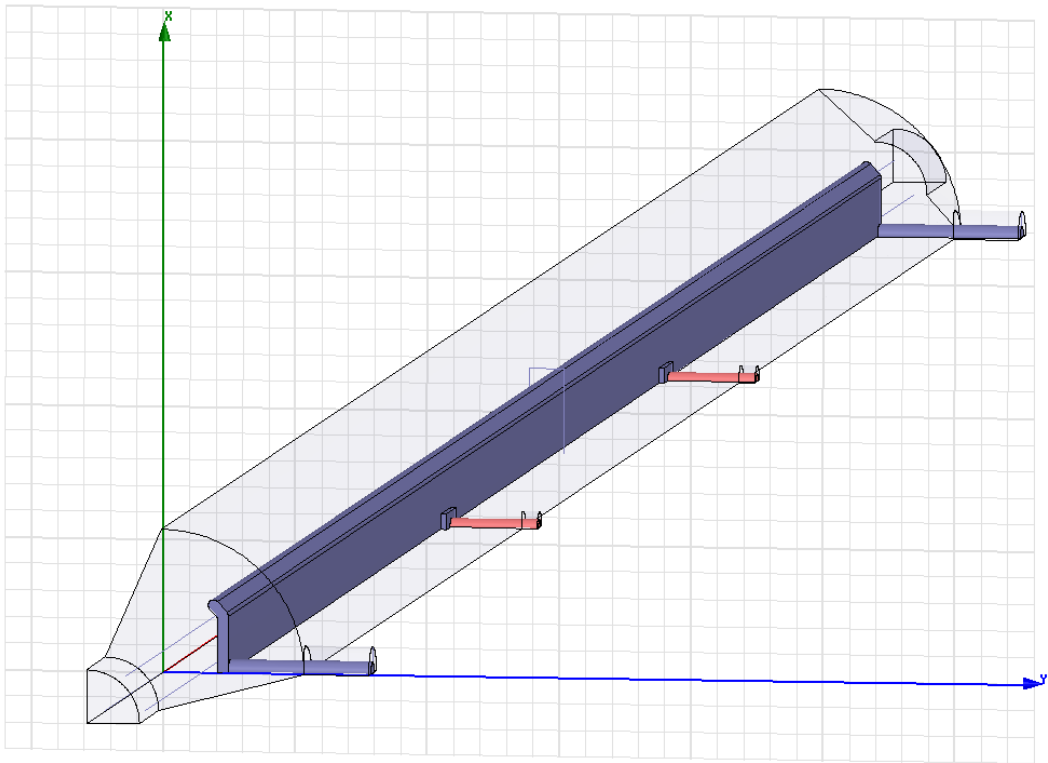


Fig. 4.13 CTF3 extraction kicker EM model

RF power input is carried out using the coaxial ports. The averaged power to be defined in the HFSS simulation to obtain the same peak voltages and currents as in the pulsed power device is $P_{1DC}/4$, which results 1048 kW (Fig. 4.14). The output coaxial port is automatically connected to 50 Ohm impedance.

Edit Sources						
Source	Type	Solved Magnitude	Solved Phase	Scaling Factor	Offset Phase	Unit
EntradaPositiva:1	Port	1 W	0 deg	1048000	0 deg	
SalidaPositiva:1	Port	1 W	0 deg	0	0 deg	

NOTE: This model contains symmetry planes. You may need to adjust the scaling factor accordingly.

OK Apply Close

Fig. 4.14 HFSS power in excitation ports

4.2.5 COAXIAL TO STRIP-LINE TRANSITION: S PARAMETERS

The model is almost ready to be simulated. Only the coaxial to strip-line transition has to be decided. This represents the most important part in the strip-line kicker for a good transmission of the pulse from the power supply to the absorbing loads. The S parameters of CTF3 strip-line kicker have been simulated using two different transitions (Fig. 4.15 and Fig. 4.16).

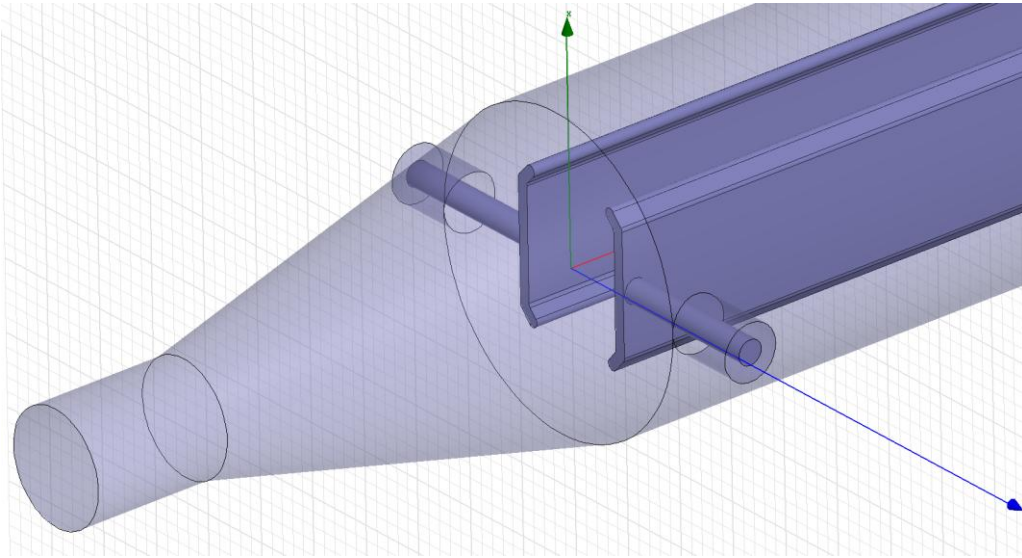


Fig. 4.15 Direct coaxial to strip-line transition

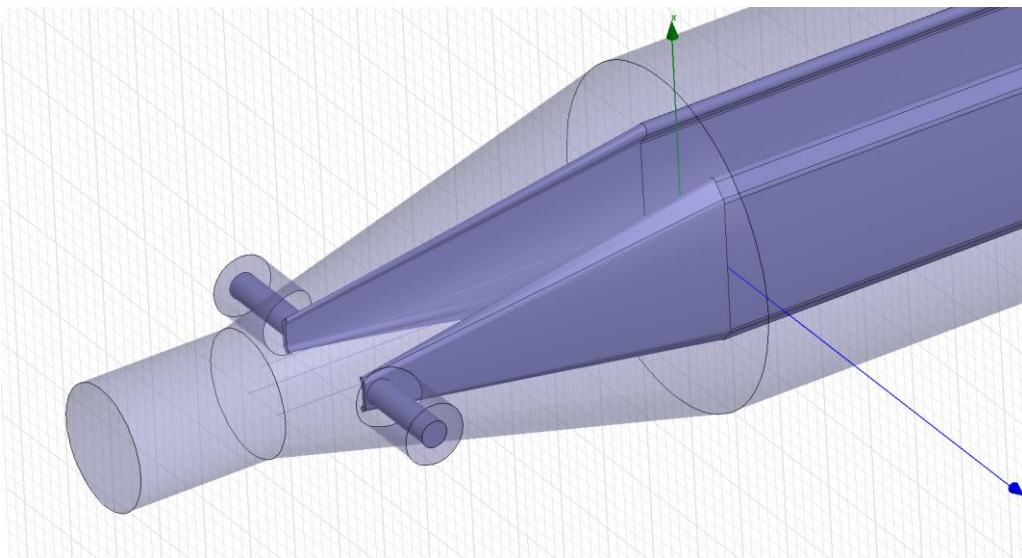


Fig. 4.16 Dual tapered coaxial to strip-line transition

Fig. 4.15 represents a direct connection of the feedthrough to the strip-line electrode. The transition is abrupt and a large reflection is expected for the highest frequencies. On the other hand, Fig. 4.16 represents a highly optimized transition proposed by the author of this Thesis, where the feedthrough is connected to a tapered electrode inside the tapered transition from the beam pipe to the kicker tube. This transition is expected to perform much better transmission of high frequency signals.

Reflection scattering parameters (S_{11}) for both transitions can be observed in Fig. 4.17 and Fig. 4.18 up to 2 GHz. Matched transmission in Fig. 4.17 happens at multiple $\lambda/4$ frequencies as indicated in chapter 2, where $\lambda/4$ corresponds approximately to the electrode plus the transition length (about 1.76 m). The matched frequencies are therefore $(3 \times 10^8 / 1.76) * (1/4) = 42.6$ MHz, $(3 \times 10^8 / 1.76) * (3/4) = 127.8$ MHz, $(3 \times 10^8 / 1.76) * (5/4) = 213$ MHz, etc.

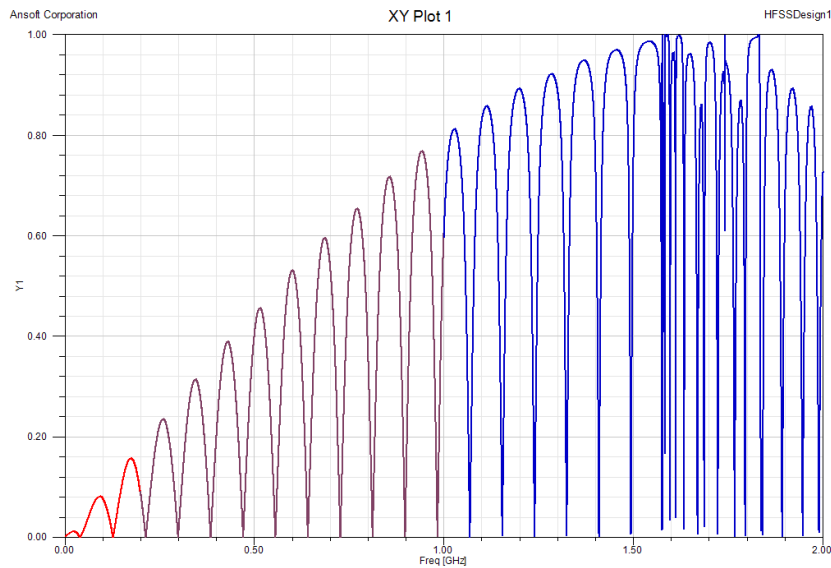


Fig. 4.17 S_{11} in direct coaxial to strip-line transition

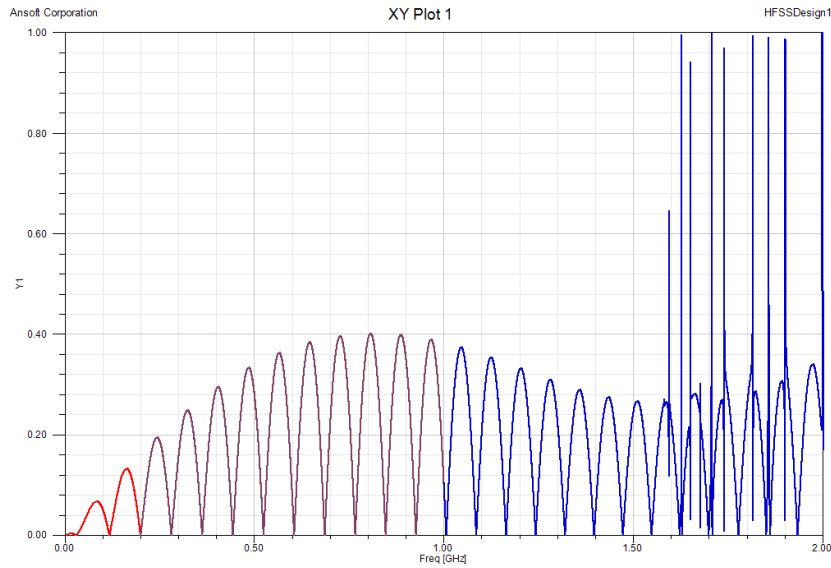


Fig. 4.18 S_{11} in dual tapered coaxial to strip-line transition

Dual tapered transition presented in Fig. 4.16 features excellent transmission of high frequency signals up to 2GHz (note the resonant frequencies appearing over 1.5 GHz coupled to the coaxials). However, the reflected power of the simpler direct transition is less than 0.03 % from 0 to 50MHz⁹. The dual tapered transition is harder to assemble if the kicker is made using a commercially available tube (as in this case) and the electrode has to be necessarily CNC machined. Consequently, it is not worth using the dual tapered cross section for this design. However it could successfully be applied to faster pulsed kickers when good power transmission is totally essential in spite of the costs.

4.2.6 NUMERICAL RESULTS

All parts of the strip-line kicker are now selected and dimensioned. The model can now be simulated in HFSS to obtain the rest of the numerical values.

⁹ The Fourier transform of the kicker pulse given in the specifications shows negligible frequency content over 50 MHz. This is very conservative as only frequencies below $0.5/T_r$ should be considered as shown in chapter 1.

The 3D homogeneity has been numerically calculated by means of Eq. 2.56 using HFSS calculator commands. The value obtained for the CTF3 strip-line kicker is about ± 0.69 %, which is even a bit lower than in the 2D straight section. This is possible because the electrode end effects are being cancelled somewhere along the 3D integration. However, 3D integration is always less precise than 2D calculation, and therefore the precision of this value is limited. Anyway, it is well below ± 1 % and consequently it is assumed to be valid.

The power losses inside the structure have been estimated using the power difference between input and output ports by means of the Poynting vector. The result of this integration is 8184 W peak power per electrode. Using Eq. 2.41 it is possible to estimate the equivalent power for a 50 Hz repetition rate, which results in 0.082 W per electrode, a negligible power to evacuate.

The transverse voltage is calculated by integrating the Lorentz force along the kicker axis. The frequency of the simulation is very low and consequently the field is almost constant along the structure. Therefore the peak field integrated to obtain the transverse voltage can be considered acceptable. The result of this calculation in the CTF3 strip-line kicker is 2418789 V which perfectly agrees with the analytical value obtained before.

Electrode peak voltage and current are also calculated as indicated in chapter 2. The numerical values are 14513 V for voltage and 290.4 A for current, very similar to the analytical results. The values of electric field Y component along the kicker (see axes definition in Fig. 4.13) are plotted in two 3D graphs obtained from HFSS data. One of them is plotted shifting X and Z coordinates (plane Y=0, Fig. 4.19) and the other shifting Y and Z coordinates (plane X=0, Fig. 4.20).

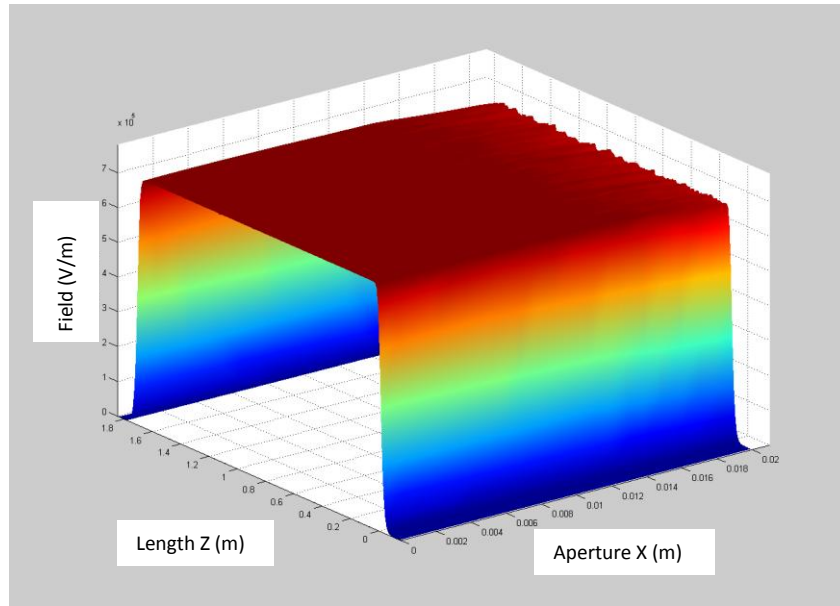


Fig. 4.19 Electric field distribution in plane Y=0

The field in a central cylinder with 15 mm radius is very constant along all the length of the kicker. The border effects at the end of the electrodes in Fig. 4.20 (Z=0 and Z=1.7 out of the 15 mm homogeneity radius) are caused by coaxial connections in this area.

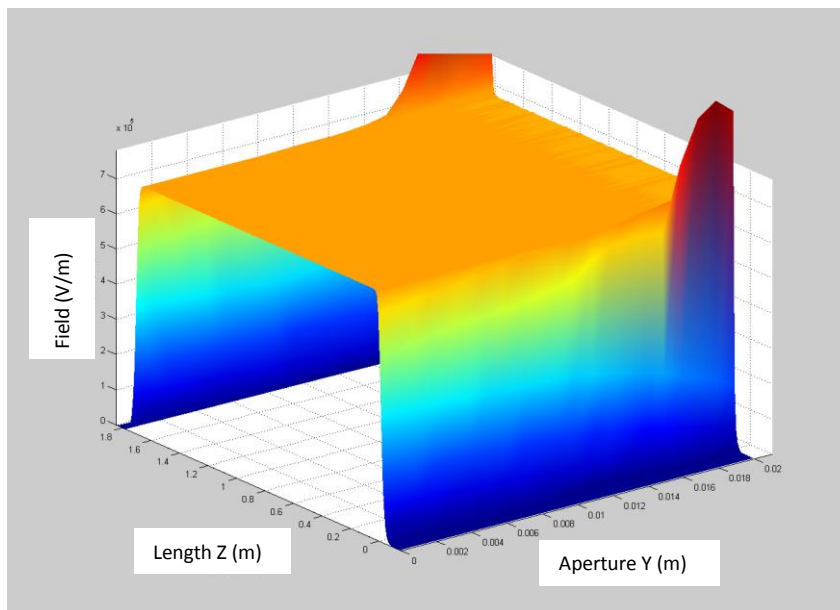


Fig. 4.20 Electric field distribution in plane X=0

4.2.7 HIGH ORDER MODE (HOM) ANALYSIS

When the beam passes through the kicker, it induces electromagnetic fields that could resonate inside the cavity¹⁰. The dangerous modes in CTF3 Combiner Ring devices are the ones that arbitrarily accelerate or decelerate the particles (longitudinal E field). Bunches should be grouped at exact distances for the TBA method to work correctly. The dangerous HOMs in this case are then Transverse Magnetic (TM) modes, and the frequency range to search for HOMs is defined using Eq. 2.58. The cut-off frequency of the beam pipe for TM₀₁ mode is 5.74 GHz and for the kicker tube (without electrodes) is 2.12 GHz. Therefore all the possible TM modes should appear between 2.12 GHz and 5.75 GHz. TM modes cannot be excited by the coaxials and therefore they cannot be calculated from a frequency sweep feeding the kicker by the coaxials.

An eigenmode simulation has been set-up using HFSS (Fig. 4.21). The model has been simplified removing coaxials to reduce the memory requirements. However, it is almost impossible to simulate over 3 GHz frequencies with the available computers. 3GHz wavelength is 0.1 m, which requires many small elements inside the 2.1 m structure to obtain a precise solution. This increases memory requirements enormously, especially when finite conductivity is used for the materials, which is usually needed to automatically calculate Q factors¹¹ for every mode.

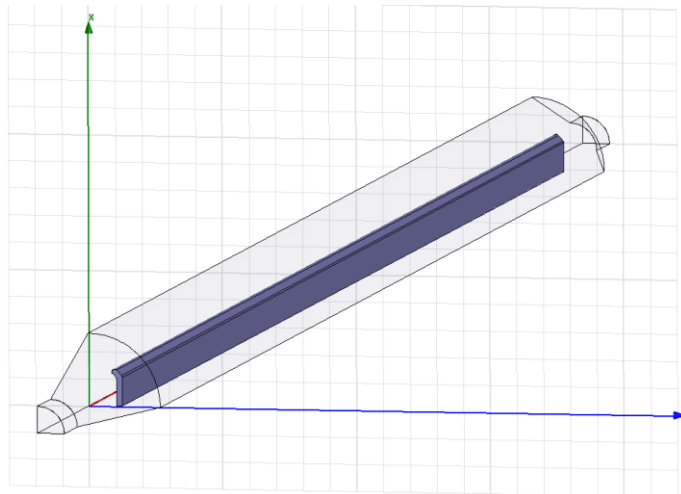


Fig. 4.21 HFSS model for HOM calculation

¹⁰ HOMs excited by the pulsed power supply are not possible in this design given the low frequency of the pulse.

¹¹ The quality factor of a mode can show the seriousness of an undesired resonance for a given device. Low Q means bad resonance but a large frequency range for the resonance. High Q is the opposite.

Anyway, many simulations have been developed up to 3 GHz using both magnetic symmetry planes to find TM or TEM modes only. Many modes appear starting in 2.1 GHz cut-off frequency (Fig. 4.22). There are also modes below 2.1 GHz which appear due to the presence of the electrodes inside the kicker tube (they would not appear if electrodes were not present). The quality factor of these modes is around 1500 in the majority of them, which in principle does not represent a threat to the beam. The stainless-steel structure rapidly damps the EM energy spread by the beam. In addition, the first 20 modes presented in Fig. 4.22 do not have longitudinal electric field in the axis and their resonance would not affect to the beam longitudinal dynamics nor they can be excited by the beam wakefields.

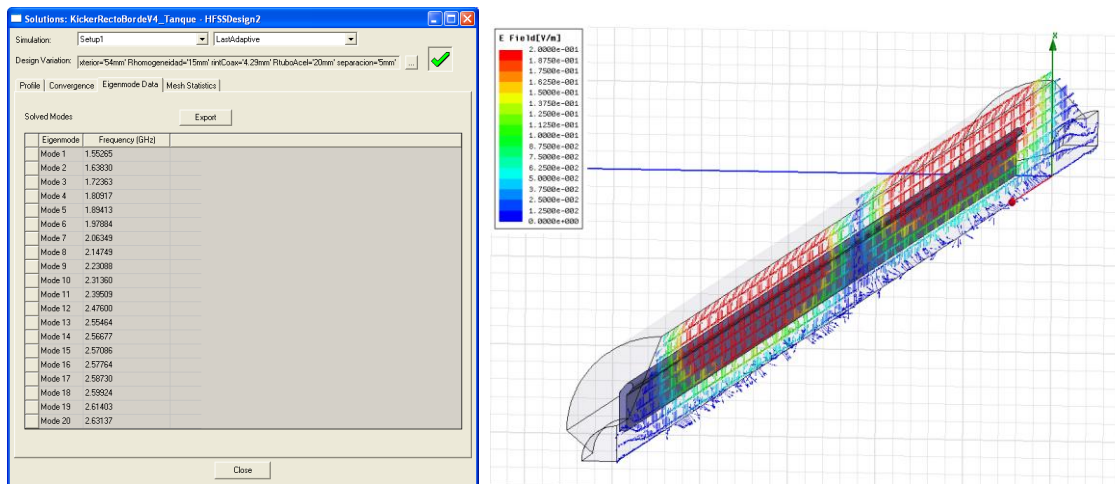


Fig. 4.22 First 20 TM modes calculated from 1.5 GHz (left) and plot of 15th mode (right)

The calculated modes using magnetic symmetries in Fig. 4.22 are TEM modes. The kicker tube together with the two electrodes forms a pseudo-coaxial line which can transmit TEM modes at low frequencies. In contrary, TM modes in such a pseudo-coaxial line would present a very high cut-off frequency (see section 3.5 in [3]), which has also been calculated with a short coaxial line model using HFSS (result is about 8 GHz). Only over this frequency the TM modes can penetrate inside the electrodes gap and an electric field in the axis appears. These TM high frequency modes over 8 GHz can be excited by the beam.

Given the enormous number of TEM modes calculated by HFSS in the estimated frequency range and the impossibility to calculate and analyze other TM modes at their cut-off frequencies, it seems not possible to obtain any other conclusion from this simulation. The simulation using a wire would present similar problems at high frequencies. Therefore, a time domain simulation is the best suited algorithm to find possible dangerous modes excited by the beam.

4.2.8 WAKEFIELD SIMULATIONS

The CTF3 strip-line kicker is located in the Combiner Ring where the beam will only rotate four times before being extracted. Therefore, the effect of the long range wakefields and induced HOMs is expected to be small. Moreover, the stainless-steel structure produces a very bad resonance of the modes (low Q and high attenuation) and therefore matched frequencies should quickly decay due to the high resistivity walls.

The available computers for this analysis are not able to handle a long structure like the CTF3 kicker when the bunch is 3 mm size. Since the device is very long compared to the bunch size, the finite difference method commonly used in time-domain simulation must use plenty of elements in the sake of a good accuracy. The number of meshcells required for a precise simulation of the kicker in CST Particle Studio is higher than 400 million. Indeed, at least twenty elements per wavelength are needed to obtain a good time-domain simulation. That yields an enormous memory requirement (about 50 GB), not affordable by standard computers. That is why the problem was divided into smaller parts which were first studied independently: the input section (Fig. 4.23), the output section (Fig. 4.24), and a full model using a larger sigma bunch (Fig. 4.26), all of them using CST Particle Studio. The end cross section of partial simulations was modelled with an absorbing port to simulate an infinitely long structure, without wake reflection. All the models were configured with absorbing ports in the coaxials, which damp the wakefields for the coupled frequencies up to the first hundred coaxial modes.

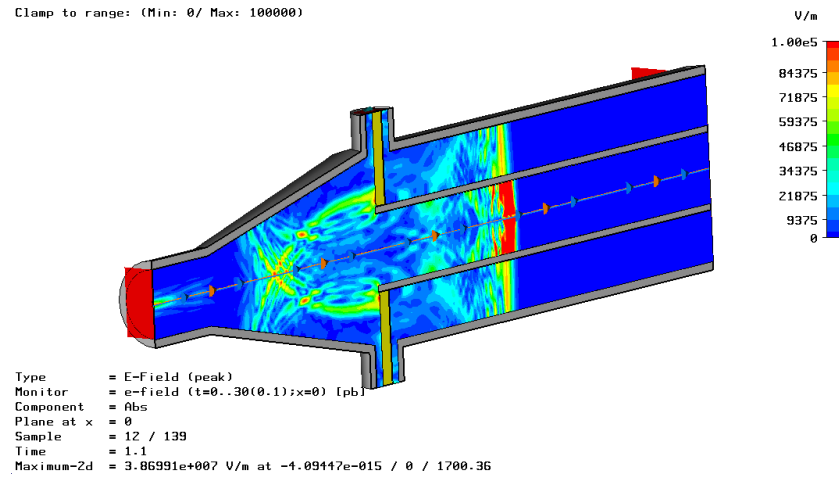


Fig. 4.23 Input section simulation in CST Particle Studio

The simulation of Fig. 4.24 does not exactly represent the exit of a bunch. A bunch exiting the kicker should carry the EM trailing wakefields generated when it first entered the kicker. In Fig. 4.24, the bunch enters through the ideal cross section port and thus there are no scattered wakefields travelling with it when it arrives to the exit discontinuity.

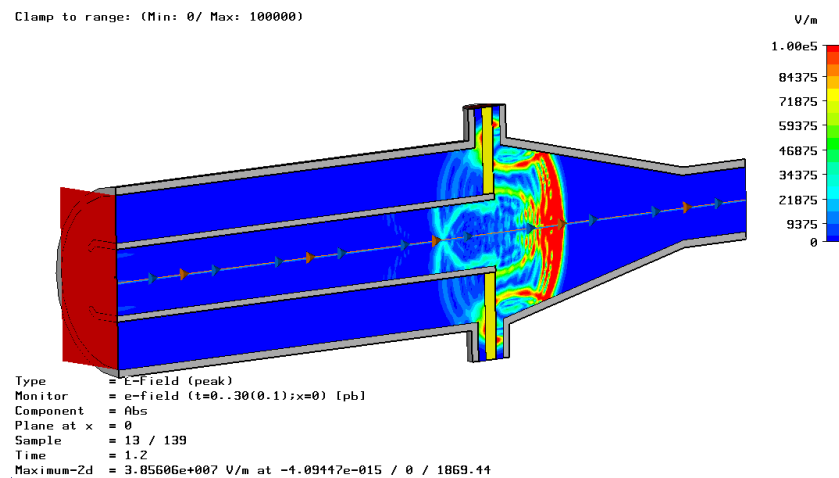


Fig. 4.24 Output section simulation in CST Particle Studio

The partial simulations of the kicker did not have the required precision. More than 66 hours computing and 8 GB of memory were required for each one, though with no real success. Fig. 4.25 shows the wake potential of the simulation presented in Fig. 4.23. The wake potential is not physically possible at the beginning because it appears positive like the bunch excitation. The wake potential should have an initial shape as shown in Fig. 4.9, opposite to the bunch charge. This happens because the wakefields cannot accelerate the head of the same bunch that produces the wakefields; it is not physically possible due to the causality effect and it seems a numerical error.

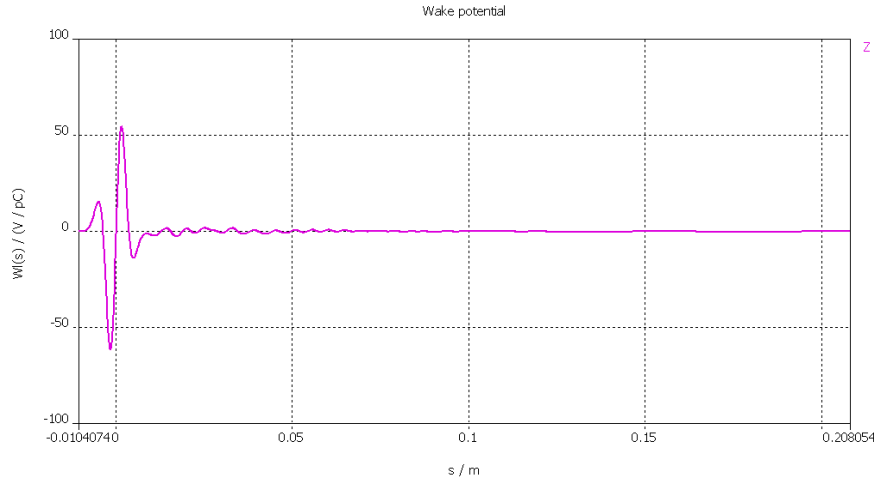


Fig. 4.25 Z wake potential detail up to 0.2 m (calculated up to 4.15 m)

The wake loss factors of simulations presented in Fig. 4.23 and Fig. 4.24 are, respectively, 5.99 V/pC and 4.96 V/pC. Nevertheless, these numbers do not seem very reliable due to the possible numerical errors already indicated and will require further simulations.

Originally, the transitions between the beam pipe and the kicker chamber were done by two identical conical transitions, as previously presented. The results of the wakefield simulations for the full kicker geometry using conical transitions and a longer bunch (Fig. 4.26) were obtained in CST Particle Studio for longitudinal wakes (Fig. 4.27).

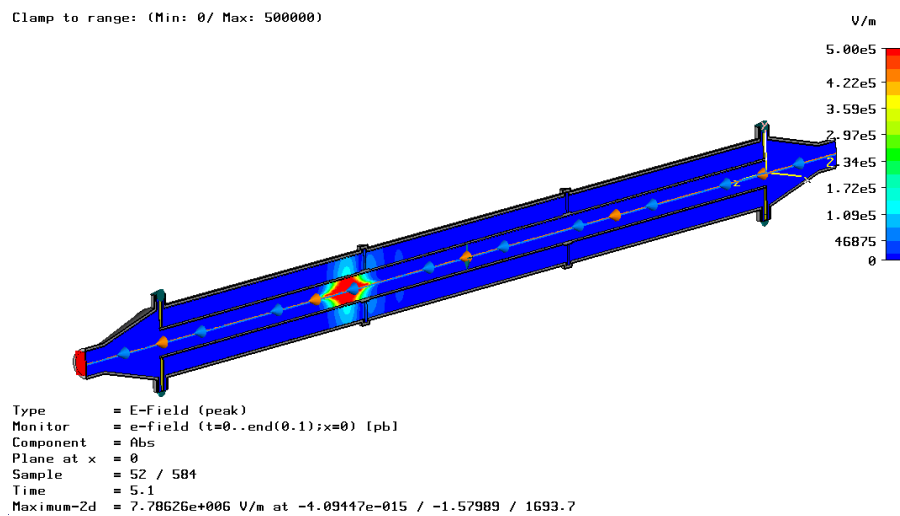


Fig. 4.26 Full kicker simulation in CST Particle Studio (bunch of $\sigma = 28$ mm)

The absorbing effect of the coaxial ports in the second and following reflections of the wake is clearly shown in Fig. 4.27. The wake frequencies coupled to the coaxial ports are rapidly absorbed by them and therefore the second reflection of the wake is almost negligible. The distance between the first two peaks is about twice the device length as shown in the 2D axi-symmetric case. Now, starting wake seems physically possible.

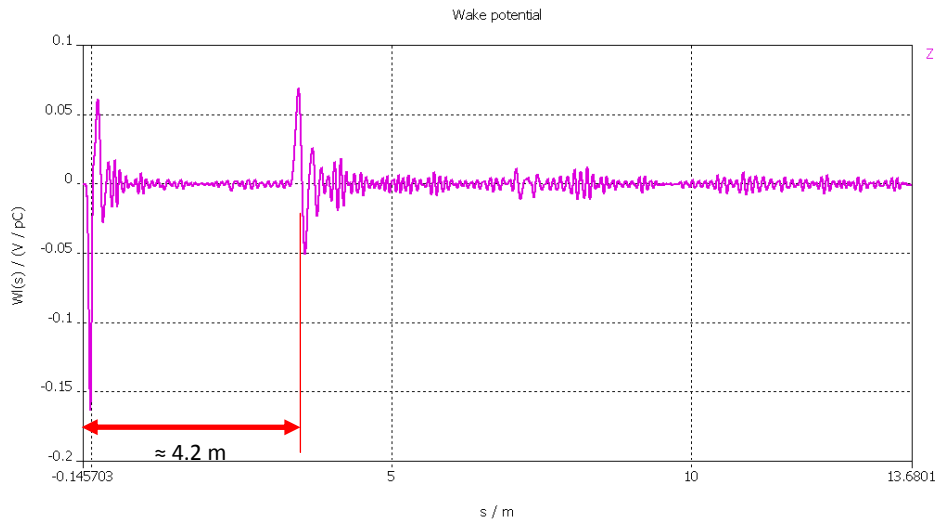


Fig. 4.27 Long range longitudinal wake in CST Particle Studio ($\sigma=28$ mm)

The long bunch used in the simulation (necessary to reduce required memory) is not valid to show neither the real short range wakefield behavior nor the frequency response above 6.3GHz¹². The frequency response of the kicker (wake impedance) is shown in Fig. 4.28.

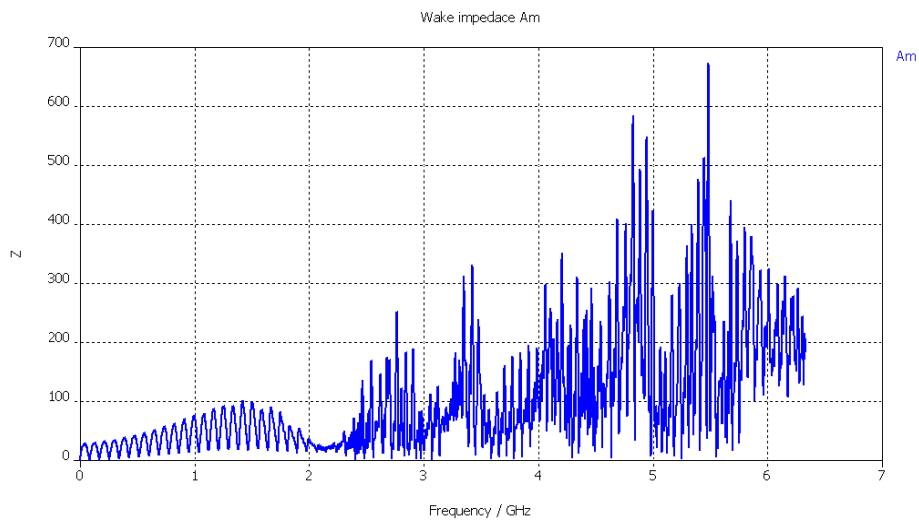


Fig. 4.28 Kicker wake impedance up to 6.3 GHz ($\sigma=28$ mm)

¹² The frequency content of a $\sigma=28$ mm Gaussian bunch is only up to 6.3 GHz.

The kicker behaviour can be clearly observed in Fig. 4.28, where there are many peaks up to 6.3 GHz, which is consistent with HFSS previously calculated modes. The lower frequency part (Fig. 4.29) show the exact maximum-minimum pattern of HFSS simulations, but the other way round¹³.

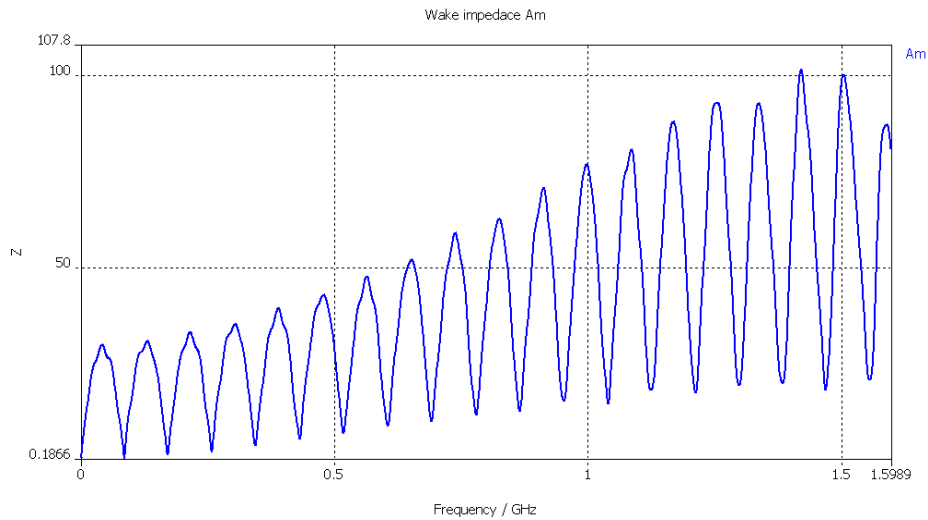


Fig. 4.29 Detailed wake impedance at low frequency ($\sigma=28$ mm)

The high frequency response (Fig. 4.30) presents many impedance peaks. Some of them correspond to modes calculated in HFSS. Furthermore, some of the impedance peaks have been identified as equivalent wavelengths of several characteristic distances in the kicker (separation between electrodes, tube diameter, etc).

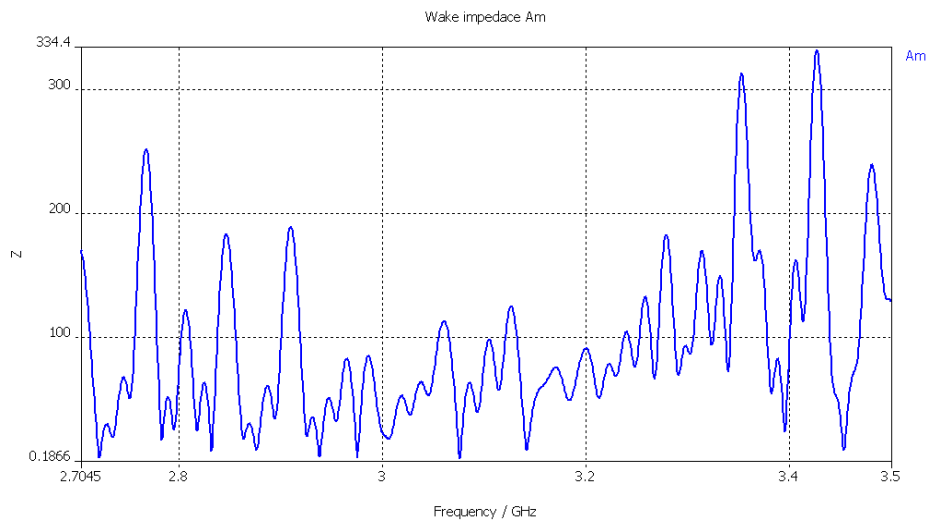


Fig. 4.30 Detailed wake impedance in Z at high frequency (2.7-3.5 GHz, $\sigma=28$ mm)

¹³ The frequency peaks in this simulation correspond to S_{11} parameter drops in HFSS. Peak impedance means a possible resonance which is detected in transmission as a null reflection. However peaks in low frequency modes present very small beam impedance because those modes are hardly coupled to the beam.

The calculated wake loss factor for the $\sigma=28$ mm bunch is 0.0889 V/pC. This value will be higher for the $\sigma=3$ mm bunch.

The kicker was fully simulated for $\sigma=3$ mm bunch (Fig. 4.31 and Fig. 4.32) using GDFidl at CERN (time domain code referenced in chapter 2). CTF3 team in charge of beam stability did not detect major problems after analyzing wake impedance values around resonating frequencies and, therefore, no high order mode damping seems necessary inside the kicker structure.

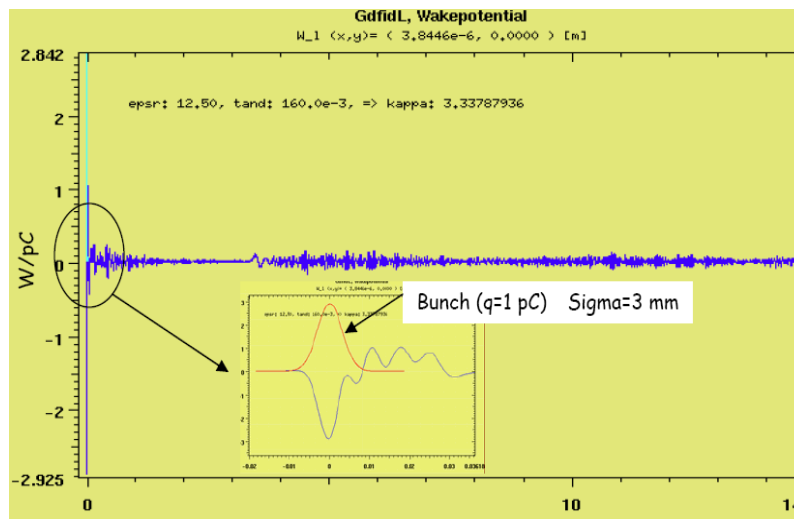


Fig. 4.31 Transverse wake in GDFidl up to 14 m

Fig. 4.32 shows the kicking strength of the kicker when “powered” by the wakefields of 1pC, $\sigma=3$ mm bunch (wake potential in the kicking plane). The kick experienced by particles travelling up to a distance twice the electrode length from the bunch is about 0.1 V/pC. For CTF3 2.33 nC bunch, the undesired kick experienced by those trailing particles is about 233 Volts, a negligible energy compared to particle’s energy.

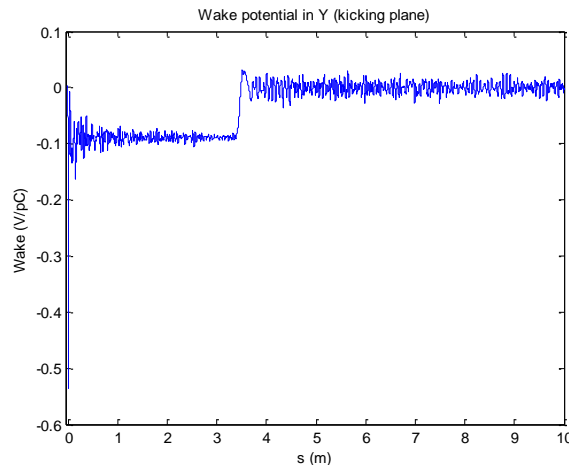


Fig. 4.32 Transverse wake potential in kicking plane (GDFidl)

Due to some modifications on the CTF3 combiner ring layout, the definitive transitions are not symmetric. One half meter long conical transition was designed to fit inside a quadrupole aperture while improving the beam impedance. The other end was made with a short circular to racetrack transition, as it will be detailed in following section. New beam pipe to kicker transitions require updated wakefield calculations. Nevertheless, no major differences are expected.

Calculations using the new transitions (Fig. 4.33) were only developed with GDFidl at CERN servers because of their complexity. Indeed, the required memory is even higher due to the increased length of the device when using the new transitions. Moreover, the CPU processing time is also higher because of the different input and output transitions, which makes the Shobuda-Napoly integration applied to 3-D [4] necessary for good precision.

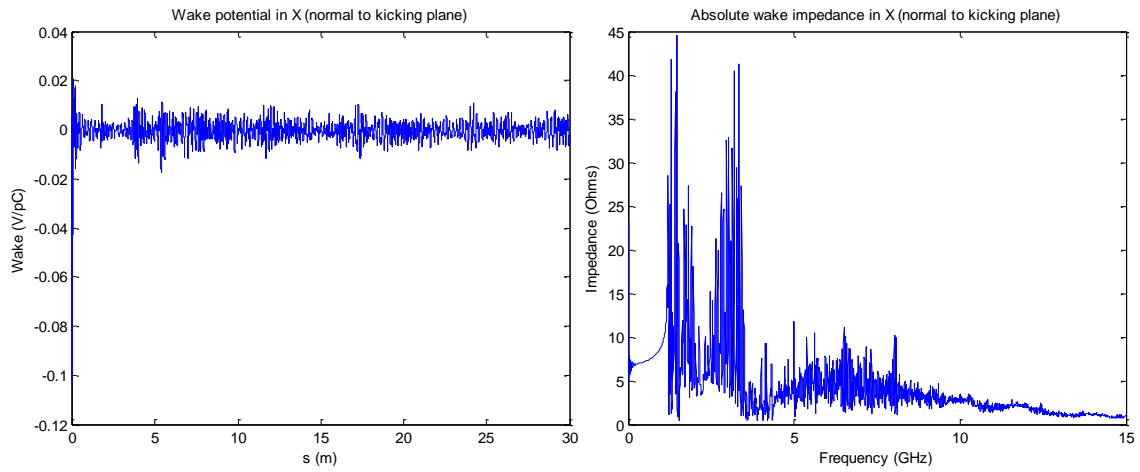


Fig. 4.33 Transverse wake potential and impedance for new transitions in GDFidl

However, it was possible to simulate a shorter length electrode (500 mm) using the final transitions in CST Particle Studio (Fig. 4.34) for a real bunch of $\sigma = 3\text{mm}$. This simulation is developed in order to check the matching between the wake loss factor in ABCI and CST.

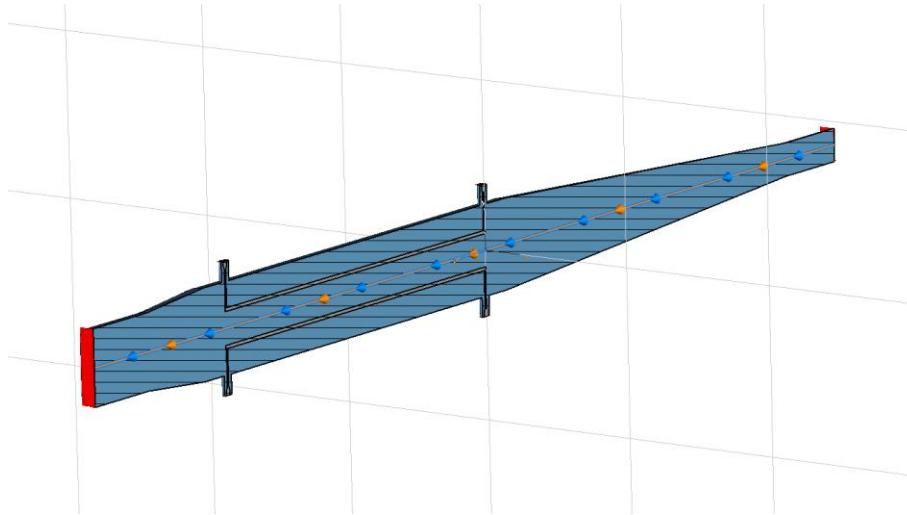


Fig. 4.34 CST Particle Studio model of a short kicker

The wake loss factor is mainly dependant on the beam pipe abrupt transitions. Therefore, the straight part of the electrode should not make a large contribution to the loss factor and can be removed. The 3 mm bunch travelling through the "short" structure can be seen in Fig. 4.35.

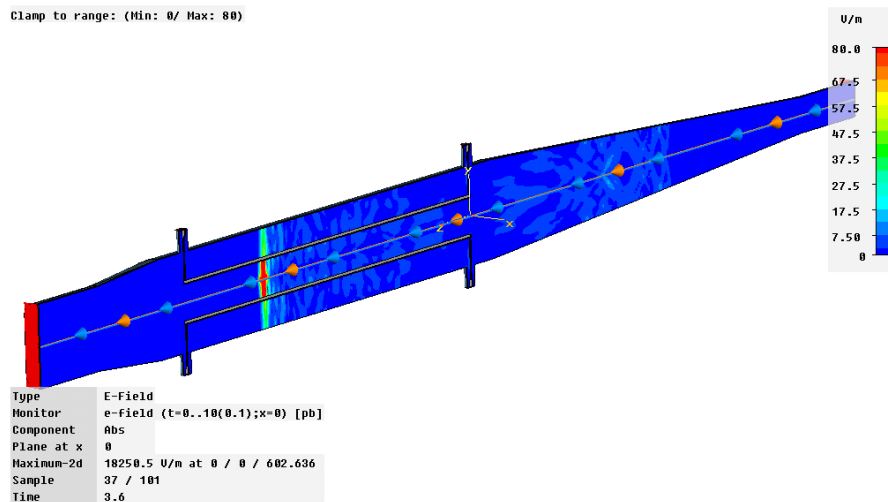


Fig. 4.35 $\sigma = 3$ mm bunch travelling through the "short" kicker

The wake loss factor obtained in the simulation of Fig. 4.35 was 2.28 V/pC^{14} . This figure is in the same range of the ABCI's calculated value for the new transitions (1.74 V/pC). Obviously, ABCI is not considering the real racetrack beam pipe and thus the smaller loss factor. This result validates the axi-symmetrical simulation as an approximate solution for kicker-like structures.

¹⁴ This number is not calculated with high precision because the different input and output transitions in 3D require a direct integration method which is much less precise for a given mesh.

All these results were analyzed by CTF3 team and it was concluded again that no major problems are expected regarding the wakefield behaviour for the CTF3 Combiner Ring kicker.

4.3 CTF3 KICKER MANUFACTURING ISSUES

Many ideas have been shown in chapter 3 as general recommendations for manufacturing a strip-line kicker. Consequently, in this section, only specific manufacturing issues regarding the CTF3 CR kicker will be presented.

The kicker has been drawn using 3D CAD software [5] starting from previous electromagnetic models. Minor modifications have been applied to the EM models to make the prototype, most of them due to mechanical considerations.

4.3.1 MATERIAL SELECTION

Stainless-steel was the preferred option for the manufacturing of the whole kicker. It is easily weldable to the commercial feedthroughs and stainless-steel flanges, it is stiff enough to be able to design thin and long electrodes and it should damp resonant frequencies very well. The aluminium structure would present many difficulties for welding (flanges, feedthroughs, supports) and more problems if heated up in a bake-out operation (stiffness loss). Therefore it was consulted to CTF team for beam issues when using stainless-steel and they agreed to build the whole kicker (tank and electrodes) in stainless-steel.

The stainless-steel used for the whole kicker is named AISI 304L (DIN 1.4306), which is a very good material for high vacuum purposes.

4.3.2 FEEDTHROUGHS

About 14.5 kV are required to feed each strip-line. Then it is necessary to find a feedthrough capable of this voltage level. It is also recommended to obtain a constant impedance feedthrough at 50 Ω . However it was not possible to find any commercial feedthrough featuring constant impedance at 15 kV. The alternative was to select a SHV type feedthrough which can support up to 20 kV (Fig. 4.36).

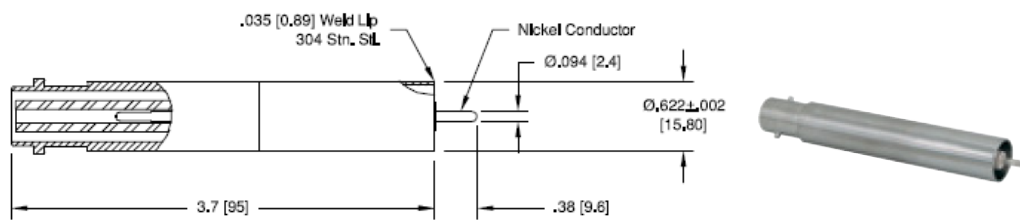


Fig. 4.36 Ceramaseal SHV 20 kV feedthrough

The feedthrough is weldable to the kicker tank. Nevertheless, the thickness of the weld lip is less than 1 mm and therefore a case (Fig. 4.37) was designed as an interface for welding to the thicker kicker tube.

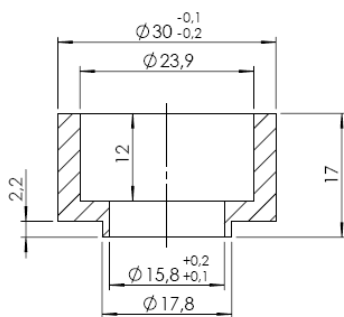


Fig. 4.37 Case to weld the feedthroughs to the kicker tube (left) and feedthrough welded to the kicker tube (right)

The connection to the electrode was done using a highly flexible copper cable. The feedthrough pin was connected to the cable using a barrel type connector (Fig. 4.38) and the cable was connected to the electrode using an electrical terminal fixed by a bolt. The flexible cable length was calculated to absorb the longitudinal expansion of the electrode up to a temperature increment of 100 °C¹⁵ relative to the tube temperature.

¹⁵ The electrode is fixed in the middle and therefore only the half longitude enlarges when heated. The linear expansion coefficient of stainless-steel is 18e-6. For 1.7/2 m, the maximum elongation at 100 °C is 18e-6*100*1.7/2 = 1.5 mm.

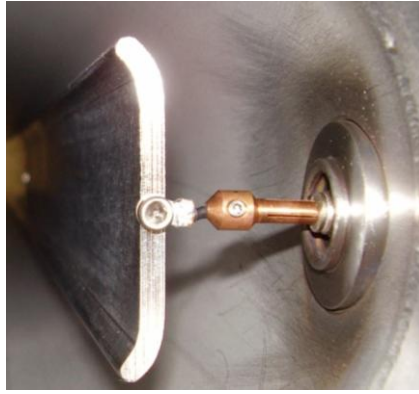


Fig. 4.38 Flexible connection between the feedthrough and the electrode

The air side plug obviously supports 20 kV and it features a bayonet fixation like BNC connectors (Fig. 4.39).



Fig. 4.39 Air side plug for SHV 20 kV feedthroughs

4.3.3 STAND-OFFS SUPPORT

The stand-offs should hold the electrodes in their position and insulate the high voltage from the tube as it was described in section 3.2.3. They were selected to support 20 kV in vacuum. The selected stand-offs were taken from Allectra manufacturer, reference 273-CSO-50-20, 51 mm high and 19 mm diameter. Both ends are threaded for an ANSI 10-32 screw.

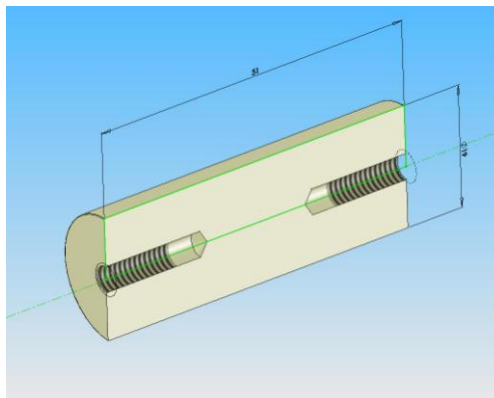


Fig. 4.40 Allectra steatite stand-off

Many problems were found when screwing the bolts in the stand-off thread. The precision is poor and the ceramic is very fragile. Therefore it was decided to avoid screwing if possible. The thermal interference method exposed in chapter 3 was used to fix the stand-off to the kicker tube thus avoiding one of the bolts (Fig. 4.41).

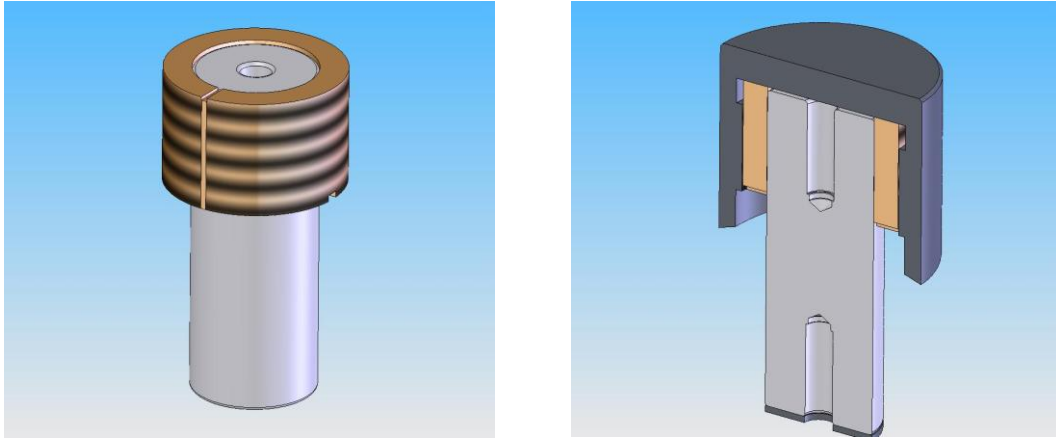


Fig. 4.41 Thermal interference method to fix the stand-offs

The copper case was machined at 40 microns smaller diameter than the ceramic to ensure thermal fixation without breaking the ceramic or the case. Stresses simulated in FEM code did not show values above ceramic break stress or copper fluency limit. A copper washer was installed in the ceramic-to-electrode contact zone to avoid direct ceramic to steel friction.

In the electrodes side, the stand-offs were fixed by simple bolts. Four stand-offs were screwed by interleaving a separator ring to allow sliding due to the thermal movement of the electrodes (Fig. 4.42).

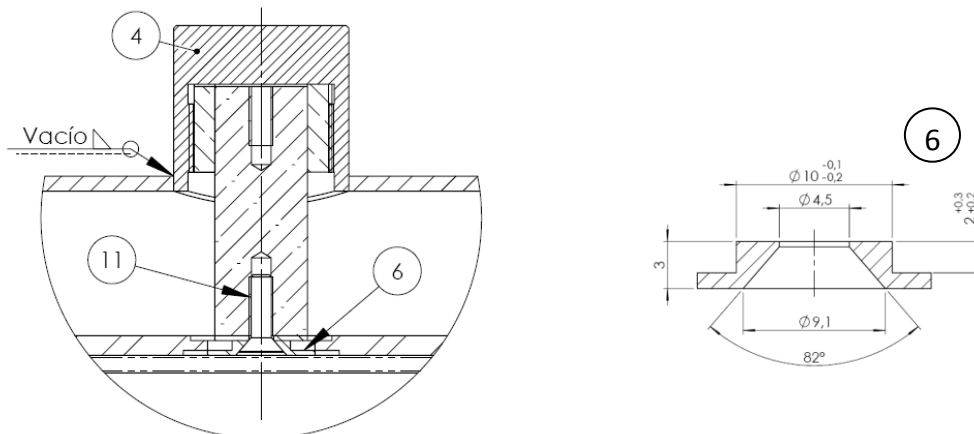


Fig. 4.42 Sliding stand-offs fixation method (left) and separator ring (right)

The fixed stand-off was simply screwed to the electrode (Fig. 4.43).

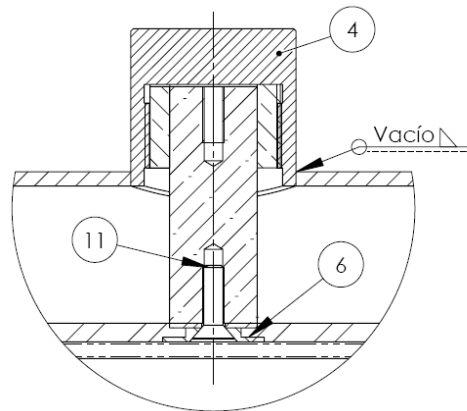


Fig. 4.43 Fixed stand-off fixation method

4.3.4 ELECTRODES

The electrodes were manufactured from a 4mm thickness stainless-steel sheet. The edges were folded to 42 degrees and then cut to the final dimension (Fig. 4.44). The edges were finished by milling.

Five holes were machined in the electrodes to support the stand-offs (Fig. 4.45). Four of them were sliding for thermal expansion and the middle one was round and fixed. Two screwed holes were machined in the electrode ends to connect the feedthroughs.

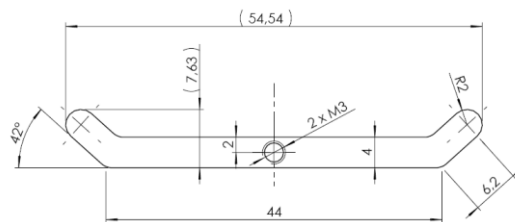


Fig. 4.44 Kicker electrode cross section

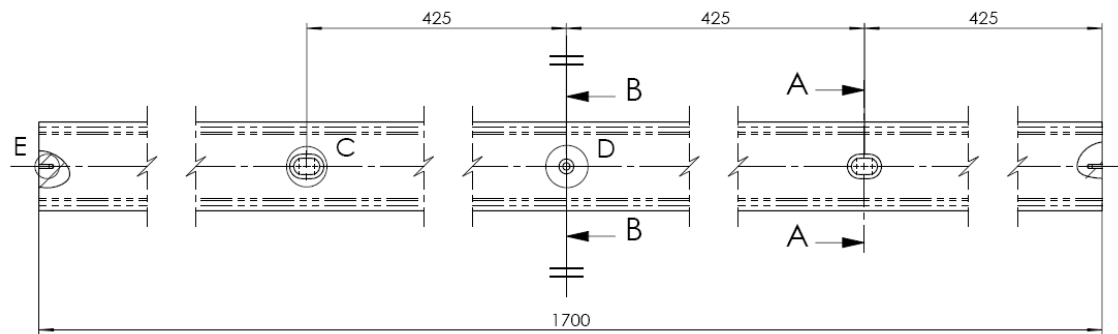


Fig. 4.45 Kicker flat electrode with support holes

4.3.5 FLANGES

The flanges to seal the kicker tube were standard CF150 machined from a blank flange and slightly modified to improve their characteristics. The usual welding preparation (welding slot) was eliminated to allow a smooth internal surface. In addition, the inner diameter of the flange is exactly the same as the inner kicker diameter.



Fig. 4.46 CF 150 Flange

4.3.6 BEAM PIPE TRANSITIONS

Initially, the beam pipe transitions were both designed and manufactured in a conical shape (Fig. 4.47). Two different commercial cones were welded to form the longer transition.

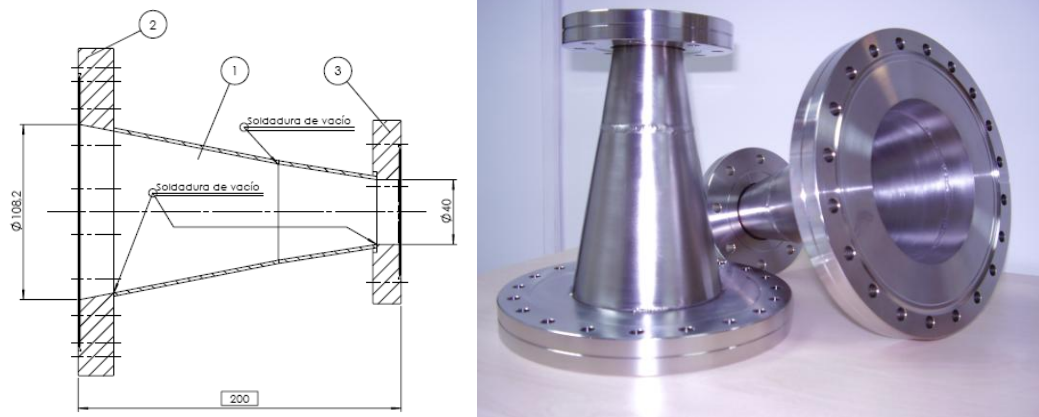


Fig. 4.47 Previous beam pipe transitions

Due to last minute modifications and to fit one kicker transition inside the aperture of a corrector magnet, both transitions were redesigned and manufactured. One was designed conical, 561 mm long and the other, racetrack, 106 mm long (Fig. 4.48).

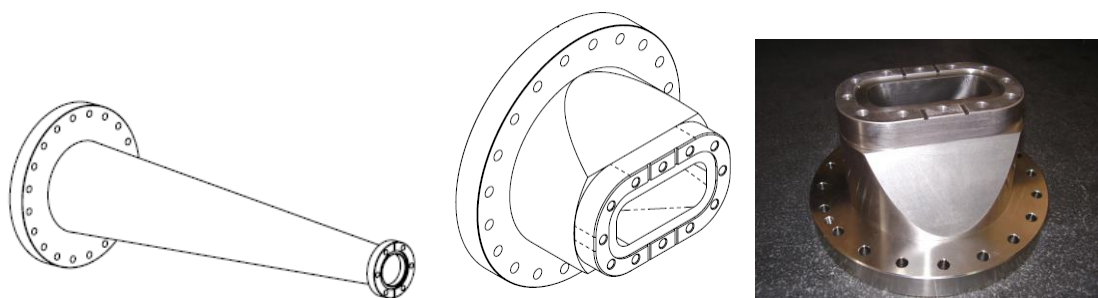


Fig. 4.48 New transitions design

The inner design of both new transitions was optimized to maintain a smooth transition from the kicker tube to the beam pipe. Therefore, CNC was used to machine the inner part of the racetrack transition.

4.3.7 MECHANICAL SUPPORTS AND ALIGNMENT TARGETS

Two flat supports were added to fix three male centering pieces according to CERN specifications. The flat surfaces were precision machined in reference to the kicker axis. The distance from the kicker axis to the flat support surfaces was 132 ± 0.1 mm.

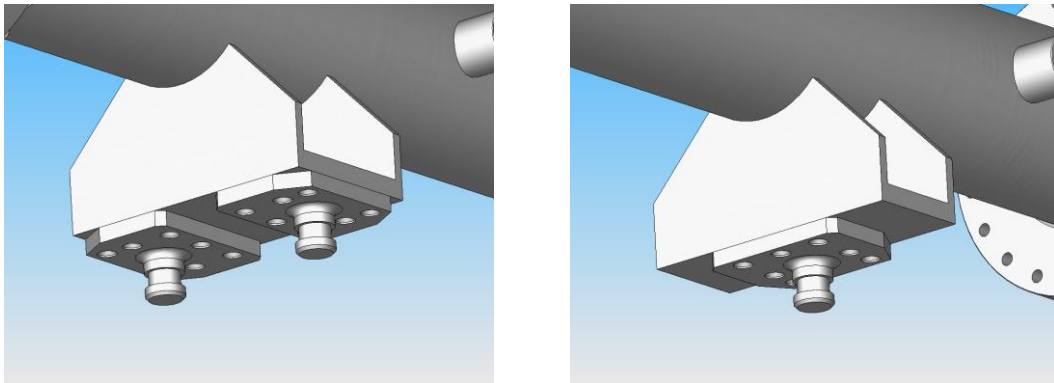


Fig. 4.49 Three male supports attached to the CTF3 kicker flat surfaces

Two additional flat surfaces were machined in the top of the kicker to position the alignment devices (Fig. 4.50). The elevation from the device axis was 274 ± 0.1 mm. The flat surfaces were supported by a very rigid structure to avoid vibrations when machining.

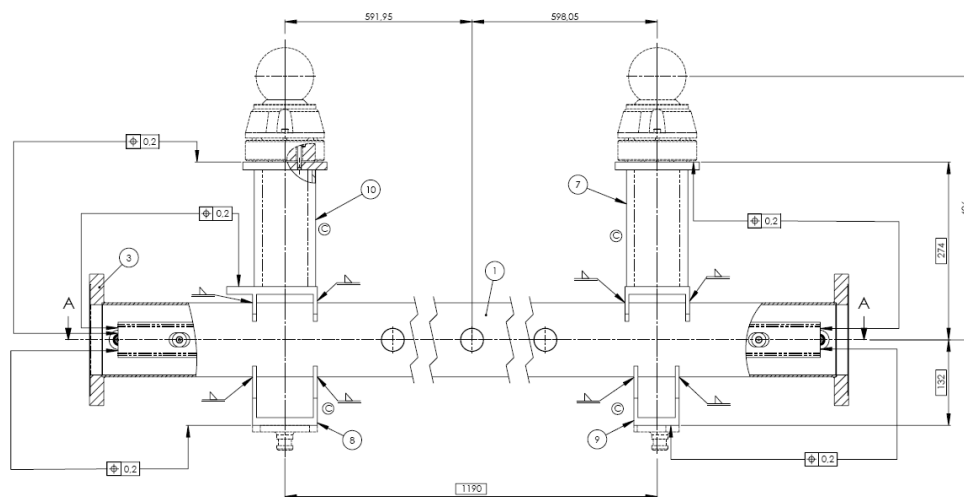


Fig. 4.50 Alignment devices in the top of the structure



Fig. 4.51 Final manufactured device before installing the new transitions

4.4 TESTS RESULTS

The CTF3 CR kicker was tested in INFN/LNF RF laboratory at Frascati (Italy). All the required equipment (such as the pulser, DC power supply, loads, etc.) was not available in our laboratory and the costs were too much to afford at that time. The following chapter 5 will show a device fully manufactured and tested in our laboratory.

The tests were done using the old beam pipe transitions design because the new design was not available yet. Nevertheless, the EM tests developed are not affected by the transitions installed.

4.4.1 *RF NETWORK ANALYZER TESTS*

The RF test was developed using a 2 port network analyzer (Fig. 4.52). Therefore, hybrid junctions were necessary to split and de-phase the signals as indicated in chapter 3.



Fig. 4.52 2 port network analyzer used for the RF tests

All the connections using the hybrids are effectuated as it was presented in chapter 3. Fig. 4.53 shows the hardware connection of one hybrid to one of the ends of the strip-lines. The fourth port of the hybrid should be terminated with a $50\ \Omega$ load to avoid signal reflection and measurement mismatch.

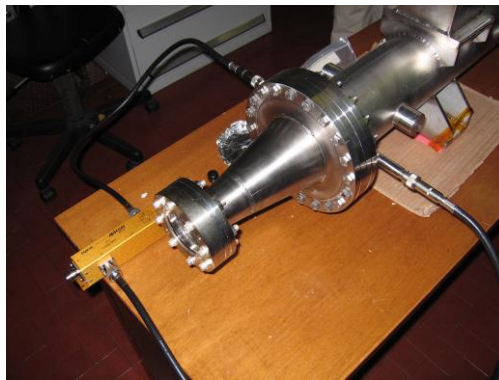


Fig. 4.53 Hybrid connection to the kicker end

Many problems arose due to the cables and calibrations at high frequencies in the tests (over 1 GHz). Therefore we only assume to be valid the measurements at medium and low frequency. This fact does not represent a problem because the real pulse has frequency contents up to 30-50 MHz (200 ns pulse) and the high frequency response is not so important.

Two different hybrids were used for the tests featuring different frequency response ranges. Thus it was possible to detail the lowest frequency response of the kicker.

The measured frequency response (Fig. 4.54) is fairly similar to the HFSS results shown in Fig. 4.17, especially at low frequency.

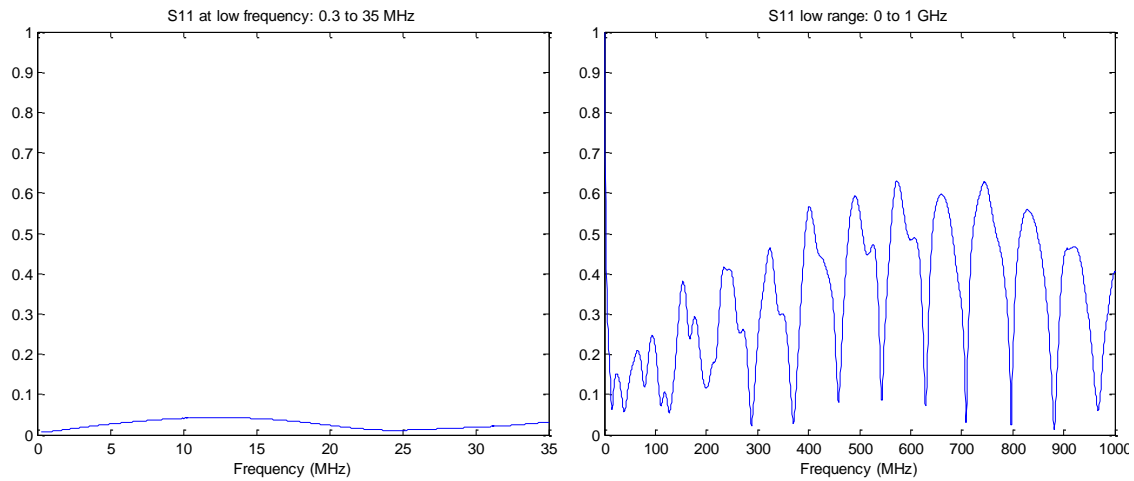


Fig. 4.54 S_{11} at low and medium frequency

The S_{11} value for the 0 to 1 GHz range shown in Fig. 4.54 presents wrong values at lowest frequency because of the hybrid own frequency band (2MHz to 2 GHz). The multiple peaks below 300 MHz are because the calibration of the cables and hybrids was not perfect.

Both strips were also measured separately without using hybrids (matching the other strip-line using 50 Ω loads). The results were quite similar in both strips (Fig. 4.55), except from several peaks in one strip-line that seem to be connection problems in the tests which we were not able to avoid. An HFSS model to compare these measurements was not developed because it required a full 3D simulation (no symmetries) whose memory demands were above our computer capabilities.

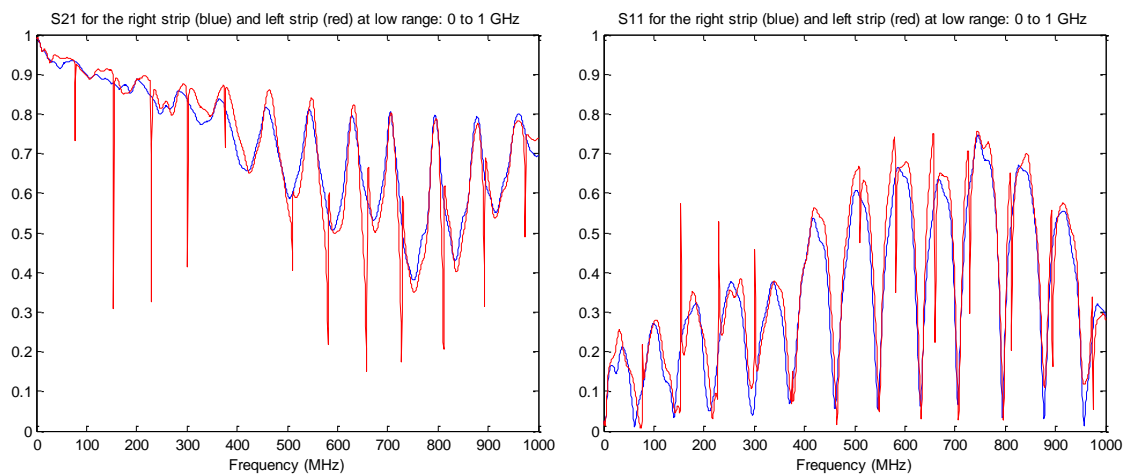


Fig. 4.55 S_{21} and S_{11} in both strip-lines

4.4.2 UNLOADED VOLTAGE TESTS

High vacuum is required to effectuate the high voltage tests in order to avoid the electric breakdown of air. The kicker was leak tested using helium in a bag just after manufacturing, to check all the vacuum welds and feedthroughs. The leak test was successful and 1.2×10^{-10} mbar.l/s leak rate was achieved.

In order to develop the high voltage tests, the kicker was pumped during three days using a standard turbo-molecular pump. 2×10^{-7} mbar were achieved after that time. Although cleaning and handling of every kicker component was done according to section 3.3.6, further bake-out was required to install the kicker in the CTF3 Combiner Ring in order to reach 10^{-8} mbar. However, 2×10^{-7} mbar were more than enough for high voltage tests.

After the vacuum was stabilized, the kicker electrodes were independently tested with DC voltage (no current) up to 17.68 kV. Except for some sparks in the initial instants¹⁶, no further problems were found in the DC high voltage test.



Fig. 4.56 DC High voltage test up to 17.68 kV

¹⁶ Small surface impurities or invisible dirt can be the origin of some sparks when the voltage is first applied. However, the sparks should end when all the impurities are burnt.

4.4.3 50 OHM LOADED VOLTAGE TESTS

The only pulser available in Frascati was about 16 kV peak, 5 ns duration. This is far away from kicker pulse specifications. However, the high frequency content of the pulse can determine if the kicker is effectuating a good conduction of the EM power. A slower pulse will always pass through the kicker with fewer problems. The pulser had only one output port and therefore the pulse was applied to one of the strip-lines at once (Fig. 4.57). The pulser was connected to one coaxial port and the 50 Ohm load was connected to the other coaxial port of the same strip-line.



Fig. 4.57 Assembly of the high voltage pulse test

The pulse was firstly directly discharged over the loads without passing through the kicker (Fig. 4.58). The real pulse was therefore characterized and compared to the pulse passing through both strip-lines of the kicker.

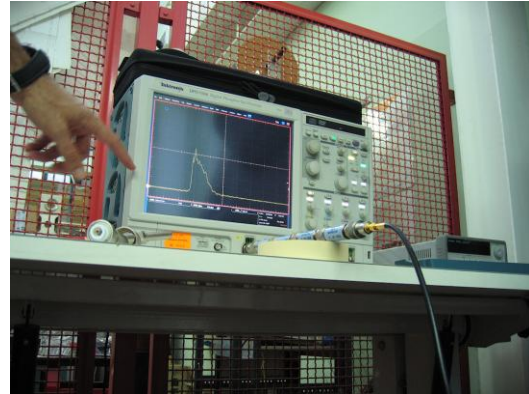
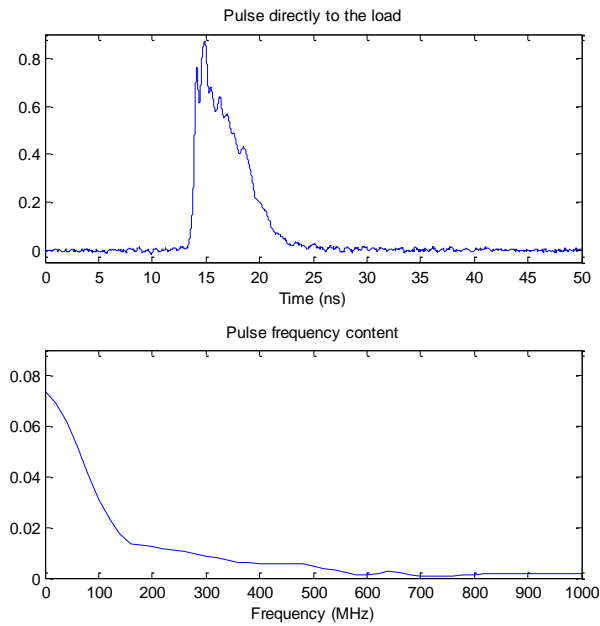


Fig. 4.58 Pulse directly over the 50 Ohm load

The very fast pulse passed through the kicker with minor modifications (Fig. 4.59). Only the highest frequencies above 500 MHz were appreciably smoothed. The oscillating frequency content of the pulse between 100 and 500 MHz is due to the maximum-minimum pattern of the kicker scattering parameters (Fig. 4.54). However, the kicker was designed for pulses 40 times slower, and these results can be considered excellent. The transmission of the real pulse (70 ns rise time, 200 ns flat top) is expected to be perfect.

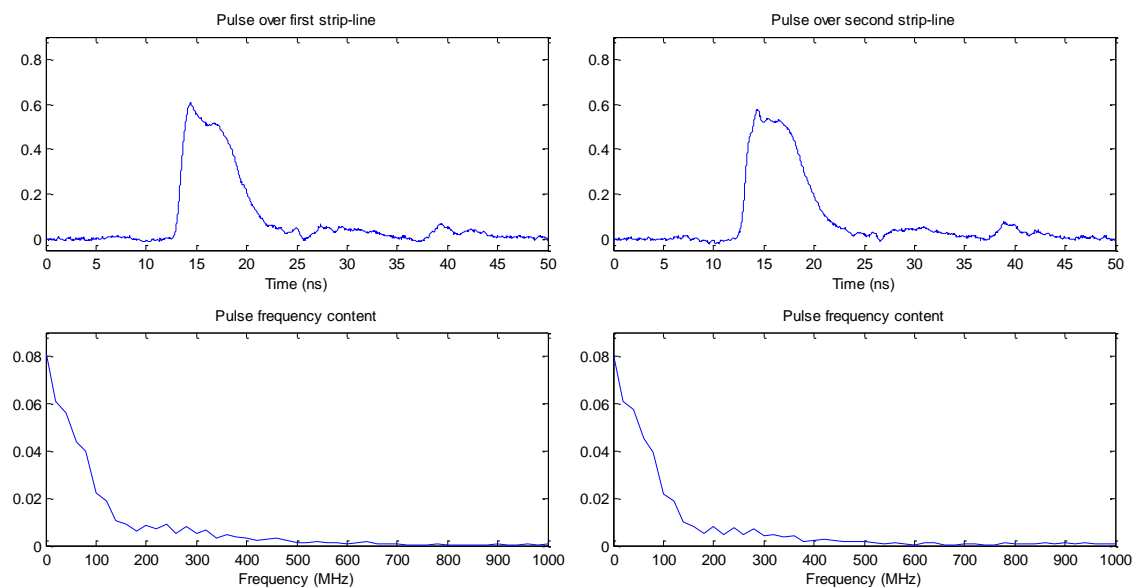


Fig. 4.59 Pulse passing through the kicker along both strip-lines

4.5 CONCLUSIONS

The calculation methodology and fabrication procedures developed by the author in the previous chapters have been successfully applied to the CTF3 Combiner Ring kicker.

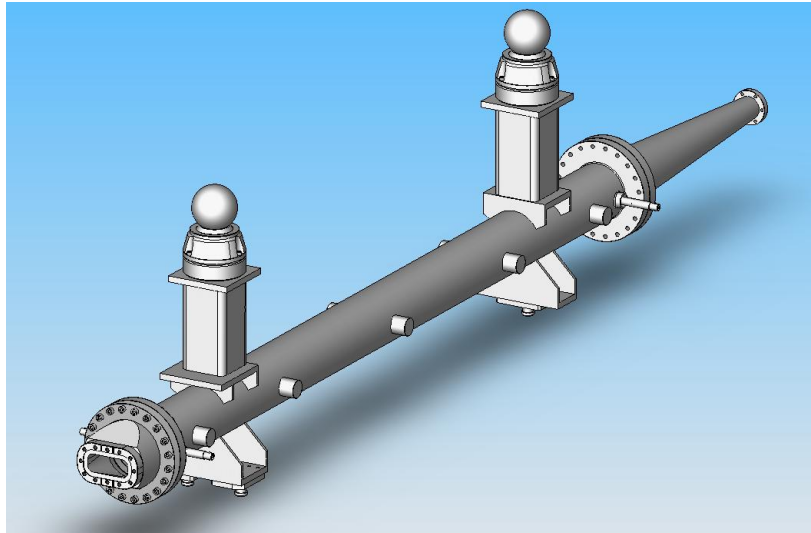


Fig. 4.60 Full 3D manufacturing model of the CTF3 strip-line kicker

Starting from a few specifications, the full design, simulation and manufacturing of the kicker has been carried out bearing in mind many considerations: available materials, ease of fabrication, RF response optimization and wakefield behaviour. The author has been in charge of the full calculation and design process, together with the monitoring of the fabrication and tests. Each device has its own challenges and there is no simple method to effectively automate the design phase. For example, HOMs analysis and wakefield behaviour represent a challenging calculation, different for every device and accelerator. However, the proposed method has been shown effective to simplify the virtually undocumented task of designing a strip-line kicker from the beginning.

The kicker was installed in the CTF3 Combiner Ring at CERN (Geneva) on mid-2008 and it is now successfully working together with many other devices of the accelerator (Fig. 4.61).

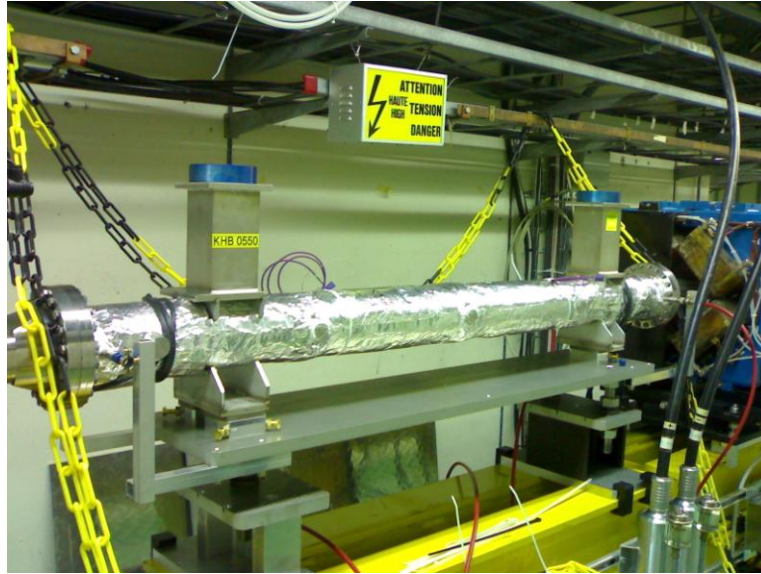


Fig. 4.61 Kicker installed and working in the Combiner Ring

4.6 REFERENCES

- [1] **The CLIC Study Team.** A 3 TeV e^+e^- Linear Collider based on CLIC technology. Geneva : CERN 2000–008, 2000.
- [2] *An introduction to CTF3; CTF3 Meeting.* **Corsini, R.** Geneva : s.n., 2000.
- [3] **Pozar, David M.** *Microwave Engineering.* s.l. : Wiley, 2004. 978-0471448785.
- [4] **Henke, H. and Bruns, W.** Calculation of wake potentials in general 3D structures. Edinburgh : EPAC, 2006. WEPCH110.
- [5] **SolidWorks Corp.** SolidWorks :: 3D CAD Design Software. [Online] Dassault Systèmes, 2008. <http://www.solidworks.com/>.

CHAPTER 5

SECOND APPLICATION TO A REAL DEVICE: CTF3 TL2 TAIL CLIPPERS

5.1 PURPOSE OF THE CTF3 TL2 TAIL CLIPPERS

As it was presented in previous chapter, the CLIC Test Facility-3 (CTF3) is to demonstrate the concept behind the high frequency RF generation with a drive beam of electrons [1]. This drive beam must have a definite bunch length to achieve high efficiency for RF generation and, consequently, the bunch length control of the drive electron beam is essential. The Transfer Line-2 (TL-2) will transport the electron beam at nominal energy of 150 MeV (peak energy 200 MeV) from the Combiner Ring (CR) to the CLEX area (CLIC Experimental area, Fig. 5.1). This transfer line will be used not only for proper transport of the beam but also to finally control the bunch length of the electron beam in a magnetic bunch compressor, just before the beam delivery to the experimental area. The beam length is also controlled in the TL-2 to allow for testing of different beam lengths in CLEX RF equipment. Keeping these points in view as well as that the CTF3 is a test facility, the TL-2 is designed so that it can control the bunch length and the beam length over a wide range.

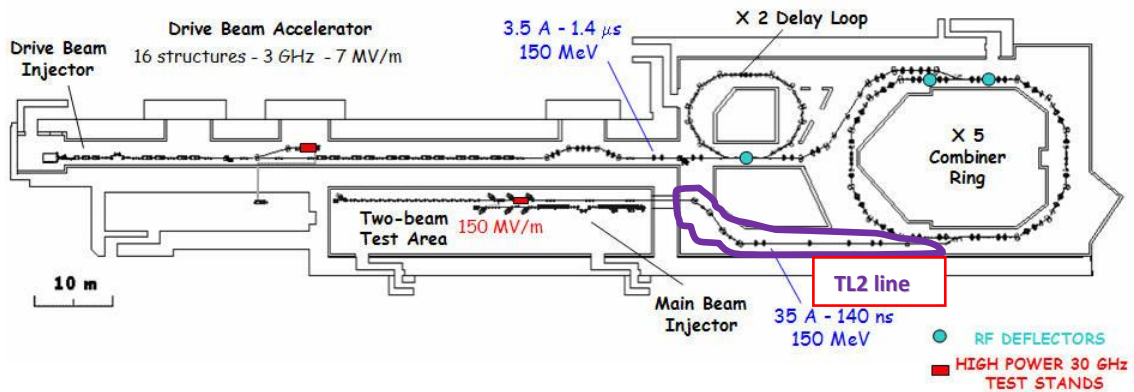


Fig. 5.1 TL-2 line location in the CTF3 layout

The straight zone of the TL-2 line (Fig. 5.2) locates the main structures used to shorten the beam; the Tail Clippers. The Tail Clippers are a system of kicker and a collimator which will allow shortening the bunch trains (beam) for conditioning the CLIC RF equipment in CLEX. These devices work by cutting the beam at a given length and discarding then the unused beam into a damping system. Their response must be very fast since the beam is usually only few tens of nanoseconds long. Furthermore, the field rise time must be extremely fast to allow a sharp cut without affecting the leading bunches when the beam is passing. Therefore, Tail Clippers must be designed using strip-line kicker technology.

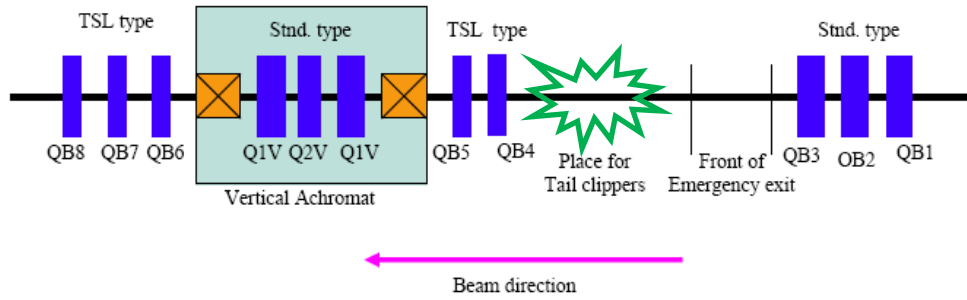


Fig. 5.2 Straight zone of TL-2 line where Tail Clippers are installed

The specifications of the Tail Clippers are presented in Tab. 5.1. As CTF3 is a test facility, the beam energy specifications are a bit over the nominal to allow for testing. Field homogeneity is very relaxed, as the beam affected by the kick is discarded and there is no need to exert a homogeneous kick over all the particles. The deflection is done in a vertical plane, which requires the electrodes to be parallel to the horizontal plane.

Tab. 5.1 Tail Clipper specifications

Magnitude	Value	Units
Beam Energy	200	MeV
Deflection Angle (in vertical plane)	1.2	mrad
Strip-line plate separation	≥40	mm
Field homogeneity (±20%)	30	mm
Characteristic impedance	50±1	Ω
Pulse length (max.)	140	ns
Maximum field rise-time (0.25 to 99.75%)	5	ns
Maximum timing jitter	1	ns
Repetition rate (nominal-maximum)	5-50	Hz
Number of strip-line sections	4	
Total available straight section length	1625	mm
Pumping ports	none	
Material	Stainless steel or Antico¹	

A specific challenge of this design is the need to split the device in 4 smaller units. This is required to allow for the field to fill in the strip-lines fast enough between two bunches in order to avoid deflecting unwanted bunches or using an extremely fast rise time power supply [2]. The maximum permissible pulse rise time is given in Eq. (5.1).

$$T_r = \left(\frac{l_b}{c}\right) - \left(\frac{2 l_s}{N c}\right) \quad (5.1)$$

where l_b is the relativistic length between bunches, l_s is the overall strip-line length and N is the number of strip-lines in which l_s is divided. Longitudinal bunch size in CTF3 is negligible for these calculations (3 mm).

For the CTF3 inter-bunch spacing ($l_b/c = 5$ ns), it would be impossible to completely raise the field in about 1.5 meter individual strip-line before the next bunch enters the kicker². Therefore, splitting the strip-line is necessary to avoid using an extremely high voltage power supply for a too short individual strip-line.

¹ Anticorodal® -110 is an aluminium alloy with good corrosion resistance and welding properties, perfect for machined parts and welded constructions.

² The pulse needs to travel the strip-line length (opposite direction) in a time shorter than 5/2 ns before the following bunch arrives.

The maximum strip-line length in CTF3 (for an ideal pulsed power supply) would therefore be 0.75 m (Fig. 5.3). The pulse enters the strip-line at $t=0$ ⁽³⁾ through the opposite side from which the bunch enters the kicker⁴. The bunch travels at c and also the pulse (in opposite directions). At $t=l_b/2c$, the bunch has arrived the kicker entrance and the pulse has also arrived the output feedthrough. The field in the kicker is now constant along its length and the bunch is homogeneously deflected.

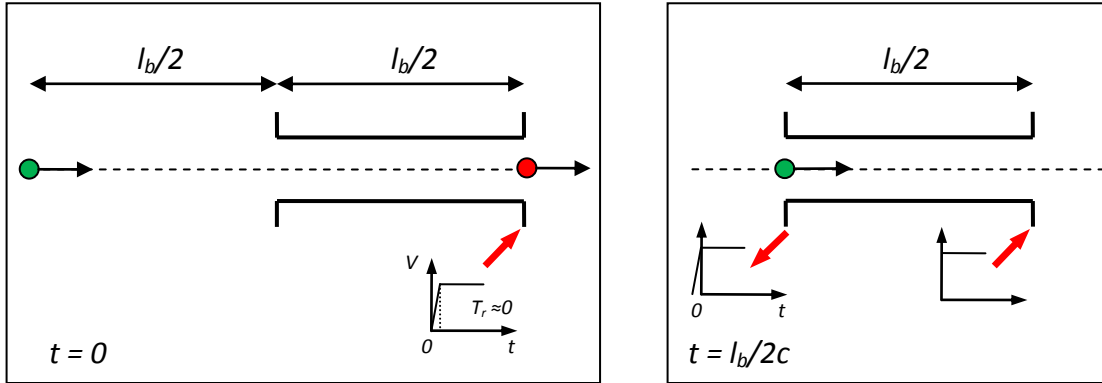


Fig. 5.3 One $l_b/2$ length strip-line fed by $T_r=0$ pulser

However, there is no power supply featuring $T_r=0$. Splitting the strip-line of Fig. 5.3 in two parts (Fig. 5.4), the maximum permissible pulse rise time increases to 2.5 ns, as indicated by Eq. (5.1). Identical logic can be applied to understand the split system just bearing in mind the rise time of the pulse.

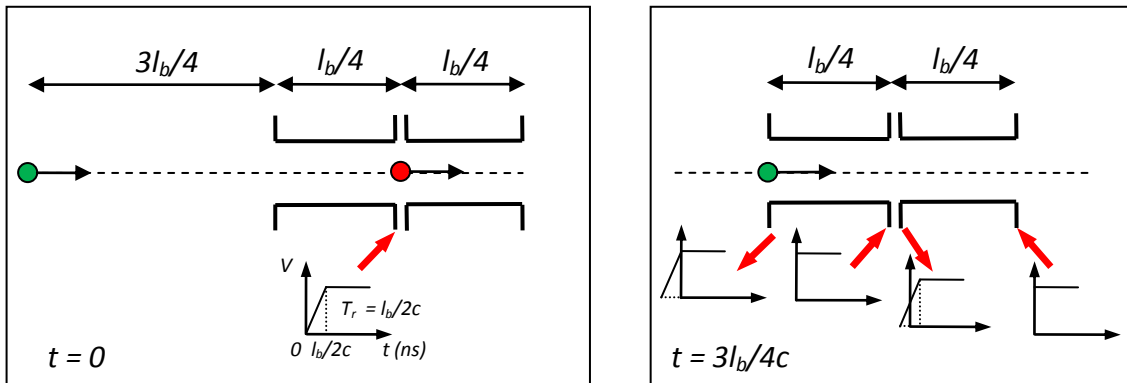


Fig. 5.4 Two $l_b/4$ length strip-lines fed by $T_r = l_b/2c$ pulser

The split length calculation process for the CTF3 Tail Clippers will be detailed in section 5.2.2.

³ At $t=0$ the previous bunch has just exited the kicker.

⁴ As it was indicated in chapter 1, this is required to avoid electric and magnetic fields force cancellation over the particles.

5.2 CALCULATIONS

5.2.1 THE CROSS SECTION CHOICE

The characteristic impedance selected for the whole design is again $50\ \Omega$ to permit commercial components to be used and also an optimal trade between power transmission and losses.

The cross section choice process has been developed as it was done for the Kicker in previous chapter. The selected external coverage for the strip-lines is cylindrical to ease fabrication. The three possible cross sections analyzed for this design in HFSS can be observed in Fig. 5.5. All of them feature $50\ \Omega$ characteristic impedance.

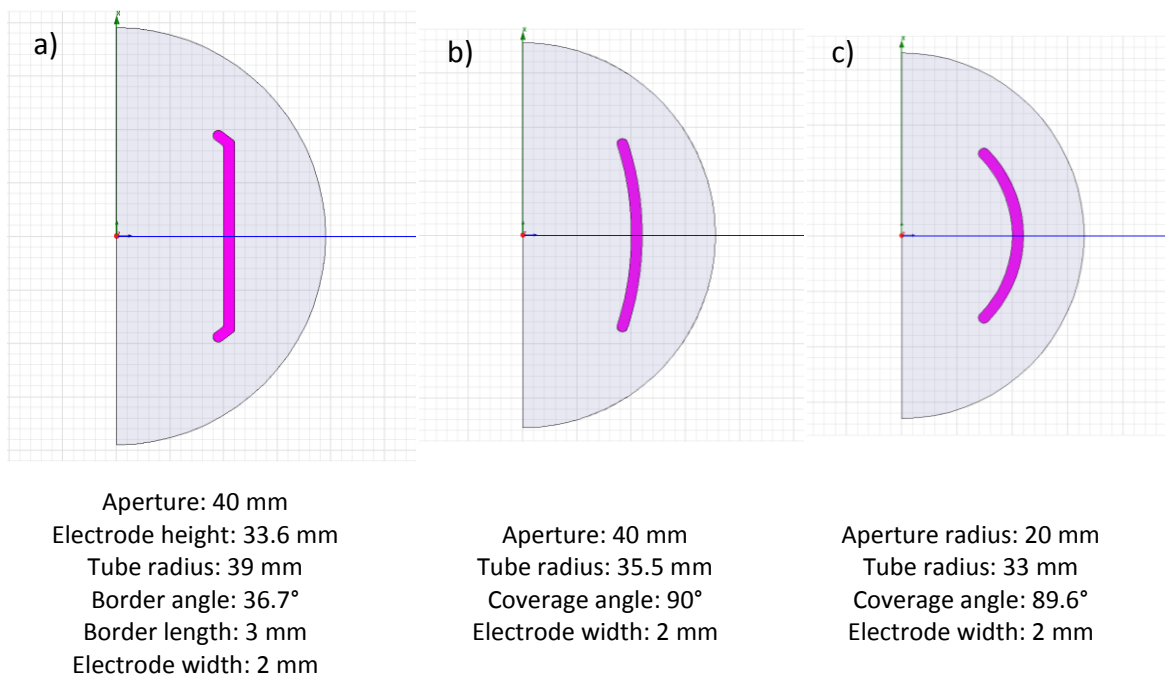


Fig. 5.5 Possible cross sections for the Tail Clipper: a) planar electrodes rectangle aperture; b) Elliptical electrodes; c) Circular electrodes

The homogeneity requested in Tab. 5.1 is not very tight and therefore the size of the cross section can be smaller than for the CTF3 strip-line kicker. This small chamber will improve the wakefield behaviour in the final design.

Measured homogeneities have been $\pm 10\%$, $\pm 15\%$ and $\pm 19\%$ for a , b and c cross sections respectively. The c cross section is in the limit of the homogeneity specifications. However it features the smallest external dimension and the curved electrode increases the electric and magnetic field in the axis for a given electrode voltage and current. In addition, c cross section electrodes are easy to manufacture and the external 66 mm inner diameter tube is almost a commercial dimension for stainless-steel tubes. Therefore, the preferred cross section for this design is the one with circular electrodes.

5.2.2 DEVICE LENGTH AND KICK STRENGTH

The Tail Clipper length is limited by the maximum flange-to-flange distance (main specification given in Tab. 5.1), the maximum pulser power supply voltage and the minimum pulse rise time⁵. The need to split the strip-lines was presented in section 5.1. To aim for a minimum voltage, the strip-lines should be as long as possible. Using Eq. (5.1) for CTF3 bunch spacing, it is possible to obtain the relation l_s/N using $T_r=2.75$ ns, which results in 0.3375 m of length per strip. For integer values of N , the maximum value of l_s to fit in the available space is 1.35 m. Therefore, the Tail Clipper will be divided in four strip-lines of about 0.3375 m of length.

However, splitting the Tail Clipper in 4 units implies increased longitudinal space requirements for the additional feedthroughs and flanges. Indeed, 0.3375 m electrodes cannot be fit in 1.625 m due to manufacturing issues (Fig. 5.6). The 10 additional CF63 flanges increase the required space by 175 mm⁶. Besides, the space between the CF63 flanges and the feedthroughs cannot be smaller than 14 mm to permit welding of the feedthrough case and allow fitting the bolts of the CF flange. The resulting space requirement is over 1700 mm without considering the variable length transitions from the CF40 to the CF63 flanges.

⁵ Minimum rise time and maximum voltage is given by the pulsed power supply MOSFET technology [2]. The power supply should not work over ± 2.7 kV and the rise time should not be lower than 2.75 ns.

⁶ The idea of manufacturing without using intermediate CF63 flanges was discarded because of its assembly difficulty. The four devices should be manufactured independently and assembled by flanges.

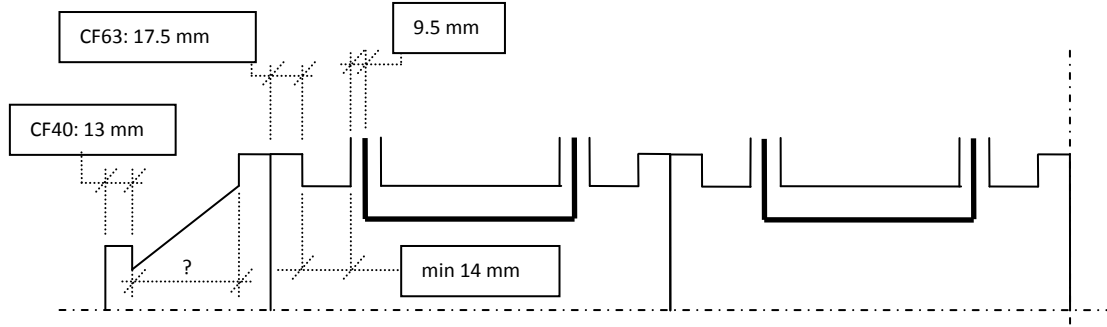


Fig. 5.6 Schematic view of the longitudinal distances to fit 4 devices in the given length

To allow fitting two small transitions, the electrode's maximum length cannot be larger than 300 mm. This is consequently the chosen length for each strip-line. The minimum pulse rise time is now $T_r=3$ ns.

Deflection angle specified in Tab. 5.1 can be obtained using an integrated transverse voltage of 240 kV (Eq. 2.4). This results in 60 kV per strip-line. The required electrode-to-ground voltage can be obtained using Eqs. 2.38 and 2.39, and it is about 2 kV, which loosely fits the power supply maximum voltage⁷.

The transverse shunt impedance in DC (Eq. 2.37) is 22500 Ω .

5.2.3 VOLTAGE, CURRENT AND POWER. 2D WAKEFIELDS.

The voltage, current and power of the electrodes have been calculated by means of Tab. 2.1. The values given in Tab. 5.2 are for only one section of the Tail Clipper. The duty cycle is 7×10^{-6} for the maximum repetition rate and pulse length.

⁷ Indeed, CTF3 team decided that the Tail Clipper could operate at ± 2.7 kV per strip-line to get an increased deflecting angle or to be able to use one section as spare. However, all the calculations will be developed for 1.2 mrad deflection angle (0.3 mrad per section).

Tab. 5.2 TL2 Tail Clippers electrical requirements

Magnitude	Value	Units
Pulse maximum instantaneous power (P_{DC})	160	kW
Pulse maximum instantaneous power per electrode (P_{1DC})	80	kW
Averaged power per electrode (P_{1avg})	0.56	W
Flat-top pulse voltage (electrode to ground, V_k)	2	kV
Flat-top pulse current per electrode (I_k)	40	A

The four Tail Clippers have been simulated in ABCI to obtain an approximation of the wakefield behaviour. The beam passes only once through the Tail Clippers (TL2 is a transfer line) and the cross section is designed to be small compared to the beam pipe. Therefore, the wakefield behaviour should not represent a concern for this design.

The transitions have been assumed conical and the geometry is as shown in Fig. 5.7, using 300 mm electrodes.

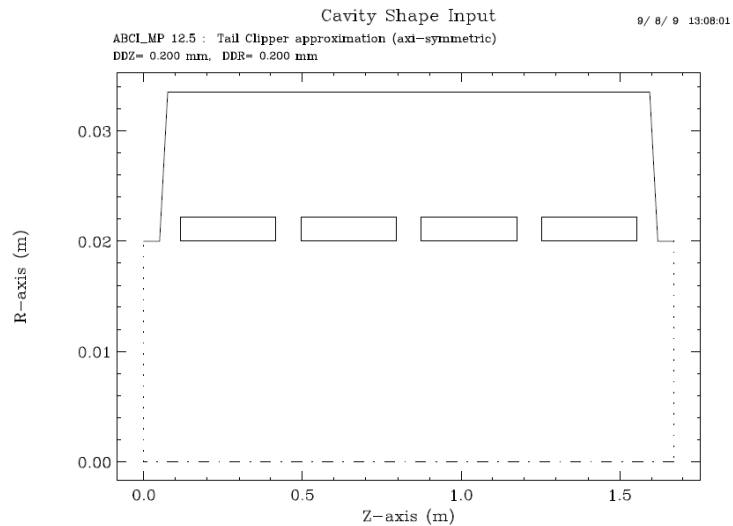


Fig. 5.7 Tail Clippers geometry in ABCI

The wake loss factor calculated for this structure is 1.01 V/pC for 3mm bunch (Fig. 5.8). For 2.33 nC bunch, the energy lost when passing through the Tail Clippers (Eq. 2.47) is 2353 eV.

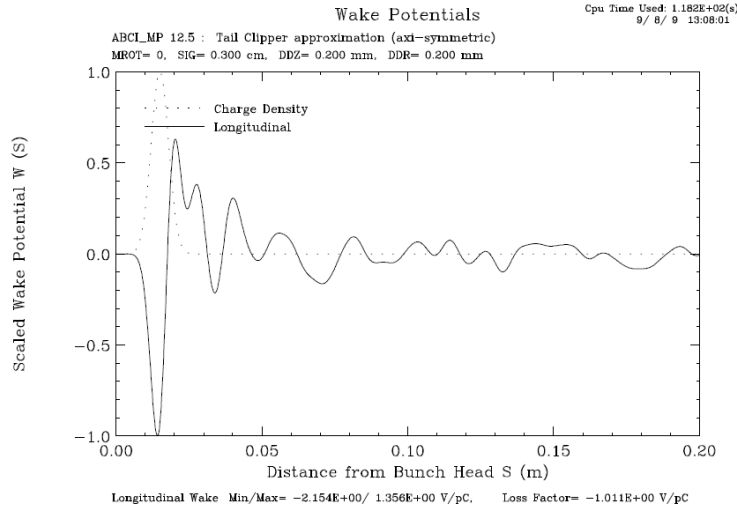


Fig. 5.8 Wake potential for 3mm bunch passing through 4 Tail Clippers

The maximum energy spread accumulated by the bunch is given by Eq. 2.48, resulting in 8.2 keV. These values represent a small fraction of the beam's energy.

5.2.4 COAXIAL TO STRIP-LINE TRANSITION

The Tail Clippers design specifications are very tight in terms of pulse rise time. The pulse must rise very fast to allow the EM field to fill the Tail Clippers between two bunches. A fast rise time pulse contains very high frequencies in a Fourier analysis (up to 400 Mhz for 2.5 ns rise time pulse). Therefore, excellent high frequency transmission is required for the Tail Clippers and an optimized coaxial to strip-line transition is mandatory.

For this design, it is not possible to put electrode tapers inside tube transitions as proposed by the author in section 2.3.1.3. The splitting of the Tail Clipper in several devices makes impossible to take advantage of end tapers. However, it is also possible to taper only the electrodes to improve the high frequency transmission (Fig. 5.9).

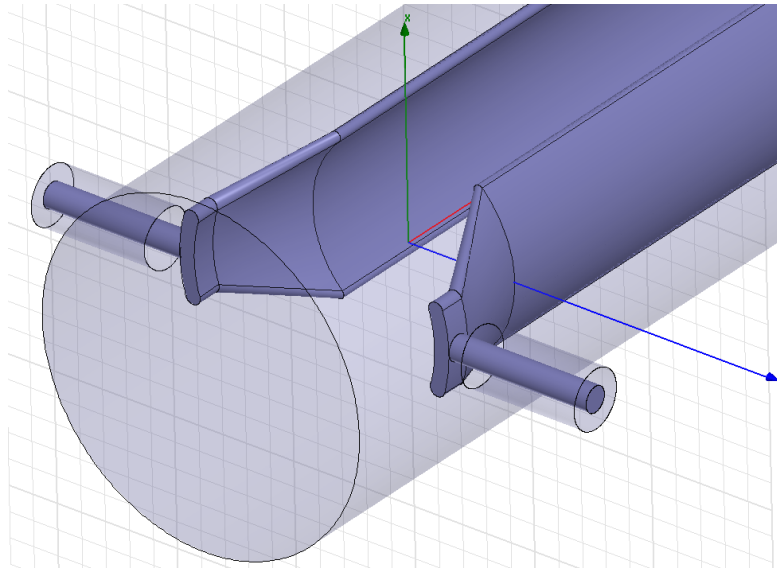


Fig. 5.9 Tapered coaxial to strip-line transition

The optimization of the transition has been developed using HFSS code as it was detailed in section 2.3.1.3 for tapered electrodes. The chosen transition length (25 mm) is a compromise between good high frequency transmission (long) and higher kicking power (short). The starting cross section features $50\ \Omega$ characteristic impedance (see Fig. 2.31) and the connection to the straight part of the electrode is smooth and progressive. There is no need to optimize the characteristic impedance in several intermediate cross sections of the transition. The transition is very short and impedance is assumed constant.

The distance between feedthroughs (300 mm) should remain unchanged due to device length restrictions⁸ and therefore the kicking power and 3D homogeneity of the device are slightly deteriorated by the transitions. This will be taken into account when calculating transverse voltage and homogeneity in the full 3D simulation. However, as the Tail Clippers do not require very good field homogeneity, the tapered design is expected to be valid just slightly increasing the electrodes voltage.

⁸ The straight part of the electrodes is therefore reduced to 250 mm.

5.2.5 FREQUENCY DOMAIN 3D MODEL SET-UP: S PARAMETERS

The 3D model can now be built using the transition dimensions shown in previous section and the already dimensioned cross section. Only the simulation of one section of the Tail Clippers is required in the frequency domain code. The coupling between consecutive strip-lines is expected to be almost negligible (see section 5.2.6) and the four devices can be considered independent.

Only one stand-off per electrode has been projected and the short electrodes make unnecessary any deformation calculation.

The symmetry used for the model is one half (Fig. 5.10), using an electric wall in the cutting plane to simulate the differential excitation. There is no need to model $\frac{1}{4}$ symmetry because the device is small enough for fast simulation. This eases power input calculations in the model because coaxial ports are not cut by the symmetry. Many lines parallel to the axis have been drawn to calculate integrated fields.

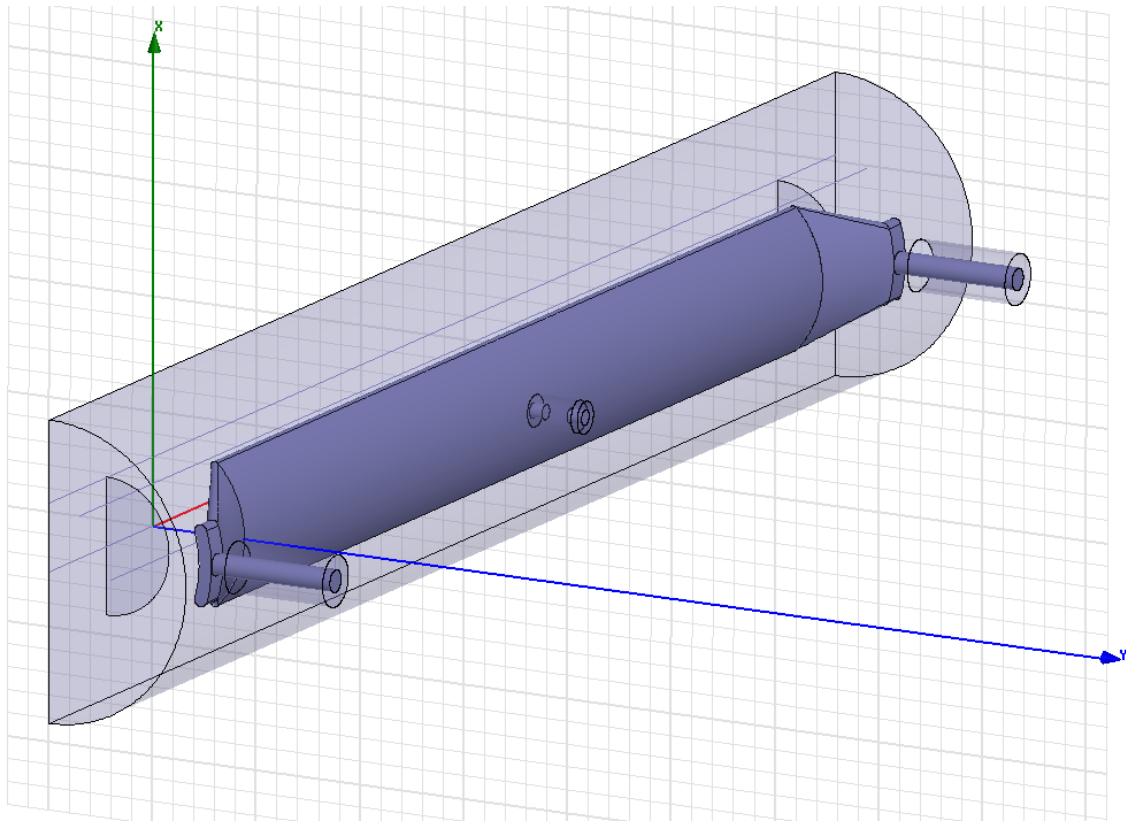


Fig. 5.10 Tail Clipper section 3D model for frequency domain

The RF power input used for the simulation in HFSS has been calculated from the analytical results. The averaged power defined in this simulation to obtain the same peak voltages and currents as in the pulsed mode is $P_{1DC}/2$, which results in 40 kW. However, analytical calculations do not consider the real curved geometry of the strip-lines and the fields (and also the transverse voltage) are expected to be a bit higher in numerical simulations than in analytical calculations.

Reflection scattering parameter (S_{11}) is plotted in Fig. 5.11 up to 2 GHz for a lossy model⁹. For a lossless model, the reflection parameter is about 0.01 lower in the entire frequency band. The reflected power is lower than 0.3 % up to 400 MHz, which is the top frequency content of the pulse. The nodes of the transmission due to the matching reflection in the transitions happen close to the odd multiples of $\lambda/4$ for the approximate electrode length (0.3 m) at about $(3 \times 10^8 / 0.3) * (1/4) = 250$ MHz, $(3 \times 10^8 / 0.3) * (3/4) = 750$ MHz, $(3 \times 10^8 / 0.3) * (5/4) = 1250$ MHz, etc. On the other hand, the simulation of the stand-offs in the model has been proved to negligibly affect the transmission results.

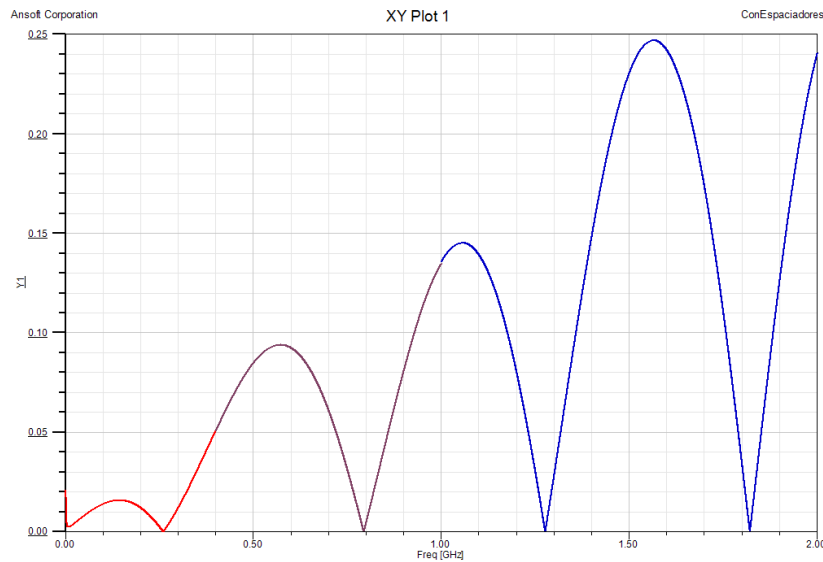


Fig. 5.11 S_{11} simulation for the Tail Clipper

⁹ The small model permits a simulation using real materials (stainless-steel, aluminium, ceramic, etc.). The material selection will be explained in manufacturing section.

5.2.6 CROSS TALK BETWEEN ADJACENT DEVICES

The four Tail Clippers are put together in the TL2 close to each other as shown in Fig. 5.6. Therefore, a pulse entering by the coaxial port of one device can induce undesired power on the closest device. This RF coupling between strip-lines depends on the frequency and the distance between the different Tail Clippers. In order to estimate the coupling or cross talk between two adjacent Tail Clippers, a frequency domain analysis of two devices has been carried out (Fig. 5.12).

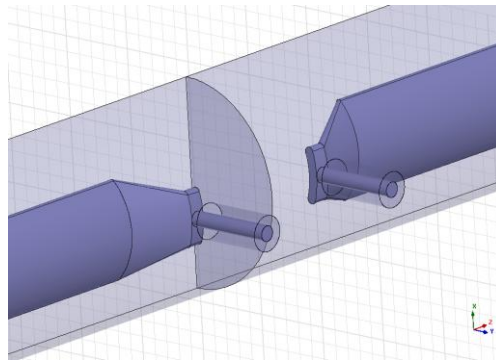


Fig. 5.12 Model in HFSS for cross-talk calculation

The distance between the feedthroughs is 55 mm in the simulation. This value is smaller than the final distance, and therefore the results are conservative. The transmission between ports shown in Fig. 5.12 is presented in Fig. 5.13.

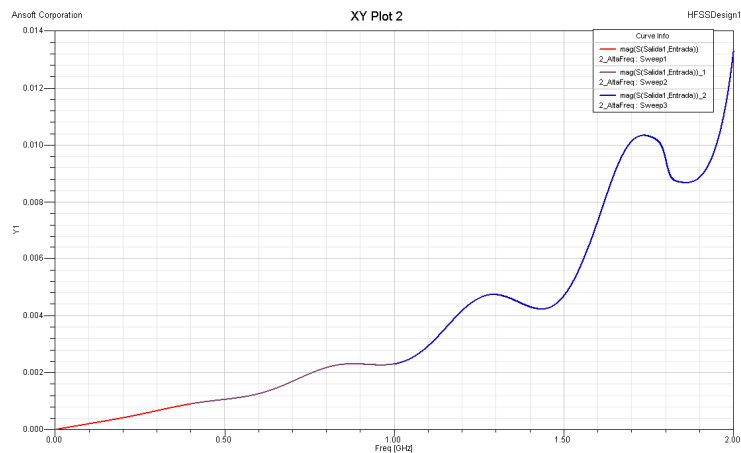


Fig. 5.13 S_{12} parameter between two adjacent ports

The transmitted power from one strip-line to the adjacent is extremely small. The coupling up to 2 GHz is negligible even for 55 mm distance.

5.2.7 ADDITIONAL RESULTS

The transverse voltage has been numerically calculated in the axis of one of the Tail Clippers. For the previously analytically calculated power, the transverse voltage obtained in the 3D model is about 62848 Volts. This figure is a bit higher than the required transverse voltage (60 kV). The curved geometry of the electrodes is not being considered by analytical expressions. However, the 25 mm per transition diminish the integrated transverse voltage. Nevertheless, the curved electrodes counteract the transitions and the overall transverse voltage is a bit higher than the analytically calculated value for 0.3 m straight electrodes. This confirms the validity of the transitions design (not too long neither too short). The drawback of this curved design relies on the field homogeneity. The 3D homogeneity has been obtained using the transverse voltage calculated along different longitudinal paths¹⁰. The transverse voltage has been calculated over straight lines parallel to the device axis passing through 5, 10 and 15 mm radius and 0, 30, 45, 60 and 90 degrees (Fig. 5.14). The calculated 3D homogeneity in the 30 mm diameter zone is about 25%, which is between +8% and -17% (in reference to the value in the axis). This homogeneity is even better than the 2D homogeneity of the cross section and this happens due to the different 3D field in the transitions, which affects the integrated value. The design is consequently correct.

¹⁰ This is exactly the same as calculating the homogeneity by using the electric field alone as indicated in chapter 2.

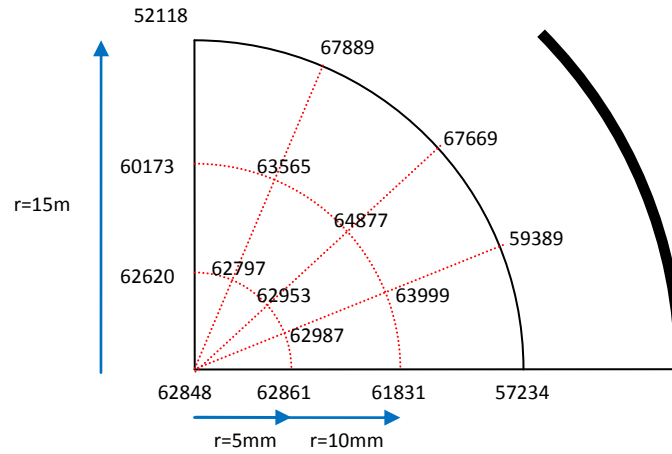


Fig. 5.14 Transverse voltages in different integration paths in the 15 mm radius circle

The numerical voltage and current on the electrodes are similar to the analytical values (1998 V and 39.7 A).

The power losses inside the structure are totally negligible, given the small averaged power passing through the electrodes.

5.2.8 HOM ANALYSIS

The HOM analysis conditions for the Tail Clippers are identically determined as for the kicker analyzed in the previous chapter, because the Tail Clippers are installed just before the power beam generation. Therefore the beam quality conditions are identical. The dangerous modes for this design are therefore the ones with electric field in the longitudinal axis (TM modes). The frequency range to search for TM modes in the equivalent pipes (40 and 67 mm diameter) is between 3.43 GHz and 5.74 GHz.

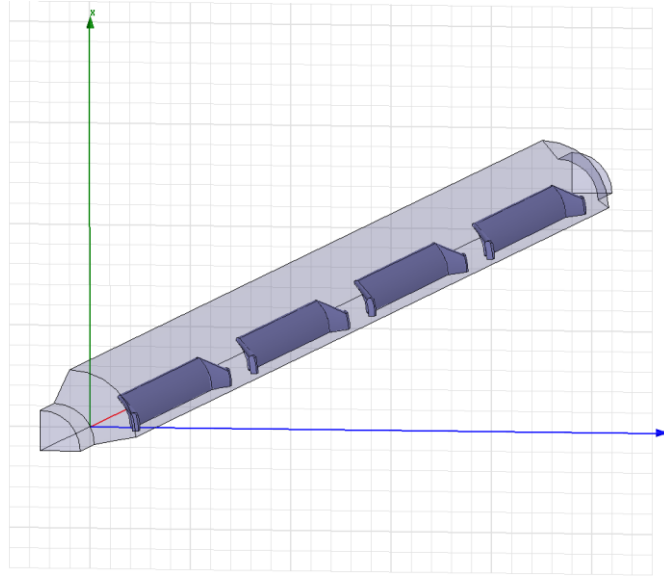


Fig. 5.15 HFSS model for HOMs calculation

An eigenmode simulation (Fig. 5.15) has been set-up using HFSS code and perfect magnetic plane symmetries. The coaxials have been removed to reduce the memory requirements of the simulation. The simulation using resistive materials has been possible over 3 GHz given the short device (about 1.7 m) and the small diameter.

The first 20 HOMs starting in 3.2 GHz are shown in Fig. 5.16. There are plenty of possible modes in the given frequency range. The quality factor of the analyzed resonant modes is never higher than 3500.

Solutions: TailClipperV2HOMs - Modelo

Simulation: Setup1 [LastAdaptive]

Design Variables: [0mm] RadioApertura=20mm RadioApertura0=25mm RadioCamara=33mm RintCoax=2.425mm

Profile | Convergence | Eigenmode Data | Mesh Statistics

Solved Modes [Export]

Eigenmode	Frequency [GHz]	Q
Mode 1	3.28313 +j 0.000639933	2565.22
Mode 2	3.28607 +j 0.000642002	2559.23
Mode 3	3.28894 +j 0.000645664	2546.94
Mode 4	3.29175 +j 0.000649638	2548.43
Mode 5	3.63778 +j 0.000515332	3529.95
Mode 6	3.65273 +j 0.000515761	3541.11
Mode 7	3.67491 +j 0.000505325	3636.19
Mode 8	3.72627 +j 0.000630244	2956.22
Mode 9	3.73593 +j 0.000573640	3256.34
Mode 10	3.77267 +j 0.000615659	3063.92
Mode 11	3.79903 +j 0.000621176	3057.94
Mode 12	3.83443 +j 0.000567277	3379.68
Mode 13	3.83608 +j 0.000570310	3363.15
Mode 14	4.10606 +j 0.000723940	2812.60
Mode 15	4.10919 +j 0.000709631	2894.48
Mode 16	4.11315 +j 0.000673908	3024.78
Mode 17	4.13397 +j 0.000625716	2503.20
Mode 18	4.13550 +j 0.000626293	2502.44
Mode 19	4.13677 +j 0.000621703	2517.19
Mode 20	4.13824 +j 0.000816847	2533.06

Close

Fig. 5.16 HOMs calculated for the Tail Clipper

Significant electric field in the longitudinal axis only appears between two consecutive strip-lines in some resonating modes (Fig. 5.17), and it is alternatively opposite between them.

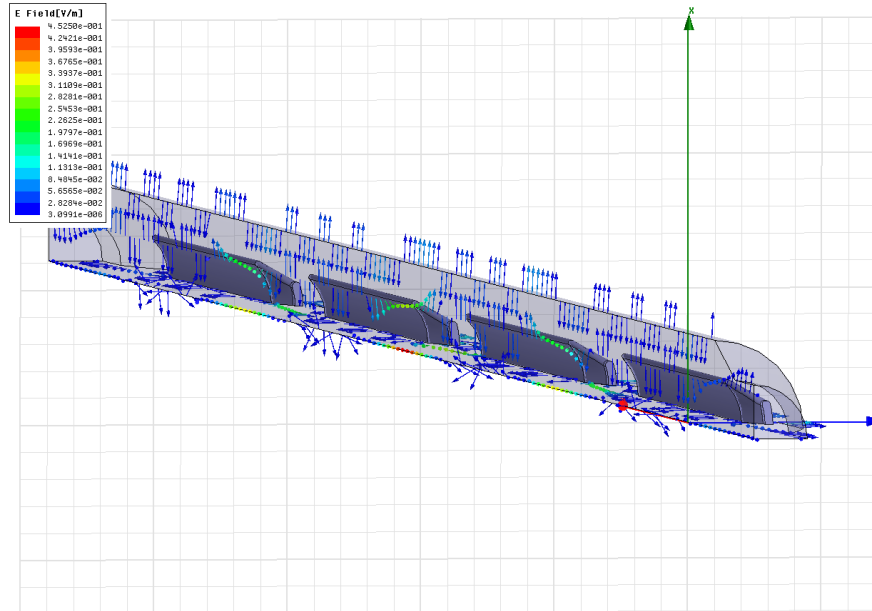


Fig. 5.17 5th mode vector plot of the electric field map

Given that the beam only passes one time through the Tail Clippers, the possibility to excite dangerous HOMs is very small. In case that any frequency matches the HOM, it is rapidly damped by the resistive walls in a couple of oscillations (low quality factor). Therefore, no HOM damping has been foreseen for this design.

5.2.9 WAKEFIELD SIMULATIONS

The 2D axi-symmetrical model has been updated in ABCI to include the effects of the tapers in the wakefield simulations. The ABCI input file with the geometry of the Tail Clippers yields the structure shown in Fig. 5.18, where all the materials are lossless.

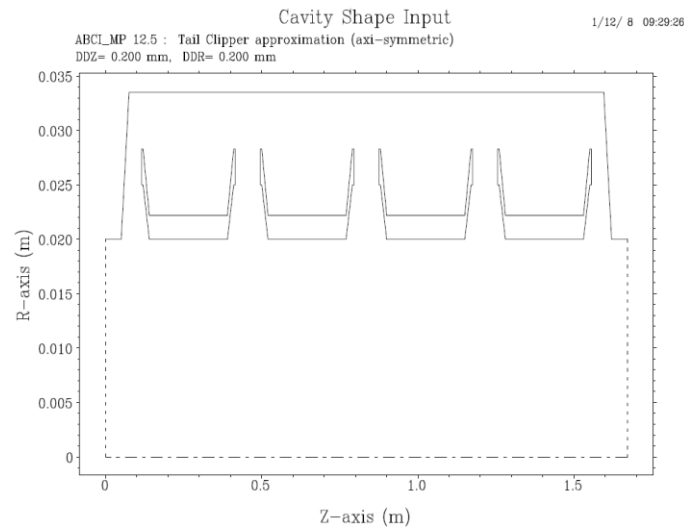


Fig. 5.18 Tail Clippers geometry in ABCI using tapered electrodes

The wake loss factor calculated for this structure is 2.34 V/pC for 3mm bunch (Fig. 5.19). For 2.33 nC bunch, the energy lost when passing through the Tail Clippers (Eq. 2.47) is 5452 eV.

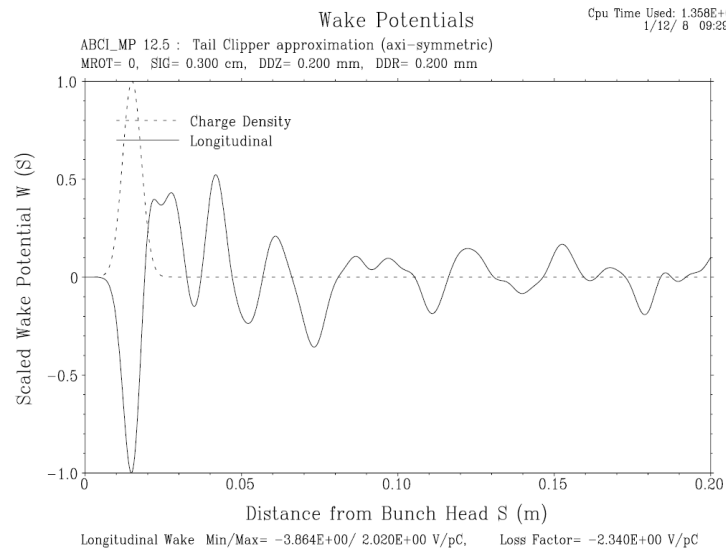


Fig. 5.19 Wake potential for 3 mm bunch passing through 4 tapered Tail Clippers

The maximum energy spread accumulated by the bunch is given by Eq. 2.48, resulting in 13.7 keV. These values, though a bit higher, still represent a small fraction of the beam's energy.

The long range wake potentials up to 30 meters are presented in Fig. 5.20. The large number of discontinuities inside the Tail Clipper vacuum chamber creates a great amount of reflected waves which forms that apparently random pattern of wake potentials.

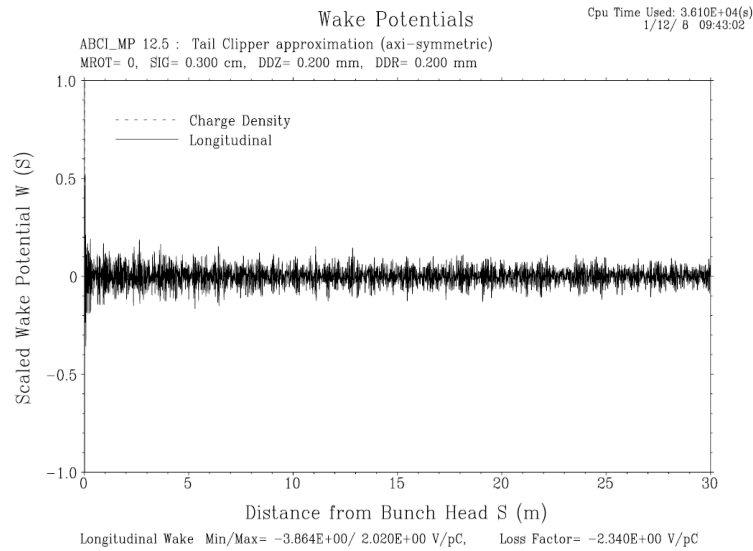


Fig. 5.20 Long range wake potential in tapered electrodes Tail Clippers

Nevertheless, the real Tail Clipper will be made of stainless-steel and/or aluminium, which should considerably damp the long range wakefields in the resistive surfaces. In addition, the resonant frequencies coupled with the coaxials should also damp the long range wakefields, which is not considered in ABCI's axi-symmetrical simulation.

A full 3D simulation of the structure in GDFidl was not possible for this device due to problems in the simulation server at CERN. Nevertheless, the ABCI's axi-symmetrical simulation can be considered as a good approximation of the Tail Clippers wakefield behaviour, as it was demonstrated for the kicker design in the previous chapter.

However, it was possible to simulate the wakefields in available computers using a shorter structure, where the straight part of the strip-lines is 50 mm instead of 250 mm (Fig. 5.21). The wake loss factor is mainly given by the abrupt transitions inside the beam pipe and therefore the result is expected to be in the same range as the wake loss factor calculated by ABCI.

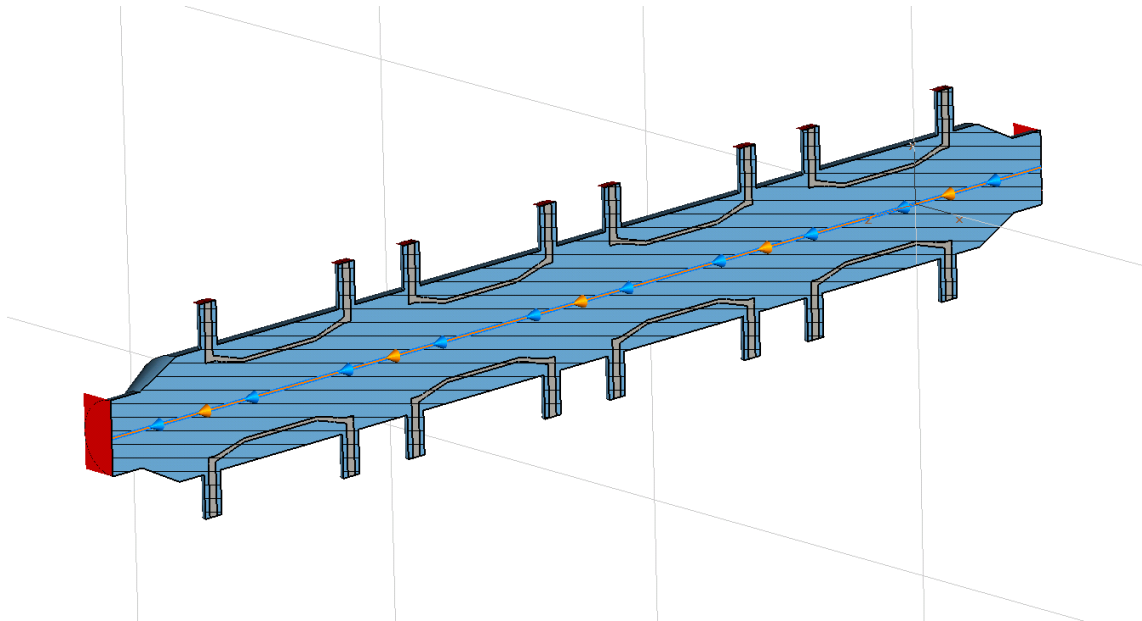


Fig. 5.21 CST Particle Studio short model of the Tail Clippers

The wake loss factor obtained in the simulation of the structure shown in Fig. 5.22 was 2.22 V/pC, smaller but very similar to the ABCI's calculated value for the full structure. This confirms the validity of ABCI calculations on the safe side.

Clamp to range: (Min: 0/ Max: 200)

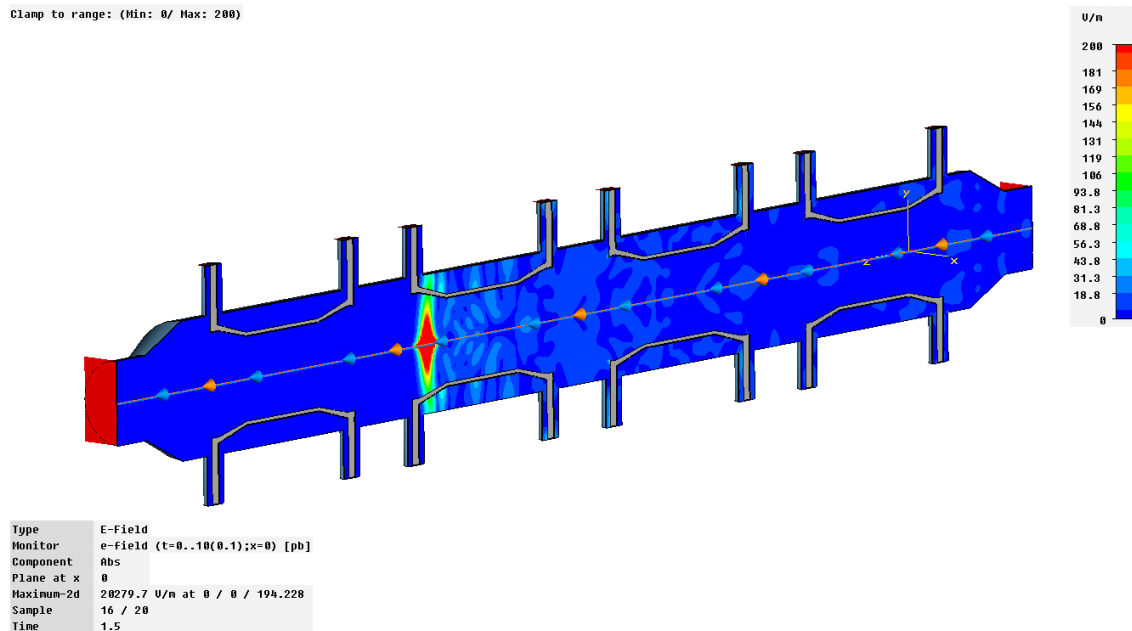


Fig. 5.22 Simulation of the 3 mm bunch passing through the "short" Tail Clipper

ABCI and CST simulations were checked and validated by CTF3 team. Therefore, no damping seems necessary for this structure.

5.3 TL2 TAIL CLIPPERS MANUFACTURING ISSUES

5.3.1 MATERIAL SELECTION

The material preferred for the whole assembly is stainless steel, type AISI 304L (DIN 1.4306). This stainless steel allows for an easy welded assembly of the feedthroughs as it was presented in the CFT3 extraction kicker chapter. However, the curved electrodes of the Tail Clippers are not so easy to manufacture as the planar kicker electrodes. CNC machining from a massive block seems to be the best method for the electrode manufacturing. Aluminium (AL6082) features good mechanical properties and easy machining and therefore is the best-suited material for CNC machining of the electrodes. AL6082 also well supports mild-bake out if required, although it is not expected to raise the electrode temperature over 100 °C.

No noticeable problems are expected by using aluminium electrodes inside stainless steel tank. The electrodes are short and curved and therefore mechanical stiffness is good even using 2 mm thick aluminium electrodes. The electromagnetic behaviour should be quite similar although possible HOMs in the structure will be slightly less damped.

5.3.2 FEEDTHROUGHS

The electromagnetic design was developed bearing in mind the feedthroughs voltage requirements. Due to the good high frequency transmission requirements, only constant impedance feedthroughs are valid for the Tail Clippers. Constant impedance feedthroughs (50 Ω) over 7 kV DC are not commercially available. However, Tail Clipper nominal design voltage is 2 kV, and 2.7 kV is the maximum expected voltage. Therefore, commercial feedthroughs perfectly fit Tail Clipper requirements.

The length of the full Tail Clipper assembly represents a great concern in the design, as indicated in previous sections. Therefore, feedthroughs based on flange assembly methods are not acceptable as they require more longitudinal space to be assembled with the Tail Clipper tube. The selected feedthrough is shown in Fig. 5.23, which is a weldable type HN¹¹ feedthrough supporting up to 7 kV DC voltage and 7 A in steady state. The manufacturer confirmed the possibility of using of these feedthroughs for 60 A pulse (3000 V/50 Ω) every 20 ms.

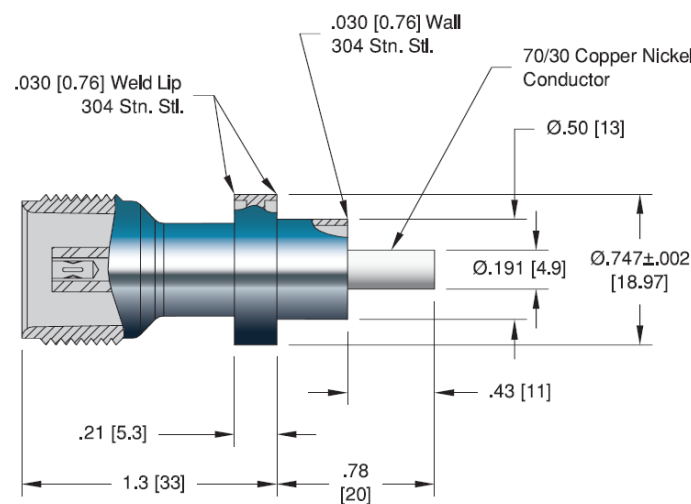


Fig. 5.23 Ceramaseal 50 Ω HN feedthrough

The feedthroughs must be adapted to the Tail Clipper tube in order to weld them because of the very different wall thicknesses. A stainless steel case (Fig. 5.24) was prepared for the thickness adaptation, as presented in the previous chapter for the kicker. The steel case is circularly milled in the bottom part to keep a smooth inner tube surface and improve coaxial to strip-line transition. A mock-up was required to determine the welding parameters so the correct positioning of the electrodes could be achieved in the final prototype.

¹¹ Type HN connector is a larger and higher voltage version of the type N connector. Type N only supports up to 1500 V.

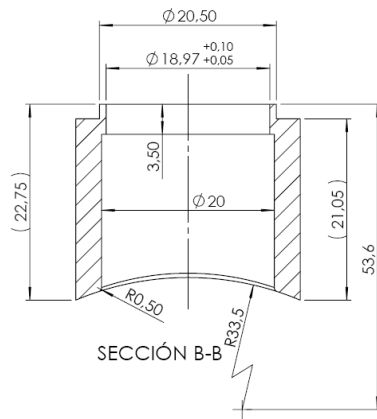


Fig. 5.24 Case used to weld the feedthroughs to the tube (left) and a feedthrough welded to the case and positioned in the tube (right)

The connection between the feedthrough pin and the electrode was done using a sliding contact to allow for thermal differential expansion of the electrodes. The pin is screwed to a copper washer that slides in the hole machined at the electrode ends (Fig. 5.25).

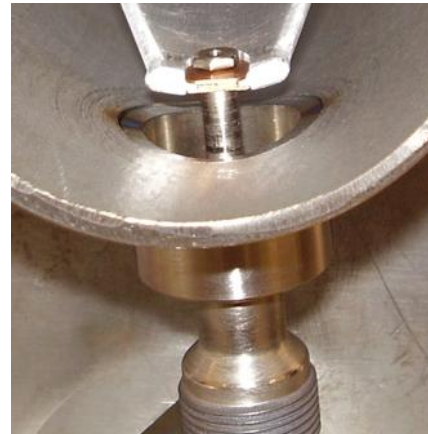
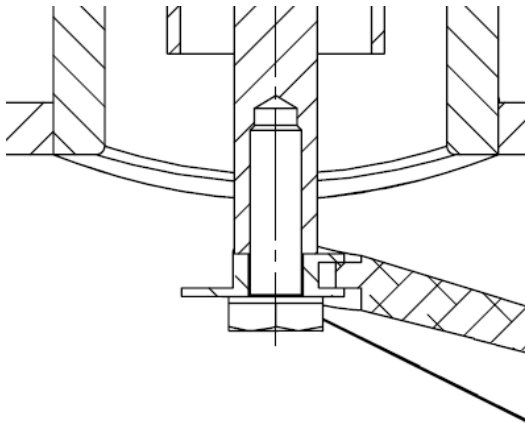


Fig. 5.25 Sliding contact between feedthrough pin and electrode

The original feedthrough pin is solid and has no threaded hole to fit the screw. However, all the feedthroughs were manually drilled and threaded in a very complex process. The feedthrough copper nickel pin is extremely delicate because it is brazed to the ceramic part of the feedthrough. Therefore, no radial forces can be exerted over the pin, and minimum axial forces are permitted. A custom-made tool was required to support the pin when making the threaded hole, thus avoiding dangerous forces.

In addition, no oil-based lubricant¹² can be used for the screw tap and alcohol is a much less effective lubricant for the threading process.

Each feedthrough was tested for vacuum tightness after the threading and welding process. A custom-made vacuum transition (Fig. 5.26) was designed to connect the case (already welded to the feedthrough) to a DN flange, which was connected to a standard vacuum pump. This ensures that a defective feedthrough will not spoil the full prototype when welded to the main tube.

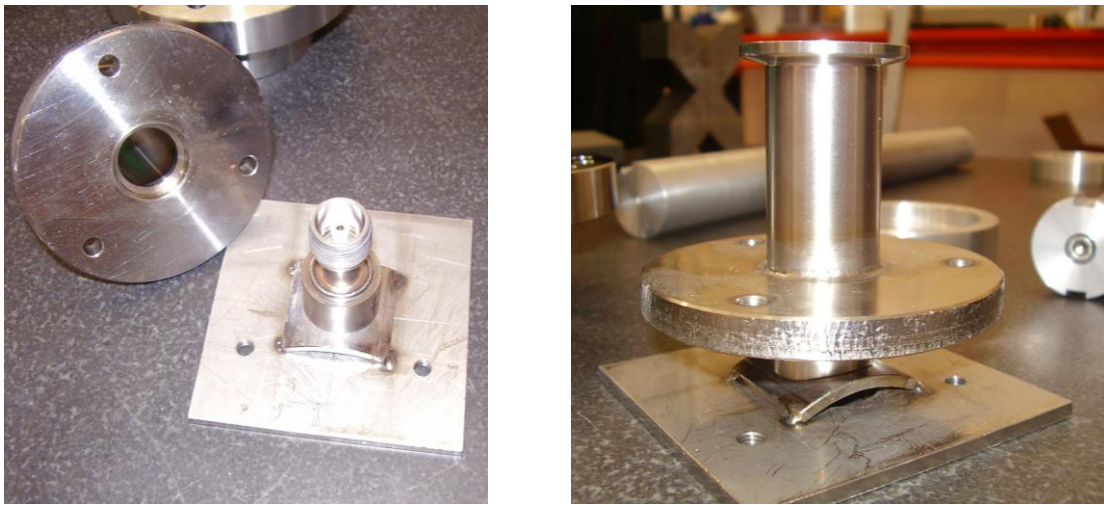


Fig. 5.26 Transition designed to test the feedthroughs before final welding

Even with this careful handling, several feedthroughs and screw taps were damaged in the threading process of sixteen feedthroughs.

5.3.3 *STAND-OFFS SUPPORT*

Only one stand-off was projected to support the electrodes. The aluminium electrode is very light and does not require multiple fixations¹³. In addition, one fixation point makes the sliding supports unnecessary.

¹² Oil produces contamination of vacuum materials and it requires an ultrasonic bath to be removed from small fissures and corners. The feedthroughs cannot be safely cleaned by an ultrasonic bath because of the fragile brazed parts.

¹³ The feedthrough pins cannot be used as a mechanical support and therefore they will not be considered.

The selected stand-offs were taken from Ceramaseal, reference 10420-01-A. They support up to 10 kV in vacuum and they are made of Steatite. Both ends are threaded in ANSI 6-32 screw and the main dimensions are shown in Fig. 5.27.

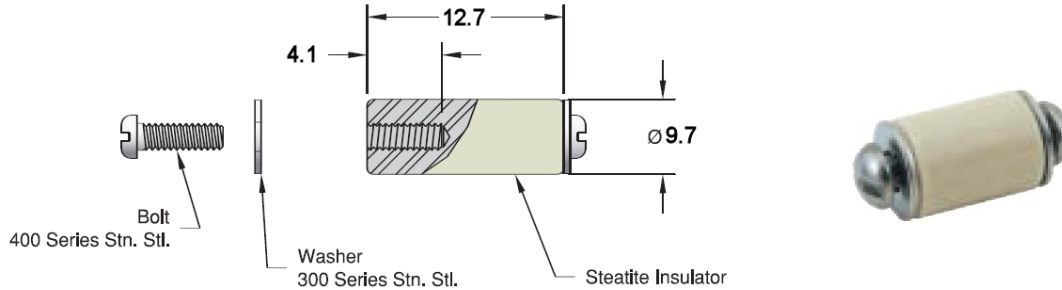


Fig. 5.27 Ceramaseal stand-off used for the Tail Clippers

The stand-offs are fixed to the electrode and to the tube by means of screws (Fig. 5.28). An interference fitting method is not possible given the small size of the stand-off. However, the fixation is good because the electrode is not very heavy and threads in the ceramic are precise enough for the assembly.

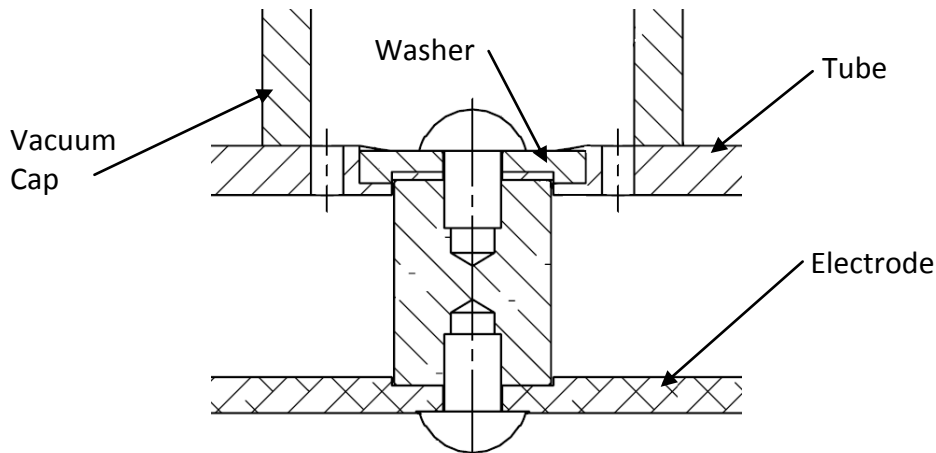


Fig. 5.28 Stand-off fixation method

A small washer is utilized to make possible the assembly process. It provides a plane surface to locate the stand-off in the curved tube. It is screwed to the stand-off and then point welded to the tube. Afterwards, a steel cap is vacuum welded to the tube. Small holes allow for the air to be pumped from the steel cavity.

5.3.4 ELECTRODES

The electrodes (Fig. 5.29) were manufactured using CNC machining on a bulk AL 6082 block. The measured tolerances demonstrated that there were no residual stresses in the electrodes after machining.

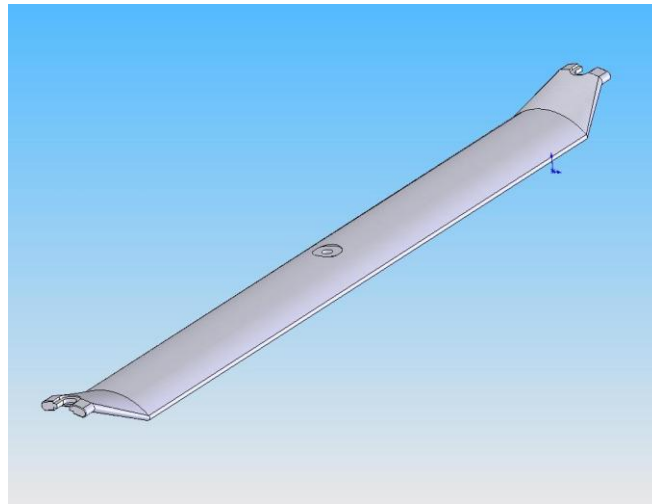


Fig. 5.29 Tail Clipper electrode model

No oil-based lubricants were used for machining. Besides, the electrodes were carefully cleaned in an ultrasonic bath just before assembly (Fig. 5.30) to remove grease and other kind of dirt which could affect the required ultra high vacuum level. All the handling process was carried out using gloves as it was indicated in section 3.3.6.



Fig. 5.30 Ultrasonic bath cleaning of Tail Clipper electrodes

One hole was machined in the middle of the electrodes to fit the ceramic stand-off. Two open sliding holes were machined in both ends of the electrodes to fix the sliding contact for the feedthroughs. The final electrode is almost identical to the model used for electromagnetic simulations (Fig. 5.31).

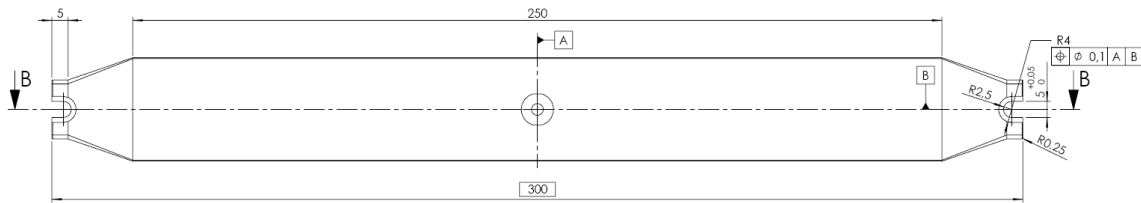


Fig. 5.31 Tail Clipper definitive electrode drawing

5.3.5 FLANGES

The CF63 flanges used to connect consecutive Tail Clippers were slightly modified to improve electromagnetic behaviour (Fig. 5.32). The inner diameter is identical to the inner diameter of the Tail Clipper tube. Besides, the copper gasket is also machined to the same inner diameter in order to avoid abrupt transitions in the inner surface.

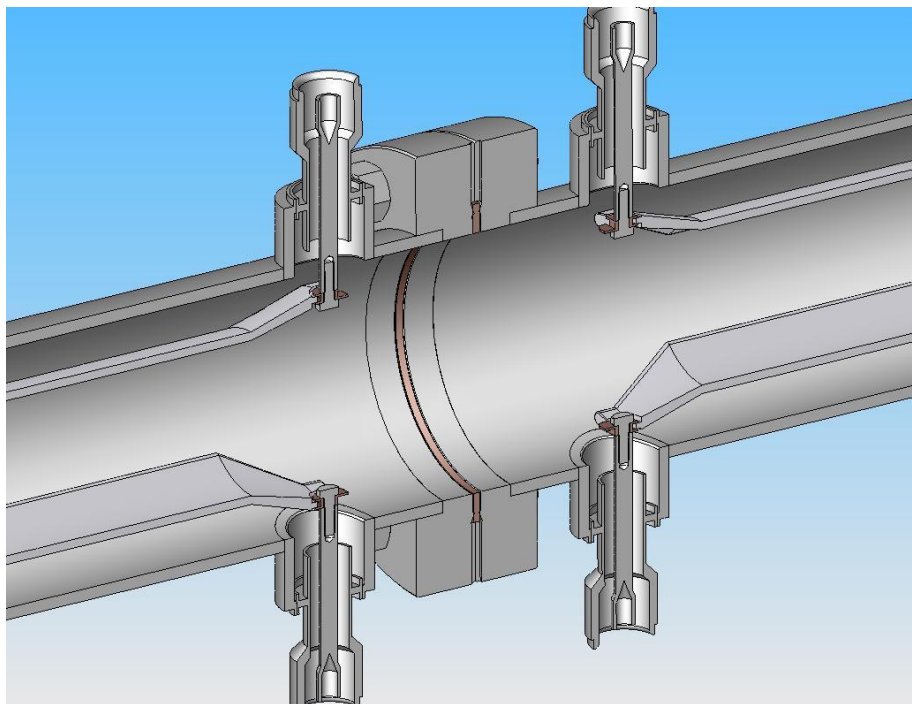


Fig. 5.32 3D model of flange assembly

The CF flanges are made of AISI 316LN Stainless Steel (DIN 1.4429), as shown in Fig. 5.33. 316LN stainless steel is especially indicated to allow firing in ultra high vacuum applications, and it is a CERN standard for manufactured devices. However, this is not so crucial for 10^{-8} mbar vacuum level in the Tail Clippers. The copper gaskets feature an 11 μm silver coating to improve vacuum sealing.

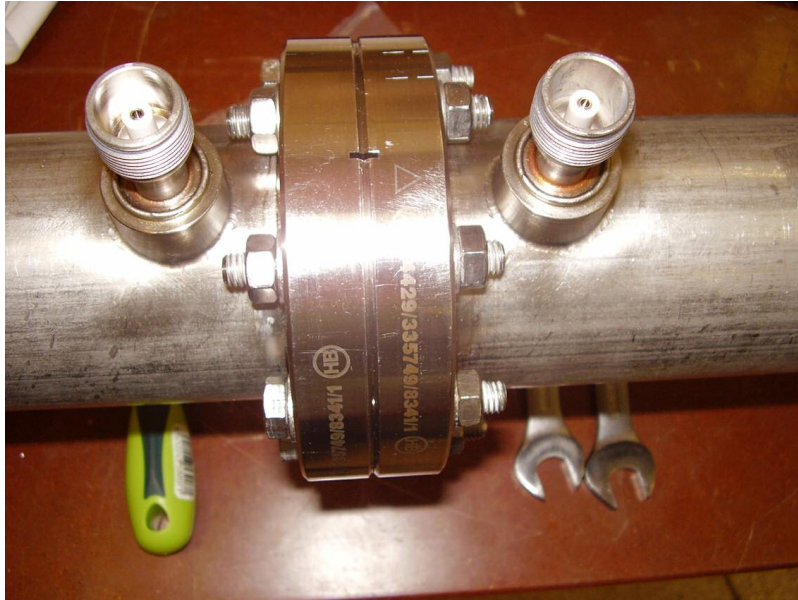


Fig. 5.33 316LN Flanges between Tail Clippers

5.3.6 BEAM PIPE TRANSITIONS

Two identical transitions are required to connect the full Tail Clipper assembly (CF63 flanges) to the beam pipe (CF40 flanges). The transitions are optimized to smooth the inner surface between CF40 and CF63 flanges. Due to space restrictions, they are quite short and therefore the conical inner surface fills the whole distance between the two flanges in order to decrease the angle of the transition as much as possible (Fig. 5.34).

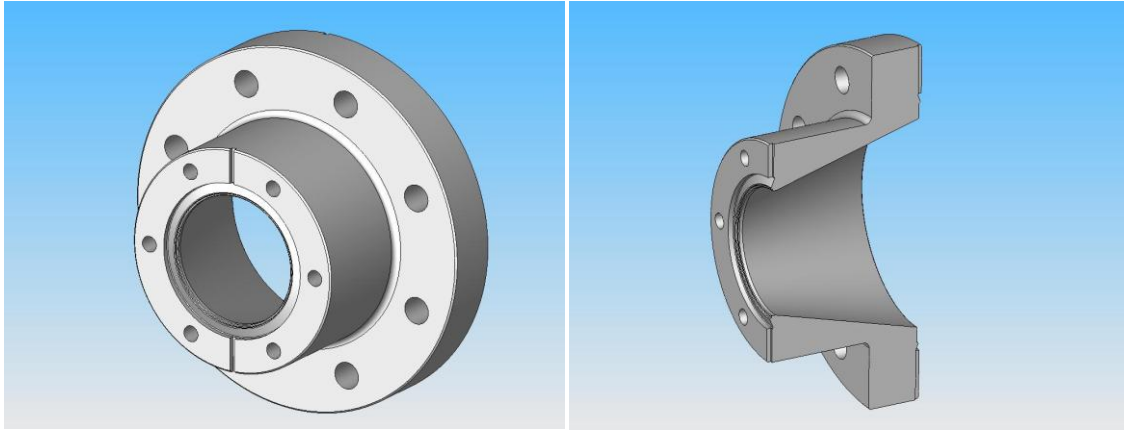


Fig. 5.34 3D model of Tail Clipper transitions

The transitions are custom manufactured by turning and then the faces are machined to the standard dimensions of CF40 and CF63 flanges.

5.3.7 MECHANICAL SUPPORTS AND ALIGNMENT TARGETS

The mechanical supports and alignments are identical to the ones used for the kicker in previous chapter, according to CERN specifications. Minor modifications were required to attach the supports to the smaller Tail Clipper tube. Surfaces for supports and alignments were precisely machined in reference to the common axis of the four Tail Clippers once assembled (Fig. 5.35).

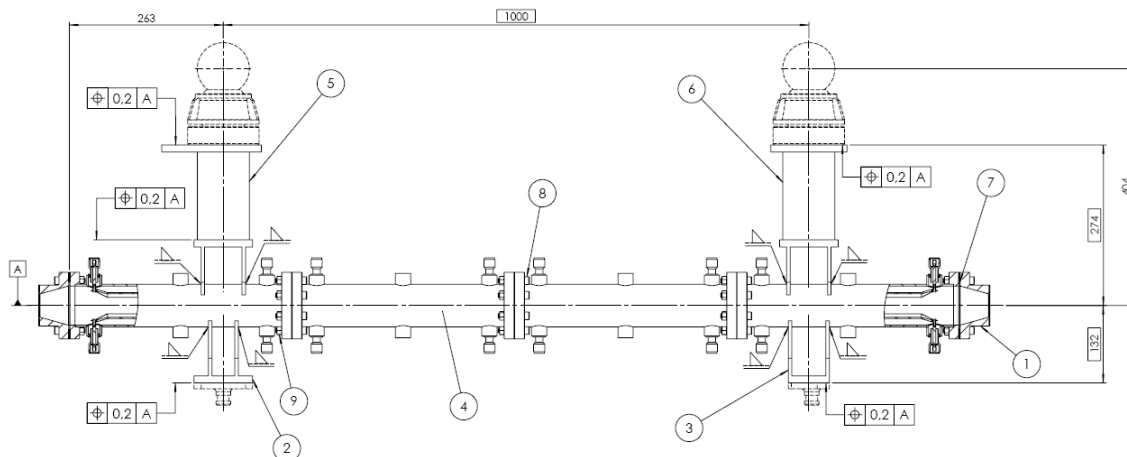


Fig. 5.35 Tail Clipper drawing with supports and alignment devices

No special positioning devices were used for aligning the four devices in the assembly process. The maximum axis deviation in a careful assembly of three CF63 flanges is smaller than the required tolerance for this design.

The full device before the electromagnetic tests can be observed in Fig. 5.36.

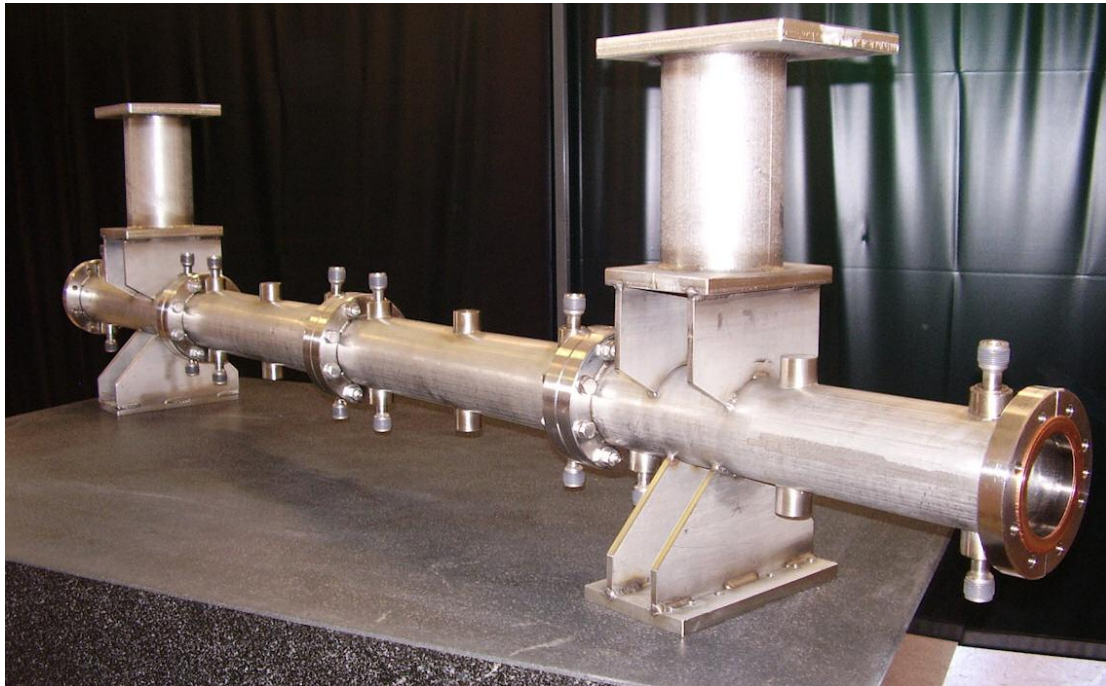


Fig. 5.36 Manufactured device without transitions

5.4 TESTS RESULTS

All the Tail Clipper tests were developed in CIEMAT Accelerator Group laboratory. The required components such as the 50 Ω loads, the high voltage pulsed power supply, the hybrids, etc. were purchased specifically for these tests. This doubled the cost of this device, but it was useful to do a more exhaustive testing of the prototype and it will be needed for optimizing and testing other similar devices in the future.

The four Tail Clippers were assembled together, numbered and tested independently. This does not affect to any of the electromagnetic tests because the Tail Clippers are negligibly coupled between them.

5.4.1 RF NETWORK ANALYZER TESTS

A two port network analyzer was used for the RF tests. Therefore, 180 degree de-phasing of signal was used via hybrid junctions, as shown in Fig. 5.37. The cables were connected as indicated in Chapter 3.

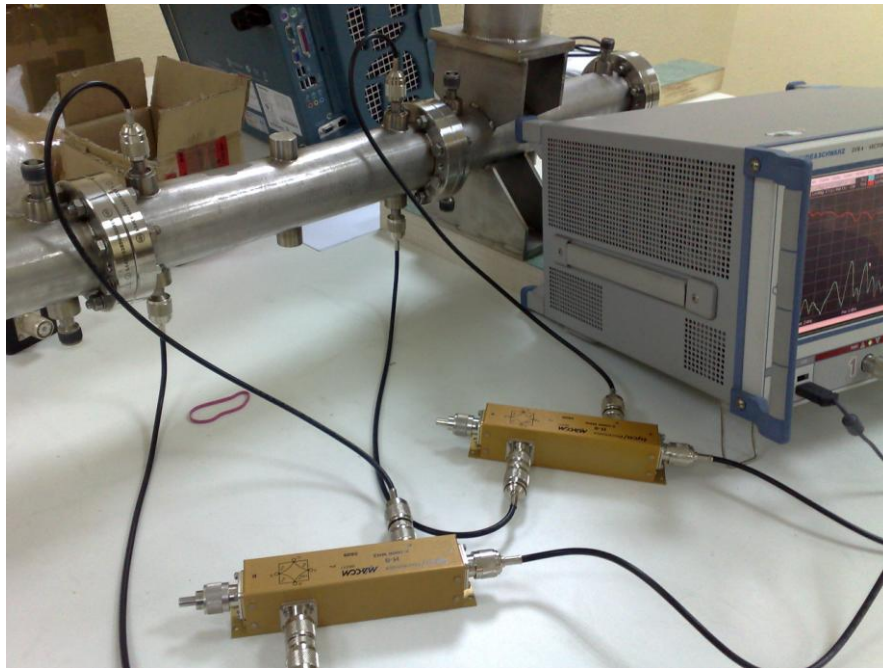


Fig. 5.37 RF tests using hybrids in one Tail Clipper

However it was not possible to avoid distortion in the measurements due to the hybrids. The selected hybrids feature a large 2MHz-2GHz frequency range which limits their performance. The strip-lines are so well matched that the hybrid response is not negligible in the system. A well calibrated system is therefore required for good results, and this was not possible because an adequate calibration kit was not available for the measurements.

Nevertheless, the Tail Clippers can also be directly tested without using hybrids by connecting the network analyzer to the ports of one strip-line and then matching the unused ports to the characteristic impedance (Fig. 5.38). The cable calibration is then an easy process.

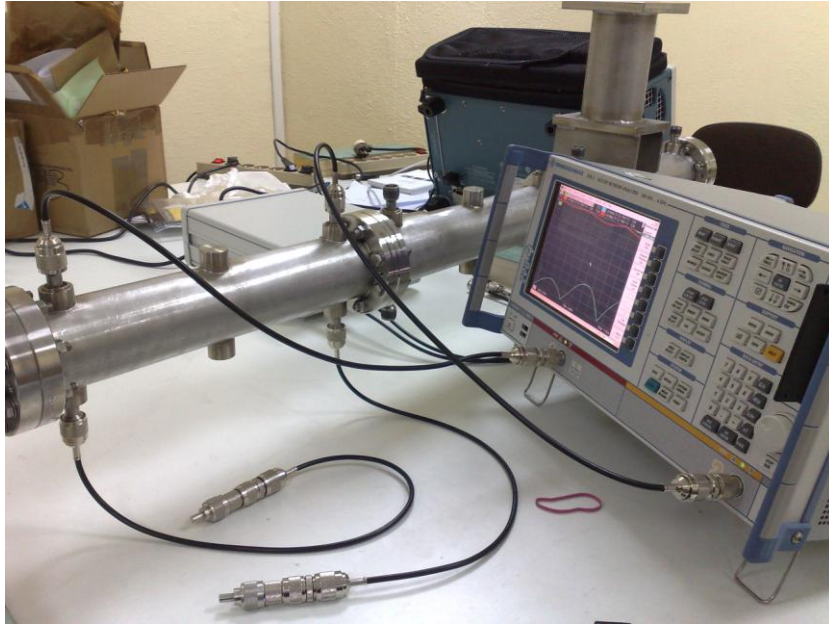


Fig. 5.38 Direct S parameter measurement

Obviously, the scattering parameters obtained (S_{11} and S_{21}) are not the same as when the other strip-line is fed by opposite signal¹⁴ and cannot be compared to Fig. 5.11. Indeed, the scattering parameter obtained is different because the device structure is also different¹⁵. However, the purpose of this test is to confirm that the device is working as designed. Therefore, the direct scattering parameter measurement can also be simulated in HFSS in order to compare real and simulated response. The simulation is direct straightforward by using a full structure with 4 ports instead of the one shown in Fig. 5.10, and the results can be observed in Fig. 5.39.

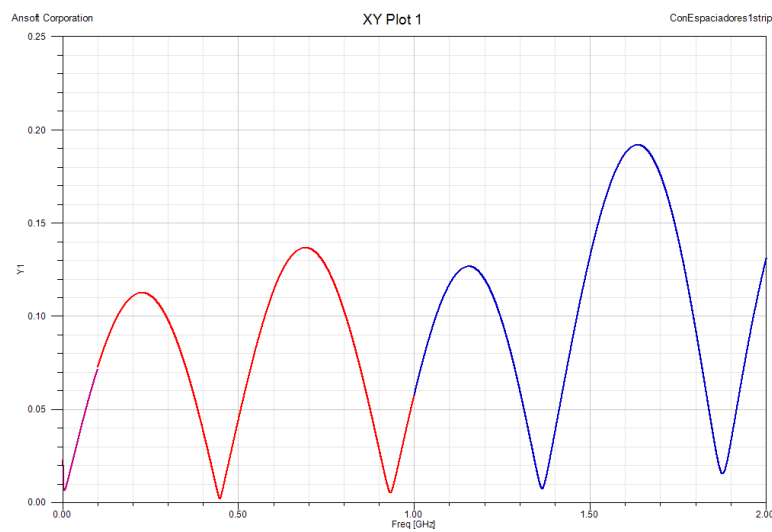


Fig. 5.39 Full 4-port HFSS simulation using real materials

¹⁴ Like in HFSS simulations using electric wall symmetry.

¹⁵ The electric wall cannot be present in the measurements unless using an opposite signal.

The nodes of the transmission due to the matching reflection in the transitions happen at $\lambda/2$ for the approximate electrode length (0.3 m). This represents a $\lambda/4$ frequency shift of the first node in the electric wall symmetry simulation. The almost perfectly matched strip-line (50 Ω) is now unmatched for the new configuration¹⁶ and the scattering parameter response is the same as for a simple unmatched transmission line [3]. The destructive interference of the reflected wave is not affected now by two single unmatched discontinuities in the transmission line (the coax-to-stripline transitions) but by the whole unmatched transmission line.

The measurements from both strip-lines of Tail Clipper number 2 are presented in Fig. 5.40.

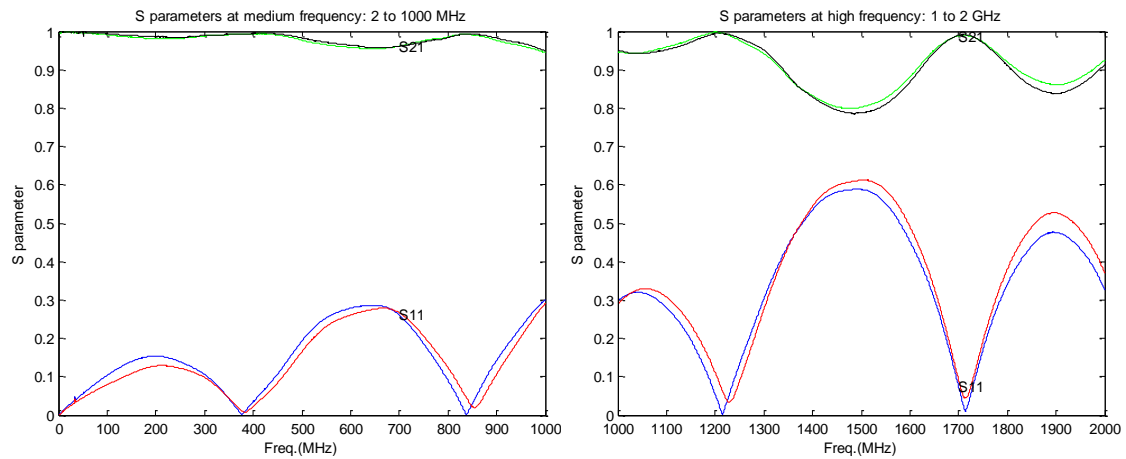


Fig. 5.40 Tail Clipper no. 2 measurements on both strip-lines

Both strip lines in Fig. 5.40 behave quite similarly. The frequency response looks like HFSS simulations. However, at higher frequencies, the measured reflection seems to be much higher than simulated, and the nodes are also displaced. The first can happen because of the roughness of the surfaces which increases the surface resistivity (and losses) of the transmission line, which is much more noticeable at higher frequencies. The second is due to the slightly different transitions in the real device which shift the nodes of the transmission. None of these differences indicate a problem in the device because RF tests are quite “synthetic” tests for pulsed devices. The pulsed power supply test shown in following sections will indicate the real behavior of the strip-lines.

¹⁶ The opposite strip-line is not powered and therefore the electromagnetic fields are not mirrored. The characteristic impedance is therefore different than designed for differential powering (50 Ω).

The four Tail Clippers feature a very similar frequency response. Because of that, only one of them is represented in Fig. 5.40. However, Fig. 5.41 shows a scattering parameter comparison in the 2 to 1000 MHz frequency range for the first strip-line of the four Tail Clippers. The differences between devices are negligible, which indicates a very good and reproducible manufacturing.

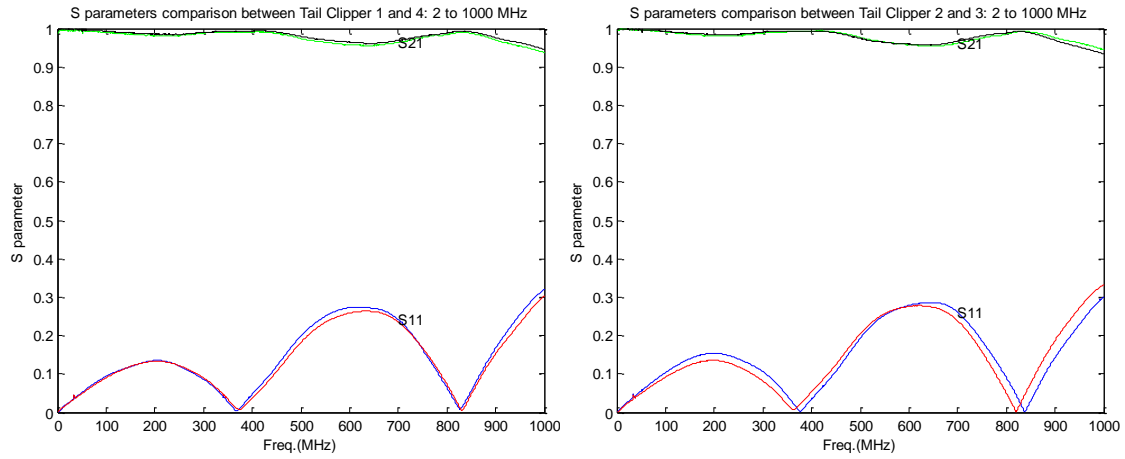


Fig. 5.41 Tail Clippers response comparison

5.4.2 UNLOADED VOLTAGE TESTS

Prior to the dielectric rigidity tests, the full Tail Clipper assembly was leak tested using a Helium mass spectrometer and a calibrated leak. The standard procedure used according to CERN specifications returned a leak value of 2.53×10^{-11} mbar.l/s, which easily fulfils the maximum leak requirements (10^{-10} mbar.l/s).

After 24 hours pumping by using an ALCATEL ATH200 turbo pump, the vacuum measured in the opposite end of the four Tail Clippers was 5.8×10^{-6} mbar. The device is very long and thin and presents high impedance when pumping only from one of its ends. Nevertheless, this vacuum level is enough for the voltages used in this test. However, mild bake-out is required to achieve 10^{-8} mbar specifications.

All the Tail Clipper electrodes were independently tested with DC voltage up to 3 kV to ground (Fig. 5.42)¹⁷. No sparks or other anomalies were observed during the test, which confirms the good dielectric design and manufacturing of the 8 electrodes.



Fig. 5.42 DC high voltage test up to 3 kV

5.4.3 50 OHM LOADED VOLTAGE TESTS

This is the most important test to check the conformity of the Tail Clippers when exposed at working conditions (fast, high voltage pulses). A specific high voltage pulsed power supply was customised for these tests. The pulsed power supply was manufactured by FID GmbH [4]. It features two synchronized pulsed outputs of maximum +5kV and -5 kV respectively, adjustable starting from 1 kV. The pulse duration is also adjustable from 20 ns to 200 ns flat top.

Two 50 Ohm power loads were also necessary to absorb the mirror pulses once they have passed through the Tail Clippers. Both loads have a measuring output port attenuated 50dB from where the high voltage pulse is safely measured in an oscilloscope.

¹⁷ Thanks to the brave people holding the high voltage cables.

The test set-up (Fig. 5.43) is therefore extremely close to the real working regime of the Tail Clipper once it is installed in the accelerator. The pulse width selected for the tests was 20ns, 130 ns and 200 ns, at a fixed flat top voltage of about 3300 V¹⁸.

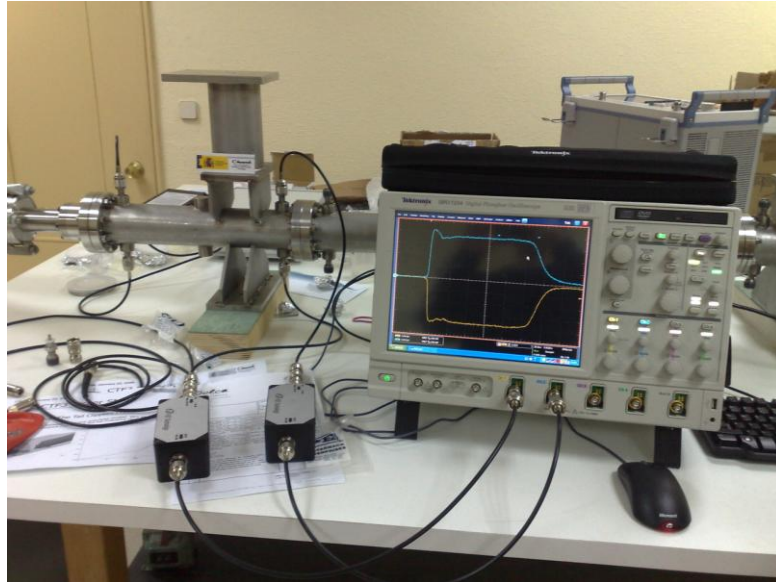


Fig. 5.43 Assembly of the high voltage pulse test

The bare pulses were characterized by directly discharging them on the loads. The pulses passing through the Tail Clippers were afterwards compared to check for discrepancies.

The four Tail Clippers showed identical behaviour, and therefore only the plot of one of them is presented in Fig. 5.44 and Fig. 5.45. These plots show the shape of both mirror pulses when directly discharged to the loads (red and green lines) and when discharged passing through the Tail Clipper (blue and black lines). Pulses were almost unchanged when passing through the strip-lines, which indicates an excellent matching of the strip-lines for the pulse frequency content.

¹⁸ This voltage is slightly higher than in the DC voltage tests because the Kilpatrick criterion predicts increased dielectric rigidity at high frequencies. The real working pulsed voltage will never be over 3000V, and the testing voltage ensures wide conformity with specifications.

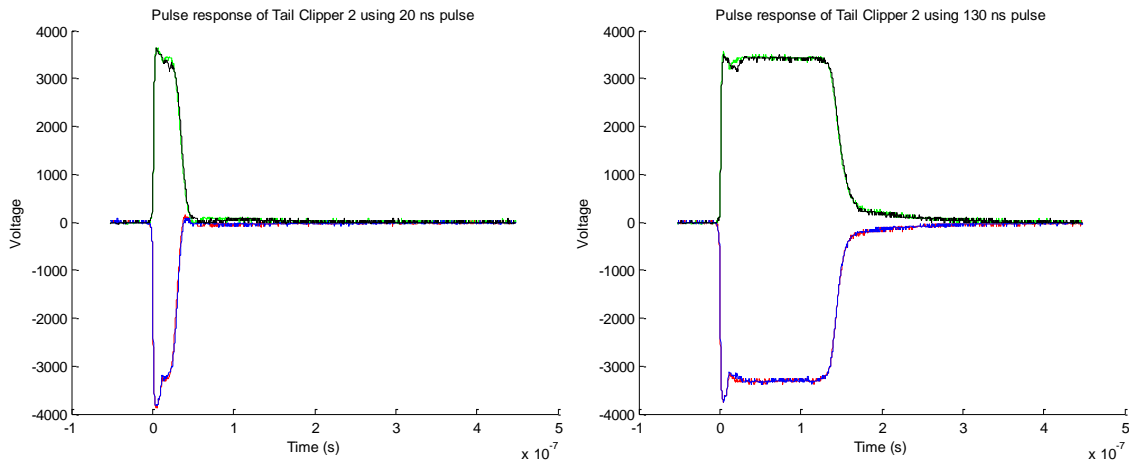


Fig. 5.44 20 ns (left) and 130 ns (right) pulses over the Tail Clipper no. 2

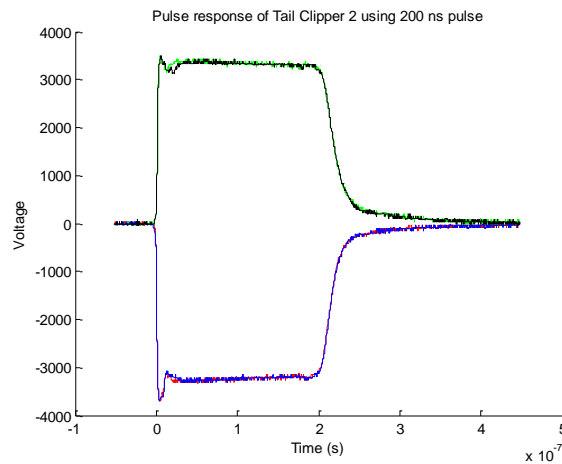


Fig. 5.45 200 ns pulse over the Tail Clipper no. 2

However, both mirror pulses are not exactly anti-symmetrical. It can be observed that the first nanoseconds are slightly different in the positive and negative pulses. This has been demonstrated to happen because of the power loads, which feature slightly different frequency response in the range up to 2 GHz. If one interchanges the loads connection between both strip-lines, the pulse response is also interchanged as expected, which proves that the asymmetry is in the loads, and not in the strip-lines.

The frequency content of 20 ns pulses (first direct to load and then passing through one strip) is depicted in Fig. 5.46. The Fast Fourier Transform of both signals does not show any significant change, even at frequencies over 2 GHz. The high frequency transmission of Tail Clippers can be considered excellent.

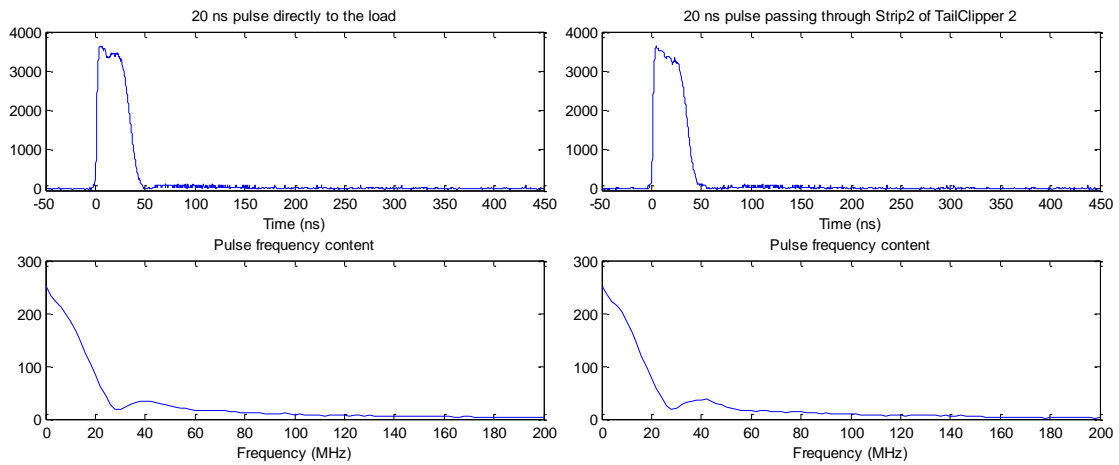


Fig. 5.46 20 ns pulse frequency content: directly to the load (left) and passing through a strip-line of Tail Clipper no. 2 (right)

5.5 CONCLUSIONS

The calculation methodology and fabrication procedures developed by the author in the previous chapters have been successfully applied to the CTF3 TL2 Tail Clippers. The resulting device installed at its final location (CERN's CTF3 accelerator facility) is shown in Fig. 5.47.



Fig. 5.47 Tail Clippers installed at CERN in CTF3 TL2 zone

The Tail Clippers are the result of the second application of the proposed method, which was firstly applied to the CTF3 CR Kicker. The know-how acquired with the CR Kicker has been therefore applied to the design and manufacturing of these new devices. However, the challenges of the Tail Clippers (mainly the good high frequency transmission) are quite different to the kicker's ones and therefore the know-how has been greatly increased.

Like with the kicker, the author has been in charge of the full calculation and design process, together with the monitoring of the fabrication and tests. Some specifications of the electromagnetic design have been developed in close cooperation with CERN (maximum length and voltage, homogeneity, etc.). The manufacturing has also represented a feedback process with the responsible company [5].

5.6 REFERENCES

- [1] **Geschonke, G. and Ghigo, A.** CTF3 Design Report. *CTF3 Note 2002-047*. Geneva : CERN/PS, 2002.
- [2] **Barnes, M.J., et al.** Design of the modulator for the CTF3 Tail Clipper kicker. Albuquerque, New Mexico : Proceedings of the 2007 IEEE Particle Accelerator Conference, 2007.
- [3] **Pozar, David M.** *Microwave Engineering*. s.l. : Wiley, 2004. 978-0471448785.
- [4] **FID Technology GmbH.** <http://www.fidtechnology.com>.
- [5] **Trinos Vacuum Projects.** <http://www.vacuum-projects.net/>.

CHAPTER 6

POWER SUPPLY CONSIDERATIONS: PULSED POWER SUPPLY

6.1 PULSE SWITCHING TECHNOLOGIES

6.1.1 INTRODUCTION

Today, many processes require reliable, high power, variable pulse width, and high voltage pulses. Not only high energy physics and accelerators benefit from this technology, but also industrial metal treatment, food sterilization, waste treatment, pollution control and medical diagnostics. Nevertheless, accelerators are the most technology demanding devices among the other applications due to the stability, reproducibility and repetition rate of the required pulses.

Pulsed power supplies are the complementary devices for strip-line kickers. They generate the pulsed power required for the electromagnetic fields between the strip-lines and, therefore, they must fulfil some of the main specifications of a kicker: Flat top stability and reproducibility, pulse repetition rate, rise/fall times, pulse duration, etc. The pulsed power supply should be designed to match the kicker specifications and it is usually customized for the kicker itself. That is the reason why this chapter shows an introduction to pulsed power supply technologies available for strip-line kickers, although this is not the purpose of the present Thesis. The design and optimization of a solid-state pulsed power supply for a strip-line kicker could itself be the subject of a full PhD Thesis. However, the author considers that a brief summary of technologies and a simulation of a pulsed power supply have to be presented in this document as a future starting point for further developments in fast kicker related technologies.

The ideal objective of a pulsed power supply is to provide an instantaneous rise/fall time pulse and perfect flat top (Fig. 6.1), regardless of load current and repetition rate.

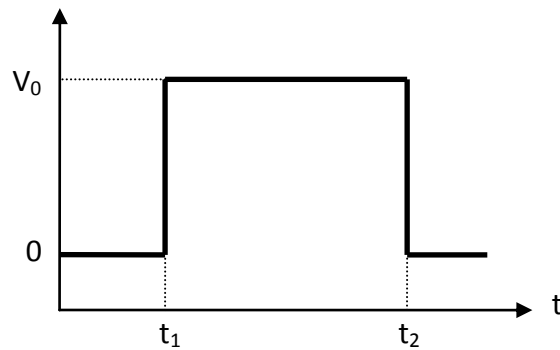


Fig. 6.1 Ideal pulse shape

Basically, an ideal pulsed power supply is formed by a high voltage DC power supply and a simple ideal fast switch. The desired properties of such an ideal switch would be infinite voltage hold-off, infinite off-resistance, zero on-resistance and immunity to transients and voltage reversals.

Historically, vacuum switch tubes or thyratrons have been used as the switches of high-voltage pulsed power supplies [1]. The non-ideal behaviour of these conventional switches includes a large effective voltage drop, limited current capability and speed, high maintenance and complex driving and protection circuitry. Nevertheless, they have provided a nearly exclusive solution to the problem of high-voltage switching until recently because no cost-effective alternatives were available.

As accelerator requirements become more demanding, some of these conventional switching devices are inadequate in terms of lifetime, repetition rate and pulse width modulation. Recent developments of semiconductor devices for power conditioning and traction industries have led to a new generation of high power, high voltage switches which can successfully replace the traditional vacuum tube switches. These devices are the Metal Oxide Semiconductor Field Effect Transistors (MOSFETs) and Insulated Gate Bipolar Transistors (IGBTs), which can be considered very close to the “ideal switches” in comparison with the old vacuum tubes. They can switch on and off large amounts of power using small energy in the triggering circuitry. MOSFETs are ideal for extremely fast applications while IGBTs can handle more power and voltage [2]. Both switches are suitable for pulsed power supplies in kicker devices and they feature the following advantages compared to traditional systems:

- Efficiency > 90%
- Low component cost
- Very high pulse power density ($> 10 \text{ MW/m}^3$ peak power)
- High pulse repetition rate (up to 400 kHz)
- Very small rise/fall times
- Variable pulse lengths
- High reliability

However, for systems like the Tail Clippers presented in chapter 5, only the MOSFETs feature the required switching speed.

6.1.2 SWITCHING TOPOLOGIES

Solid state switches can only manage a couple of thousand volts and amps. Indeed, the higher is the voltage supported, the lower is their switching frequency. Its series/parallel association is therefore required to achieve higher voltages and currents for fast pulse generation. Two circuit topologies can be successfully used to build a pulsed power supply for accelerator applications [3]: Stacked switch topology and inductive adder topology.

Stacked switch topology

This topology is made by connecting in series as many solid state devices as required to achieve the voltage requirements (Fig. 6.2).

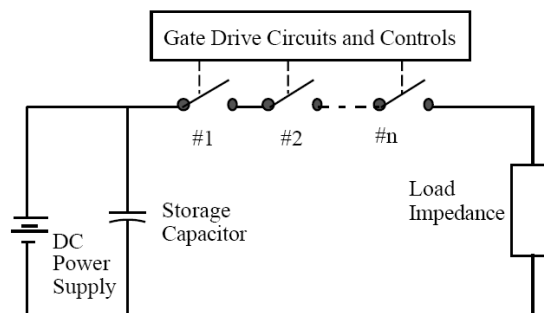


Fig. 6.2 Stacked switch topology

A DC power supply charges a capacitor bank when the switches are opened. The pulse width and repetition rate are given by the time that the switches are closed. The maximum pulse width is only limited by the capacitor charge, starting in a minimum pulse width given by the capabilities of the switches. The rise/fall times of the pulses are determined by the switching characteristics of the solid state devices.

The uniform triggering of the series solid state devices is extremely important. They should be triggered simultaneously to avoid high voltage grading accumulated in a few switches because these devices are extremely sensitive to over-voltages. An equalizing circuit is necessary for a safe and reliable operation. In addition, transient state voltages can also be very dangerous if not carefully studied. This topology is simple to build and cheap but triggering and protection systems are complex. Therefore it is not very robust.

Inductive adder topology

The voltages generated by a number of 1:1 pulse transformers are stacked in series in the secondary windings, as show in Fig. 6.3.

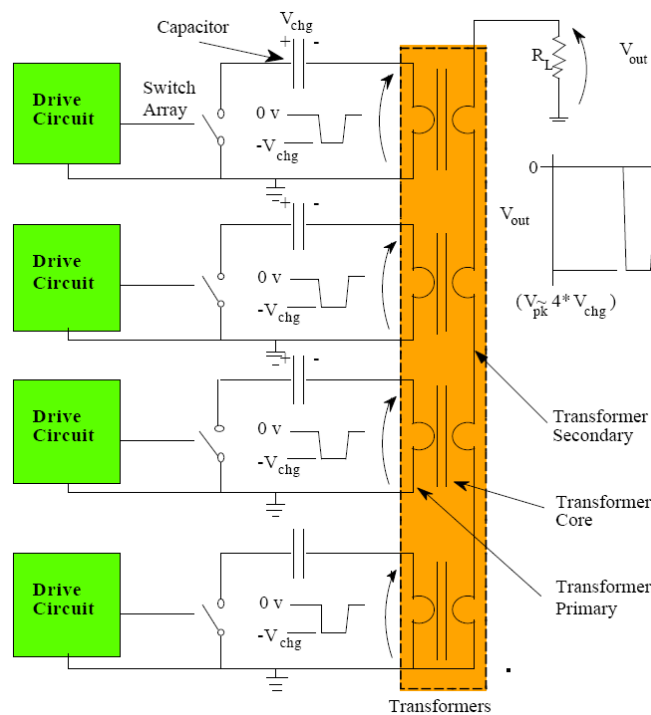


Fig. 6.3 Inductive adder topology [3]

This design does not need to handle high voltages in the solid state devices. The high voltage is confined in the secondary winding of the transformers, which can be a simple metal rod inside a coaxial transformer [4]. In addition, DC power supply and capacitors do not need to support the voltage requirements of the load. The electric insulation ensures a more reliable operation of the power supply. However, the transformers must be carefully designed to reduce inductance (allowing fast pulses) and permit long pulse widths, which are very limited by the magnetic core characteristics. The magnetic cores must be demagnetised after every pulse to obtain good pulse reproducibility.

Although the transformers represent a challenge in the design and a cost increase, the lower voltage and easier triggering circuits make this topology suitable for many pulsed power supplies.

A presentation dealing with these two solutions, advantages and disadvantages for the first designs of the CTF3 pulsed power supplies can be found in [5; 6]. The same approach can be found in [7] applied to an electric kicker.

6.2 SIMPLIFIED MATLAB-SIMULINK MODELS OF POWER SUPPLY TOPOLOGIES

Both previously presented topologies have been modelled and simulated using MATLAB-SIMULINK SimPowerSystems blockset. These simulations are very simplified models which aim to show the feasibility of both topologies for the power supply of one Tail Clipper. Triggering control in the models has been simulated as ideal. For further information and schematics about real devices, check the given references.

6.2.1 STACKED SWITCH TOPOLOGY

The simulated model is presented in Fig. 6.4. MOSFET characteristics have been taken from [8]. The selected MOSFETs can deal with 1200 V and 88 A peak. Therefore, for Tail Clipper specifications shown in Chapter 5, three stacked MOSFETs are required.

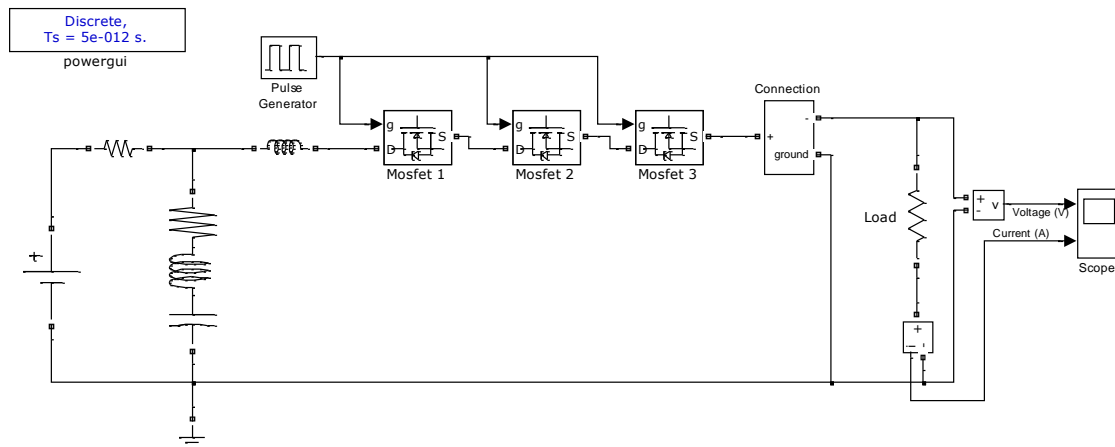


Fig. 6.4 Stacked MOSFET schematic

The snubber protection circuit for MOSFETs is a 2 k Ω resistance. The gate is controlled by an ideal Simulink pulse generator, which simultaneously closes the three MOSFETs at $t=25$ ns and opens them at $t=125$ ns (100 ns pulse width). In a real application, and considering the very short time ranges, the different inductances in the gate circuits should produce some delays in the switching signals that may be dangerous for the devices (overvoltages). Equalization electronic circuits are able to balance these delays but require a particular adjustment.

The DC high voltage power supply outputs 2800 V in open circuit and charges a 1 μ F capacitor bank which is simulated together with its inductance (15 nH) and resistance (5 m Ω). The capacitors are already charged when the simulation starts.

The output proposed for the power supply is a 5 cm coaxial cable¹ directly connected to a 50 Ω load (labelled as “Connection” in the model of Fig. 6.4). This will be afterwards changed to include the Tail Clipper in the simulation.

¹ This block will be detailed in the following section.

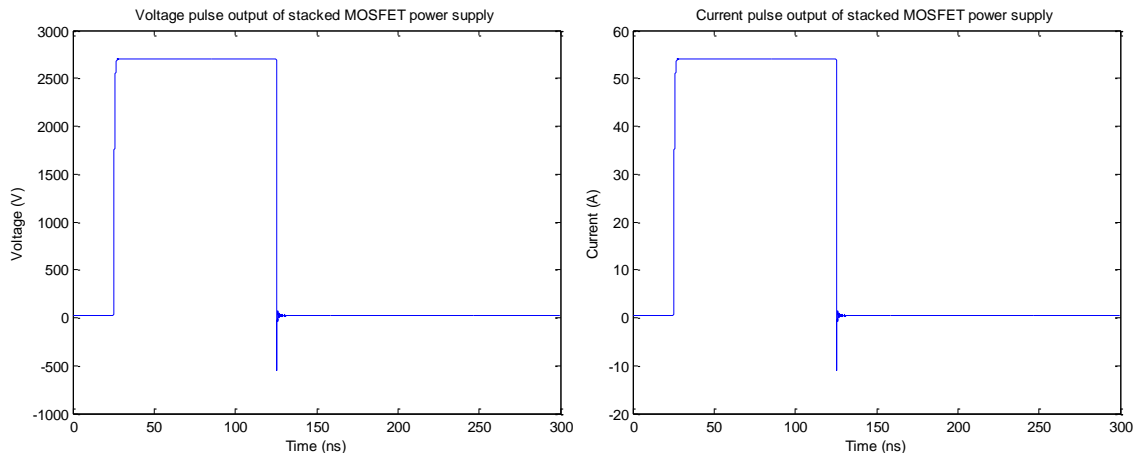


Fig. 6.5 Voltage and current pulses directly over a 50 Ohm load

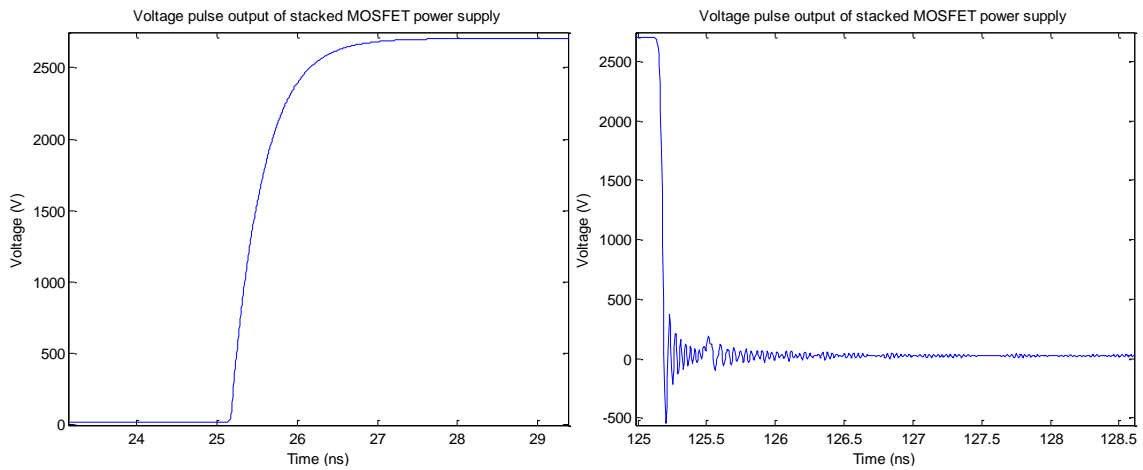


Fig. 6.6 Rise and fall time details

The pulse shape obtained in the simulation is shown in Fig. 6.5. The pulse is very good because of the simplifications. Flat-top voltage and currents obtained are the maximum values specified for the Tail Clippers application. The rise time is about 2 ns (Fig. 6.6). However, there is some overshoot in the pulse decay caused by the connection of the distributed inductance and capacitance of the coaxial cable.

6.2.2 INDUCTIVE ADDER TOPOLOGY

An inductive adder model (Fig. 6.7) has been built using the topology presented in [4]. However, the MOSFET selected for this example is identical to the stacked topology MOSFET (rated to 88 A peak) and consequently it is not required to install 6 sub-circuits of two parallel MOSFETs (as shown in [4]) to handle the Tail Clippers current (Fig. 6.8). However, the required voltage is higher than indicated in [4] and therefore three secondary transformers have been connected in series to obtain the desired voltage.

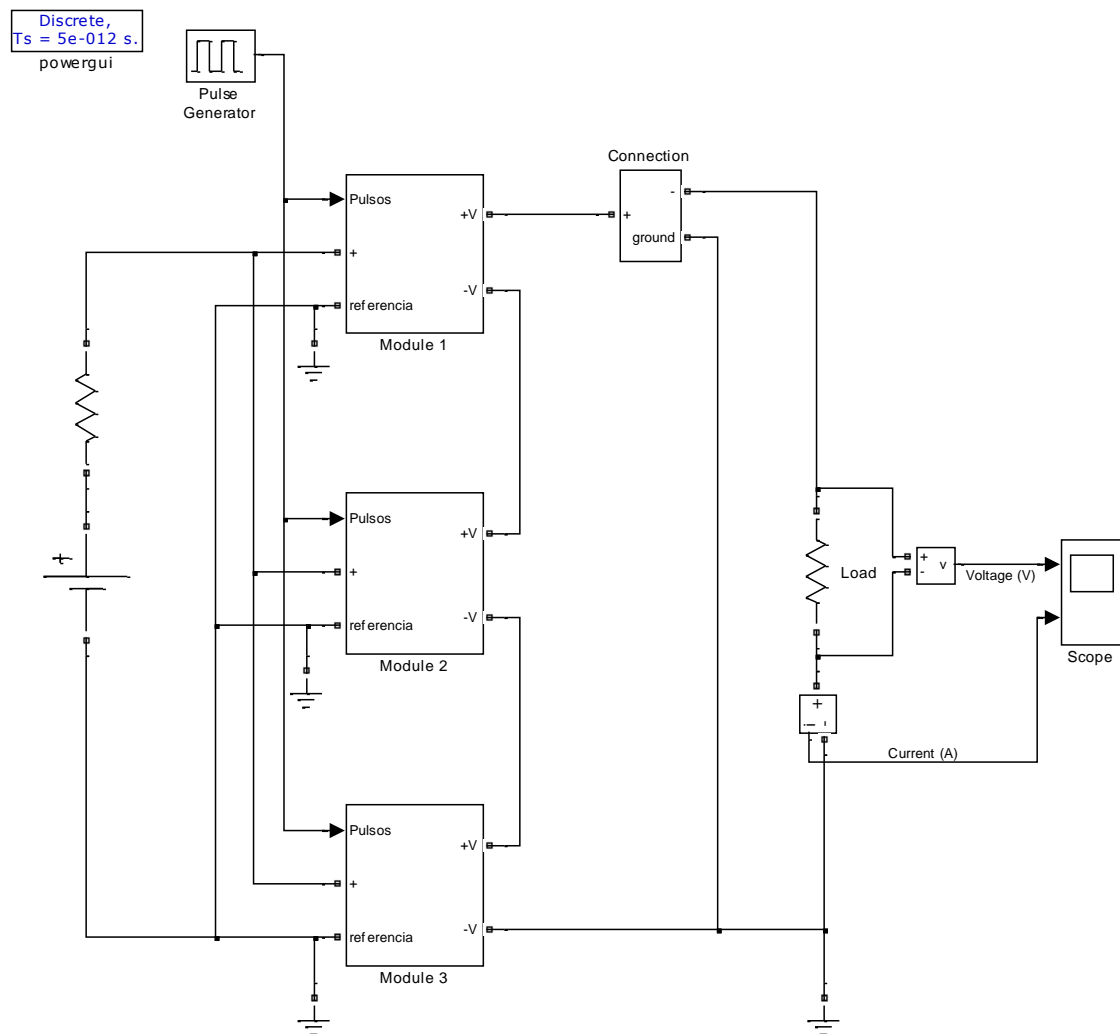


Fig. 6.7 Inductive adder schematic

Each module (Fig. 6.8) is composed by a MOSFET sub-circuit (Fig. 6.9), a diode to control the charge and discharge of the capacitor and a 1:1 transformer² for insulation. The three modules are connected in parallel to a DC power source of 1/3 the required voltage of the load (933 V). The MOSFET subcircuit contain the storage capacitor (1 μ F, 15 nH and 5 m Ω), the DC power input inductance and the MOSFET device. The capacitors are already charged when the simulation starts.

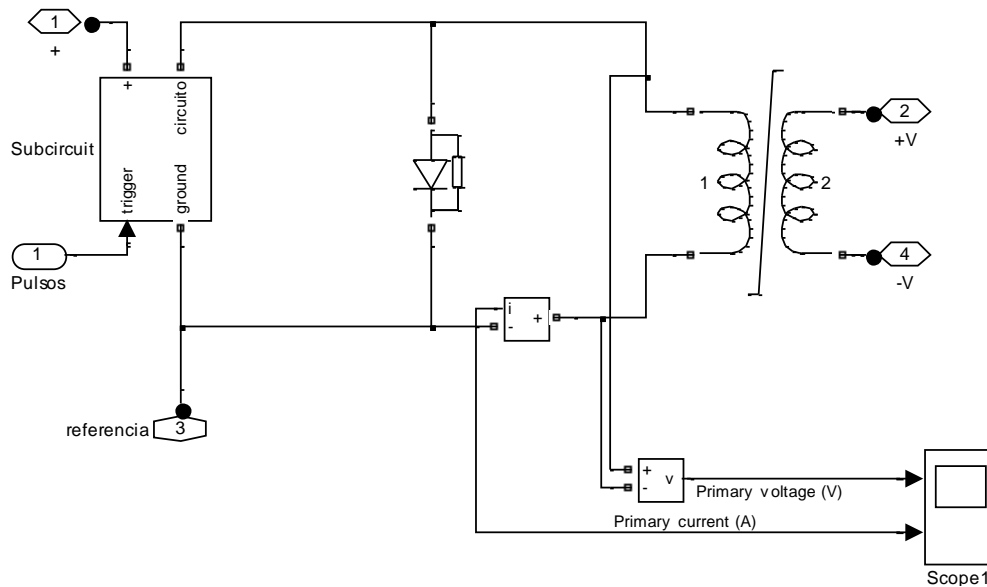


Fig. 6.8 Inductive adder module circuit

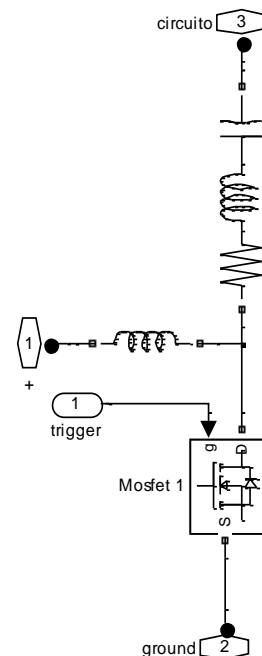


Fig. 6.9 MOSFET sub-circuit

² The transformer is the most complex part of this topology. It is coaxial shaped and uses a Metglas® core to improve pulsed performance. For more information, check the given references.

The schematic circuit of an inductive adder module is presented in Fig. 6.10 for an easier view of the circuit formed by Fig. 6.8 and Fig. 6.9. This circuit presents a Cuk type topology. When switch is OFF, the diode is forward biased and the capacitor is charged through the DC power input inductance. When the switch is triggered to ON state, the voltage of the capacitor is applied over the diode and turns it OFF. The capacitor is consequently discharged through the transformer winding. When the switch is turned OFF again, the diode turns ON and the capacitor is recharged from the DC power source.

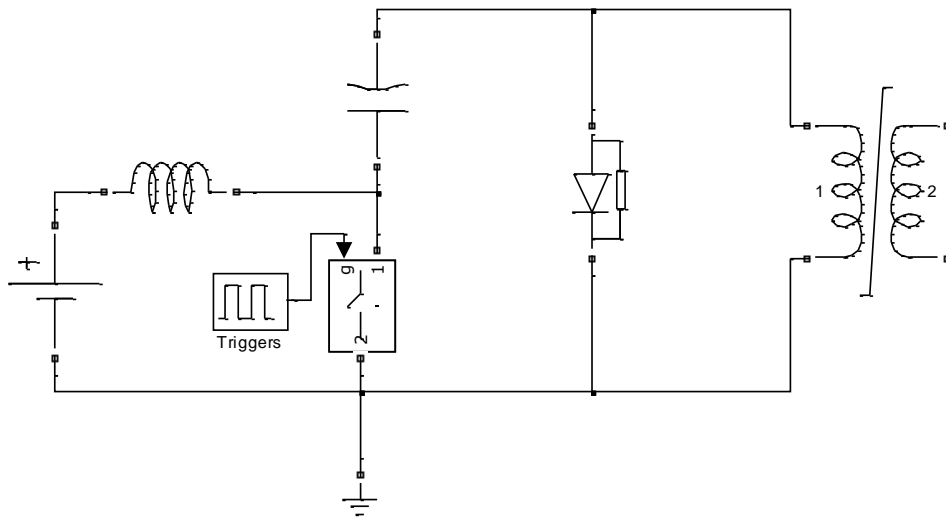


Fig. 6.10 Simplified schematic of an inductive adder module

The secondary of the transformers is connected to a 5 cm long coaxial cable directly connected to a 50 Ω load. This will be afterwards changed to include the Tail Clipper in the simulation.

The results obtained from the simulation can be observed in Fig. 6.11 and Fig. 6.12. The voltage and current in the load are in the expected range and the pulse is perfectly shaped. However, the rise time is close to 4 ns, longer than the maximum acceptable rise time for the Tail Clipper 0.3 m strip-lines (3 ns). The rise time can be reduced by altering the parameters of the transformer windings (mainly reducing the inductances). Indeed, this simulation is useful to determine the transformer parameters required for a given application, which is the key point of this topology; nevertheless, since a commercial power supply was used for the commissioning of the Tail Clipper (see section 5.4.3), the study has not been considered in this brief simulation.

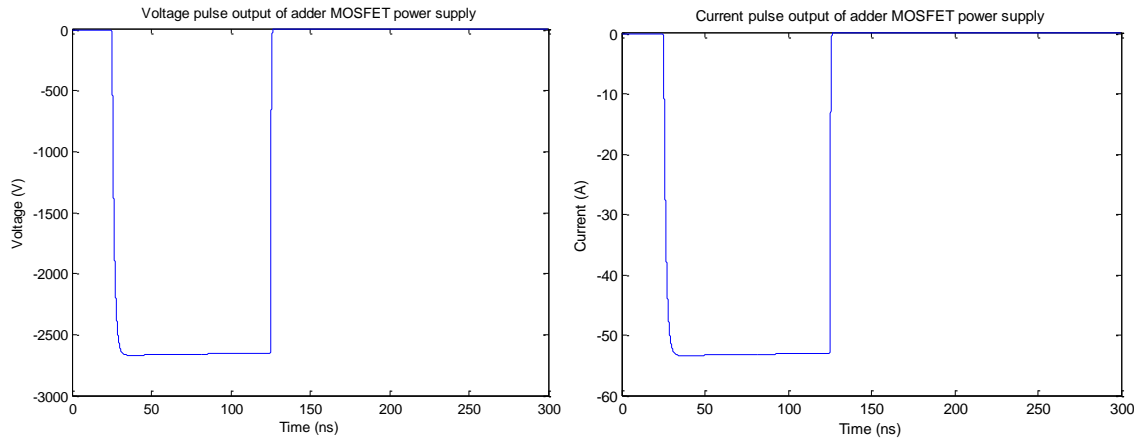


Fig. 6.11 Voltage and current pulses directly over a 50 Ohm load

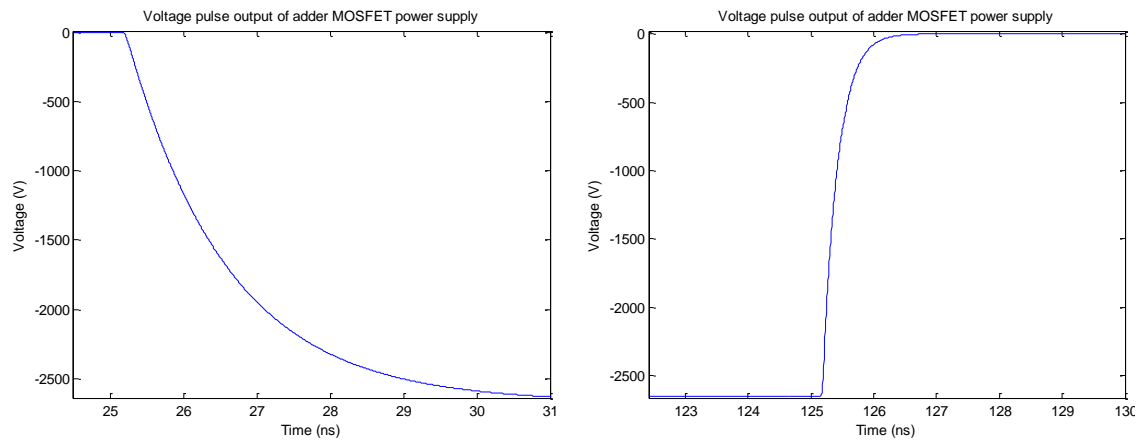


Fig. 6.12 Rise and fall time details

6.3 TRANSMISSION LINE MODEL OF THE CTF3 TL2 TAIL CLIPPER

The Tail Clipper and the coaxial cables that connect it to the pulsed power supply are RF transmission lines. These devices can be simulated like any distributed parameters line by dividing them in small sections (Fig. 6.13) where the electric and magnetic fields (voltage and current) can be considered constant at a given time instant.

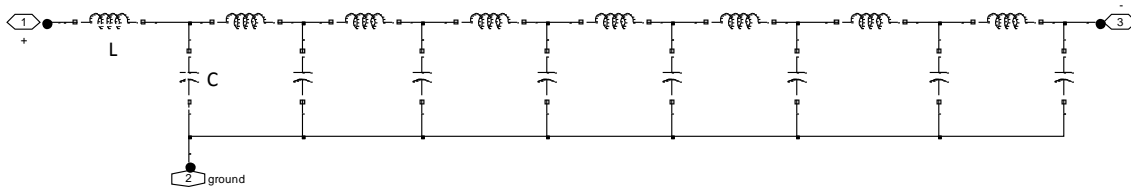


Fig. 6.13 Distributed impedances forming a lossless transmission line

A safe-side approximation is that the fields can be considered constant in $1/20$ of the wavelength, which is 15 mm for 1 GHz frequency. The Tail Clipper (0.3 m electrodes) is therefore well defined for this simulation if the inductance and capacitance per unit length are divided in 20 parts of 15 mm³.

The Tail Clipper inductance L_0 and capacitance C_0 parameters per unit length are obtained from the characteristic impedance, as it was shown in Chapter 2. The inductance value of one of the 20 inductances of the transmission line model is calculated as $L_0 \cdot l/20$. The capacitance is also calculated as $C_0 \cdot l/20$. Obviously, only one of the strip-lines is simulated, the other would need a similar power supply synchronized in opposition. The coaxial cables are modelled as lossless RG-58/U cables whose typical capacitance and inductance have been obtained from manufacturer's catalogues.

6.4 PUTTING ALL TOGETHER

One Tail Clipper module strip has been connected to the pulsed power supply and to the 50 Ω load using 0.5 m RG-58/U cables⁴. The following sections show the simulations of both pulsed power supply topologies feeding the 50 Ω load through the Tail Clipper transmission line.

³ Note here that losses are not being considered for the modelling of the transmission lines. This is a good approach for these circuit topology simulations.

⁴ RG58/U cable does not support high voltage (about 2000 V peak max.). However, the extremely fast pulsed application in this case permits the overrating of its characteristics.

Stacked switch topology feeding the Tail Clipper

The simulated circuit is presented in Fig. 6.14. The Tail Clipper module is connected between the RG-58/U cables and then to the load. The rest of the circuit parameters are similar to the previously simulated power supply in section 6.2.1.

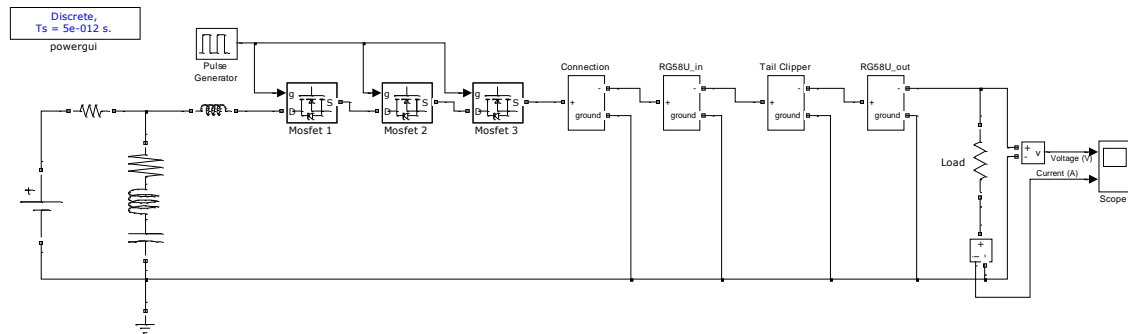


Fig. 6.14 Stacked switch power supply connected to the Tail Clipper

The pulse is barely affected by the integration of the Tail Clipper (Fig. 6.15), which confirms the experimental results of Chapter 5. There is an additional ripple after the pulse rise and decay (Fig. 6.16) due to small resonances between the new inductances and capacitances introduced by the Tail Clipper model together with the power supply components.

In addition, the pulse is a bit delayed after the 25 ns triggering time (visually about 5 ns). This is expected because of the required time for the power transmission to travel from the power supply to the load. The transmission lines are 0.5+0.5+0.3 m long, which corresponds to about 4.3 ns time at the speed of the light⁵. This delay also appears in the pulse decay.

⁵ The simulated delay time is longer because of the velocity factor of the coaxial cables. The wave does not propagate at the speed of light because of the coaxial cable dielectric, whose influence is included in the capacitance value of the transmission line.

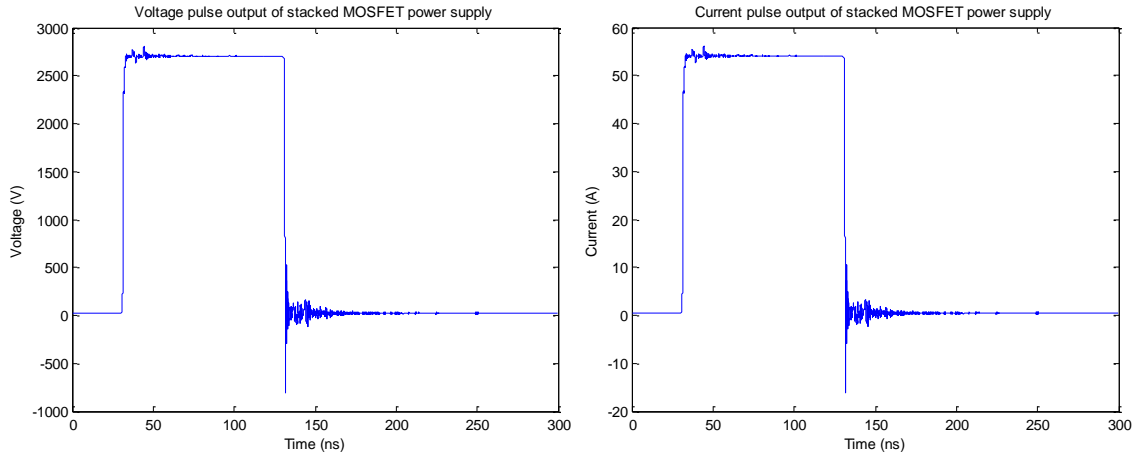


Fig. 6.15 Voltage and current pulses passing through Tail Clipper

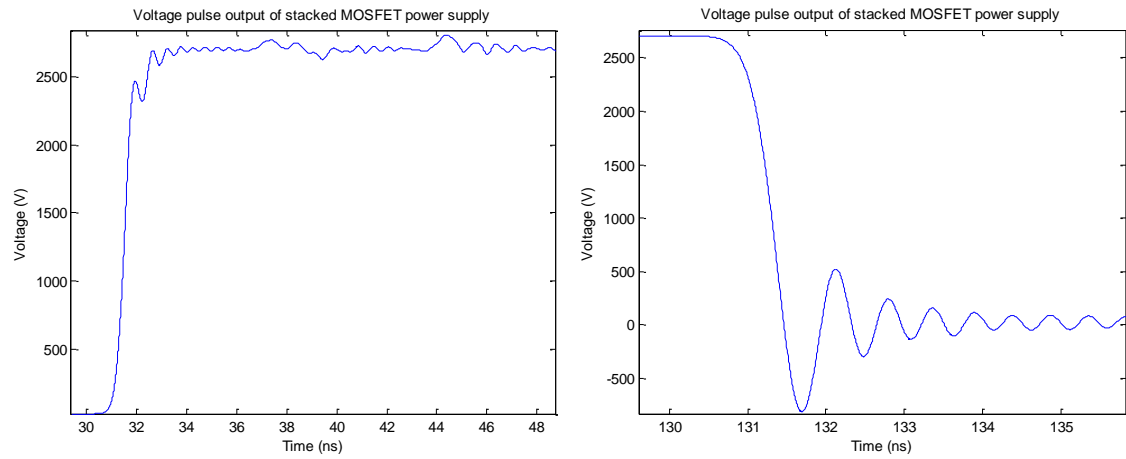


Fig. 6.16 Rise and fall time details

Inductive adder topology feeding the Tail Clipper

The complete diagram using the inductive adder power supply can be observed in Fig. 6.17. The Tail Clipper and its connection cables have been integrated as for the stacked circuit simulation, without changing the power supply parameters of section 6.2.2.

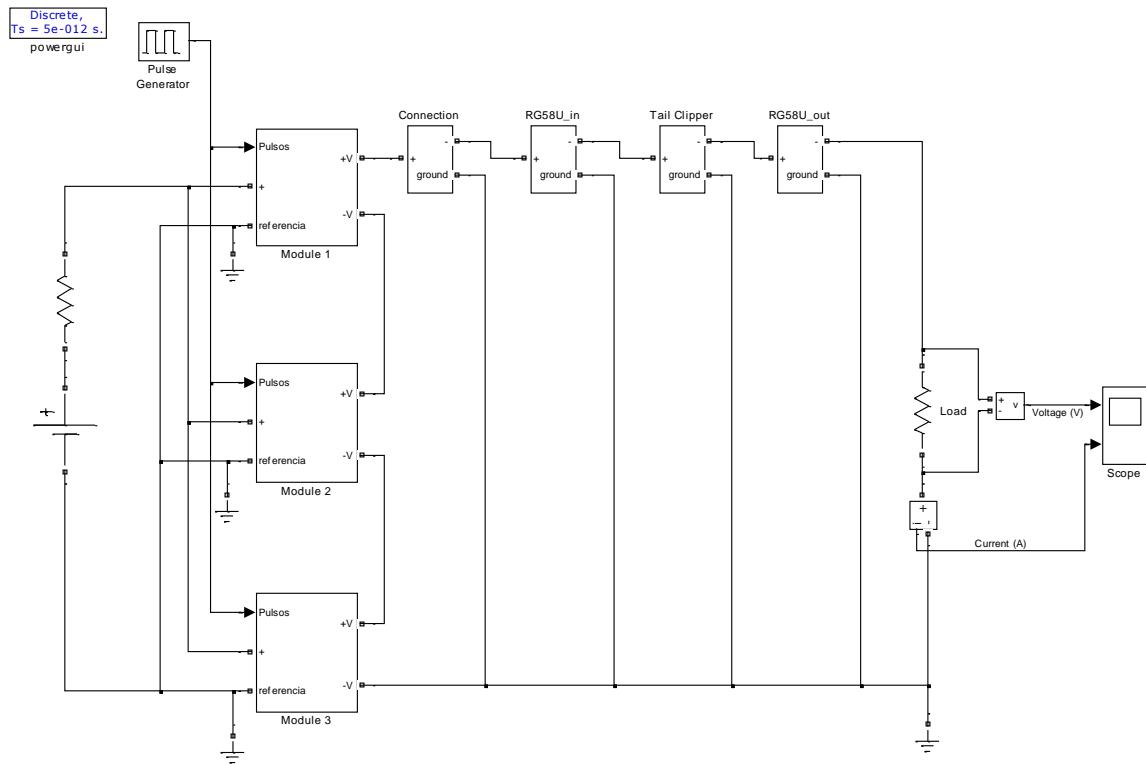


Fig. 6.17 Inductive adder power supply connected to the Tail Clipper

The pulse is again barely affected by the Tail Clipper system (Fig. 6.18). An additional ripple also appears in the pulse but it is less significant than in the stacked topology due to the transformer smoothing effect.

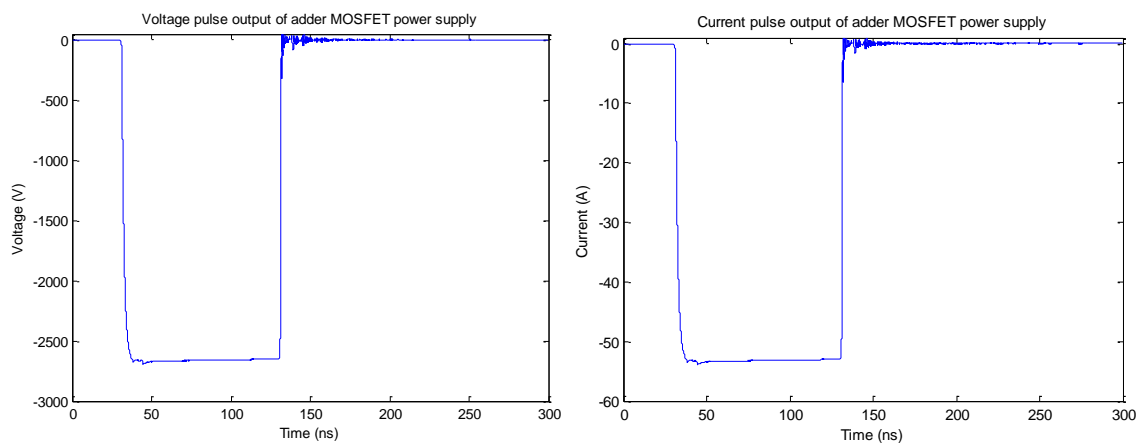


Fig. 6.18 Voltage and current pulses passing through Tail Clipper

The delay of the pulse after triggering (Fig. 6.19) is identical to the delay in the stacked simulation because it only depends on the transmission lines.

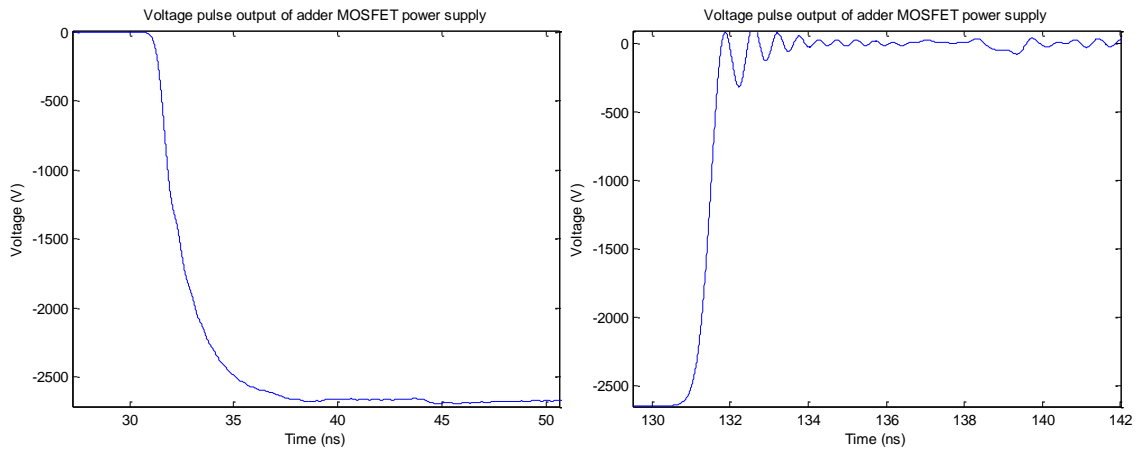


Fig. 6.19 Rise and fall time details

6.5 CONCLUSIONS

A brief summary of power switching technologies valid for strip-line kickers has been shown in this chapter. Strip-line kickers require very fast pulsed power supplies and present solid-state devices can be used to obtain extremely fast switching speeds together with low power consumption and high reliability.

Both analyzed topologies, namely stacked switch and inductive adder power supplies, have their own advantages and disadvantages. Nevertheless, the inductive adder topology presents more reliable characteristics both from the point of view of operation and transient behaviour. MATLAB/Simulink simplified models developed by the author showed the feasibility of using both topologies for strip-line kicker applications. However, a much deep study of each alternative (especially regarding to MOSFET triggering control and transformer construction) is required to design and manufacture any of them. Much more detail on these technologies can be found on given references.

To summarize, this chapter only constitutes an introduction to solid-state, high voltage pulsed power supplies applied to strip-line kickers. However, the indicated references can be very useful for further developments in extremely fast pulsed power supplies using solid-state devices. Indeed, a future work proposed for this Thesis is the complete analysis of both pulsed topologies to identify the best technology to create extremely fast, high voltage pulses in a cost competitive power supply. The manufacturing of several prototypes could be an extremely interesting way to compare the performance and costs of solid-state power supplies in comparison to traditional devices. This technology is promising and it will soon fully displace the old vacuum tube switches even in high voltages and currents applications. Future linear accelerators like CLIC or ILC will require extremely high voltage, fast switching pulses (burst mode) which would benefit from the development of this technology.

6.6 REFERENCES

- [1] **Fann, Chyi-Shyan, et al.** Simulation of Kicker Pulser with Matlab Simulink. *Proceedings of the 2001 Particle Accelerator Conference*. Chicago : s.n., 2001.
- [2] **Kutkut, Nasser.** High Efficiency Power Switches. *Technical Note*. Madison, WI : PowerDesigners, LLC.
- [3] **Cook, E.G.** Review of Solid-State modulators. Monterey, California : XX International Linac Conference, 2000.
- [4] **Wang, L., Caporaso, G.L. and Cook, E.G.** Modelling of and Inductive Adder Kicker Pulser for a Proton Radiography System. Las Vegas : Lawrence Livermore National Laboratory, 2001.
- [5] **Barnes, Mike.** CTF3 Strip-line Kicker. <https://edms.cern.ch/document/734146/1>. Geneva : EDMS, CERN, 2006. 734146.

- [6] **Barnes, Mike y Fowler, Tony.** Kickers for CTF3 and CLIC. *Presentation to CTF3 team.* Geneva : s.n., 2006.
- [7] **Barnes, Mike and Wait, Gary D.** A 25-kV 75kHz Kicker for Measurement of Muon Lifetime. *IEEE TRANSACTIONS ON PLASMA SCIENCE.* October 2004. Vol. 32, 5.
- [8] **Advanced Power Technology.** POWER MOS 7 FREDFET.
http://www.microsemi.com/datasheets/12057B2FLL_LFLL.PDF. s.l. : Microsemi Corporation, 2004. 050-7083 Rev C.

